International Compilation of Research and Studies in
ENGINEERING

EDITOR

PROF. DR. SELAHATTIN BARDAK

PROF. DR. COŞKUN ÖZALP

SERÜVEN
YAYINEVİ

Genel Yayın Yönetmeni / Editor in Chief • C. Cansın Selin Temana

Kapak & İç Tasarım / Cover & Interior Design • Serüven Yayınevi

Birinci Basım / First Edition • © Aralık 2025

ISBN • 978-625-8682-05-2

Serüven Yayınevi / Serüven Publishing
Türkiye Adres / Turkey Address: Kızılay Mah. Fevzi Çakmak 1. Sokak
Ümit Apt No: 22/A Çankaya/ANKARA
Telefon / Phone: 05437675765
web: www.seruvenyayinevi.com
e-mail: seruvenyayinevi@gmail.com

Baskı & Cilt / Printing & Volume
Sertifika / Certificate No: 47083

INTERNATIONAL COMPILATION OF RESEARCH AND STUDIES IN ENGINEERING

EDITORS

PROF. DR. SELAHATTIN BARDAK

PROF. DR. COŞKUN ÖZALP

CONTENTS

Chapter 1

Chapter 2

Chapter 3

Chapter 4

Chapter 5

Chapter 6

Chapter 1

INVESTIGATION OF THE USABILITY OF FRUIT PEELS AND SEEDS IN DYE ADSORPTION

Çiğdem SARICI ÖZDEMİR[1]

---

[1] Prof. Dr. Inonu University, Faculty of Engineering, Department of Chemical Engineering, Malatya, Turkey, https://orcid.org/0000-0003-2129-3044

1. INTRODUCTION

Technology developed to meet human needs brings both advantages and disadvantages. Chief among these is the pollution it causes to the environment. As a result, water becomes polluted, then contaminated with agricultural products, and then contaminated with our food and drink, entering our bodies and poisoning us. Many methods are used to remove pollution. Adsorption, the trapping of liquid and gas molecules in the pores of solids, is the most common. Adsorption can be performed in two ways: batch and continuous. In batch systems, a certain amount of adsorbent is added to the solution to be contaminated, and mixing is performed over time. In continuous adsorption processes, a bed of adsorbent is prepared in a column, and the solution is continuously added to this bed until the bed reaches saturation. Both methods have parameters that affect adsorption performance. In batch systems, the properties of the adsorbent and the adsorbed are more important, such as time, concentration, adsorbent amount, and pH. In continuous systems, where changes such as bed volume, bed height, and column diameter are also considered, the adsorbed and adsorbent properties, as well as the properties of the column in which the process takes place, also affect the efficiency[1-3].

In the adsorption mechanism, which involves many steps, the adsorbent, or solid, plays the most important role. After molecules are transported from the solution phase to the solid surface, the entire retention process develops and varies depending on the pore size, structure, and shape of the surface. The methods for obtaining such a crucial adsorbent will also be of great importance. Various adsorbents can be produced from different raw materials using chemical or physical activation methods, depending on temperature and time. The key is that this production process is economical and possesses the desired properties. With new developments in agriculture, product diversity is also increasing. Fruit peels, seeds, and pulp are discarded into the environment after processing, creating problems. Studies have revealed that agricultural waste can be used as adsorbents by improving their surface properties using appropriate methods[4-5].

Adsorption efficiency varies depending on many factors. These include changes in the amount of adsorbent, temperature, time, solution concentration, and pH. Studies involving concentration changes at constant temperature provide information about the type of adsorption isotherm. Numerous empirical adsorption isotherm equations exist. Numerous analyses, which can be defined as whether adsorption is homogeneous or heterogeneous, occurs in a single layer or in multiple layers, and the heat of adsorption is effective, have led to the emergence of different adsorption isotherms. Linear adsorption model is also referred to Henry's isotherm and it assumes that neighbouring adsorbed molecules do not interact and support the monolayer adsorption mechanism. Therefore, it describes the adsorption process at low concentrations of the adsorbate where the adsorption capacity is linearly related to the equilibrium concentration (C_e, mg.L^{-1}) as

$$q_e = K_{He} * C_e \tag{1}$$

where q_e (mg.g^{-1}) the amount of equilibrium dry adsorbed onto adsorbent, K_{HE} represents Henry's equilibrium constant, which can be obtained from the slope of the graph between C_e and q_e [6].

This study will investigate the adsorption of methylene blue using various agricultural wastes. Methylene blue, a synthetic dye used in various medical fields, can cause undesirable toxicological effects when overdosed. This study will examine the changes in adsorption efficiency with temperature and concentration, and will use apricot kernel shells(AKS), walnut shells(WS), chestnut shells(CS), almond shells(AS), peanut shell (PS) olive stone(OS) and pine cone (PC), as adsorbents.

Adsorption equilibrium data will be used to examine compliance with Langmuir and Freundlich isotherms.

2. MATERIALS and METHODS

2.1. Materials

Agricultural wastes were milled and sieved under 200 mesh. Wastes were dried at 110 °C to prepare adsorbent.

Methylene blue was used as adsorbate in this work. Methylene blue(MB) is cationic dye. MB has the molecular formula $C_{16}H_{18}N_3SCl$ and the molecular weight of 319.85 g.mol $^{-1}$. MB was supplied by Merck. The spectrophotometric determination of MB was carried out using a Shimadzu UV/Vis spectrophotometer in 662 nm. Measurement in 5 milliliters of cuvettes were used.

2.3. Adsorption experiments

Methylene blue solution was prepared in distilled water at the desired concentrations. Adsorption experiments were carried out by agitating 0.1 g of adsorbent with 50 mL solutions of the desired concentration (50 to 250 mg.L^{-1}) at 25 , 40, 60 ºC a thermostatic bath operating at 400 rpm. The amount of dry adsorbed onto adsorbent, q_t (mg.g^{-1}) was calculated by the mass balance relationship, as shown in Eq (1):

$$q_t = (C_0 - C_t)\frac{V}{W} \tag{2}$$

where C_0 and C_t are the initial and time ‘t’ liquid-phase concentrations of the dry material (mg.L^{-1}) respectively. V is the volume of the solution (L), and W is the weight of the dry adsorbent used (g).

3. RESULT AND DISCUSSION

3.1. SEM Analysis

SEM is an important characterization method in determining the surface properties of the adsorbent. With this method, the pore structure of the adsorbent and different formations on the surface can be detected. SEM images of the adsorbents used in this study are given in Figure 1. When the figure is examined, pore formation was detected in all adsorbents. In image (a) of the walnut shell, pore formations of different sizes were detected on the surface, while micropore groups waiting to open were observed in deeper parts. The fibrous structure of the chestnut shell manifests itself in the form of layers with pore formations located between layers. The apricot kernel shell revealed its densely arranged micropore structures in the SEM image. The layered structure of the pistachio shell, similar to the chestnut shell, arises from its soft fibrous texture. Almond shell, which contains secondary groups with a higher mesopore volume, reveals a different SEM image. Layered structures with more dispersed distances between them are observed in pine cone samples. When the SEM image of the olive pit is examined; In some places, mesoporous structures and partially microporosity are noted.

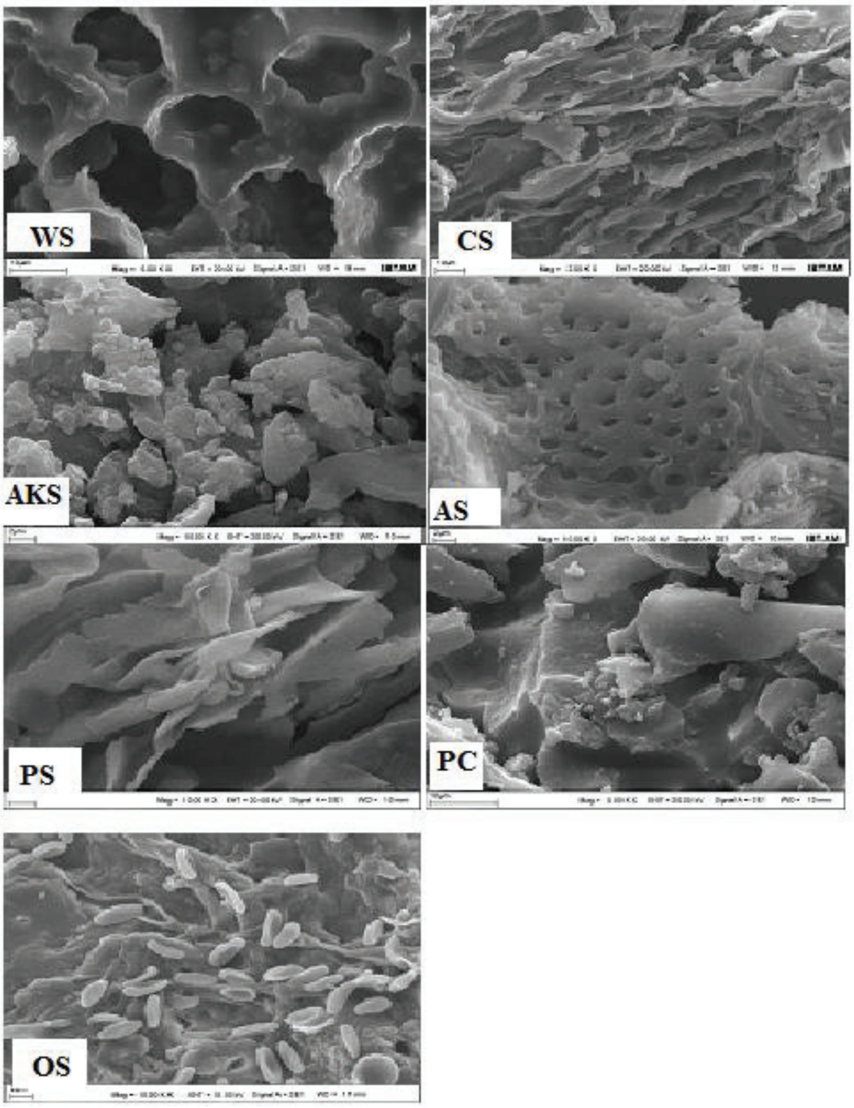

Figure1. SEM figures of samples

3.2. FTIR Analysis

FTIR analysis is crucial for identifying functional groups within the structure. During adsorption, these functional groups can provide evidence of the mechanisms that may be involved in removing molecules from the environment.The FTIR graph of agricultural waste is shown in Figure 2. An examination of the figure reveals that the bands in the 1000-1200 cm^{-1} range in the waste originate from the C-O-C and C-O groups within the structure. The

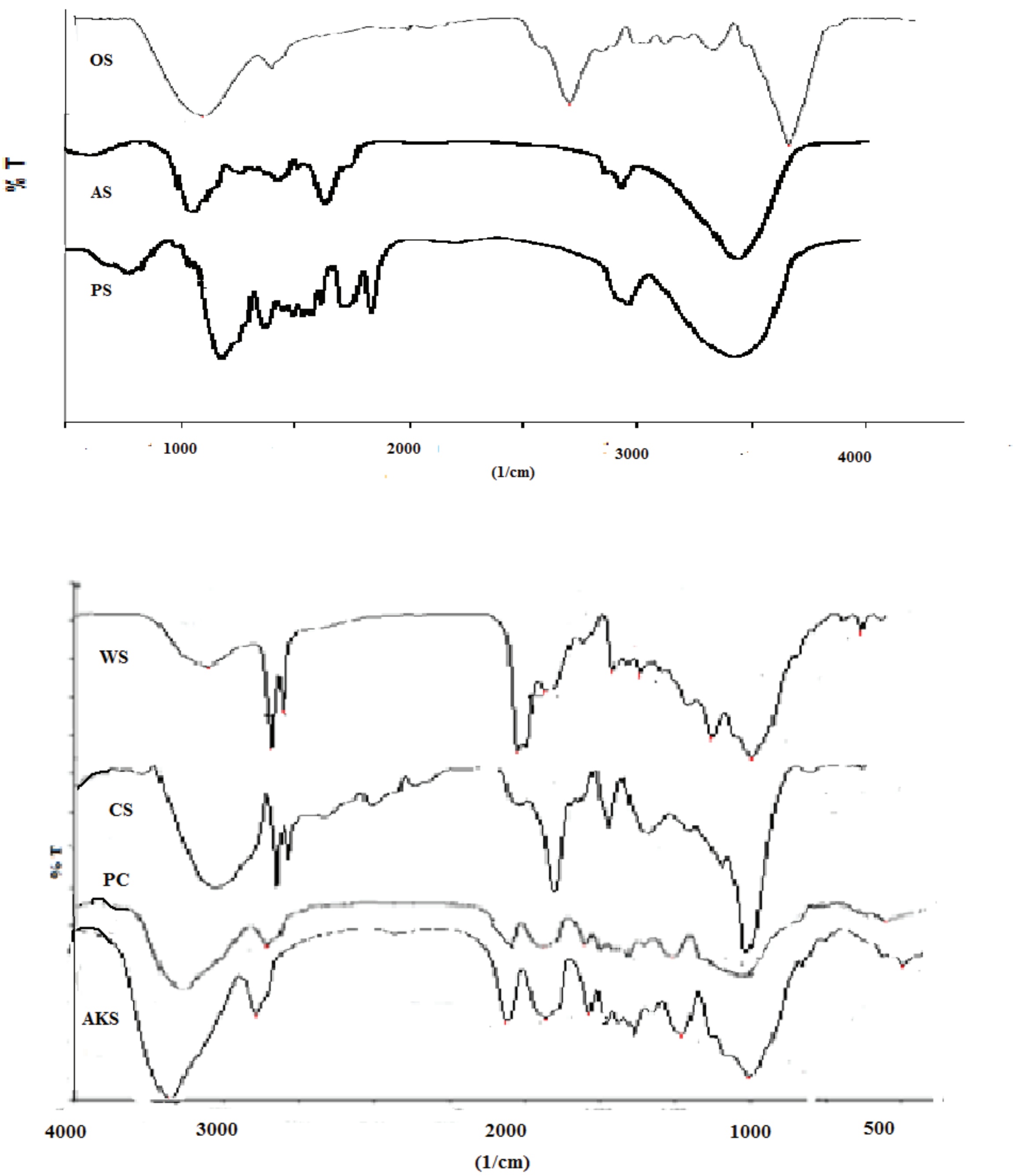

Figure 2. FTIR figures

aromatic C-H group is prominent in the 3200-3500 cm^{-1} range. The peaks appearing at 1600-1700 cm^{-1} belong to carboxylic groups, and these peaks occur at different vibrations in all wastes. Peaks belonging to carboxylic, phenolic, and lactonic groups were identified in all wastes. The aromatic C-H group, with a broad peak area, was observed at the same vibration in all except olive stone waste. The presence of aliphatic groups was more pronounced in olive stone waste[7].

3.3. Effect of temperature and concentration on adsorption

Temperature changes can have different effects on adsorption processes. These effects are particularly evident in adsorption capacity and diffusion pressure changes. Adsorption is generally an endothermic process, occurring spontaneously due to negative Gibbs free energy. Therefore, as temperature increases, adsorption efficiency increases. However, this may not always be observed. It can vary depending on the surface properties of the adsorbent, its structural integrity, and the resulting desorption mechanism. The change percentages in methylene blue adsorption of different types of agricultural wastes are given in Figure 3.

The change in adsorption efficiency depending on temperature and concentration variations can be explained by the diffusion mechanism of molecules into the pores. Migration and transfer of dye molecules from the solution to the adsorbent surface occurs. Dye molecules move towards micropores under the influence of the chemical potential in the mass transfer mechanism. Molecules that settle inside the pores are adsorbed in this way and separated from the solution environment.

An examination of the figure reveals that adsorption efficiency decreases with concentration for all wastes. Adsorption efficiency values are around 80% for AKS, WS, CS, and OS adsorbents, 60% for PC, and 40% for AS and PS. The primary reason for the decrease in efficiency with concentration is pore filling. As the active sites attached to the solid surface are filled with dye molecules, there is no room left for additional dye molecules. When the effect of adsorption temperature on yield is examined, yield values for pine cones, apricot kernel shells, and almond kernel shells increase with increasing temperature. This is due to the secondary groups and similar pore development of the wastes, as can be seen from SEM analyses. For other wastes, efficiency decreases with increasing temperature. This can occur when the adsorption rate coincides with the desorption rate. In other words, while a molecule adsorbs into the pores of a solid, it can simultaneously re-diffuse because the molecule's diameter does not match the pore size. In this case, the adsorption value measured at equilibrium may differ.

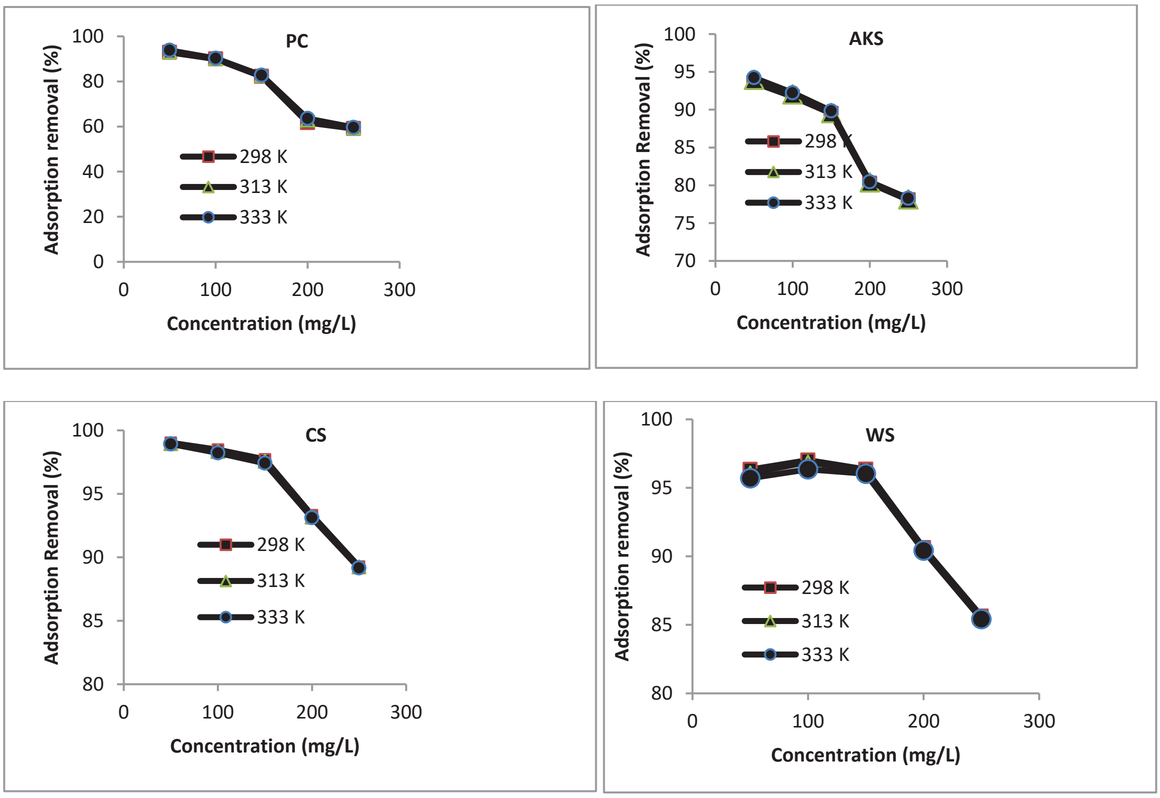

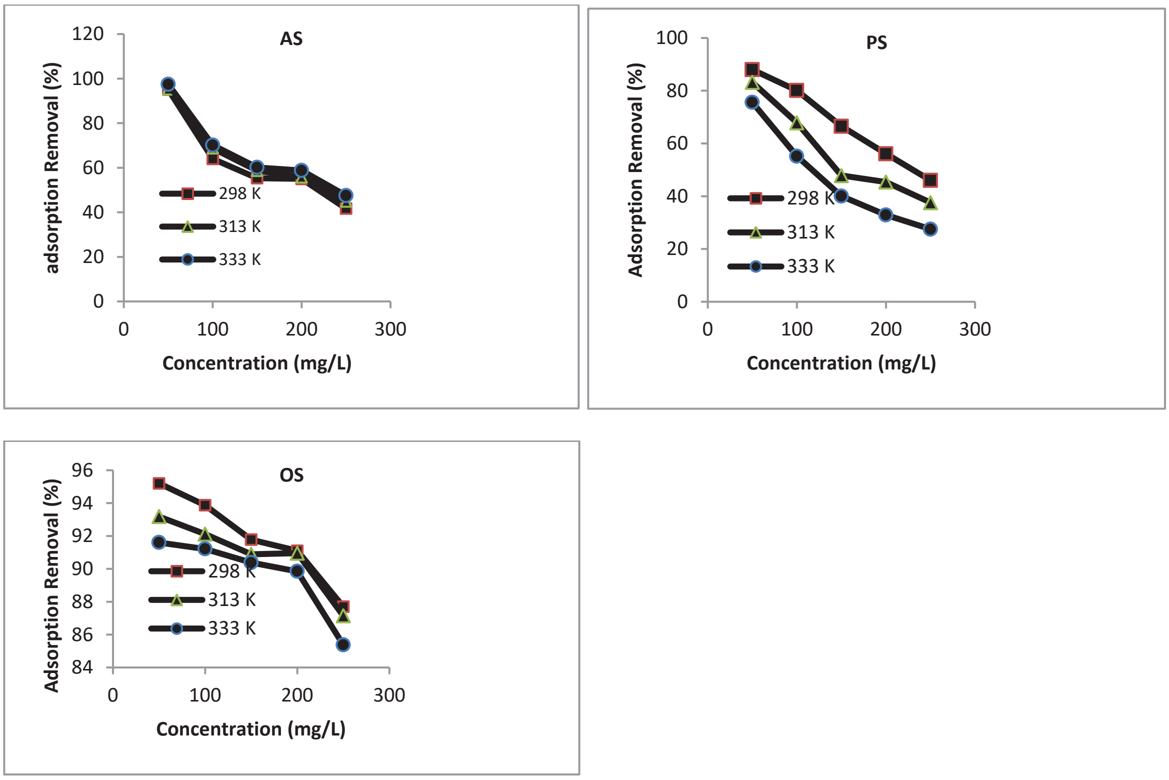

Figure.3. Change of adsorption removal with temperature

3.4. Adsorption isotherms

In the Freundlich isotherm, which is an isotherm derived from the Henry isotherm, it is assumed that the heterogeneous adsorption process takes place on the solid surface. There are different types of adsorption sites. The Freundlich isotherm is expressed as follows[8]:

$$q_e = k_f \times C_e^{\frac{1}{n}} \tag{3}$$

Where Freundlich coefficient k_f and correction factor n can be found by plotting isotherms between $\ln q_e$ and $\ln C_e$.

Another isotherm equation, the Langmuir equation, is valid for chemical adsorption, monolayer physical adsorption, and adsorption from solution. This isotherm equation was developed based on certain assumptions:

- In the adsorption mechanism, a single layer forms on the surface.

- Active centers are equivalent and homogeneous. The surface is perfectly smooth at the microscopic level.

- Adsorption enthalpy is independent of surface adhesion.

- The ability of a molecule to adsorb at a given site is independent of whether neighboring sites are occupied or unoccupied.

The nonlinear isotherm equation is given below[9].

$$q_e = \frac{Qo*b*Ce}{1+b*Ce} \tag{4}$$

The parameter Q_0 (mg.g^{-1}) is the maximum adsorption capacity and b (L.mg^{-1}) is the Langmuir constant.

Using adsorption equilibrium data, the Langmuir constants were calculated from the slope and shift values by plotting C_e against the C_e/q_e value and are given in Table 1. An examination of the table revealed that the values of the constants changed with temperature changes. The maximum adsorption capacity value of 200 mg/g was obtained from adsorption studies conducted with olive pits. Subsequently, higher values were found in studies conducted with apricot pit shells, walnut shells, and chestnut shells. The maximum adsorption capacity obtained from studies conducted with almond pit shells, pistachio shells, and pine cones remained around 70 mg/g. This was similarly determined in the adsorption efficiency calculations. Freundlich isotherm constants were calculated from the shift and slope values by plotting $\ln q_e$ versus $\ln C_e$ graphs. When k_f and n values were examined, it was determined that the lowest k_f and n values were in the olive pit shell. Correlation coefficient (R^2) values indicated that the wastes mostly conformed to the Langmuir isotherm in dye adsorption.

Table1. Isotherm constant

	Langmuir Isotherm			Freundlich Isotherm		
Adsorbent/ Temp.(K)	Q_o (mg.g^{-1})	b (L.mg^{-1})	R^2	k_f (L.g^{-1})	n	R^2
PC						
298	76,93	0,1262	0,984	18,859	3,31	0,864
313	76,93	0,1287	0,987	18,972	3,27	0,871
333	76,93	0,1340	0,989	19,473	3,31	0,888
AKS						
298	125	0,0727	0,984	15,256	2,10	0,949
313	125	0,0761	0,985	15,879	2,11	0,952
333	125	0,0792	0,984	16,379	2,18	0,951
CS						
298	126,01	0,4210	0,995	38,129	2,80	0,930
313	126,01	0,4000	0,995	36,966	2,73	0,935
333	126,01	0,3809	0,995	36,307	2,70	0,943
WS						
298	125,30	0,1778	0,989	25,559	2,29	0,989
313	125,30	0,1702	0,987	24,729	2,26	0,987
333	142,86	0,1321	0,985	22,897	2,15	0,985
AS						
298	58,82	0,0651	0,955	18,784	4,90	0,877
313	62,50	0,0675	0,969	18,859	4,61	0,927
333	66,67	0,0681	0,957	21,955	5,21	0,888
PS						
298	62,51	0,0889	0,999	13,999	3,25	0,935
313	52,63	0,0547	0,978	12,781	5,00	0,966
333	37,03	0,0684	0,997	9,216	4,57	0,976
OS						
298	166,67	0,0659	0,989	14,717	1,64	0,988
313	200	0,0393	0,964	10,288	1,40	0,979
333	200	0,0340	0,942	8,818	1,36	0,964

When the correlation coefficients were examined, the highest results, with a value of 0.99, were obtained from studies conducted with PS and CS adsorbents. When the surface properties of these adsorbents were examined, it was observed from both SEM and FTIR graphs that they consisted of similar structures. The layered structure in the SEM graph is an indicator of single-layer adsorption, one of the fundamental steps in the formation of the Langmuir isotherm[10]. Once the molecule to be adsorbed is placed on this layer, other molecules cannot adhere to it.

4. CONCLUSION

The effects of temperature and concentration on the efficiency of methylene blue removal from different agricultural wastes using a batch adsorption process were determined. Adsorption efficiency decreased with increasing concentration due to the filling of pores on the surface. Regarding the effect of temperature on efficiency, a decrease was observed with OS, PS, WS, and CS samples, while an increase was observed with AS, AKS, and PC wastes.

Following SEM and FTIR analyses conducted to determine the surface properties of adorbentin, the aliphatic, aromatic, and carboxylic groups within the structure were identified in the samples at different vibrations using FTIR analysis. Porosity variations and layered structure examples were determined on waste surfaces by SEM analysis.

After equilibrium studies to determine the adsorption isotherm model, fit to the Langmuir model, a single-layer homogeneous adsorption model, was observed in all samples.

REFERENCES

[1] Guru PS, Panda B, Parida KN (2025) Adsorption of textile dyes on hydroxyapatite based adsorbent: A review of surface functionality and adsorption mechanism Next Materials, 9:101042

[2] Chen J.P., Lin M.S., (2001) Equilibrium and kinetics of metal ion adsorption onto a commercial H-type granular activated carbon;experimental and modeling studies, Water Res. 35:2385–2394.

[3] Aksu Z, Gönen F (2004) Biosorption of phenol by immobilizedactivated sludge in a continuous packed bed: Prediction ofbreakthrough curves, Process Biochem. 39: 599–613.

[4] Albert M, Lessin MS, Gilchrist B F. (2003) Methlene blue, dengerous dye for neonates. J. Pediatric Sur. 38: 1244-1245.

[5] Zhou Y, Zhang L, , Cheng Z. (2015) Removal of organic pollutants from aqueous solution using agricultural wastes: A review, Journal of Molecular Liquids 212:739–762.

[6] Kaur M , Krishnan U, Sharma P, Kaur K, Sharma R, Kumarf A (2025) MXenes in action: Adsorption strategies for environmental contaminants Journal of Alloys and Compounds 1034:181350.

[7] Sarıcı-Özdemir Ç, Kılıç F (2016) Experimental and modeling studies of methylene blue adsorption onto particles of peanut shell, Particulate Science And Technology 34:658–664

[8] Langmuir I (1918) The adsorption of gases on plane surfaces of glass, mica and platinum, J. Am. Chem. Soc. 40 :1361–1368.

[9] Freundlich H M F (1906) Über die adsorption in iösungen, Phys. Chem., 57:385–470.

[10] Sarıcı Özdemir Ç (2012) Adsorption and desorption kinetics behaviour of methylene blue onto activated carbon, Physicochem. Probl. Miner. Process. 48:441−454

Chapter 2

CHIRALITY AND ENANTIOMERIC SEPARATION: PRINCIPLES AND ANALYTICAL METHODS[1]

Nagihan SOYER[2], Sema SALGIN[3], Uğur SALGIN[4]

---

[1] This book chapter is derived from the master's thesis entitled 'The Effect of the Chiral Selector on the Enantiomeric Separation of the Antidepressant Fluoxetine Mixture' conducted at the Institute of Science of Sivas Cumhuriyet University. The thesis is accessible under thesis number 302658 at the National Thesis Center of the Republic of Turkey. (Supervisor: Prof. Dr. Sema Salgın)

[2] Asst. Prof. Dr., Sivas Cumhuriyet University, Faculty of Engineering, Department of Chemical Engineering, 58140, Sivas, Turkiye. ORCID: 0000-0003-1342-2037

[3] Prof. Dr., Sivas Cumhuriyet University, Faculty of Engineering, Department of Chemical Engineering, 58140, Sivas, Turkiye ORCID: 0000-0001-6354-3553

[4] Prof. Dr., Sivas Cumhuriyet University, Faculty of Engineering, Department of Chemical Engineering, 58140, Sivas, Turkiye ORCID: 0000-0002-5683-7569

1.1 Molecular Basis of Chirality and Enantiomeric Behavior

Chirality, determined by the three-dimensional spatial arrangement of atoms within a molecule, is a fundamental property that directly influences interactions with biological targets, thereby playing a critical role in both biological systems and pharmaceutical applications. A molecule is considered chiral if it cannot be superimposed on its mirror image, and the two non-superimposable mirror images of such molecules are referred to as enantiomers (Figure 1.1). Enantiomers are largely similar in terms of their physicochemical properties; however, their optical activities, biological efficacies, and pharmacological effects can differ significantly (Paris et al., 2004). These differences emphasize the pharmacological significance of chiral molecules and the necessity for their individual evaluation.

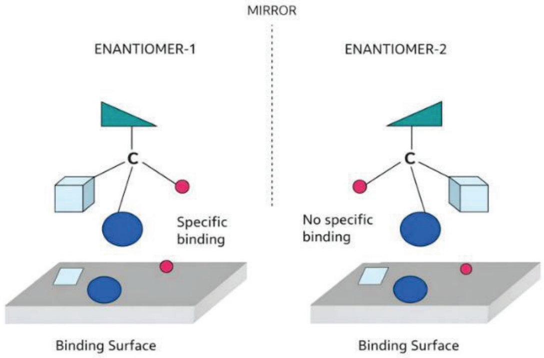

Figure 1.1 Mirror-image relationship between enantiomers.

In pharmaceutical chemistry, most chiral drugs are synthesized as racemic mixtures, comprising equal proportions of R- and S-enantiomers. Nevertheless, the biological activity of these enantiomers is rarely equivalent, with typically only one enantiomer exhibiting pharmacological efficacy. The other enantiomer, while not necessarily entirely inactive, may attenuate the activity of the active form or contribute to undesirable side effects. These distinct biological behaviors directly influence the pharmacokinetic and pharmacodynamic profiles of chiral drugs, making the isolation of pure enantiomers, or at minimum the precise control of enantiomeric ratios, a critical requirement in drug development. The separation of enantiomers enhances pharmacological efficacy while minimizing potential adverse effects, thereby enabling safer, more precise, and more effective dosing protocols (Mastai et al., 2002; Salgın et al., 2007).

The criticality of chiral molecules in drug design is further exemplified by the stereoselective nature of biological systems. Human proteins and enzymes frequently possess stereoselective binding sites, meaning that only specific molecular configurations can elicit the desired biological response. For instance, amino acids and sugars naturally occur in a single enantiomeric form (L-amino acids and

D-sugars), reflecting the inherent stereoselectivity of molecular recognition mechanisms in living organisms. This principle necessitates the separation and characterization of chiral compounds as an essential step in pharmaceutical synthesis and biochemical investigations.

The significance of chirality extends beyond pharmacological activity to encompass toxicological and environmental considerations. Inactive enantiomers can sometimes undergo metabolic transformation into deleterious products or engage in off-target interactions, leading to adverse effects. Moreover, chiral environmental contaminants and pharmaceutical residues may exhibit distinct behaviors in ecosystems, influencing their ecological impact. Accordingly, the isolation and application of single enantiomers during drug development is recognized as a sustainable and safe approach from both clinical and environmental perspectives.

In conclusion, chirality and enantiomeric distinctions are crucial not only at the molecular level in pharmaceutical chemistry but also in the context of clinical applications, drug safety, and environmental impact. Consequently, contemporary pharmaceutical research and drug development processes increasingly prioritize the separation, analysis, and utilization of pure enantiomers as indispensable practices for achieving effective, safe, and sustainable therapeutic agents.

1.2 Optical Activity of Enantiomers

One of the defining characteristics of chiral molecules is their ability to rotate the plane of plane-polarized light. This phenomenon, known as optical activity, is observed exclusively in structurally asymmetric (chiral) molecules. Although enantiomers—molecules that are non-superimposable mirror images of one another—are identical in most physical and chemical properties, they exhibit distinct and opposite behavior in their interaction with electromagnetic radiation.

Plane-polarized light is a specialized form of light in which the electric field vector oscillates within a single plane. When such light passes through a solution containing a chiral compound, the plane of polarization is rotated by a characteristic angle as a consequence of the molecule’s three-dimensional asymmetry. This rotation arises from the differential propagation velocities of left- and right-circularly polarized light components within the chiral medium and is therefore directly associated with molecular chirality (Köseali, 2005).

Based on the direction of optical rotation, enantiomers are classified into two categories: those that rotate the plane of polarized light in a clockwise direction are termed dextrorotatory (+), whereas those that rotate it in a counterclockwise direction are referred to as levorotatory (–). This classification is purely empirical and does not necessarily correlate with the molecule’s absolute configuration, as defined by the R/S nomenclature.

1.2.1 Measurement of Optical Rotation and Specific Rotation

Optical activity is quantitatively determined using a polarimeter, an analytical instrument designed to measure the angle by which a chiral substance rotates the plane of plane-polarized light. The experimentally observed angle of rotation, denoted as α and expressed in degrees, represents the net optical rotation induced by the sample under the specified measurement conditions. However, the magnitude of the observed rotation is not an intrinsic property of the substance alone; rather, it is influenced by several experimental variables, including the concentration of the solution, the wavelength of the incident light, the temperature at which the measurement is conducted, and the optical path length of the sample cell.

To enable meaningful comparison between measurements performed under different conditions, the concept of specific rotation, denoted as $[\alpha]$, has been introduced. Specific rotation normalizes the observed optical rotation with respect to both the path length and the concentration of the optically active substance is incorporated into the calculation of specific rotation, which is given by Eq. (1).

$$[\alpha] = \frac{\alpha}{l \cdot c} \tag{1}$$

where α is the observed angle of rotation (in degrees), l is the optical path length of the sample cell expressed in decimeters (dm), and c is the concentration of the solution, typically reported in grams per milliliter (g mL^{-1}) or grams per 100 milliliters, depending on convention.

Specific rotation is reported at a defined wavelength—most commonly the sodium D line at 589 nm—and at a specified temperature, as both parameters can significantly influence optical rotation. Under these standardized conditions, specific rotation constitutes a characteristic physical constant for a given enantiomer. Consequently, it serves as a valuable parameter in the identification of chiral compounds, the assessment of enantiomeric purity, and the characterization of products obtained from asymmetric or stereoselective syntheses.

1.3 Racemic Mixtures and Optical Inactivity

The optical rotation exhibited by a pair of enantiomers is equal in magnitude but opposite in direction. Consequently, racemic mixtures, which contain equimolar amounts of both enantiomers, do not display net optical activity. In such systems, the individual optical rotations generated by each enantiomer cancel each other completely, resulting in an observed rotation that is approximately zero when measured using a polarimeter.

Although racemic mixtures are optically inactive, this characteristic should not be interpreted as an indication of chemical or biological inactivity. In biological environments, interactions between enantiomers and chiral entities—such as enzymes, receptors, and transport proteins—are highly stereospecific. As a result, the pharmacodynamic and pharmacokinetic properties of racemic compounds often differ significantly from those of their individual enantiomers. For this reason, racemic mixtures are frequently evaluated on an enantiomer-by-enantiomer basis in medicinal chemistry and drug development studies.

1.3.1 Chemical and Biological Significance of Optical Activity

Optical activity represents one of the fundamental concepts of stereochemistry and holds critical importance across organic chemistry, biochemistry, and pharmaceutical sciences. The optical behavior of enantiomers serves as a primary analytical tool for the determination of absolute configuration, the verification of asymmetric synthesis outcomes, and the development and validation of chiral separation techniques.

Furthermore, understanding the interaction between chiral molecules and polarized light provides valuable insight into molecular recognition processes and stereoselective biological mechanisms. Such interactions underpin a wide range of phenomena, including enzyme–substrate specificity, receptor–ligand binding, and the differential biological activity of enantiomeric drug pairs.

In the analysis of chiral compounds, merely establishing the presence of optical activity is insufficient; determining the quantitative distribution of enantiomers within a system is of paramount importance. One of the most widely used parameters for this purpose is enantiomeric excess, also referred to as enantiomeric purity and expressed as %ee.

Enantiomeric excess describes the molar predominance of one enantiomer over the other in a chiral mixture and is quantitatively given by Eq. (2).

$$\%ee = \frac{|n_1 - n_2|}{n_1 + n_2} \times 100 \tag{2}$$

where $n_1$and $n_2$represent the molar amounts of the two enantiomers. A value of 0% ee corresponds to a racemic mixture, whereas a value of 100% ee indicates an optically pure enantiomer.

Polarimetry provides a straightforward and historically significant method for estimating enantiomeric excess, based on the proportional relationship between the observed optical rotation of a mixture and that of the optically pure enantiomer. When the specific rotation of the pure enantiomer is known, the enantiomeric excess can be calculated using the ratio of the observed rotation to the reference value, assuming ideal linearity and equal but opposite rotations for the two enantiomers.

Polarimetry is one of the oldest and most direct analytical techniques employed for the determination of enantiomeric excess. The fundamental assumption underlying this method is that the total optical rotation of a solution represents the algebraic sum of the individual contributions arising from each enantiomer present in the system. This linear relationship can be expressed by Eq. (3):

$$\alpha_{\text{obs}} = \alpha_{+} - \alpha_{-} \tag{3}$$

where α_{obs} denotes the observed optical rotation of the enantiomeric mixture, and α_{+} and α_{-} represent the contributions of the dextrorotatory and levorotatory enantiomers, respectively.

If the specific rotation of the optically pure enantiomer, $[\alpha]_{\text{pure}}$, is known, the enantiomeric excess of a mixture can be determined using the observed specific rotation, $[\alpha]_{\text{obs}}$, according to the Eq. (4):

$$\%ee = \frac{[\alpha]_{\text{obs}}}{[\alpha]_{\text{pure}}} \times 100 \tag{4}$$

This approach assumes that the two enantiomers exhibit optical rotations of equal magnitude and opposite sign and that the optical response of the system is linear with respect to enantiomer composition.

1.4 Polarimetric Determination of Optical Activity

A polarimeter is an analytical instrument used to quantify the extent to which optically active substances rotate the plane of polarized light either to the right or to the left. The measured angle of rotation provides direct information about the optical activity of the sample and is widely employed in the characterization and analysis of chiral compounds.

A conventional polarimeter consists of four principal components: a light source, a polarizer, a sample tube, and an analyzer (Figure 1.2). The light source, typically a monochromatic lamp such as a sodium vapor lamp emitting at the D line (589 nm), provides a stable and well-defined wavelength to ensure reproducible measurements. The emitted light is passed through the polarizer, which converts unpolarized light into plane-polarized light by restricting the oscillation of the electric field vector to a single plane (Köseali, 2005).

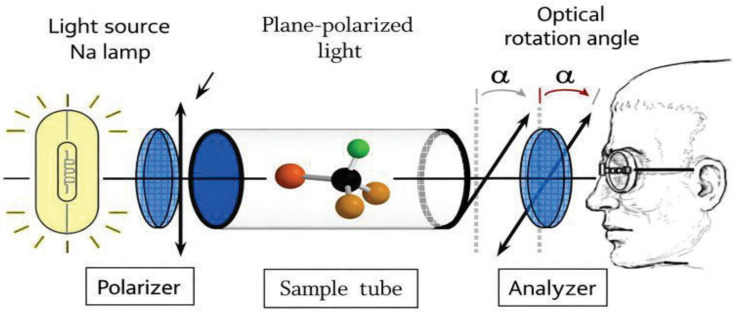

Figure 1.2 Schematic representation of a polarimeter.

The plane-polarized light then traverses the sample tube, which contains the optically active solution. As the light propagates through the chiral medium, interactions between the electromagnetic field and the asymmetric molecular structure induce a rotation of the polarization plane by an angle characteristic of the substance and its concentration. The magnitude and direction of this rotation depend on intrinsic molecular properties as well as experimental parameters such as path length, temperature, and wavelength.

Finally, the rotated light reaches the analyzer, which is rotated until the maximum or minimum light intensity is detected. The angular displacement of the analyzer relative to its initial position corresponds to the observed optical rotation. This value is subsequently used to calculate specific rotation and, when appropriate, enantiomeric excess. Owing to its simplicity, sensitivity, and non-destructive nature, polarimetry remains a fundamental technique in stereochemical analysis, particularly in organic, pharmaceutical, and biochemical research.

The polarimetric method offers several practical advantages, particularly in the rapid assessment of asymmetric syntheses, reaction optimization, and the preliminary screening of crude products. Owing to its simplicity, non-destructive nature, and minimal sample preparation requirements, polarimetry is frequently employed as an initial analytical tool in stereoselective synthesis workflows. However, despite these advantages, polarimetry also presents inherent limitations with respect to the accurate determination of enantiomeric purity.

Optical rotation is sensitive to a range of experimental parameters, including solvent identity, temperature, wavelength, and sample concentration. Consequently, strict control and precise reporting of these variables are essential to ensure reproducibility and meaningful interpretation of polarimetric data. In addition, structurally distinct chiral compounds—or even closely related molecules sharing the same absolute configuration—may exhibit markedly different specific rotation values, limiting the generalizability of optical rotation as a standalone descriptor of stereochemical purity.

Furthermore, in certain chiral systems, non-linear optical behavior or conformational effects may be observed, particularly in flexible molecules or systems capable of conformational interconversion. Under such conditions, polarimetric measurements may not accurately reflect the true enantiomeric excess of the sample. For this reason, modern stereochemical analysis typically employs polarimetry in conjunction with complementary techniques, such as chiral high-performance liquid chromatography (HPLC), chiral gas chromatography (GC), nuclear magnetic resonance (NMR) spectroscopy using chiral shift or derivatizing agents, and circular dichroism (CD) spectroscopy.

In conclusion, although polarimetry represents a foundational and historically significant technique for the determination of enantiomeric purity, the most reliable results are obtained only when measurements are conducted under carefully controlled experimental conditions and interpreted using appropriate reference values. Within this context, polarimetry continues to serve as a rapid, cost-effective, and conceptually robust tool in the broader framework of chiral analysis.

1.5 Absolute Configuration and Stereochemical Nomenclature

Enantiomers are commonly described using the R/S system, also known as the Cahn–Ingold–Prelog (CIP) nomenclature, which provides an unambiguous method for assigning the absolute configuration of chiral centers. In this system, the designation R (*rectus*) indicates a clockwise sequence, whereas S (*sinister*) denotes a counterclockwise sequence, as determined by a set of standardized priority rules. It is important to emphasize that the R/S notation describes molecular geometry and does not necessarily correlate with the direction of optical rotation.

The determination of the absolute configuration of a chiral center is carried out according to the following steps:

1. Priority Assignment: The substituents directly attached to the stereogenic center are ranked according to their atomic numbers, with the substituent containing the atom of highest atomic number assigned the highest priority. In cases where two substituents are identical at the first point of attachment, the comparison proceeds sequentially along each substituent chain until the first point of difference is encountered.

2. Molecular Orientation: The molecule is oriented such that the substituent with the lowest priority is positioned away from the observer, behind the plane of the page or projection. This orientation is essential for the correct assignment of the absolute configuration.

3. Configuration Assignment: The remaining three substituents are then traced in order of decreasing priority (1 → 2 → 3). If the path follows a clockwise direction, the stereogenic center is designated as R; if the path proceeds in a counterclockwise direction, the configuration is assigned as S (Figure 1.3).

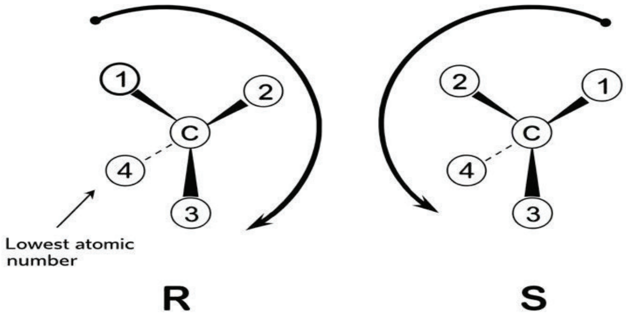

Figure 1.3 R and S configurations of enantiomers.

Racemic mixtures are conventionally denoted as (R,S) and represent systems in which both enantiomers are present in equal molar amounts. Such mixtures are optically inactive due to the mutual cancellation of the optical rotations of the individual enantiomers. Table 1. summarizes the possible stereochemical configurations and their general characteristics.

Table 1. Classification of Stereochemical Descriptors

Type of Configuration	Abbreviations	Designation Criteria
Relative configuration	D, L	Assigned by comparing the three-dimensional arrangement of atoms or groups at a stereogenic center relative to a reference compound.
Absolute configuration	R, S	Assigned based on the absolute three-dimensional spatial arrangement of atoms or groups at a stereogenic center according to the Cahn–Ingold–Prelog (CIP) priority rules.
Specific rotation (optical activity)	(+), (−) or d, l	Assigned according to the direction in which plane-polarized light is rotated, either to the right (dextrorotatory) or to the left (levorotatory).

2. Chiral Separation Techniques for Enantiomerically Pure Compounds

Several methodologies employed for the preparation of enantiomerically pure compounds are fundamentally based on the formation of diastereomeric salts or complexes, followed by their subsequent separation. In these approaches, a chiral resolving agent or auxiliary—capable of converting enantiomers into diastereomers with distinct physicochemical properties—is introduced into the system. The resulting diastereomeric species can then be separated using conventional techniques such as crystallization, extraction, or chromatography, after which the desired enantiomer is regenerated in its optically pure form.

For this purpose, enantioenriched or enantiomerically pure chiral building blocks that can be readily transformed into the target compound are commonly employed. The widespread occurrence of naturally available chiral compounds, particularly amino acids and carbohydrates, provides a significant advantage in the practical implementation of such methods. These naturally occurring chiral sources are readily accessible, structurally diverse, and often inexpensive, making them highly attractive for use in enantiomeric resolution and asymmetric synthesis strategies (Yurdakul, 2006).

Depending on the nature of the starting material, the methodologies for obtaining enantiomerically pure compounds can be broadly classified into three main categories. The first involves the stereoselective synthesis of chiral substrates, in which the desired enantiomer is generated directly through controlled reaction pathways. The second category comprises the resolution of racemic mixtures, wherein a racemate is separated into its individual enantiomers using physical, chemical, or biochemical techniques. The third approach is the asymmetric synthesis of prochiral compounds, in which a prochiral substrate is converted into a chiral product under the influence of a chiral catalyst, reagent, or auxiliary, leading to preferential formation of one enantiomer over the other.

2.1 Stereoselective Synthesis of Chiral Substrates

Stereoselective synthesis represents a fundamental strategy for the preparation of enantiomerically enriched or enantiomerically pure compounds and plays a central role in modern organic and pharmaceutical chemistry. This approach relies on the controlled formation of one stereoisomer over another during a chemical transformation and is commonly achieved through the use of chiral starting materials, chiral auxiliaries, or the establishment of a chiral reaction environment, even when reacting with otherwise achiral substrates (Ghanem, 2004).

One of the most widely applied stereoselective strategies is the chiral pool approach, which exploits naturally occurring chiral compounds as starting materials. Although these compounds are not always enantiomerically pure, they are optically active and possess well-defined stereochemical frameworks that can be preserved or selectively transformed during synthesis. Nature provides an abundant and diverse array of such chiral building blocks, including alkaloids, terpenes, carbohydrates, α-amino acids, and α-hydroxy acids, all of which collectively constitute the so-called *chiral pool*. The availability, structural diversity, and relative low cost of these materials make them particularly attractive for large-scale and industrial applications.

A classical and industrially relevant example of the chiral pool strategy is the use of (R)-limonene, which is isolated from orange peels as a by-product of the citrus juice industry. This naturally occurring terpene serves as a key starting material in the commercial synthesis of (R)-carvone, the compound responsible for the characteristic spearmint flavor. In this process, the pre-existing chirality of limonene is efficiently transferred and retained in the final product, illustrating the practical advantages of stereoselective synthesis based on natural chiral sources.

In addition to chiral pool substrates, non-racemic chiral auxiliaries are frequently employed to induce stereoselectivity in chemical reactions. These auxiliaries may be of chemical or biological origin and are covalently attached to an achiral substrate prior to the key stereochemistry-defining step. The presence of the chiral auxiliary introduces diastereomeric interactions during the reaction, leading to preferential formation of one stereoisomer. Importantly, chiral auxiliaries must be used in stoichiometric amounts and are typically removed after completion of the reaction to yield the optically active product. When properly designed and applied, this methodology can afford chiral compounds with optical purities approaching 100% enantiomeric excess.

Alternatively, stereoselectivity can be achieved by creating a chiral reaction environment without covalent modification of the substrate. This can be accomplished through the addition of chiral solvents, chiral ligands, or chiral catalysts to the reaction medium. In such systems, the chiral environment alters the relative free energies of competing diastereomeric transition states, thereby favoring one reaction pathway over the other. As a result, the formation of one enantiomer or diastereomer is kinetically preferred, leading to stereoselective product formation (Yurdakul, 2006).

Overall, stereoselective synthesis provides a versatile and powerful framework for the preparation of chiral compounds. By leveraging naturally occurring chirality, chiral auxiliaries, or chiral environments, this approach enables precise control over molecular stereochemistry and continues to be a cornerstone of asymmetric synthesis in both academic research and industrial practice.

2.2 Resolution of Racemic Mixtures

Resolution refers to the process by which a compound present as a racemic mixture is separated into its individual enantiomers. To achieve this separation, a variety of physical and chemical methods have been developed, with crystallization-based techniques historically playing a central role.

Racemic resolution has broad practical significance, particularly in fields such as pharmaceutical chemistry, agrochemicals, and materials science (Yurdakul, 2006).

In many biologically active compounds, especially pharmaceuticals, molecular chirality plays a decisive role in biological activity. When a drug candidate is a dissymmetric molecule, typically only one enantiomer exhibits the desired therapeutic effect, whereas the other enantiomer may be pharmacologically inactive or possess significantly reduced activity. In some cases, the undesired enantiomer may even elicit adverse effects. Because conventional chemical syntheses often yield racemic products, post-synthetic resolution of the racemate is frequently required to isolate the biologically active enantiomer.

A wide range of methods has been developed for the resolution of enantiomers. These approaches are commonly classified into four major categories: preferential crystallization, conversion to diastereomers, chromatographic resolution, and kinetic resolution. The choice of method depends on factors such as the physical properties of the racemate, scalability, cost, and the required enantiomeric purity (Ong et al., 2022).

Preferential crystallization is widely applied in industrial-scale processes, particularly when the racemic compound crystallizes as a conglomerate. In such systems, the solid phase consists of a mechanical mixture of separate crystals of each enantiomer present in equal amounts, rather than a racemic compound in which both enantiomers are incorporated into the same crystal lattice. Under carefully controlled conditions, selective crystallization of one enantiomer can be induced, enabling its physical separation from the mixture (Subramanian, 2001).

Despite its industrial relevance, preferential crystallization is applicable to only a limited number of compounds. It is estimated that fewer than 20% of racemic compounds crystallize as conglomerates, which significantly restricts the general applicability of this method.

One of the most widely used and versatile methods for racemate resolution involves the conversion of enantiomers into diastereomers. This is typically achieved by reacting a racemic compound—most commonly a carboxylic acid or an amine—with an enantiomerically pure, optically active base or acid to form diastereomeric salts. Unlike enantiomers, diastereomers possess different physical properties, including melting points, solubilities, and crystallization behaviors.

These differences allow the diastereomeric salts to be separated by conventional techniques such as fractional crystallization using an appropriate solvent. Following separation, the desired enantiomer can be regenerated by treating the isolated diastereomeric salt with a mineral acid or base, resulting in proton transfer and release of the optically pure free acid or base.

In general, the optically active acids and bases employed for diastereomeric salt formation are naturally occurring organic compounds, many of which are readily available and structurally diverse. Common resolving agents include tartaric acid derivatives, camphorsulfonic acid, and various alkaloids. The broad availability of such resolving agents contributes to the widespread use and practical importance of diastereomeric crystallization in enantioresolution processes (Yurdakul, 2006).

2.2.1 Chromatographic Methods

Chromatography represents one of the most versatile and widely applied techniques for the resolution of enantiomers. When optically active solid materials—such as carbohydrates including glucose, sucrose, and lactose—are employed as stationary phases in column chromatography, a racemic solution passed through the column interacts differentially with the chiral surface. As a result, one enantiomer is retained more strongly than the other, leading to effective enantioseparation. If the column length and separation efficiency are sufficient, fractions collected at the column outlet may contain predominantly a single enantiomer. The enantiomer retained on the column can subsequently be eluted using an alternative solvent system (Subramanian, 2001).

Although liquid chromatography was historically regarded as an expensive and relatively inefficient purification technique, significant technological advancements have transformed it into one of the preferred methods for large-scale chiral separation. Improvements in column packing materials, detector sensitivity, and solvent delivery systems have substantially enhanced separation efficiency and reproducibility. Moreover, the relatively high yield of enantiomerically enriched products obtained through liquid chromatographic methods partially offsets their operational costs, particularly in pharmaceutical and fine chemical applications.

Similar to crystallization-based approaches, chromatographic separation can also be applied to diastereomeric derivatives formed by reaction with chiral derivatizing agents, as well as directly to enantiomeric mixtures. In the former case, the resulting diastereomers are separated under achiral chromatographic conditions using conventional techniques. However, such methods often encounter limitations similar to those observed in classical resolution strategies, including incomplete separation and additional derivatization steps.

Among chromatographic techniques, high-performance liquid chromatography (HPLC) occupies a particularly prominent position in enantioseparation. Most chiral HPLC methods employ chiral stationary phases (CSPs) that act as chiral selectors and enable differential interactions with enantiomers. The continuous development of chromatographic instrumentation, coupled with the increasing commercial availability and structural diversity of CSPs, has made HPLC one of the most powerful tools for large-scale chromatographic resolution. Nevertheless, HPLC is inherently a batch-wise technique, which limits its suitability for true production-scale applications. In such cases, continuous separation processes are often preferred to improve efficiency and throughput.

Gas chromatography (GC) constitutes another approach for chiral separation; however, its applicability is largely restricted to racemic mixtures composed of volatile compounds, such as anesthetic agents, hormones, and monoterpenes. Consequently, the number of studies employing GC for chiral resolution is relatively limited. In most reported applications, cyclodextrin-derived chiral stationary phases have been utilized as chiral selectors, owing to their ability to form inclusion complexes with enantiomers and discriminate between them based on stereochemical fit.

Fundamentally, all chiral chromatographic separation techniques rely on the establishment of a chiral environment in which the two enantiomers of a mixture exhibit different affinities toward a chiral selector. This selector interacts with each enantiomer to a different extent, resulting in distinct retention behaviors and enabling separation. An ideal chiral selector should possess several key attributes, including high loading capacity, strong enantioselectivity, chemical and thermal stability, low cost, and broad applicability across different classes of compounds.

Among all chiral separation techniques, HPLC has proven to be the most versatile, reproducible, and widely applicable method, making it a cornerstone of modern enantioseparation science (Subramanian, 2001).

2.2.2 Kinetic Resolution

Another important method employed for the resolution of racemic mixtures is kinetic resolution, which is based on differences in the reaction rates of the two enantiomers in the presence of a chiral reagent or catalyst. The success of this method depends on the ability of the chiral input to discriminate kinetically between enantiomers, such that one enantiomer is converted into product more rapidly than the other.

The chiral input used in kinetic resolution may function as a biocatalyst, such as an enzyme or microorganism, or as a chemical catalyst, including chiral metal complexes, chiral acids, or chiral bases. These chiral catalysts are typically employed in catalytic amounts. Among kinetic resolution strategies, lipase-catalyzed transformations are the most widely applied. Lipase enzymes are capable of distinguishing between the two enantiomers present in a racemic mixture and selectively catalyzing the transformation of one enantiomer over the other.

As a result, one enantiomer is preferentially converted into the corresponding product, while the remaining enantiomer accumulates in unreacted form. Kinetic resolution is particularly attractive due to its mild reaction conditions, high selectivity, and compatibility with a wide range of functional groups. However, its theoretical yield is inherently limited to 50% unless combined with additional strategies such as dynamic kinetic resolution (Yurdakul, 2006).

2.3 Membrane-Based Chiral Separation

In recent years, the application of membrane technology in separation processes has increased substantially, reaching a level of performance that rivals established methods used in water purification and food processing. Beyond these traditional domains, membrane-based separation techniques have emerged as highly effective tools in biomedical, environmental, and chemical engineering applications. Owing to their operational versatility and energy efficiency, membrane technologies are increasingly recognized for their potential contributions to the chemical industry, while ongoing advances in membrane materials and design continue to stimulate future research and development efforts.

The separation of enantiomers has become a critical challenge across multiple disciplines, particularly in the pharmaceutical industry, where the preparative-scale isolation of individual enantiomers is essential for independent toxicological and pharmacological evaluation. In this context, membrane-based chiral separation has gained considerable attention due to its inherent advantages as an industrial separation technology, including continuous operation, mild processing conditions, and compatibility with large-scale implementation.

Conventional chiral resolution techniques—such as preferential crystallization, stereoselective transformations using optically active resolving agents, high-performance liquid chromatography (HPLC), and electrophoretic methods—are widely employed in the production of pharmaceuticals and agrochemicals. However, these approaches often suffer from significant limitations, including low overall efficiency, high consumption of chemicals and solvents, and substantial energy requirements. In contrast, membrane-based chiral separation processes offer a compelling alternative due to their low operational costs, ease of scale-up, continuous process capability, and reduced energy demand (Jirage et al., 2019; Wang et al.,2006).

Membrane-based chiral separation strategies can be broadly classified into two main categories: separation using non-chiral-selective membranes and separation using enantioselective (chiral-selective) membranes. Among these, enantioselective membranes—constructed from solid polymeric materials or liquid membrane systems that permit the selective transport of only one enantiomer from a racemic mixture—are generally considered more effective (Subramanian, 2001; Salgın et al.,2018).

Affinity ultrafiltration systems represent a typical example of non-chiral-selective membrane-based separation. In such systems, stereoselective ligands—including bovine serum albumin (BSA), Lglutamic acid derivatives, and cyclodextrins—are introduced into the bulk solution, where they selectively bind one enantiomer, thereby enabling its separation from the unbound counterpart. Despite their effectiveness, these systems face challenges related to membrane fouling and regeneration of chiral selectors, which can limit long-term operational stability (Salgın et al.,2018).

Another example of non-chiral-selective membrane systems includes supported liquid membranes incorporating enantioselective carriers such as chiral crown ethers, chiral copper complexes, cyclodextrins, and enzymes. These membranes often exhibit high enantioselectivity in the permeate stream; however, their practical application is hindered by limited mechanical stability and losses of the liquid phase or carrier molecules over time.

In contrast, chiral-selective membranes are fabricated by coating the membrane surface with a chiral-selective layer or by immobilizing chiral selectors within the membrane matrix. Membranes based on chiral polymers, such as polysaccharide and poly(amino acid) derivatives, demonstrate enantioselective transport behavior but frequently suffer from low permeation fluxes and performance instability.

An alternative approach involves the use of molecularly imprinted membranes, prepared via cross-linked polymerization or membrane fabrication in the presence of a guest (template) molecule. Compared to purely synthetic methods, molecular imprinting enables the formation of well-defined molecular recognition sites that closely match the target enantiomer. However, molecularly imprinted membranes are inherently selective toward specific enantiomeric pairs associated with the template molecule, which limits their broader applicability.

Finally, separation processes based on chiral selectors immobilized on or within solid membranes represent a promising class of membrane-based systems. In these configurations, the immobilization of the chiral selector enhances membrane stability while maintaining selective recognition and transport. Such systems combine the advantages of membrane robustness with high enantioselectivity, making them attractive candidates for future development in industrial chiral separation technologies.

References

Ghanem, A., Aboul-Enein, H. Y. (2004). Lipase-mediated chiral resolution of racemates in organic solvents. *Tetrahedron: Asymmetry, 15*, 3331–3351. https://doi.org/10.1016/j.tetasy.2004.09.019.

Jirage, K. B., Martin, C. R. (1999). New developments in membrane-based separations. *Trends in Biotechnology, 17*, 197–200. https://doi.org/10.1016/s0167-7799(98)01296-7.

Köseali, Y. K. (2005). *α-Hydroxy ketonların enantiyoseçimli olarak biyotransformasyonla üretimi*. (master's thesis) Ankara University, Institute of Science, Ankara, Türkiye.

Mastai, Y., Sedlák, M., Cölfen, H., Antonietti, M. (2002). The separation of racemic crystals into enantiomers by chiral block copolymers. *Chemistry-A European Journal, 8*(11), 2429–2437. https://doi.org/10.1002/1521-3765(20020603)8:11<2429::AID-CHEM2429>3.0.CO;2-6.

Ong, C. S., Oor, J. Z., Tan, S. J., Chew, J. W. (2022). Enantiomeric separation of racemic mixtures using chiral-selective and organic-solvent-resistant thin-film composite membranes. *ACS Applied Materials & Interfaces, 14*, 10875–10885. https://doi.org/10.1021/acsami.1c25175.

Paris, J., Molina-Jouve, C., Nuel, D., Moulin, P., Charbit, F. (2004). Enantioenrichment by pervaporation. *Journal of Membrane Science, 237*, 9–14. https://doi.org/10.1016/j.memsci.2004.02.001.

Salgın, U., Salgın, S., Takaç, S. (2007). The enantioselective hydrolysis of racemic naproxen methyl ester in supercritical CO_2 using *Candida rugosa* lipase. *The Journal of Supercritical Fluids, 43*, 310–316. https://doi.org/10.1016/j.supflu.2007.06.006.

Salgın, S., Salgın, U., Tuzlalı, N. (2018). Enantiomeric separation of antidepressant drug fluoxetine based on chiral membranes. *Desalination and Water Treatment, 105*, 245–249. https://doi.org/10.5004/dwt.2018.22130.

Subramanian, G. (2001). Techniques in preparative chiral separations. In G. Subramanian (Ed.), *Chiral separation techniques* (pp. 3-13, 129-140). Weinheim, Germany: Wiley-VCH Verlag GmbH.

Wang, J., Fu, C., Lin, T., Yu, L., Zhu, S. (2006). Preparation of chiral selective membranes for electrodialysis separation of racemic mixtures. *Journal of Membrane Science, 276*, 193–198. https://doi.org/10.1016/j.memsci.2005.09.049.

Yurdakul, D. (2006). *Majör depresyonlu hastaların polimorf nüveli lökosit fonksiyonları üzerine antidepresan ilaç tedavisinin etkisinin araştırılması*. (master's thesis). Marmara University, Institute of Science, Istanbul, Türkiye.

Chapter 3

THE ROLE AND APPLICATION POTENTIAL OF GOOGLE EARTH ENGINE (GEE) IN URBAN ENVIRONMENTAL STUDIES

AZİZ SARAÇOĞLU[1]

---

[1] Assistant Professor, Firat University, Department of Civil Engineering, Faculty of Technology, Orcid:0000-0003-3781-3964

1. INTRODUCTION

In recent years, the increasing availability of supercomputers and high-performance computing (HPC) systems has opened new horizons in earth sciences (Nemani, et al., 2011). Concurrent with this development, there has been a substantial increase in the volume of remote sensing data. Archives on the petabyte scale from institutions such as NASA, the U.S. Geological Survey (USGS), and NOAA have been made freely accessible (Woodcock, et al., 2008), (Loveland & Dwyer, 2012). In a similar vein, the European Space Agency (ESA) has augmented this data repository by disseminating its data under the aegis of the Copernicus program (Anon., 2025). A multitude of software frameworks have been developed to process these massive data stacks, including TerraLib (Camara, et al., 2000), Hadoop-based spatial tools (Whitman, et al., 2014), GeoSpark (Yu, et al., 2015) and GeoMesa (Hughes, et al., 2015). However, the effective use of these tools often involves serious technical barriers, such as advanced technical expertise, parsing complex file formats, and IT infrastructure management, which distract researchers from their primary scientific questions.

Google Earth Engine (GEE) is a cloud-based platform designed to eliminate these technical barriers and democratize geospatial analysis on a planetary scale. The platform utilizes Google's substantial computational capabilities to address high-impact societal issues, including deforestation, drought, disaster management, and urban monitoring. Contrary to conventional systems, GEE boasts a multi-petabyte data catalog that is "co-located" with high-performance parallel processing power. This integrated structure enables researchers to prioritize directly on algorithm development without expending resources on processes such as data management and server optimization. Users can access the system via a web-based interface and application programming interfaces (APIs) to perform complex analyses using JavaScript or Python (Gorelick, et al., 2017). A visual representation of this web-based interactive development environment (IDE), where users develop algorithms and visualize results instantaneously, is presented in Figure 1.

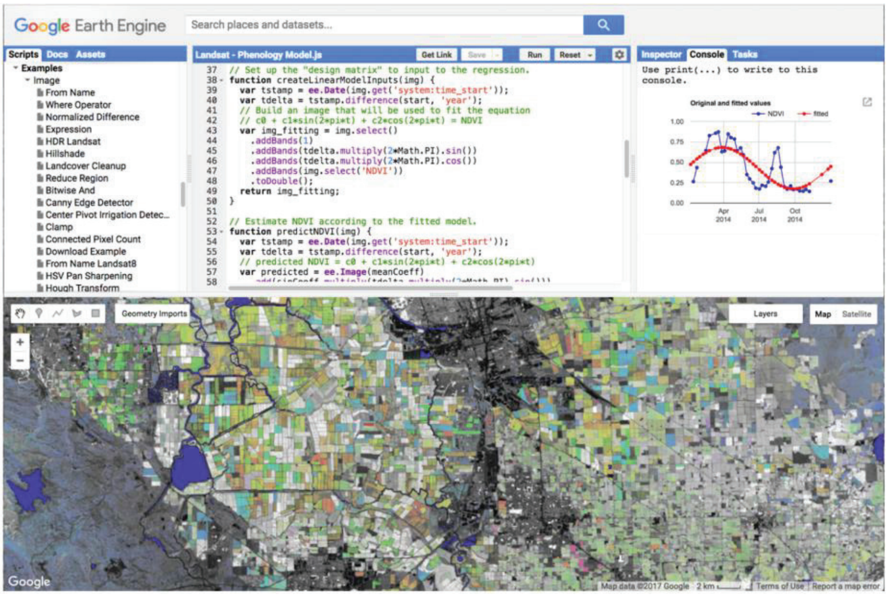

```
// Set up the "design matrix" to input to the regression.
function createLinearModelInputs(img) {
  var tstamp = ee.Date(img.get('system:time_start'));
  var tdelta = tstamp.difference(start, 'year');
  // Build an image that will be used to fit the equation
  // c0 + c1*sin(2*pi*t) + c2*cos(2*pi*t) = NDVI
  var img_fitting = img.select()
    .addBands(1)
    .addBands(tdelta.multiply(2*Math.PI).sin())
    .addBands(tdelta.multiply(2*Math.PI).cos())
    .addBands(img.select('NDVI'))
    .toDouble();
  return img_fitting;
}

// Estimate NDVI according to the fitted model.
function predictNDVI(img) {
  var tstamp = ee.Date(img.get('system:time_start'));
  var tdelta = tstamp.difference(start, 'year');
  // predicted NDVI = c0 + c1*sin(2*pi*t) + c2*cos(2*pi*t)
  var predicted = ee.Image(meanCoeff)
```

```
Use print(...) to write to this
console.
```

Figure 1. The Google Earth Engine interactive development environment (IDE). The interface integrates script management (left panel), a code editor for JavaScript API implementation (center top), an interactive map for immediate visualization of spatial results (bottom), and a console for statistical outputs and charts (right panel). This unified environment allows for rapid prototyping and iterative algorithm development (Source: Gorelick et al., 2017)

GEE's data catalog offers a vast archive covering optical and radar satellite imagery, primarily the Landsat and Sentinel series, as well as climate data and geophysical datasets. A distinguishing feature of the platform is its adoption of an "information-preserving" approach to data processing, which entails storing data in its original projection and resolution. This approach prevents data loss that could arise from resampling to a fixed grid. To expedite the analysis of users, the system employs a pyramid-based, multi-scale tiling system and retrieves only the requisite resolution level during visualization. This methodological framework facilitates expeditious transitions between disparate spatial scales, a particular advantage in the context of studies examining heterogeneous structures, such as urban areas.

One of the most significant advantages offered by GEE for urban environmental analyses is the "lazy computation" model. In this model, the system does not calculate the result immediately; instead, it defers the operation until the user requests an output. Subsequent to the definition of the projection, resolution, and geographic bounds of the requested output, the system performs a dynamic calculation of only the pixels required for the current view or analysis. This feature enables researchers to produce rapid prototypes and interactively test their algorithms in computationally intensive subjects such as urban heat islands, land cover change, or flood risk mapping.

The efficacy of GEE has been demonstrated in both academic research and operational contexts. Pioneering studies, including the global forest change study (Hansen, et al., 2013) and the global surface water change maps (Pekel, et al., 2016), have shown the platform’s strong analytical capabilities. In the domain of urban studies, researchers have underscored the effectiveness of Geographically Explicit (GEE-based) models in mapping settlements and monitoring population dynamics (Patel, et al., 2015) and (Zhang, et al., 2015). The platform expedites the transformation of scientific knowledge into societal benefit by facilitating the dissemination of analysis results through web-based applications.

2. DATA CATALOG AND SYSTEM ARCHITECTURE

Google Earth Engine derives its capabilities from its foundation on Google's data center technologies. The system utilizes fundamental infrastructure components such as Borg for cluster management (Verma, et al., 2015), Bigtable (Chang, et al., 2008) and Spanner (Corbett, et al., 2013) for distributed database operations, and Colossus (the successor to the Google File System) as the file system (Ghemawat, et al., 2003). Moreover, the FlumeJava framework is employed for the management of parallel data processing pipelines (Chambers, et al., 2010). The integration of these technologies enables GEE to process petabytes of data simultaneously and distribute the work across thousands of CPUs.The data catalog includes over 40 years of Landsat data, Sentinel-1 and Sentinel-2 archives, MODIS products, and various atmospheric datasets. In accordance with the methodology outlined by Gorelick et al. (2017), each image that is integrated into GEE is segmented into tiles measuring 256 by 256 pixels, thereby ensuring expeditious access. While these tiles are stored to preserve the original properties of the data, image pyramids at different resolutions are also created to enhance visualization performance. Vector data, which is frequently utilized in urban studies, can be processed in a structure that is compatible with Google Fusion Tables alongside their feature attributes (Gonzalez, et al., 2010).

3. COMPUTATIONAL MODELS, PERFORMANCE, AND SCALABILITY

The Google Earth Engine platform processes user-defined code by converting it into a Directed Acyclic Graph (DAG) executable on the server side. This graph structure employs functional programming techniques, including referential transparency and lazy evaluation, to enhance performance. In the context of urban environmental analysis, the computational models employed by the system can be categorized into three primary modes:

- **Image Tiling:** Pixel-based operations, including band mathematics and spectral index calculations, are parallelized by processing each 256x256 tile independently. This method facilitates the expeditious calculation of urban indices across an entire city or metropolitan region.
- **Spatial Aggregations:** Operations necessitating the calculation of regional statistics are executed using a "scatter-gather" model. The target region is subdivided, distributed to worker nodes, and the results are subsequently aggregated on the master server.
- **Streaming Collections:** In the context of time-series studies, image collections are processed through spatial and temporal filtration. The "streaming" method is a process of analyzing time-series data with millions of pixels without exceeding memory limits.

In addition to these computational models, the overall performance of the GEE execution engine is strengthened by its Java Just-In-Time (JIT) compilation framework, which optimizes graph execution at runtime. Experimental evaluations have demonstrated that this architecture can exhibit up to 50% higher performance compared to comparable dynamic graph systems written in C++, contingent on workload characteristics. However, the most significant advantage of the platform is its horizontal scalability, which refers to its ability to distribute tasks across a large number of CPUs within Google's data centers. This capability enables GEE to achieve near-linear increases in throughput as more worker nodes are allocated. This capability has been demonstrated in large-area experiments, such as the processing of full Landsat 8 archives for both the Conterminous United States (CONUS) and the African continent. In these experiments, the system maintained efficient performance despite the scale of the input data.

4. EXAMPLE APPLICATIONS IN URBAN ENVIRONMENTAL ANALYSIS

Despite the fact that Google Earth Engine (GEE) obscures a significant portion of its internal computational processes through the implementation of graph execution, tiling, and distributed processing, these mechanisms become manifest in the context of common urban environmental workflows. The operationalization of complex analyses by the platform is illustrated by several representative examples, which demonstrate its ability to utilize short and declarative user scripts.

4.1. Vegetation and Surface Condition Assessment (NDVI Example)

The standard workflow commences with the loading of a Sentinel-2 surface reflectance image collection, subsequently followed by the implementation of filtering based on parameters such as date range and cloud coverage. The Normalized Difference Vegetation Index (NDVI) is subsequently calculated using the conventional formulation: (NIR − Red) / (NIR + Red). While the calculation appears straightforward in code, GEE internally partitions the imagery into tiles and evaluates the index in parallel across the entire metropolitan area. This facilitates high-resolution vegetation monitoring, thereby supporting applications such as tracking peri-urban greening, detecting degraded vegetation patches, and assessing seasonal changes in plant cover. A practical demonstration of this workflow, applied to the assessment of seasonal vegetation dynamics in Istanbul using Sentinel-2 imagery, is illustrated in Figure 2.

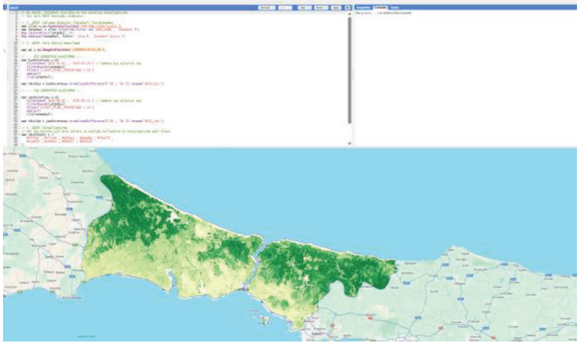

Figure 2. An operational NDVI analysis workflow in Google Earth Engine. The code editor (top) demonstrates the script for filtering Sentinel-2 collections and computing seasonal indices, while the map interface (bottom) displays the resulting spatial distribution of vegetation density over the Istanbul metropolitan area.

4.2. Land Surface Temperature (LST) Retrieval

Urban thermal analyses frequently employ thermal infrared bands from sensors such as Landsat 8 (TIRS) or MODIS to estimate Land Surface Temperature. Following the implementation of the requisite radiometric and atmospheric corrections, the resulting temperature maps can be summarized across administrative units or urban morphological zones. These zonal computations are predicated on GEE's scatter-gather architecture, which distributes the pixel-level calculations across multiple worker nodes and then aggregates the results centrally. This distributed approach facilitates the condensation of millions of pixels into neighborhood-scale statistics without exceeding local memory limits, rendering it particularly valuable for regional-scale thermal assessments. To demonstrate this capability, Figure 3 presents an LST analysis of Istanbul derived from Landsat 8 Collection 2 Level 2 data, effectively visualizing the Surface Urban Heat Island (SUHI) effect where densely built-up areas exhibit significantly higher temperatures than the northern forest belt.

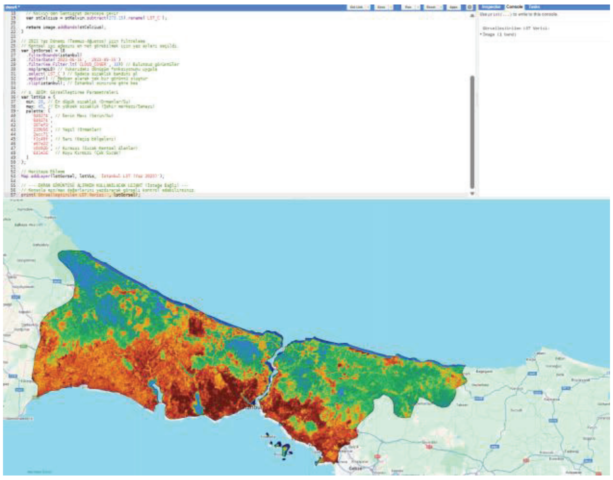

Figure 3. Operational workflow for Land Surface Temperature (LST) mapping in Google Earth Engine. The interface (top) shows the script used to process Landsat 8 thermal bands, while the map (bottom) displays the resulting spatial distribution of surface temperatures in Istanbul. The stark contrast between the warm urban core (red/orange) and the cool northern forests (green/blue) illustrates the urban heat island phenomenon.

4.3. Urban Heat Island (UHI) and Temporal Trend Analysis

Long-term assessments of urban climate conditions frequently necessitate the analysis of satellite archives that span multiple decades. In the majority of applications, researchers filter Landsat or Sentinel image collections by season and generate composite images to examine year-to-year or seasonal variability. These workflows depend on GEE's streaming execution model, which facilitates the efficient processing of extensive time-series imagery without surpassing memory constraints. The resulting pixel-based time series facilitate the quantification of the intensification of the Urban Heat Island effect, the evaluation of long-term thermal patterns, and the comparison of conditions before and after major urban developments. Figure 4 demonstrates such a temporal analysis for Istanbul, visualizing the thermal anomaly by calculating the difference in mean Land Surface Temperature (LST) between the summer periods of 2014 and 2023.

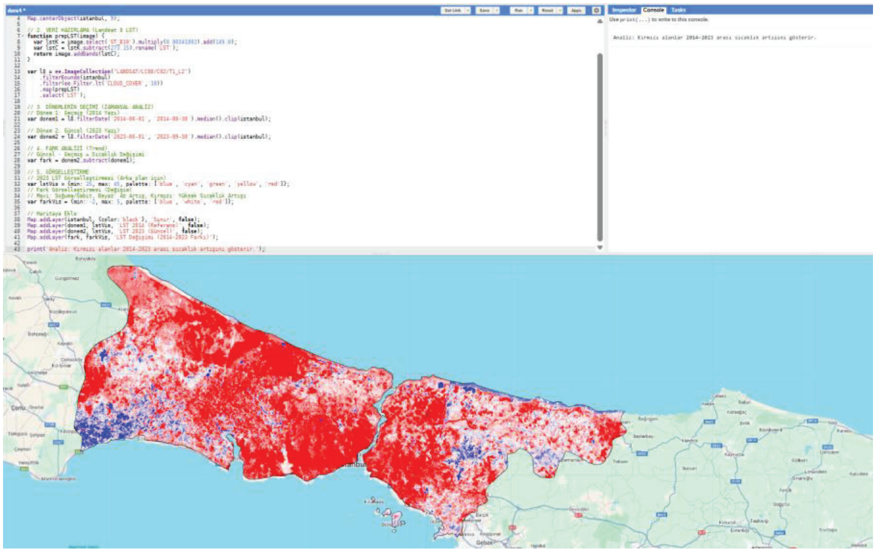

```
Map.centerObject(istanbul, 9);

// 2. VERİ HAZIRLAMA (Landsat 8 LST)
function prepLST(image) {
  var lstK = image.select('ST_B10').multiply(0.00341802).add(149.0);
  var lstC = lstK.subtract(273.15).rename('LST');
  return image.addBands(lstC);
}

var l8 = ee.ImageCollection("LANDSAT/LC08/C02/T1_L2")
    .filterBounds(istanbul)
    .filter(ee.Filter.lt('CLOUD_COVER', 10))
    .map(prepLST)
    .select('LST');

// 3. DÖNEMLERİN SEÇİMİ (ZAMANSAL ANALİZ)
// Dönem 1: Geçmiş (2014 Yazı)
var donem1 = l8.filterDate('2014-06-01', '2014-09-30').median().clip(istanbul);

// Dönem 2: Güncel (2023 Yazı)
var donem2 = l8.filterDate('2023-06-01', '2023-09-30').median().clip(istanbul);

// 4. FARK ANALİZİ (Trend)
// Güncel - Geçmiş = Sıcaklık Değişimi
var fark = donem2.subtract(donem1);

// 5. GÖRSELLEŞTİRME
// 2023 LST Görselleştirmesi (Arka plan için)
var lstVis = {min: 25, max: 45, palette: ['blue', 'cyan', 'green', 'yellow', 'red']};
// Fark Görselleştirmesi (Değişim)
// Mavi: Soğuma/Sabit, Beyaz: Az Artış, Kırmızı: Yüksek Sıcaklık Artışı
var farkVis = {min: -2, max: 5, palette: ['blue', 'white', 'red']};

// Haritaya Ekle
Map.addLayer(istanbul, {color: 'black'}, 'Sınır', false);
Map.addLayer(donem1, lstVis, 'LST 2014 (Referans)', false);
Map.addLayer(donem2, lstVis, 'LST 2023 (Güncel)', false);
Map.addLayer(fark, farkVis, 'LST Değişimi (2014-2023 Farkı)');

print('Analiz: Kırmızı alanlar 2014-2023 arası sıcaklık artışını gösterir.');
```

```
Use print(...) to write to this console.

Analiz: Kırmızı alanlar 2014-2023 arası sıcaklık artışını gösterir.
```

Figure 4. Temporal trend analysis of Land Surface Temperature in Istanbul using Google Earth Engine. The code computes the pixel-wise difference between the mean summer LST of 2023 and 2014. Red regions indicate areas with a positive thermal anomaly (temperature increase), highlighting zones of recent urbanization or surface intensification over the decade.

4.4. Monitoring Urban Expansion and Impervious Surface Growth

Urban expansion studies frequently employ spectral indices or supervised classification techniques to map impervious surfaces. The integration of training samples with machine-learning algorithms, such as Random Forest or CART, enables researchers to delineate built-up areas with a high degree of accuracy. GEE implements these classification models in parallel across extensive regions, thereby facilitating metropolitan- or continental-scale urbanization analyses that would otherwise exceed the capabilities of local computing systems. This scalable framework has supported a wide range of studies, including global settlement mapping and regional monitoring of urban sprawl. To illustrate this capability, Figure 5 presents a high-resolution map of impervious surfaces in Istanbul, generated using machine learning techniques to automatically distinguish built-up areas from natural land cover.

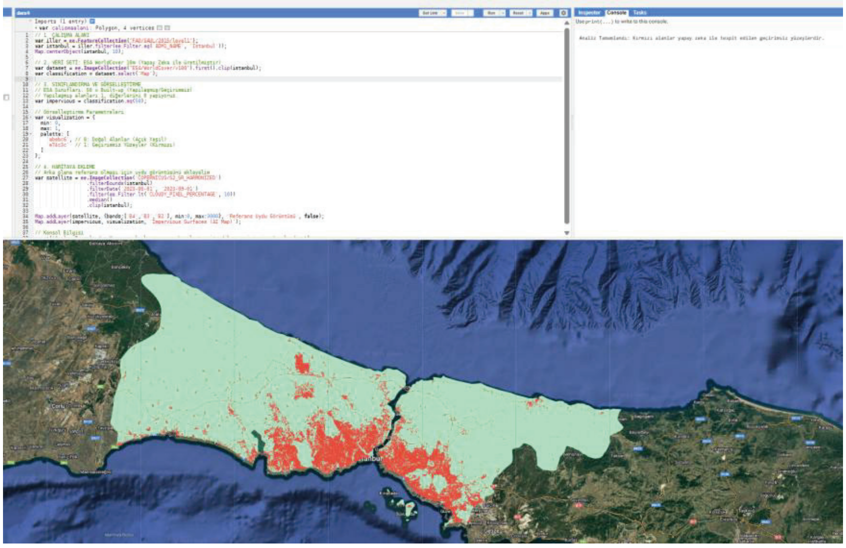

```
Imports (1 entry)
• var calismaalani: Polygon, 4 vertices
// 1. ÇALIŞMA ALANI
var iller = ee.FeatureCollection("FAO/GAUL/2015/level1");
var istanbul = iller.filter(ee.Filter.eq('ADM1_NAME', 'Istanbul'));
Map.centerObject(istanbul, 10);

// 2. VERI SETI: ESA WorldCover 10m (Yapay Zeka ile Üretilmiştir)
var dataset = ee.ImageCollection("ESA/WorldCover/v100").first().clip(istanbul);
var classification = dataset.select('Map');

// 3. SINIFLANDIRMA VE GÖRSELLEŞTIRME
// ESA Sınıfları: 50 = Built-up (Yapılaşmış/Geçirimsiz)
// Yapılaşmış alanları 1, diğerlerini 0 yapıyoruz
var impervious = classification.eq(50);

// Görselleştirme Parametreleri
var visualization = {
  min: 0,
  max: 1,
  palette: [
    'abebc6', // 0: Doğal Alanlar (Açık Yeşil)
    'e74c3c'  // 1: Geçirimsiz Yüzeyler (Kırmızı)
  ]
};

// 4. HARİTAYA EKLEME
// Arka plana referans olması için uydu görüntüsünü ekleyelim
var satellite = ee.ImageCollection('COPERNICUS/S2_SR_HARMONIZED')
                  .filterBounds(istanbul)
                  .filterDate('2023-06-01', '2023-09-01')
                  .filter(ee.Filter.lt('CLOUDY_PIXEL_PERCENTAGE', 10))
                  .median()
                  .clip(istanbul);

Map.addLayer(satellite, {bands:['B4', 'B3', 'B2'], min:0, max:3000}, 'Referans Uydu Görüntüsü', false);
Map.addLayer(impervious, visualization, 'Impervious Surfaces (AI Map)');

// Konsol Bilgisi
```

```
Use print(...) to write to this console.

Analiz Tamamlandı: Kırmızı alanlar yapay zeka ile tespit edilen geçirimsiz yüzeylerdir.
```

Figure 5. Mapping impervious surfaces using Machine Learning in Google Earth Engine. The analysis utilizes 10-meter resolution data to delineate the urban footprint of Istanbul. Red pixels represent impervious surfaces (buildings, roads, and infrastructure), while light green pixels correspond to natural vegetation and permeable surfaces, demonstrating the platform's capacity for rapidand accurate urban morphological analysis.

4.5. Flood Susceptibility and Surface Water Dynamics

The utilization of surface-water detection techniques has become a prevalent method for the purpose of monitoring urban flooding and alterations in water bodies. Analyses frequently entail multi-temporal compositing or change-detection workflows applied to datasets such as Sentinel-1 SAR or Landsat optical imagery. These tasks underscore GEE's aptitude for expeditiously managing sizable and heterogeneous image collections. The outputs from such workflows support rapid flood mapping, long-term tracking of water-body dynamics, and risk management efforts. The platform's automated processing capabilities are of particular value for emergency response and regional hydrological assessments. Figure 6 visualizes the long-term surface water dynamics of Istanbul using the JRC Global Surface Water dataset, specifically highlighting the distribution and frequency of inland water bodies such as reservoirs and lakes which are critical for hydrological risk modeling.

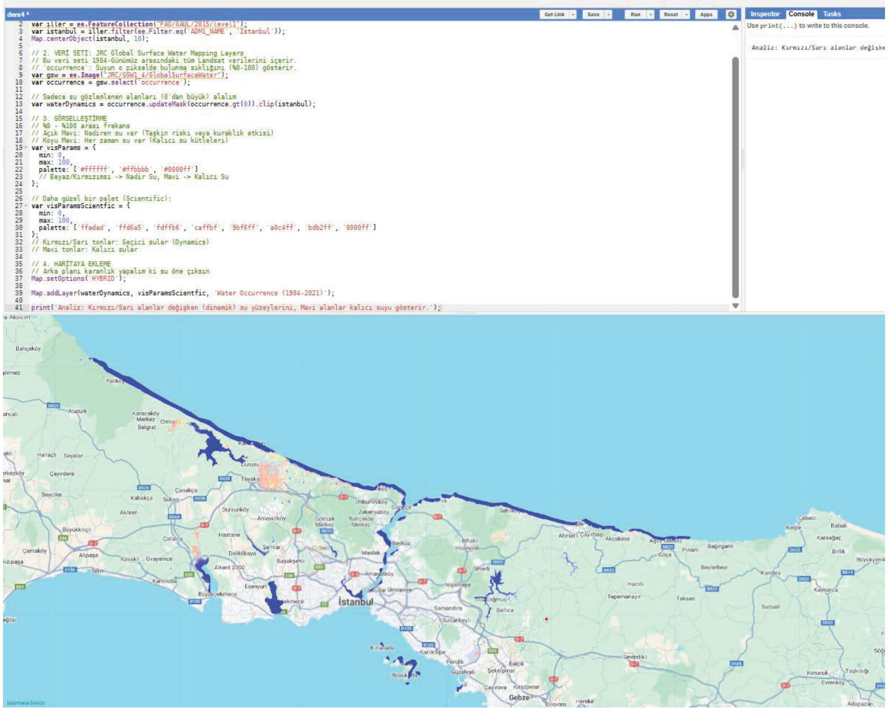

```
var ıller = ee.FeatureCollection("FAO/GAUL/2015/level1");
var istanbul = iller.filter(ee.Filter.eq('ADM1_NAME', 'Istanbul'));
Map.centerObject(istanbul, 10);

// 2. VERİ SETİ: JRC Global Surface Water Mapping Layers
// Bu veri seti 1984-Günümüz arasındaki tüm Landsat verilerini içerir.
// 'occurrence': Suyun o pikselde bulunma sıklığını (%0-100) gösterir.
var gsw = ee.Image("JRC/GSW1_4/GlobalSurfaceWater");
var occurrence = gsw.select('occurrence');

// Sadece su gözlemlenen alanları (0'dan büyük) alalım
var waterDynamics = occurrence.updateMask(occurrence.gt(0)).clip(istanbul);

// 3. GÖRSELLEŞTİRME
// %0 - %100 arası frekans
// Açık Mavi: Nadiren su var (Taşkın riski veya kuraklık etkisi)
// Koyu Mavi: Her zaman su var (Kalıcı su kütleleri)
var visParams = {
  min: 0,
  max: 100,
  palette: ['#ffffff', '#ffbbbb', '#0000ff']
  // Beyaz/Kırmızımsı -> Nadir Su, Mavi -> Kalıcı Su
};

// Daha güzel bir palet (Scientific):
var visParamsScientfic = {
  min: 0,
  max: 100,
  palette: ['ffadad', 'ffd6a5', 'fdffb6', 'caffbf', '9bf6ff', 'a0c4ff', 'bdb2ff', '0000ff']
};
// Kırmızı/Sarı tonlar: Geçici sular (Dynamics)
// Mavi tonlar: Kalıcı sular

// 4. HARİTAYA EKLEME
// Arka planı karanlık yapalım ki su öne çıksın
Map.setOptions('HYBRID');

Map.addLayer(waterDynamics, visParamsScientfic, 'Water Occurrence (1984-2021)');

print('Analiz: Kırmızı/Sarı alanlar değişken (dinamik) su yüzeylerini, Mavi alanlar kalıcı suyu gösterir.');
```

```
Analiz: Kırmızı/Sarı alanlar değişke
```

Figure 6. Long-term inland surface water dynamics in Istanbul (1984–present). Derived from the JRC Global Surface Water dataset, the map illustrates water occurrence frequency within the metropolitan boundaries. Dark blue areas represent permanent water bodies (e.g., Terkos and Ömerli reservoirs), while lighter tones indicate seasonal or ephemeral water zones, effectively mapping the city's active hydrological network excluding the surrounding sea.

5. ADVANTAGES AND LIMITATIONS OF GEE IN URBAN RESEARCH

Google Earth Engine has been hailed as a paradigm shift in geospatial analysis due to its efforts to democratize access to high-performance computing. However, it is imperative for researchers to understand both the distinct advantages and the inherent operational constraints of this platform if they are to utilize it effectively.

5.1. Advantages

The primary benefit of GEE is the elimination of the "IT burden" associated with traditional remote sensing. By co-locating a multi-petabyte data catalog with computational resources, the platform eliminates the need for researchers to download, store, or manage vast raster archives locally. This architecture enables analyses to scale from a single neighborhood to a continental level without necessitating alterations to the underlying code or hardware infrastructure. Additionally, the platform facilitates scientific collaboration through its web-based integrated development environment (IDE), which enables the immediate sharing of scripts and workflows among researchers. The integration of this capability with the capacity to disseminate interactive web applications (Google Earth Engine Apps) has the potential to expedite the conversion of raw scientific data into actionable insights for policymakers and the general public.

5.2. Limitations

Notwithstanding its substantial processing capabilities, GEE functions as a shared service, exhibiting certain constraints that are in place to ensure the system's overall effectiveness. Initially, the client-server programming model can present a learning curve; users must understand that their local Python or JavaScript code merely constructs a request that is executed remotely, which prevents the mixing of client-side logic with server-side objects. Secondly, interactive computations in the code editor are subject to a "soft" timeout and quotas on simultaneous requests. These mechanisms are designed to prevent any single user from monopolizing resources. In conclusion, while the system demonstrates notable proficiency in pixel-based and local neighborhood operations, it exhibits suboptimal performance when confronted with algorithms necessitating global state knowledge or complex recursive processes. A notable example of this suboptimal performance is watershed segmentation on large scales, which can encounter memory limitations during aggregation.

6. POTENTIAL FUTURE DIRECTIONS

As urban environments become increasingly complex and data-rich, the analytical capabilities of Google Earth Engine are undergoing rapid expansion, shifting from retrospective monitoring to predictive analytics, high-fidelity modeling, and multi-platform interoperability. The future trajectory of GEE in urban studies is characterized by several transformative developments:

- **Integration with Big Data Analytics (BigQuery):** The integration of Google Earth Engine's (GEE) planetary-scale raster processing with BigQuery's columnar storage engine is leading to the development of a unified ecosystem for urban data science. Access to scalable infrastructures enables researchers to execute SQL-based analytics on voluminous feature-level datasets derived from satellite imagery. This integration facilitates the execution of complex queries, such as the correlation of zonal Land Surface Temperature (LST) statistics with socio-economic census variables, without the latency and storage burden typically associated with traditional workflows.

- **Planetary-Scale Deep Learning:** While GEE currently supports classical machine learning algorithms like Random Forest, the next major advancement will be the native deployment of deep learning (DL) architectures. The integration of frameworks such as TensorFlow facilitates end-to-end training and inference on cloud-hosted imagery. This advancement is anticipated to significantly improve tasks such as building footprint extraction, informal settlement mapping, and complex pattern recognition in diverse urban environments (Abadi, et al., 2016).

- **Foundations for Urban Digital Twins:** GEE is poised to function as a foundational geospatial layer for next-generation "Urban Digital Twins," which are dynamic, continuously updated virtual replicas of real cities. The integration of near-real-time satellite streams with Internet of Things (IoT) sensor networks and three-dimensional urban morphology datasets enables the platform to simulate microclimate dynamics, mobility patterns, and disaster response scenarios.

7. CONCLUSION

Google Earth Engine (GEE) has fundamentally reshaped the landscape of urban environmental research by providing open, free access to planetary-scale satellite archives and high-performance cloud computing. The platform has effectively eliminated the technical barriers associated with managing local storage, servers, and large raster archives, thereby enabling researchers to prioritize algorithmic innovation rather than data logistics. By consolidating data and computational resources, GEE establishes a cohesive environment that facilitates analyses ranging from neighborhood-level studies to global assessments without compromising the underlying workflow.

Google Earth Engine (GEE) has emerged as a foundational construct within the domain of contemporary urban science, encompassing a range of applications from the delineation of Urban Heat Islands (UHI) and the mapping of rapid urban expansion to the modeling of flood dynamics through the utilization of radar imagery. The system's capacity to process extensive multi-decadal time series enables researchers to discern long-term trends from seasonal fluctuations, providing insights that are not attainable through analyses of a single date. However, it is imperative for users to be cognizant of the platform's limitations. These limitations include its client-server computational paradigm and memory constraints during intensive aggregations.

As GEE evolves to incorporate deep learning workflows, BigQuery-based analytics, and digital twin architectures, it functions as a critical bridge between raw satellite observations and actionable knowledge. For urban planners, environmental managers, and scientists, GEE signifies more than a mere instrument; it denotes a paradigm shift, a transition towards transparent, scalable, and data-driven governance of the rapidly evolving cities of the 21st century.

References

Abadi, M., Agarwal, A., Barham, P., Brevdo, E., Chen, Z., Citro, C., . . . Moore, S. (2016). TensorFlow: Large-scale machine learning on heterogeneous distributed systems. *In Proceedings of the 12th USENIX symposium on operating systems design and implementation (OSDI'16)*, (s. pp. 265-283). Savannah, GA, USA.

Camara, G., Souza, R., Pedrosa, B., Vinhas, L., Monteiro, A. M., Paiva, J., & ... & Gattass, M. (2000). TerraLib: Technology in support of GIS innovation. *In II Workshop Brasileiro de Geoinformática, GeoInfo2000*, (s. Vol. 2, pp. 1-8). São Paulo.

Chambers, C., Raniwala, A., Perry, F., Adams, S., Henry, R. R., Bradshaw, R., & & Weizenbaum, N. (2010). FlumeJava: easy, efficient data-parallel pipelines. *ACM Sigplan Notices*, 45(6), 363-375.

Chang, F., Dean, J., Ghemawat, S., Hsieh, W. C., Wallach, D. A., Burrows, M., & ... & Gruber, R. E. (2008). Bigtable: A distributed storage system for structured data. *ACM Transactions on Computer Systems (TOCS)*, 26(2), 1-26.

Copernicus Data Access Policy. (2025, 12 1). http://www.copernicus.eu/main/data-access adresinden alındı

Corbett, J. C., Dean, J., Epstein, M., Fikes, A., Frost, C., Furman, J. J., & ... & Woodford, D. (2013). Spanner: Google's globally distributed database. *ACM Transactions on Computer Systems (TOCS)*, 31(3), 1-22.

Ghemawat, S., Gobioff, H., & & Leung, S. T. (2003). The Google file system. *In Proceedings of the nineteenth ACM symposium on Operating systems principles.*, (s. pp. 29-43).

Gonzalez, H., Halevy, A. Y., Jensen, C. S., Langen, A., Madhavan, J., Shapley, R., & ... & Goldberg-Kidon, J. (2010). Google fusion tables: web-centered data management and collaboration. *In Proceedings of the 2010 ACM SIGMOD International Conference on Management of data* , (s. pp. 1061-1066).

Gorelick, N., Hancher, M., Dixon, M., Ilyushchenko, S., Thau, D., & & Moore, R. (2017). Google Earth Engine: Planetary-scale geospatial analysis for everyone. *Remote sensing of Environment*, 202, 18-27.

Hansen, M. C., Potapov, P. V., Moore, R., Hancher, M., Turubanova, S. A., Tyukavina, A., & ... & Townshend, J. R. (2013). High-resolution global maps of 21st-century forest cover change. *Science*, 342(6160), 850-853.

Hughes, J. N., Annex, A., Eichelberger, C. N., Fox, A., Hulbert, A., & & Ronquest, M. (2015). Geomesa: a distributed architecture for spatio-temporal fusion. *In Geospatial informatics, fusion, and motion video analytics V SPIE.*, (s. Vol. 9473, pp. 128-140).

Loveland, T. R., & Dwyer, J. L. (2012). Landsat: Building a strong future. *Remote Sensing of Environment*, 122, 22-29.

Nemani, R., Votava, P., Michaelis, A., Melton, F., & & Milesi, C. (2011). Collaborative supercomputing for global change science. *Eos, Transactions American Geophysical Union*, 92(13), 109-110.

Patel, N. N., Angiuli, E., Gamba, P., Gaughan, A., Lisini, G., Stevens, F. R., & ... & Trianni, G. (2015). Multitemporal settlement and population mapping from Landsat using Google Earth Engine. *International Journal of Applied Earth Observation and Geoinformation*, 35, 199-208.

Pekel, J. F., Cottam, A., Gorelick, N., & & Belward, A. S. (2016). High-resolution mapping of global surface water and its long-term changes. *Nature*, 540(7633), 418-422.

Verma, A., Pedrosa, L., Korupolu, M., Oppenheimer, D., Tune, E., & & Wilkes, J. (2015). Large-scale cluster management at Google with Borg., (s. pp. 1-17). In Proceedings of the tenth european conference on computer systems.

Whitman, R. T., Park, M. B., Ambrose, S. M., & Hoel, E. G. (2014). Spatial indexing and analytics on Hadoop. *In Proceedings of the 22nd ACM SIGSPATIAL international conference on advances in geographic information systems*, (s. pp. 73-82).

Woodcock, C. E., Allen, R., Anderson, M., Belward, A., Bindschadler, R., Cohen, W., & ... WULDER, M. A. (2008). Free access to Landsat imagery. *SCIENCE*, 320: 1011.

Yu, J., Wu, J., & Sarwat, M. (2015). Geospark: A cluster computing framework for processing large-scale spatial data. *In Proceedings of the 23rd SIGSPATIAL international conference on advances in geographic information systems*, (s. pp. 1-4).

Zhang, Q., Li, B., Thau, D., & & Moore, R. (2015). Building a better urban picture: Combining day and night remote sensing imagery. *Remote Sensing*, 7(9), 11887-11913.

Chapter 4

p-AMINOPHENOL REMOVAL FROM WATER SYSTEMS

Mustafa DEMİRALP[1] , Halil İbrahim ÇETİNTAŞ[2]

---

[1] Lect. Dr., Sivas Cumhuriyet University Advanced Technology Research and Application Center,

ORCID: 0000-0002-9530-0270

[2] Assist. Prof. Dr., Sivas Cumhuriyet University Department of Chemical Engineering,

ORCID: 0000-0003-1769-0098

1. Introduction

The spread of industrialization, population growth, intensified migration towards cities, and the accompanying uncontrolled and excessive use of natural resources have brought about environmental problems. Furthermore, the threat of global water scarcity encourages research into the development of new strategic plans aimed at protecting natural water resources and improving water quality.

The uncontrolled and inadequate discharge of wastewater from manufacturing industries such as textiles, paper, paint, metal, fertilizers, batteries, food, and pharmaceuticals, along with various anthropogenic activities, poses a significant threat to both water resources and human health. This wastewater contains various toxic pollutants, primarily organic and inorganic substances. Among the main organic pollutants, pharmaceutical and phenolic compounds stand out due to their resistance to degradation and are classified as persistent organic pollutants (POPs) (Akhtar et al., 2021; Bustos Bustos et al., 2022).

Phenolic compounds such as chlorophenols and aminophenols, particularly those formed during pharmaceutical and dye production processes, are among the priority pollutants due to their persistence, toxicity, and adverse effects on human health and the environmental ecosystem (Panigrahy et al., 2022). Especially used in textile, dye, and pharmaceutical industries, *p*-aminophenol (*p*-AP) is considered an environmental contaminant with notable toxicity and persistence concerns, causing potential adverse effects on human health and aquatic ecosystems (Yin et al., 2025). Therefore, studies focusing on the removal of different types of organic pollutants, as well as monitoring even trace amounts of these pollutants with high sensitivity and selectivity using practical and environmentally friendly methods, have gained importance in recent years (Mishra et al., 2022).

2. Characteristics of *p*-Aminophenol

p-AP is a non-opiate phenolic compound. With the molecular formula C_6H_7NO, it consists of a benzene ring substituted with an amino group and a hydroxyl group (Figure 1) (Li et al., 2025). A crystalline, colorless solid, *p*-AP readily oxidizes and decomposes under the influence of air and light, taking on a dark brown color. It is an organic chemical intermediate widely used in the production of sulfur and azo dye components used in textiles, wood dyes, resins, explosives, pharmaceuticals, and pesticides, as well as in dyes, pharmaceuticals, antioxidants, and petroleum additives. It also finds application as a reducing agent in the production of black-and-white photographic films (Nemakal et al., 2019; Asheghmoalla et al., 2024).

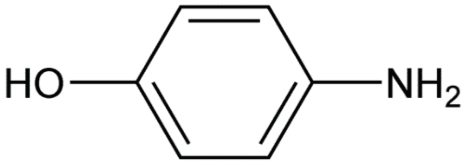

Figure 1. The structural formula of *p*-AP.

3. Toxicity and Environmental Impact of *p*-Aminophenol

p-AP is a major byproduct of paracetamol synthesis, a widely used pharmaceutical active ingredient, and is known to have high toxicity and carcinogenic properties. Considered a toxic environmental pollutant, *p*-AP exhibits the dual toxicity of phenol and aniline groups. Absorption of *p*-AP can lead to significant dermatitis, nephrotoxic and teratogenic effects on the skin, as well as eczema (Chen et al., 2020). It can cause prolonged elevated body temperature, leading to mutagenic effects and DNA breaks in living organisms. For all these reasons, the upper limit for p-AP in paracetamol is set at 5 ppm by the United States Pharmacopoeia (USP), the European Pharmacopoeia (EP), and the Chinese Pharmacopoeia (Nemakal et al., 2019).

Due to all these negative effects of p-AP on the environment and living organisms, monitoring its presence in wastewater is of great importance. For this purpose, many highly sensitive methods have been developed for the determination of *p*-AP. These include ultraviolet and fluorescence spectroscopy (Bloomfield et al., 2002; Lu et al., 2017; Goclik et al., 2019), liquid and gas chromatography (Ohtnai et al., 2007; Abdelaleem et al., 2015), capillary electrophoresis (Chu et al., 2008), and electrochemical methods (Lee et al., 2019; Krampa et al., 2020). The removal, treatment, or detection of trace amounts of *p*-AP from industrial wastewater is critically important for environmental sustainability. In this context, the development of high-sensitivity analytical techniques, as well as the engineering of low-cost, environmentally friendly, and practical removal methods, is gaining prominence (Karimi-Maleh et al., 2023). Furthermore, in pharmaceutical production processes, wastewater with a high degree of pollution is generated during operations such as equipment cleaning, cooling processes, and the development of new drug active ingredients. As a result, in order to comply with wastewater management policies, industries need to minimize wastewater generation at the source. This necessitates the application of end-of-pipe treatment methods (Asheghmoalla et al., 2024).

Although various physical, chemical, and synthetic methods have been applied to remove organic pollutants found in wastewater, the desired efficiency levels have mostly not been achieved. Therefore, in recent years, naturally derived adsorbents have been considered as a more environmentally friendly and sustainable alternative to conventional treatment methods.

4. Removal Studies of *p*-Aminophenol

Adsorption is a widely used separation, pre-concentration, and treatment technique based on the principle of molecules migrating from a gaseous or liquid medium to a solid surface. This inexpensive, efficient, easy to implement, and environmentally friendly technique stands out as one of the most effective techniques, particularly for removing phenolic and other toxic compounds from wastewater (Ahmaruzzaman, 2008; Rashid et al., 2021). However, most adsorbent materials commonly used in the removal of pollutants from wastewater have limitations due to factors such as high cost, difficulty in the synthesis phase, low selectivity, and the use of toxic chemicals (Satyam and Patra, 2024). Therefore, researchers are focusing on the preparation of low-cost, sustainable, and readily available adsorbents, and are moving towards the design, development, and use of natural, new, effective, and innovative materials.

Mishra et al. (2022) investigated the removal of *p*-AP, a toxic pollutant, from aqueous solutions using an adsorbent obtained by activating pea husks, considered agricultural waste, with sulfuric acid. In their study, they evaluated the parameters affecting the adsorption process in terms of adsorbent dose, temperature, pH, zero charge point, addition of potassium chloride and urea, and initial concentration of *p*-AP. They found that the adsorption capacity decreased with increasing temperature from 25°C to 45°C. Under optimum conditions (pH 7, 25°C), they determined the maximum adsorption capacity as 106.11 mg/g.

In a study conducted by Celarek (2017), the removal of *p*-AP from aqueous solutions was investigated using a poly(ether-block-amide) adsorbent. Suitable isotherm and kinetic models were determined for the adsorption process, and it was observed that the adsorption behavior varied depending on the concentration. It was stated that, especially at concentrations above 100 milligrams/liter, different mechanisms in addition to diffusion contributed to the process. Furthermore, the presence of electrolytes such as sodium chloride in the system significantly increased the adsorption of *p*-AP. These results demonstrate that the poly(ether-block-amide) based adsorbent is an effective material for *p*-AP removal.

Guo et al. (2016) developed an innovative catalyst-adsorbent composite for the removal of *p*-AP from water and its simultaneous conversion to p-aminophenol. In this study, a structure containing gold nanoparticles supported on functionalized mesoporous carbon was used. Gold nanoparticles showed high catalytic activity in converting p-nitrophenol (*p*-NP) to *p*-AP with the help of sodium borohydride. Simultaneously, the mesoporous carbon support played an effective role in the adsorption of *p*-AP. The study demonstrated that this composite material offers an effective and reusable method for the removal of nitroaromatic pollutants.

Tewari (2014) investigated the removal of *p*-AP and *p*-NP from aqueous solutions via adsorption onto bismuth, lead, and manganese ferrocyanides. Under neutral pH conditions, *p*-NP was adsorbed to a higher extent than *p*-AP on all three metal ferrocyanides. Manganese ferrocyanide had the highest adsorption capacity for both pollutants, while bismuth ferrocyanide showed the lowest performance. These findings suggest that metal ferrocyanides can be effective adsorbents for the removal of *p*-AP and *p*-NP, particularly depending on pH conditions.

Rahman et al. (2020) developed a sensitive electrochemical sensor for the selective removal of *p*-AP. In the study, SrO nanorods synthesized by wet chemical precipitation were coated onto the surface of a glassy carbon electrode and used as the active component of the sensor. The sensor sensitivity was calculated as 21.5443 $\mu A\ \mu M^{-1}\ cm^{-2}$ considering the active surface area of the electrode. Furthermore, the detection limit of the sensor was determined as 95.76 ± 4.79 pM based on a signal-to-noise ratio of 3. The study demonstrated that the sensor exhibited satisfactory performance in terms of repeatability, fast response time, and long-term stability.

Degradation is described as the process by which pollutants are decomposed, transformed, or eliminated into less harmful substances, with effectiveness that varies according to the characteristics of the pollutant and the prevailing environmental or treatment conditions. In this context, degradation is one of the effective methods widely used in the removal of *p*-AP from the environment.

In a recent study, Wang et al. (2025) developed a composite hydrodynamic cavitation system consisting of spiral tubes and a cascaded drainage structure capable of generating cavitation twice per pass for the degradation of *p*-AP. The system used was reported to offer advantages in terms of energy utilization and mass transfer, and to produce a high amount of hydroxyl radicals, which are effective in the degradation of organic pollutants. In batch experiments, the *p*-AP degradation efficiency reached 74.7% after 120 minutes; it was shown that intermediate products such as benzoquinone were formed during the process and nitrogen species were largely removed through deamination. The results obtained revealed that hydrodynamic cavitation is a promising method for the degradation of resistant organic pollutants and nitrogen removal.

Patil and Bhandari (2022) proposed a novel solvent-assisted cavitation-based degradation approach for the removal of organic pollutants. The study demonstrated that adding suitable solvents at low concentrations (1–5%, v/v) to the conventional hydrodynamic cavitation process significantly increased pollutant removal efficiency. *p*-AP was used as the model pollutant, and different solvents (1-octanol, cyclohexanol, 1-octane, and toluene) were tested. It was determined that relatively more polar solvents increased pollutant removal efficiency by over 65% and reaction rates by more than 200% compared to hydrodynamic cavitation alone. Furthermore, degradation models per pass showed that 3–4 times higher degradation was achieved with polar solvents. The results showed that classical solvent extraction plays no role in the process, no secondary contamination occurs in the wastewater, and the cost of the method is 2–3 times lower compared to conventional hydrodynamic cavitation.

Biodegradation by microorganisms represents an effective approach for removing such pollutants from soil and aquatic environments. Khan et al. (2006) conducted a study demonstrating the effectiveness of biodegradation in the removal of *p*-AP. The study investigated the removal of *p*-AP from soil and water environments using the *Pseudomonas* sp. ST-4 strain. It was determined that this microorganism could utilize *p*-AP as its sole carbon and energy source on mineral salt medium and could grow up to 400 ppm. Under liquid culture conditions, *p*-AP degradation rates of up to 84% were reported. Furthermore, it was stated that pre-induction of cells with *p*-AP significantly increased the degradation rate, while lower degradation was observed in uninduced cells. The study emphasized that biodegradation is much more effective than auto-oxidation of *p*-AP and that bioremediation is a fundamental process in the elimination of aromatic amines. These findings demonstrate that microorganism-based degradation is a robust and sustainable approach for *p*-AP removal.

5. Conclusion

Rapidly developing industries and increasing populations have increased the release of toxic organic pollutants into aquatic environments, making the conservation of water resources a critical global issue. Among these pollutants, p-aminophenol (p-AP) stands out due to its toxic effects, persistence in the environment, and use in various industries, particularly as an intermediate or byproduct in the pharmaceutical and dye industries. Its resistance to conventional treatment processes and serious negative impacts on human health and aquatic ecosystems necessitate the development of effective, sensitive, and environmentally sustainable removal and monitoring strategies. While the number of studies in the literature is quite limited, adsorption and degradation approaches generally emerge as promising techniques for the efficient removal and control of p-AP in wastewater systems. Future research should focus on hybrid and synergistic treatment technologies, scalability, cost reduction, and real-world wastewater applications to ensure environmental sustainability and access to clean water.

REFERENCES

Abdelaleem, E. A., Naguib, I. A., Hassan, E. S., & Ali, N. W. (2015). HPTLC and RP-HPLC methods for simultaneous determination of Paracetamol and Pamabrom in presence of their potential impurities. *Journal of pharmaceutical and biomedical analysis*, *114*, 22-27.

Ahmaruzzaman, M. (2008). Adsorption of phenolic compounds on low-cost adsorbents: a review. *Advances in colloid and interface science*, *143*(1-2), 48-67.

Akhtar, A. B. T., Naseem, S., Yasar, A., & Naseem, Z. (2021). Persistent organic pollutants (POPs): sources, types, impacts, and their remediation. In *Environmental pollution and remediation* (pp. 213-246). Singapore: Springer Singapore.

Asheghmoalla, M., & Mehrvar, M. (2024). Adsorption of a multicomponent pharmaceutical wastewater on charcoal-based activated carbon: equilibrium and kinetics. *Water*, *16*(15), 2086.

Bloomfield, M. S. (2002). A sensitive and rapid assay for 4-aminophenol in paracetamol drug and tablet formulation, by flow injection analysis with spectrophotometric detection. *Talanta*, *58*(6), 1301-1310.

Bustos Bustos, E., Sandoval-González, A., & Martínez-Sánchez, C. (2022). Detection and treatment of persistent pollutants in water: general review of pharmaceutical products. *ChemElectroChem*, *9*(12), e202200188.

Celarek, M. (2017). Sorptive Removal of 4-Aminophenol from Water Using a Polymeric Sorbent.

Chen, S., Huang, R., Zou, J., Liao, D., Yu, J., & Jiang, X. (2020). A sensitive sensor based on MOFs derived nanoporous carbons for electrochemical detection of 4-aminophenol. *Ecotoxicology and Environmental Safety*, *191*, 110194.

Chu, Q., Jiang, L., Tian, X., & Ye, J. (2008). Rapid determination of acetaminophen and p-aminophenol in pharmaceutical formulations using miniaturized capillary electrophoresis with amperometric detection. *Analytica chimica acta*, *606*(2), 246-251.

Goclik, E., Chrzescijanska, E., Kusmierek, E., & Rynkowski, J. (2019). Electroanalytical and Spectrophotometric Determination of N-acetyl-p-aminophenol in Pharmaceuticals. *Portugaliae Electrochim. Acta*, *37*, 345-357.

Guo, P., Tang, L., Tang, J., Zeng, G., Huang, B., Dong, H., ... & Tan, S. (2016). Catalytic reduction–adsorption for removal of p-nitrophenol and its conversion p-aminophenol from water by gold nanoparticles supported on oxidized mesoporous carbon. *Journal of colloid and interface science*, *469*, 78-85.

Karimi-Maleh, H., Darabi, R., Karimi, F., Karaman, C., Shahidi, S. A., Zare, N., ... & Rajendran, S. (2023). State-of-art advances on removal, degradation and electrochemical monitoring of 4-aminophenol pollutants in real samples: a review. *Environmental Research*, *222*, 115338.

Khan, S. A., Hamayun, M., & Ahmed, S. (2006). Degradation of 4-aminophenol by newly isolated Pseudomonas sp. strain ST-4. *Enzyme and Microbial Technology*, *38*(1-2), 10-13.

Krampa, F. D., Aniweh, Y., Kanyong, P., & Awandare, G. A. (2020). Graphene nanoplatelet-based sensor for the detection of dopamine and N-acetyl-p-aminophenol in urine. *Arabian Journal of Chemistry*, *13*(1), 3218-3225.

Lee, S. B., Ju, Y., Lee, Y., & Kim, J. (2019). Indium tin oxide modified with dendrimer-encapsulated Pt nanoparticles as efficient p-aminophenol redox cycling platforms. *Applied Surface Science*, *473*, 461-467.

Li, H., Lin, Z. F., Chen, Z. C., Han, G. C., Feng, X. Z., & Kraatz, H. B. (2025). Research advances in chemical sensing of p-Aminophenol: A review. *Microchemical Journal*, *208*, 112424.

Lu, X., Wei, F., Xu, G., Wu, Y., Yang, J., & Hu, Q. (2017). Surface molecular imprinting on silica-coated CdTe quantum dots for selective and sensitive fluorescence detection of p-aminophenol in water. *Journal of fluorescence*, *27*(1), 181-189.

Mishra, P., Singh, K., Dixit, U., Agarwal, A., & Bhat, R. A. (2022). Effective removal of 4-Aminophenol from aqueous environment by pea (Pisum sativum) shells activated with sulfuric acid: Characterization, isotherm, kinetics and thermodynamics. *Journal of the Indian Chemical Society*, *99*(7), 100528.

Nemakal, M., Aralekallu, S., Mohammed, I., Pari, M., Reddy, K. V., & Sannegowda, L. K. (2019). Nanomolar detection of 4-aminophenol using amperometric sensor based on a novel phthalocyanine. *Electrochimica Acta*, *318*, 342-353.

Ohtnai, H., Sugimoto, N., Hirano, M., Yokota, T., & Katoh, K. (2007). Precise compositional analysis of liquid crystalline aromatic polyesters containing aromatic amide linkages by thermally assisted hydrolysis and methylation-gas chromatography. *Journal of analytical and applied pyrolysis*, *79*(1-2), 323-326.

Panigrahy, N., Priyadarshini, A., Sahoo, M. M., Verma, A. K., Daverey, A., & Sahoo, N. K. (2022). A comprehensive review on eco-toxicity and biodegradation of phenolics: Recent progress and future outlook. *Environmental Technology & Innovation*, *27*, 102423.

Patil, P. B., & Bhandari, V. M. (2022). Solvent-assisted cavitation for enhanced removal of organic pollutants-degradation of 4-aminophenol. *Journal of environmental management*, *311*, 114857.

Rashid, R., Shafiq, I., Akhter, P., Iqbal, M. J., & Hussain, M. (2021). A state-of-the-art review on wastewater treatment techniques: the effectiveness of adsorption method. *Environmental Science and Pollution Research*, *28*(8), 9050-9066.

Satyam, S., & Patra, S. (2024). Innovations and challenges in adsorption-based wastewater remediation: A comprehensive review. *Heliyon*, *10*(9).

Tewari, B. B. (2014). Removal of p-aminophenol and p-nitrophenol from aqueous solution through adsorption on bismuth, lead, and manganese ferrocyanides and their relevance to environmental issues. *Russian Journal of Physical Chemistry A*, *88*(9), 1564-1568.

Wang, B., Zhang, R., She, Z., & Li, Y. (2025). Degradation and Nitrogen Transfer of 4-Aminophenol by Cavitation Induced by a Composite Hydrodynamic Cavitator. *Reactions*, *6*(4), 68.

Yin, C. F., Pan, P., Li, T., Song, X., Xu, Y., & Zhou, N. Y. (2025). The universal accumulation of p-aminophenol during the microbial degradation of analgesic and antipyretic acetaminophen in WWTPs: a novel metagenomic perspective. *Microbiome*, *13*(1), 68.

Chapter 5

TRIBOLOGICAL RESPONSE OF AISI 4140 STEEL UNDER DRY AND FLUID-ASSISTED RECIPROCATING SLIDING CONDITIONS

Yavuz SUN[1]*, Bünyamin ÇİÇEK*[2]

---

[1] Karabuk University, Engineering And Natural Sciences Faculty, Karabük, Türkiye

ORCID: https://orcid.org/0000-0002-7336-5591

[2] Hitit University, Technical Sciences Vocational School, Çorum, Türkiye

ORDID: https://orcid.org/0000-0002-6603-7178

1. Introduction

Wear and friction remain among the most critical degradation mechanisms limiting the service life of steel components in automotive, energy, marine, and heavy industrial applications. Medium-carbon alloy steels such as AISI 4140 (EN 1.4140) are widely employed in shafts, gears, crankshafts, and load-bearing mechanical systems due to their favorable combination of strength, toughness, and hardenability. However, when subjected to repeated sliding or reciprocating contact, these steels are highly susceptible to surface damage, material loss, and energy dissipation driven by complex tribological interactions (S. Das, Prasad, Jha, Modi, & Yegneswaran, 1993; Modi, Prasad, Jha, Dasgupta, & Yegneswaran, 2003).

Wear behavior in steels is governed not only by material composition and microstructure but also by the surrounding environment, contact mechanics, and lubrication conditions. Under dry sliding, direct asperity–asperity contact typically promotes severe abrasive and adhesive wear, resulting in high friction coefficients, deep wear grooves, and accelerated material removal (Maleque et al., 1998; Das et al., 2009). Conversely, the presence of liquid media can significantly alter contact conditions by reducing metal-to-metal interaction, dissipating frictional heat, and forming protective boundary or mixed lubrication films (Wang, Chen, Chen, Yan, & Xue, 2012; Wood, 2017).

In recent decades, increasing attention has been devoted to understanding the influence of different lubricating fluids on wear mechanisms, particularly in reciprocating systems that closely simulate real operating conditions in engines, pumps, and sliding assemblies. Studies have demonstrated that lubricant chemistry plays a decisive role in friction control, wear rate reduction, and surface integrity preservation (Arumugam & Sriram, 2012; Mobarak et al., 2014; Pathak, Joshi, Mer, Katiyar, & Patel, 2019). Bio-lubricants, mineral oils, and additive-enhanced fluids have been extensively investigated as potential alternatives to conventional lubricants, with reported improvements in tribological efficiency and environmental sustainability (Balakumar, Sriram, & Arumugam, 2020; Song, Yu, Song, & Hu, 2022).

Among lubricant additives, boron-containing compounds and boron-based oils have attracted particular interest due to their ability to form tribo-chemical films with high load-bearing capacity and excellent anti-wear performance. Previous studies on boronized steels and boron-enriched lubricants have shown remarkable reductions in friction coefficient, wear depth, and surface roughness, attributed to the formation of hard boride layers or lubricious boron-rich tribofilms at the sliding interface (Ahlatci et al., 2013; Liu et al., 2021; Medvedovski, Jiang, & Robertson, 2016). Despite these promising findings, systematic experimental comparisons between conventional lubricants and boron-based oils under identical test conditions remain relatively limited, particularly for medium-carbon alloy steels such as AISI 4140.

Furthermore, most tribological studies primarily focus on single performance indicators—such as coefficient of friction or mass loss—without establishing a comprehensive relationship between frictional energy dissipation, wear rate, wear track geometry, and surface roughness evolution. However, recent investigations emphasize that integrating these parameters provides deeper insight into dominant wear mechanisms and more reliable guidelines for lubricant selection in industrial practice (Li & Hu, 2020; Matbouei, 2018).

Against this background, the present chapter aims to provide a systematic and comparative tribological assessment of AISI 4140 steel under dry sliding and three different liquid environments: water-based antifreeze, mineral motor oil, and 100% boron oil. Reciprocating wear tests were conducted under identical load, sliding distance, and ambient conditions to isolate the effect of the fluid medium on frictional response and wear behavior. The study integrates coefficient of friction, mass loss, wear rate, frictional energy dissipation, maximum wear track depth, and surface roughness measurements, supported by optical and scanning electron microscopy observations.

The experimental methodology and test configuration are illustrated in Figure 1, while quantitative tribological results are summarized in Tables 1–6, covering frictional, mechanical, and surface-related parameters. Representative SEM and optical microscopy images of wear tracks are presented in Figures 2 and 3, enabling direct correlation between numerical data and surface damage mechanisms.

By combining multiple tribological metrics with detailed surface analysis, this chapter provides a comprehensive framework for evaluating lubricant performance and wear control strategies in medium-carbon steels. The findings are expected to contribute not only to the scientific understanding of fluid-assisted wear mechanisms but also to practical lubricant selection and surface protection strategies in automotive and industrial applications.

2. Materials and Methods

2.1 Material Selection and Specimen Preparation

AISI 4140 (EN 1.4140) medium-carbon low-alloy steel was selected as the test material due to its extensive use in automotive, mechanical, and industrial applications involving sliding contact and moderate to high mechanical loads. The steel is commonly employed in components such as shafts, gears, and transmission elements where wear resistance is a critical design requirement.

Cylindrical specimens with a diameter of 15 mm and a thickness of 10 mm were prepared for tribological testing. Prior to experiments, all specimens were subjected to standard metallographic preparation procedures, including mounting, grinding, and polishing, in order to obtain a uniform and reproducible surface condition. After preparation, the samples were thoroughly cleaned to remove surface contaminants that could influence frictional behavior during testing.

2.2 Reciprocating Wear Test Setup

Reciprocating wear experiments were conducted using a laboratory-scale reciprocating tribometer (4D-DTM-25). The system provides controlled forward–backward sliding motion under a constant normal load and is designed to simulate contact conditions encountered in practical mechanical systems such as engine components and sliding assemblies.

All tests were performed at ambient temperature under a fixed normal load of 10 N. The sliding motion was applied with a stroke length of 10 mm, and the total sliding distance was set to 100 m. During testing, the lateral friction force generated at the contact interface was continuously monitored using an integrated load cell. The coefficient of friction was determined from the measured friction force and the applied normal load.

Figure 1. Experimental setup and schematic representation of the reciprocating wear test configuration.

2.3 Counter body and Contact Configuration

A tungsten carbide (WC) ball was used as the counter body material in all experiments. The ball–flat contact configuration was maintained consistently to ensure repeatable contact conditions. The high hardness of the WC counter body minimized counter face wear and ensured that the observed tribological response was primarily associated with the steel specimens.

All mechanical parameters, including normal load, stroke length, sliding distance, and counter body material, were kept constant throughout the study to isolate the influence of the surrounding environment.

2.4 Test Environments

Wear tests were carried out under four different environmental conditions: dry sliding under ambient air, water-based antifreeze, mineral motor oil (20–40W), and 100% boron oil. For liquid-assisted tests, the contact region between the specimen and the counterbody was fully immersed in the selected fluid to maintain continuous lubrication during sliding.

Each environment was tested independently while keeping all mechanical parameters unchanged, allowing direct assessment of the effect of the surrounding medium on the tribological response.

2.5 Friction Monitoring and Wear Assessment Procedure

During each test, friction force was recorded continuously through the load cell integrated into the tribometer. The coefficient of friction was obtained by normalizing the measured friction force with respect to the applied normal load.

Specimen mass measurements were performed before and after testing using a precision balance in order to quantify material removal during sliding. The wear assessment procedure was based on mass loss measurements and predefined test parameters such as load and sliding distance.

2.6 Energy Dissipation Calculation

Frictional energy dissipation during sliding was evaluated as a function of friction force and total sliding distance. This approach was used to describe the mechanical energy loss associated with reciprocating contact under different test environments.

2.7 Surface Profiling and Roughness Measurement Procedure

After completion of the wear tests, surface profiling was conducted to characterize wear-induced surface modifications. Maximum wear track depth and surface roughness measurements were performed using a portable surface profiling and roughness measurement device (Insize ISR-C300).

Surface roughness parameters, including average roughness (Ra), maximum profile height (Rz), and total roughness height (Rt), were measured perpendicular to the sliding direction to ensure consistent characterization.

2.8 Surface Morphology Examination

The worn surfaces of the specimens were examined using optical microscopy and scanning electron microscopy (SEM). Optical microscopy was employed for general observation of wear tracks, while SEM analysis provided high-resolution imaging of surface morphology and wear-related features.

3. Results and Discussion

3.1 Friction Behaviour under Different Test Environments

The coefficient of friction (COF) represents one of the most fundamental indicators of tribological performance, reflecting the nature of contact interactions and dominant wear mechanisms. Under dry sliding conditions, direct asperity–asperity contact governs frictional response, typically resulting in unstable friction behaviour and elevated resistance to motion (D. Das, Ray, & Dutta, 2009; S. Das et al., 1993; Maleque, Masjuki, & Ishak, 1998). In contrast, the presence of liquid media modifies the contact interface by introducing lubrication films that reduce solid–solid interaction and frictional energy dissipation.

In the present study, friction behaviour was systematically evaluated under dry, antifreeze, motor oil, and boron oil environments.

Table 1. Coefficient of friction and friction force values obtained under different environments.

Environments	Coefficient of friction	Friction force
Dry wear	0.342	3,42 N
Antifreeze	0.161	1.61 N
24-40w motor oil	0.189	1.89 N
%100 boron oil	0.112	1.12 N

The observed differences in frictional response can be attributed to variations in lubricant chemistry and film-forming capability. Previous studies have demonstrated that liquid lubricants significantly alter surface shear strength by promoting boundary or mixed lubrication regimes (Arumugam & Sriram, 2012; Mobarak et al., 2014; Yu, Cao, Li, Huang, & Li, 2023). In particular, boron-containing lubricants have been reported to form protective tribofilms with enhanced load-carrying capacity, thereby stabilizing frictional behavior (Ahlatci et al., 2013; Matbouei, 2018; Medvedovski et al., 2016).

3.2 Mass Loss and Wear Rate Analysis

Mass loss measurements provide a direct indication of material removal during sliding contact and are commonly employed to quantify wear severity. However, mass loss alone does not fully describe wear mechanisms and must be interpreted alongside frictional and surface-related parameters (Kravtsova, Kowalsky, & Lysyannikova, 2020; Modi et al., 2003; Wang et al., 2012).

Table 2. Mass loss values measured after wear testing.

Environments	First weight (g)	Final weight (g)	Mass loss (g)
Dry wear	8.7558	8.6574	0.0984
Antifreeze	8.5520	8.4610	0.0910
24-40w motor oil	8.2587	8.1785	0.0802
%100 boron oil	8.3520	8.2912	0.0608

The calculated wear rates, derived from mass loss, material density, applied load, and sliding distance, enable normalization of wear behaviour and facilitate comparison across different environments.

Table 3. Wear rate values expressed as volume loss per unit load and sliding distance.

Environments	Wear rate (mm^3/N.m)
Dry wear	0.01253
Antifreeze	0.01159
24-40w motor oil	0.01021
%100 boron oil	0.00774

Dry sliding conditions are widely associated with severe abrasive wear and accelerated material removal due to the absence of any protective interfacial layer (D. Das et al., 2009; Modi et al., 2003; Pillar et al., 2005). In contrast, liquid-assisted environments reduce wear by minimizing direct metal-to-metal contact and by dissipating frictional heat from the contact zone (Matbouei, 2018; Pathak et al., 2019; Wood, 2017). The differences observed among antifreeze, motor oil, and boron oil environments highlight the critical role of lubricant composition and viscosity in controlling wear mechanisms (Balakumar et al., 2020; Li & Hu, 2020; Pathak et al., 2019).

3.3 Frictional Energy Dissipation

Beyond conventional tribological parameters, frictional energy dissipation offers a comprehensive metric for evaluating the efficiency of sliding systems. Energy loss during reciprocating motion is directly associated with friction force and sliding distance and provides insight into the mechanical efficiency of the tribo system (Liu et al., 2021; Song et al., 2022).

Table 4. Friction force–based energy dissipation values.

Environments	Friction force (N)	Energy dissipation (J)
Dry wear	3.42	342
Antifreeze	1.61	161
24-40w motor oil	1.89	189
%100 boron oil	1.12	112

Lower energy dissipation indicates more efficient lubrication and reduced mechanical degradation at the contact interface. Previous studies have emphasized that lubricants capable of maintaining stable boundary films significantly reduce friction-induced energy losses and contribute to prolonged component lifetime (Mobarak et al., 2014; Song et al., 2022). Boron-based lubricants, in particular, have been shown to promote tribochemical reactions leading to low-shear-strength surface layers (Medvedovski et al., 2016; Liu et al., 2021).

3.4 Wear Track Depth and Surface Roughness Characteristics

Wear track depth provides localized information on the severity of surface damage and complements mass loss measurements by revealing the extent of subsurface deformation and material removal (Das et al., 1993; Modi et al., 2003).

Table 5. Maximum wear track depth values measured after testing.

Environments	Maximum wear track depth (mm)
Dry wear	0.025
Antifreeze	0.011
24-40w motor oil	0.013
%100 boron oil	0.008

Surface roughness parameters further reflect changes in surface topography induced by sliding contact and are closely linked to frictional stability and wear progression (Balakumar et al., 2020).

Table 6. Surface roughness parameters (Ra, Rz, Rt) for different environments.

Environments	Ra (µm)	Rz (µm)	Rt (µm)
Dry wear	1.523	4.245	6.184
Antifreeze	0.762	2.098	3.436
24-40w motor oil	0.850	2.376	3.992
%100 boron oil	0.503	1.467	2.723

Dry sliding typically results in pronounced surface roughening due to severe ploughing and micro-cutting, whereas liquid lubrication mitigates roughness evolution by smoothing asperity interactions and limiting debris formation (Maleque et al., 1998; Wood, 2017). Boron oil lubrication, in particular, has been associated with improved surface smoothness due to the formation of protective tribofilms and reduced third-body abrasion (Ahlatci et al., 2013; Medvedovski et al., 2016).

3.5 Surface Morphology and Wear Mechanisms

Microscopic examination of the worn surfaces provides direct evidence of the dominant wear mechanisms and supports the quantitative tribological findings. Optical microscopy allows the identification of macroscopic wear features, including wear grooves and material transfer regions, as illustrated in Figure 3, offering an overview of surface damage morphology. In contrast, scanning electron microscopy (SEM) enables high-resolution observation of micro-scale damage mechanisms, such as abrasive grooves, adhesive junctions, and tribofilm formation, which are clearly revealed in Figure 2. Together, the complementary information obtained from optical microscopy and SEM analyses facilitates a comprehensive interpretation of wear processes occurring under different test environments (Das et al., 2009; Wang et al., 2012).

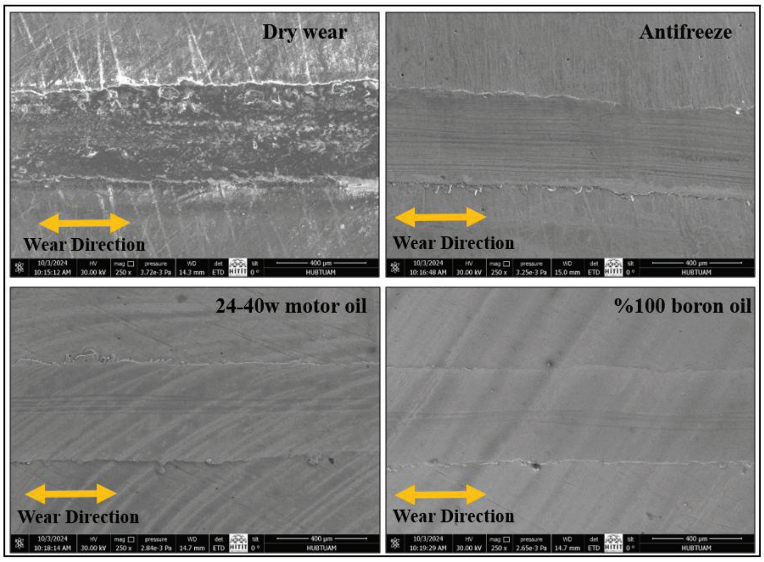

Figure 2. SEM images of wear tracks formed under different test environments.

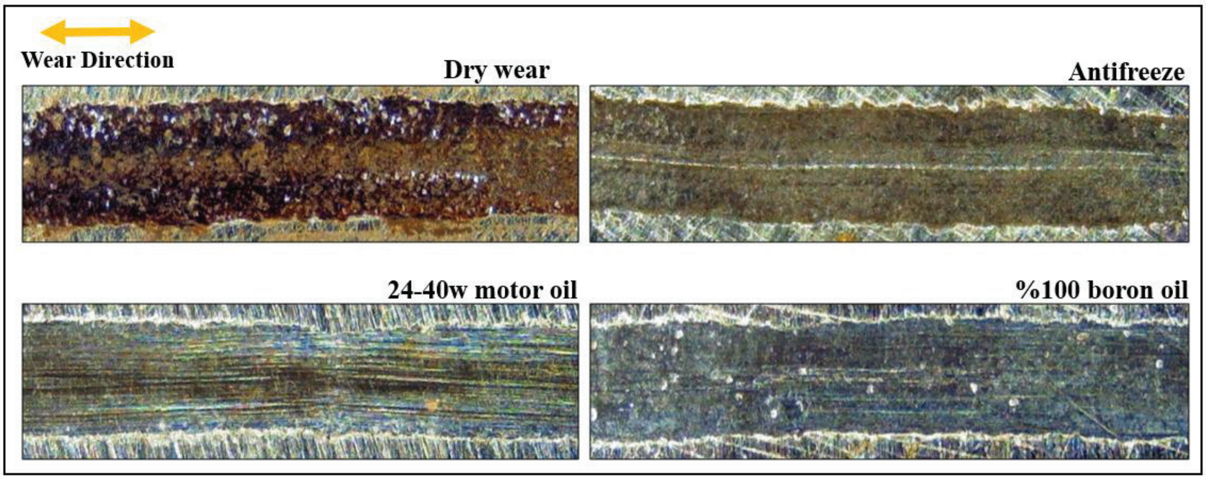

Figure 3. Optical microscopy images of wear tracks.

Under dry sliding conditions, surface morphologies are typically characterized by deep grooves, fragmented debris, and microcracks, indicative of severe abrasive and adhesive wear (Das et al., 1993; Modi et al., 2003). In contrast, liquid-assisted environments exhibit smoother wear tracks with reduced groove depth, reflecting the protective role of lubrication films. Boron oil environments, in particular, have been reported to suppress severe plastic deformation and stabilize surface morphology through tribochemical film formation (Ahlatci et al., 2013; Liu et al., 2021).

3.6 Integrated Discussion and Industrial Implications

The combined analysis of friction behaviour, wear rate, energy dissipation, wear track geometry, and surface roughness provides a holistic understanding of the tribological performance of AISI 4140 steel under different environments. While dry sliding represents a worst-case scenario dominated by severe abrasive mechanisms, liquid-assisted conditions demonstrate the effectiveness of lubrication in controlling surface damage and mechanical degradation.

Among the tested environments, boron-based lubrication emerges as a particularly promising strategy due to its ability to reduce friction, limit wear progression, minimize energy loss, and preserve surface integrity. These findings are consistent with previous reports emphasizing the superior tribological performance of boron-containing systems in steel applications (Medvedovski et al., 2016; Liu et al., 2021).

From an industrial perspective, the results highlight the importance of lubricant selection in extending component lifetime, improving energy efficiency, and reducing maintenance costs in mechanical systems subjected to reciprocating motion. The integrated evaluation framework presented in this chapter offers a valuable reference for both researchers and engineers seeking optimized wear control strategies.

4. Conclusions and Industrial Implications

This chapter presented a comprehensive tribological assessment of AISI 4140 steel under dry sliding and fluid-assisted reciprocating contact conditions. By integrating friction behavior, mass loss, wear rate, frictional energy dissipation, wear track depth, surface roughness, and microscopic surface analysis, the study provides a holistic understanding of how different operating environments influence wear mechanisms and surface degradation in medium-carbon alloy steels.

The results clearly demonstrate that the surrounding environment plays a decisive role in governing tribological performance. Dry sliding conditions promote direct asperity–asperity contact, leading to severe abrasive and adhesive wear, increased frictional resistance, elevated energy dissipation, and pronounced surface damage. These observations are consistent with classical tribological studies reporting accelerated material degradation in the absence of lubrication.

In contrast, fluid-assisted environments significantly modify the contact interface by reducing solid–solid interaction and promoting the formation of lubricating films. Antifreeze and mineral motor oil environments mitigate wear progression by lowering frictional stresses and stabilizing surface interactions, in agreement with previous investigations on liquid-mediated wear behavior in steel systems. However, the extent of protection strongly depends on the chemical composition and film-forming capability of the fluid.

Among the investigated environments, boron-based lubrication exhibits the most pronounced improvement in tribological performance. The combined reduction in friction, wear severity, energy dissipation, wear track depth, and surface roughness suggests the formation of stable, low-shear-strength tribochemical films at the sliding interface. This behavior aligns with earlier reports highlighting the superior anti-wear and surface-protective characteristics of boron-containing systems in steel applications. The microscopic observations further support this interpretation by revealing smoother wear tracks and reduced micro-scale damage under boron oil lubrication.

From an industrial perspective, the findings underline the critical importance of lubricant selection in extending component service life and improving energy efficiency in mechanical systems subjected to reciprocating motion. Components such as shafts, gears, piston–liner assemblies, and sliding guides manufactured from AISI 4140 steel can benefit substantially from optimized lubrication strategies, particularly in applications where boundary or mixed lubrication regimes dominate. Reduced frictional energy dissipation directly translates into lower power losses, diminished thermal loading, and decreased maintenance requirements.

Furthermore, the integrated evaluation approach employed in this chapter—combining mechanical, energetic, and surface-related tribological metrics—offers a practical framework for lubricant performance assessment beyond conventional single-parameter analyses. This methodology can be readily extended to other steel grades, surface treatments, and lubricant formulations, including bio-lubricants and additive-enhanced oils, to support sustainable and high-efficiency engineering solutions.

In conclusion, this study demonstrates that fluid-assisted wear control is not merely a supplementary measure but a fundamental design parameter in tribological systems. The insights presented herein provide valuable guidance for both researchers and practicing engineers seeking to optimize wear resistance, surface integrity, and operational efficiency in steel-based mechanical components operating under reciprocating contact conditions.

Acknowledgements

The authors gratefully acknowledge the financial support provided by the Scientific Research Projects Coordination Unit of Karabük University under Project No. KBÜBAP-24-DS-088. The experimental facilities, technical infrastructure, and institutional support made available through this project were essential for the successful completion of the tribological investigations presented in this chapter. The authors also thank Karabük University for providing a collaborative research environment that enabled systematic experimental work and comprehensive data analysis.

References

Ahlatci, H., Yargül, G., Çuğ, H., Cevik, E., Yaşin, S., & Sun, Y. (2013). Corrosion and wear behaviour of boronized high carbon and chromium cast steel. *ISIJ international, 53*(5), 887-893.

Arumugam, S., & Sriram, G. (2012). Effect of bio-lubricant and biodiesel-contaminated lubricant on tribological behavior of cylinder liner–piston ring combination. *Tribology Transactions, 55*(4), 438-445.

Balakumar, R., Sriram, G., & Arumugam, S. (2020). *Effect of engine oil dilution by waste ayurvedic oil biodiesel on tribological behavior of liner-ring tribo pair material.* Paper presented at the IOP Conference Series: Materials Science and Engineering.

Das, D., Ray, K., & Dutta, A. (2009). Influence of temperature of sub-zero treatments on the wear behaviour of die steel. *Wear, 267*(9-10), 1361-1370.

Das, S., Prasad, B., Jha, A., Modi, O., & Yegneswaran, A. (1993). Three-body abrasive wear of 0.98% carbon steel. *Wear, 162*, 802-810.

Kravtsova, E., Kowalsky, B., & Lysyannikova, N. (2020). *Investigation of Influence of Steel SH 15 on Oxidation and Anti-wear Properties of Mineral Oil.* Paper presented at the Proceedings of the 5th International Conference on Industrial Engineering (ICIE 2019) Volume I 5.

Li, C., & Hu, X. (2020). *Biodiesel Soot: Tribology, Properties, and Formation*: Elsevier.

Liu, M., Wang, W., Hu, H., Cai, F., Liu, S., & Xu, G. (2021). The Corrosion and Wear Behaviors of a Medium-Carbon Bainitic Steel Treated by Boro-Austempering Process. *Metals, 11*(12), 1959.

Maleque, M., Masjuki, H., & Ishak, M. (1998). Bio-fuel-contaminated lubricant and hardening effects on the friction and wear of AISI 1045 steel. *Tribology Transactions, 41*(1), 155-159.

Matbouei, M. (2018). *The Effect of Biofuel on the Corrosion and Wear of Automotive Engine Components.* University of Leicester.

Medvedovski, E., Jiang, J., & Robertson, M. (2016). Iron boride-based thermal diffusion coatings for tribo-corrosion oil production applications. *Ceramics International, 42*(2), 3190-3211.

Mobarak, H., Mohamad, E. N., Masjuki, H. H., Kalam, M. A., Al Mahmud, K., Habibullah, M., & Ashraful, A. (2014). The prospects of biolubricants as alternatives in automotive applications. *Renewable and Sustainable Energy Reviews, 33*, 34-43.

Modi, O., Prasad, B., Jha, A., Dasgupta, R., & Yegneswaran, A. (2003). Low-stress abrasive wear behaviour of a 0.2% C steel: influence of microstructure and test parameters. *Tribology Letters, 15*, 249-255.

Pathak, M. K., Joshi, A., Mer, K., Katiyar, J. K., & Patel, V. K. (2019). Potential of bio-lubricants in automotive tribology. *Automotive Tribology*, 197-214.

Pillar, R. J., Ginic-Markovic, M., Clarke, S. R., Gibson, A., Bell, W., Brown, H., . . . Matisons, J. G. (2005). The effect of gas environment on rolling oil removal from cold-rolled steel as studied by TG. *Journal of thermal analysis and calorimetry, 80*(1), 211-216.

Song, R., Yu, H., Song, H., & Hu, X. (2022). Effects of biomass fast pyrolysis fuel on the tribological behaviour of heavy-duty diesel engine lubricating oil. *Applied Sciences, 12*(5), 2360.

Wang, J., Chen, J., Chen, B., Yan, F., & Xue, Q. (2012). Wear behaviors and wear mechanisms of several alloys under simulated deep-sea environment covering seawater hydrostatic pressure. *Tribology International, 56*, 38-46.

Wood, R. J. (2017). Marine wear and tribocorrosion. *Wear, 376*, 893-910.

Yu, S., Cao, J., Li, S., Huang, H., & Li, X. (2023). The tribological and mechanical properties of PI/PAI/EP polymer coating under oil lubrication, seawater corrosion and dry sliding wear. *Polymers, 15*(6), 1507.

Chapter 6

ASSESSMENT OF THE SOIL PROPERTIES AT GAVALAK CHURCH IN GUMUSHANE KROM VALLEY THROUGH GEOPHYSICAL TECHNIQUES

Mahmut SARI [1]

---

[1] Doç. Dr. Gümüşhane University, Gümüşhane Vocational School, Construction Department

Introduction

Anatolia, with its diverse historical legacy that has accommodated various civilizations, is a significant cultural heritage site featuring numerous high-quality edifices of religious and civil architecture (Eyice, 1996; Özgüner, 2008). Historic churches, a significant aspect of this heritage, hold considerable importance not just for their architectural and artistic merit but also for illuminating the socio-cultural and political history of their respective regions. Krom Valley, situated in the interior regions of the Eastern Black Sea, is distinguished by its numerous ecclesiastical edifices associated with Christian communities who inhabited the area, especially throughout the Middle Ages and beyond (Bryer & Winfield, 1985; Özkan, 2013; Erüz, 2009).

The Gavalak Church, situated in the Krom Valley, exhibits similarities with other religious edifices in the area regarding its location, architectural design, and construction materials, and is regarded as a quintessential example of regional Christian architecture. While documentation pertaining to the precise construction date and patron of the edifice is scarce, an analysis of its design, wall construction method, and topographical context indicates that it was likely erected between the late Byzantine period and the Trabzon Empire period (Bryer & Winfield, 1985; Eyice, 1996; Özkan, 2003).

Previous research on the churches in and around the Krom Valley has predominantly emphasized architectural and art history, focusing on plan types, decorative features, and the historical context of the structures (Özgüner, 2008; Özkan, 2013). Nevertheless, a considerable number of these studies have failed to thoroughly examine the soil conditions underlying the structures and the interaction between the structures and the soil. In historical structures located in rocky environments, precisely delineating soil properties is essential for comprehending the origins of current structural degradation and efficiently organizing restoration efforts (Kramer, 1996; Oliveira et al., 2012; Sari and Şentürk;2023).

Geophysical methods give substantial benefits in assessing the ground parameters of historical structures owing to their non-destructive characteristics and the extensive coverage they afford. The methods of seismic refraction and Multichannel Surface Wave Analysis (MASW) are extensively employed to ascertain the elastic and dynamic properties of subsurface strata (Park et al., 1999; Foti et al., 2018). These methods facilitate soil classification and evaluation of soil-related hazards in regions with historical structures.

Historical structures primarily comprise load-bearing masonry systems constructed from traditional materials such as stone, brick, adobe, and wood, with a prevalent practice of situating foundations on bedrock units, reflecting the engineering principles of past eras. To ensure that interventions for the preservation, enhancement, and restoration of such structures are grounded in scientific and sustainable principles, it is essential to ascertain the geotechnical and geophysical characteristics of the soil environment interacting with the structures through a comprehensive, dependable, and integrative methodology. This study studied the geological properties of the Gavalak Church, situated in the Krom Valley inside Yağlıdere Village in the Central District of Gümüşhane Province, classed as an archaeological site, utilizing geophysical methods (Fig. 1). In the field research, Multichannel Surface Wave Analysis (MASW) and seismic refraction methods were employed; the data acquired indicated that the P-wave velocity (Vp) for the bedrock unit beneath the church was 2221 m/s, while the S-wave velocity (Vs) was 716 m/s. The engineering parameters of soil units were established using the designated seismic velocity values. The investigation indicates that the Gavalak Church is located on bedrock formations of medium to high strength. Moreover, the computed Vs_{30} value (716.5 m/s) is indicative of proximity to ZB classification, despite the soil being categorized as ZC according to the local soil classification system. The assessment indicates that the structural damage observed in the church is not attributable to ground conditions; instead, it is likely associated with deterioration of the structural system, material aging, environmental impacts, and deficiencies in previous repair or restoration efforts.

Figure 1. Gavalak Church

Geology of the study area

Located in the Eastern Black Sea Region, Gümüşhane province is bordered by Bayburt to the east, Giresun to the west, Trabzon to the north, and Erzincan to the south. With an average elevation of approximately 1210 meters, the province lies within the Eastern Pontid orogenic belt and has a complex geological evolution. The study area is situated within the boundaries of Yağlıdere Village, located in the central district of Gümüşhane Province, in the Chrom Valley (Fig. 2).

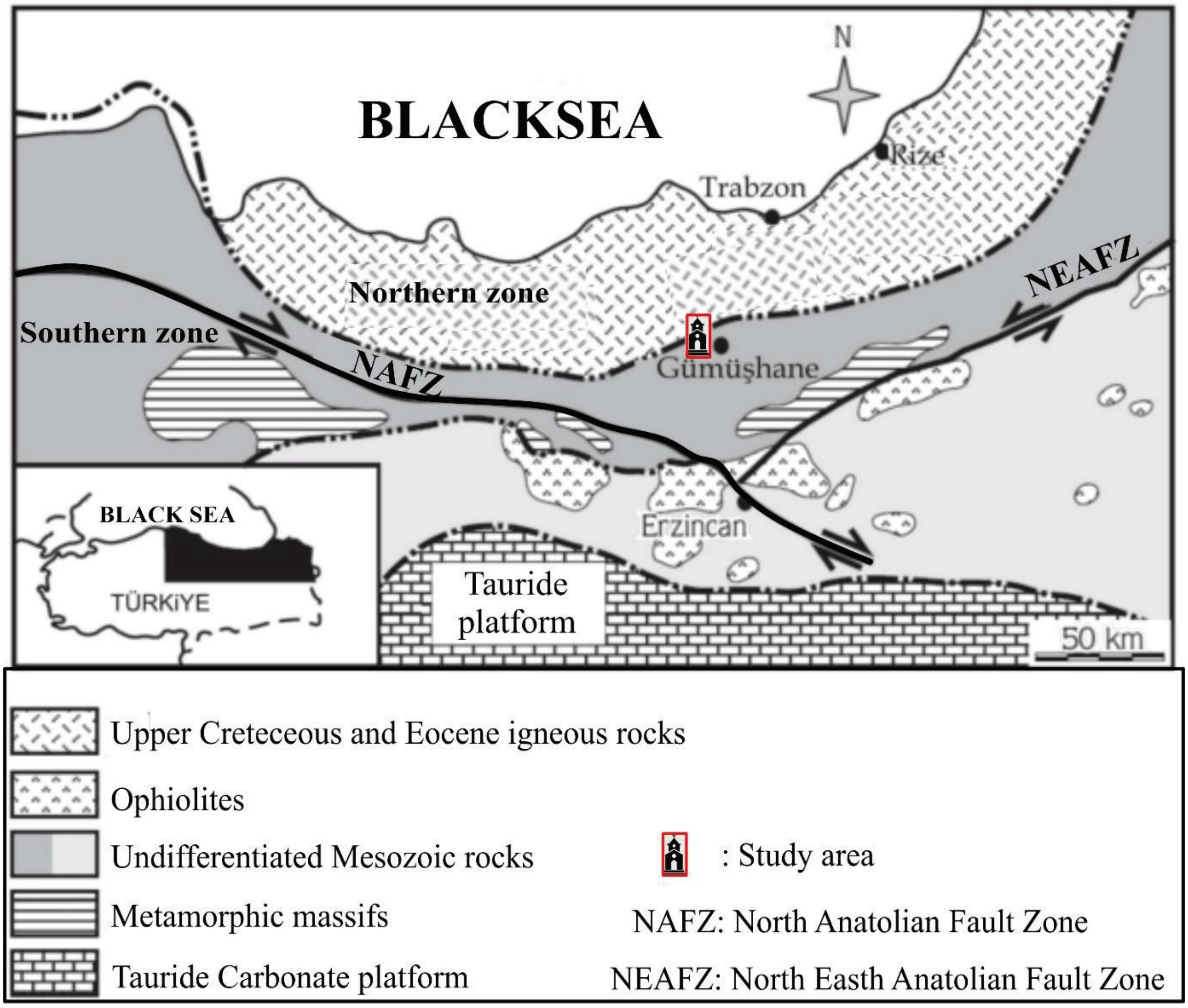

Figure 2. Geotectonic positioning of the research region (adapted from Şengör and Yılmaz (1981))

The rock formations in the studied area originated throughout an extensive temporal range from the Paleozoic to the Quaternary, with the geological development of the region influenced by multiple phases of magmatic and sedimentary activity. Intermittent magmatic activity from the Liassic period to the late Eocene has led to the significant development of volcanic, volcano-sedimentary, and intrusive rocks. When magmatic activity has halted, sedimentary deposits accumulate in marine and terrestrial habitats.

This section of the Eastern Pontides can be divided into northern and southern zones, which display notable variances in lithostratigraphic properties. In the northern zone, the metamorphic basement units consist of Paleozoic gneiss, mica schist, and chlorite schist, from base to top. The Hamurkesen Formation, succeeding these strata, is characterized by Liassic-aged basalt, andesite, conglomerate, sandstone, and marl lithologies. The Berdiga Formation, a carbonate platform from the Upper Jurassic to Lower Cretaceous, holds significant relevance in the stratigraphy of the northern region. Subsequently, the Çatak Formation, comprising Upper Cretaceous basalt, andesite, pyroclastics, and clastic rocks, along with the Kızılkaya Formation, consisting of rhyodacite, dacite, and pyroclastics, are situated (Şengör ve Yılmaz (1981).

In the region, magmatic intrusions from the Upper Cretaceous–Paleocene epoch are represented by the Kaçkar Granitoid-I, followed by the Çağlayan Formation, which has basalt, andesite, pyroclastic materials, mudstone, sandstone, and marl lithologies. The younger strata comprise the Çayırbağ Formation, which includes rhyolite, rhyodacite, and pyroclastics, and the Bakırköy Formation, consisting of Paleocene-aged sandstone, marl, and clayey limestone. In the Eocene epoch, the Kaçkar Granitoid-II and the Kabaköy Formation, comprising andesite, basalt, and pyroclastic rocks, emerged (Tanyolu, 1988; Habiboğlu, 1989). In the southern zone, with the Hamurkesen and Berdiga formations identified in the northern zone, as well as the Kaçkar granitoid-I and II and the Kabaköy Formation, the Mescitli Formation, which is distinct lithologically and stratigraphically, is also present (Fig. 3). This condition demonstrates that tectonic, magmatic, and sedimentary processes in this specific area of the Eastern Pontides display spatial diversity.

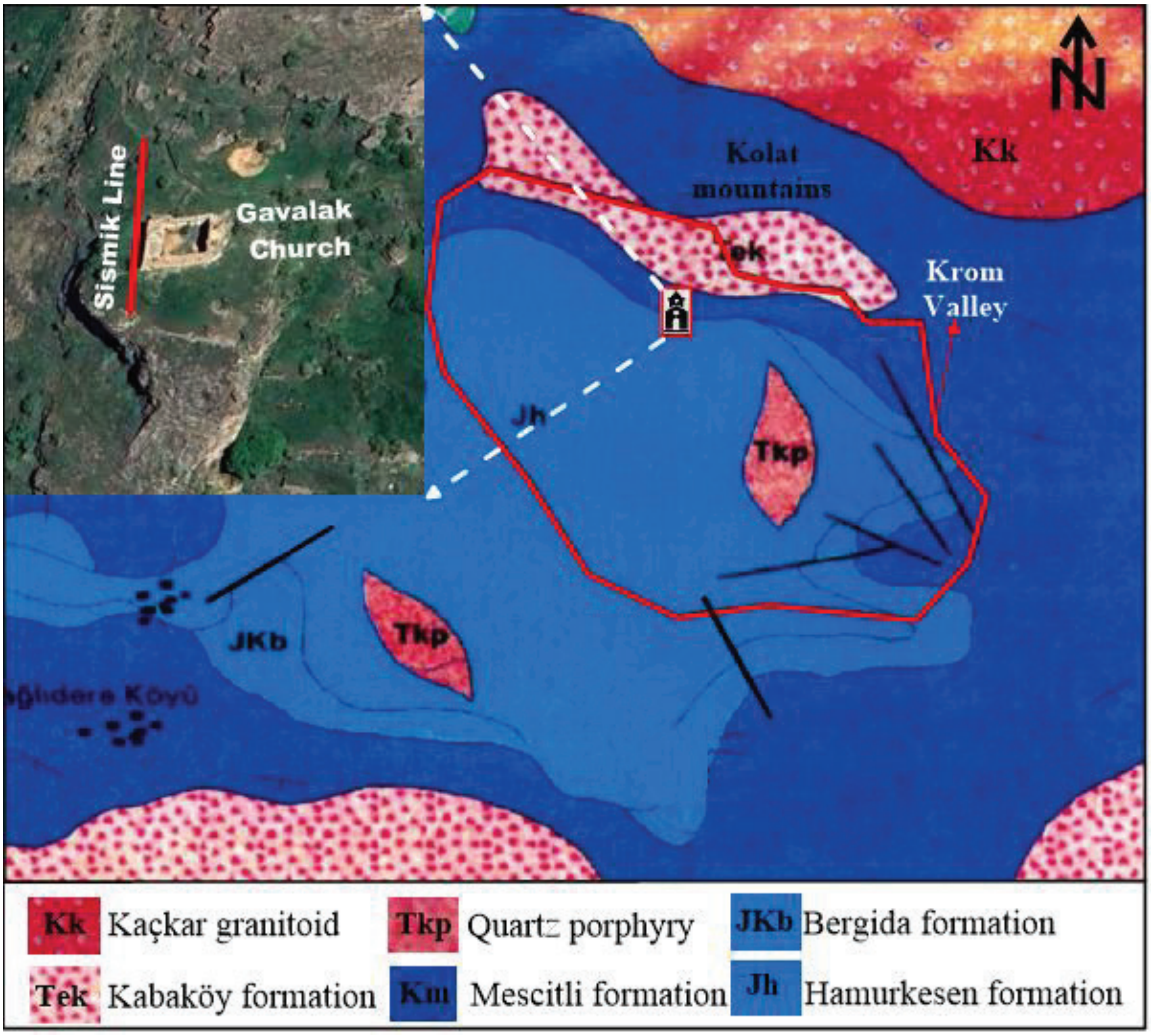

Figure 3. Geological map of the research region (adapted from MTA geological map)

Methodology and instrumentation

Seismic Refraction Tomography (SRT) and Multichannel Surface Wave (MASW) measurements were conducted along a profile right in front of the Gavalak church inside the research region (Fig. 4). Measurements were conducted at a distance of 50 m and a depth of roughly 20 m, resulting in Vp and Vs velocity data. A 24-channel Geometrics seismograph, 4.5 Hz vertical component receivers, an 8 kg sledgehammer, and a 25 cm radius iron plate were utilized for data gathering. Four vertical stacks were erected at each launch site to enhance the signal-to-noise ratio of the seismic output (Figure 4).

Sampling intervals for SKT and ÇKYD data were established at (0.250 ms, 0.5 ms), recording durations at (0.5s, 1s), and offset intervals at (3m, 9m), respectively. To assess SKT data using initial arrival tomography, data was collected at the start, conclusion, and midpoint of the profile. No filters were employed in the data gathering process.

Figure 4. Recent images of Gavaklı Church.

The dynamic modulus of elasticity (E_{dyn}) and dynamic Poisson's ratio (υ_{dyn}) were computed utilizing the Vp and Vs velocities of the layers in each profile, employing equations 1, 2, and 3 as provided by Bowles (1988) (Table 1). The shear value was ascertained utilizing empirical equation 4 put out by Keçeli (2012). The density was calculated using empirical equation 5 as presented by Keçeli (2012).

$$\upsilon_{dyn} = (V_p^{\ 2} - 2V_s^{\ 2}) / 2(V_p^{\ 2} - V_s^{\ 2}) \qquad \text{(Eq.1)}$$

$$E_{dyn} = \mu\,(3V_p^{\ 2} - 4V_s^{\ 2}) / (V_p^{\ 2} - V_s^{\ 2}) \qquad \text{(Eq.2)}$$

$$\mu = \rho\, V_s^{\ 2} / 100 \qquad \text{(Eq.3)}$$

$$\rho = 0.44 V_s^{\ 0,25} \qquad \text{(Eq.4)}$$

In this context, V_p denotes the longitudinal wave velocity (m/s), V_s represents the transverse wave velocity (m/s), ρ signifies the density (g/cm^3), υ indicates the Poisson ratio, μ refers to the shear modulus (kg/cm^2), and E_m is the modulus of elasticity (kg/cm^2).

Result and Discussions

The SRT and MASW data were analyzed with the SeisImager software. In SRT studies, following the precise identification of initial arrival timings, a two-dimensional seismic velocity depth section of the shallow subsurface structure was generated by inverse solution processing in a computational environment (Fig 5b). The MASW analyses involved determining the phase velocity and dispersion curve by frequency-wavenumber analysis, resulting in depth-varying one-dimensional S-wave velocity values of the subsurface. (Fig 5a).

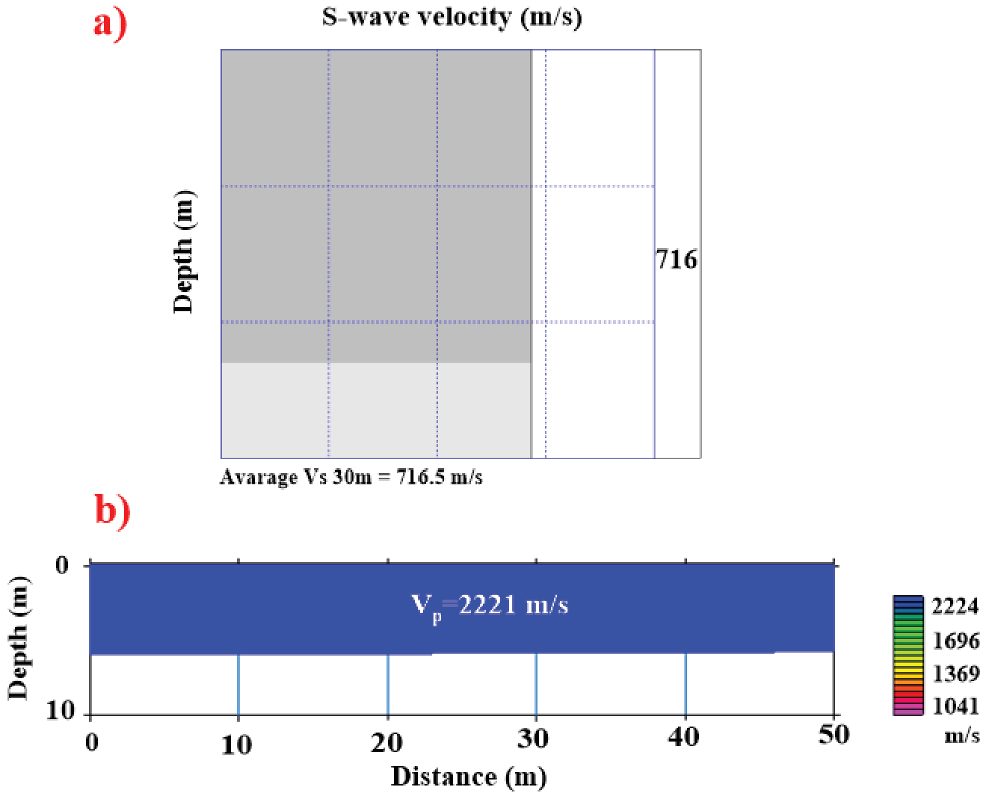

Figure 5. Velocity-depth profiles for P and S waves

Seismic measurements performed in the studied region ascertained the Vp and Vs wave velocities of the shallow subsurface structural elements. The Vp wave velocity was measured at 2221 m/s, whereas the Vs wave velocity was measured at 716 m/s. The engineering parameters derived from the velocity values acquired using geophysical techniques are presented in Table 1.

Table 1. Engineering characteristics derived from geophysical techniques.

DYNAMIC AND ELASTIC PARAMETERS				
Layer No.	**Vp (m/sec)**	**Vs (m/sec)**	**Vp / Vs**	**Layer Thickness (m)**
1	2221	716	1,84	20
Density	**Poisson's Ratio**	**Shear Modulu**	**Elasticity Modulu**	**Bulk Module**

gr/cm^3	Characterize	-	Firmness	kg/cm^2	Strength	kg/cm^2	Strength	kg/cm^2	Compression
2,13	high	0,44	very loose	10920	very solid	31493	very solid	90510	middle

Geophone interval	Offset interval	Dominant frequency (Ao)		Vs30	Ta	Tb	Dominant period
(m)	(m)	Midorikawa	Borcherdt et al. 1991	(m/sec)			(To - sec)
2,00	10,00	1,32	0,98	716	0,11	0,26	0,17

According to the shear wave velocity obtained from a MASW measurement conducted in front of Gavalak Church, and in accordance with the soil classification outlined in the "Turkish Building Earthquake Regulations" published in the Official Gazette on 18.03.2018, numbered 30364, which became effective on 01.01.2019, the units associated with the Hamurkesen formation have been classified within the ZC category of "weak rocks with highly fractured fractures," exhibiting an average velocity of 716.5 m/s, as derived from the MASW measurements. Per the categorization in TBDY, this number is nearly at the top threshold of the ZC range (360–760 m/s). This aligns with the characterization of the units in the Hamurkesen formation as "weathered, highly fractured, weak rock": while the underlying medium is rock, it may demonstrate ground behavior in certain areas due to weathering and fracturing. The measured value is near the 760 m/s threshold, indicating that stiffness approaching ZB may occur at some locations if the layer thickness or degree of weathering fluctuates in the field. Consequently, it is essential to manage the heterogeneity within the field rather of focusing on a "single class".

The predominant period derived from seismic velocity measurements in the research region is 0.17 seconds, with TA and TB values of 0.11 and 0.26 seconds, respectively. TA–TB values are regarded as pivotal intervals of the design spectrum within the Temporary Earthquake Dependency Framework (TBDY); their reduced values reinforce the notion that the spectrum is more accentuated in the short-period domain in the field. The Gavaklı church has experienced several structural problems throughout time, including functional alterations and degradation due to physical reasons. Upon evaluating the engineering characteristics derived from all geophysical methods, it was determined that the Gavaklı church is constructed on a robust, dense, and high-strength rock foundation, hence no damage attributable to unfavorable ground conditions was seen. The observable structural damage is believed to result from anthropogenic factors, including water infiltration, degradation of the stone's integrity, and the presence of clay layers or other extraneous materials within the stones, leading to detachment and separation in those regions.

Conclusions

This study meticulously assessed the soil properties of the Gavalak Church in the Krom Valley, situated within Yağlıdere Village in the Central District of Gümüşhane Province, employing non-destructive geophysical techniques.

- Seismic Refraction Tomography (SRT) and Multichannel Surface Wave Analysis (MASW studies established the P-wave velocity (V_p = 2221 m/s) and S-wave velocity (V_s = 716 m/s) of the substrate under the church; these results suggest that the soil possesses a stony composition and exhibits high stiffness.

- The engineering parameters, including dynamic modulus of elasticity, shear modulus, Poisson's ratio, and modulus of volume, derived from the seismic velocity data, indicated that the substrate beneath the church consists of a medium-to-high strength rock formation, adequate for bearing capacity.

- The computed Vs_{30} value (716.5 m/s) categorizes the soil into the ZC class as per the Turkish Building Earthquake Code (TBDY, 2018); yet, due to its proximity to the top threshold, it demonstrates characteristics akin to the ZB class in some regions. This indicates that the Hamurkesen Formation exhibits geographical heterogeneity contingent upon the extent of weathering and fracture.

- The minimal values of the dominant period (T_0 = 0.17 s) and the associated low TA–TB corner periods (0.11–0.26 s) suggest that short-period seismic activity prevails in the studied area, indicating restricted ground amplification.

- The study area, located approximately 70-80 km from the North Anatolian Fault Zone (NAFZ), may be susceptible to significant earthquakes; however, the current soil conditions are determined not to adversely influence the amplification of seismic waves.

- Upon comprehensive evaluation of all geophysical data and derived engineering factors, it has been determined that the structural damage found in Gavalak Church is not attributable to soil conditions.

- The observed cracks, stone disintegration, and surface deterioration in the structure are believed to be attributable to prolonged environmental effects, water-induced deterioration processes, material aging, clay bands within the stones' internal structure, and substandard or erroneous repair and restoration practices conducted previously.
- This study illustrates that geophysical methods serve as an effective, reliable, and non-destructive means for assessing the soil properties of historical structures, significantly enhancing the precise interpretation of structure-soil interaction, particularly in cultural heritage edifices located in rocky environments.

- It is considered that the results obtained will constitute a scientific reference in the planning of conservation, strengthening, and restoration projects for historical structures located in the Krom Valley and similar archaeological sites.

REFERENCES

Bryer, A., & Winfield, D. (1985). *The Byzantine Monuments and Topography of the Pontos*. Washington, D.C.: Dumbarton Oaks Research Library.

ERÜZ, Güler; Gümüşhane Kurum Vadisi Maden Köyü Yerleşmeleri, Karadeniz Teknik Üniversitesi *Fen Bilimleri Enstitüsü, Mimarlık Anabilim Dalı Doktora Tezi (Yayımlanmamış)*, Trabzon, 2009.

Eyice, S. (1996). *Bizans Sanatı ve Mimarlığı*. İstanbul: İletişim Yayınları

Foti, S., Hollender, F., Garofalo, F., et al. (2018). *Guidelines for the good practice of surface wave analysis*. Bulletin of Earthquake Engineering, 16, 2367–2420.

Habiboğlu, Y., 1989: Doğu Pontid Güney Zonundaki (Bayburtdemirözü) Metamorfıt-Ofiyolit Birliğinin (Pulur Masifi) Jeotektonik Anlamı: *Yüksek Lisans Tezi*, KTÜ, 104

Kramer, S. L. (1996). *Geotechnical Earthquake Engineering*. Prentice Hall.

Oliveira, C. S., Roca, A., & Goula, X. (2012). *Assessing and Managing Earthquake Risk*. Springer.

Özgüner, O. (2008). *Trabzon ve Çevresinde Bizans Dönemi Kilise Mimarisi*. Ankara: Kültür ve Turizm Bakanlığı Yayınları.

ÖZKAN, Haldun;'' Gümüşhane Krom Vadisi Kiliseleri'', Atatürk Üniversitesi Sosyal Bilimler Dergisi, C. 3, Sayı: 31, Erzurum, Aralık 2003, sf. 115-139.

Özkan, H. (2013). Krom Vadisi (Gümüşhane) Orta Çağ Dini Mimarisi. *Sanat Tarihi Dergisi*, 22(1), 45–68.

Park, C. B., Miller, R. D., & Xia, J. (1999). Multichannel analysis of surface waves. *Geophysics*, 64(3), 800–808.

SARI, M., & ŞENTÜRK, N. (2023). Evaluation Of Gumushane Chrome Valley Şamanli Chapel In Terms Of Ground Properties. *BIDGE Publications*.

Şengör, A.M.C. and Yılmaz, Y., 1981: Tethyan Evolution of Turkey, *Tectonophysics*, 75, 181-241.

Tanyolu, E. (1988). THE GEOLOGY OF THE EASTERN PART OF THE PULUR MASSIF. *Bulletin of the Mineral Research and Exploration*, *108*(108), 1-1.

Chapter 7

RADIOLOGICAL HAZARDS IN SHIPYARD GAMMA RADIOGRAPHY: COMPREHENSIVE RISK ASSESSMENT AND SAFETY MANAGEMENT A CONTEMPORARY ANALYSIS OF INDUSTRIAL RADIOGRAPHY SAFETY IN MARITIME CONSTRUCTION

Emine CAN[1], *Serap DUMAN*[2]

---

[1] Istanbul Medeniyet University, Faculty of Engineering and Natural Sciences, Department of Physics Engineering, Istanbul, Turkey

[2] Üsküdar University, Faculty of Health Sciences, Department of Occupational Health and Safety, Istanbul, Turkey

1. Introduction and Background

1.1 Evolution of Radiographic Inspection in Maritime Industries

Contemporary shipbuilding depends fundamentally upon non-destructive examination methodologies that enable thorough materials assessment without compromising component integrity. These inspection technologies evolved alongside broader advances in radiation physics and industrial quality systems, transforming vessel construction practices throughout the 20th century. Wilhelm Röntgen's 1895 discovery of X-ray phenomena laid theoretical groundwork, though practical industrial applications emerged only after welding displaced riveting as the primary joining technique in marine fabrication.

Radiographic testing distinguishes itself through unique capabilities in revealing subsurface anomalies—voids, inclusions, discontinuities—that remain imperceptible to surface examination methods. The technique exploits differential radiation absorption across materials exhibiting varying densities and atomic compositions, producing images wherein internal flaws manifest as distinct density variations. This principle proves particularly valuable in maritime contexts where weld integrity directly determines whether vessels achieve operational longevity or suffer catastrophic structural collapse.

Turkish maritime industries adopted radiographic methods during the 1960s, incorporating Cobalt-60 and Iridium-192 sealed sources that revolutionized quality verification protocols. Six decades of subsequent development have witnessed the nation's shipbuilding sector expand substantially, driven by both domestic demand and international competitiveness requirements. Radiographic capabilities enabled Turkish yards to satisfy increasingly rigorous certification standards imposed by classification societies and flag state authorities.

Current market dynamics reflect ongoing transformation within industrial radiography. Digital detection systems have captured 62% market penetration as of 2024-2025, displacing film-based approaches that dominated for nearly a century. Analysts project 5.3% compound annual growth through 2034, propelled by escalating quality expectations, regulatory mandates, and technological innovations yielding faster inspections with diminished radiation exposures. This transition presents both opportunities and challenges for shipyard operators navigating equipment investments, workforce training needs, and procedural modifications.

1.2 Quality Assurance Imperatives in Shipyard Operations

Maritime vessel integrity hinges upon thousands of welded connections distributed throughout hull structures, decks, bulkheads, and superstructures. Each joint represents a potential failure initiation site where inadequate execution could precipitate progressive collapse, particularly under dynamic loading conditions encountered at sea. Radiographic verification therefore transcends mere quality preference—it constitutes essential risk mitigation against loss of life, environmental contamination, and catastrophic financial liability.

Modern commercial freighters, naval combatants, cruise vessels, and offshore platforms incorporate increasingly sophisticated structural configurations optimizing strength-to-weight ratios while accommodating complex internal arrangements. These designs amplify inspection challenges through restricted access geometries, dissimilar material interfaces, and critical load paths requiring absolute structural reliability. Radiographic examination addresses four primary verification objectives:

Internal Weld Discontinuity Detection: Subsurface anomalies invisible to visual methods include gas porosity from inadequate shielding, fusion deficiencies at weld-base metal interfaces, entrapped slag particles, undercut conditions weakening toe regions, and incomplete joint penetration.

Individual defects may appear minor, yet collective degradation substantially compromises fatigue life and ultimate strength margins.

Crack Detection and Characterization: Thermal stresses generated during welding can induce immediate cracking in susceptible materials, while cyclic loading during service propagates fatigue cracks from stress concentrations. Early identification through radiography enables repair interventions before crack growth reaches critical dimensions threatening sudden fracture.

Material Integrity Verification: Thickness measurements confirm specifications, material substitution detection prevents unauthorized deviations, and internal corrosion mapping identifies degradation in aging vessels. These capabilities prove invaluable during major maintenance periods when hull surveys determine continued service feasibility.

Complex Assembly Assessment: Critical connections including keel-to-hull joints, transverse bulkhead attachments, and structural reinforcement welds demand exhaustive verification ensuring proper fit-up achievement and complete penetration throughout joint cross-sections. Radiography provides the only practical means for comprehensive examination of many such configurations.

Classification societies—Lloyd's Register, American Bureau of Shipping, Bureau Veritas, and comparable organizations—mandate specific radiographic coverage percentages as prerequisites for vessel certification. International Maritime Organization conventions and national flag state regulations incorporate similar requirements as safety backstops. Insurance underwriters demand documented quality programs as coverage conditions. This multilayered framework positions radiographic inspection not merely as technical quality control but as foundational to maritime safety governance architecture.

1.3 Regulatory Architecture and Compliance Framework

Radiation safety governance operates across international, national, and industry-specific tiers. This hierarchical structure evolved through decades of operational experience, incident investigations, and scientific understanding advancement. Contemporary regulatory frameworks synthesize lessons from historical accidents worldwide while accommodating technological progress and emerging risk insights.

1.3.1 Turkish National Requirements

Turkish Atomic Energy Authority (TAEK) derives regulatory authority from Law No. 2690 enacted July 9, 1982, establishing comprehensive oversight encompassing all ionizing radiation applications within national jurisdiction. Subsidiary regulations detail operational requirements for industrial radiography including source licensing protocols, personnel qualification criteria, dose limitation standards, emergency preparedness specifications, and enforcement mechanisms. This framework ensures Turkish operations maintain parity with international best practices while addressing domestic circumstances.

TAEK implements a graded approach wherein regulatory intensity scales with hazard magnitude and operational complexity. High-activity sealed sources employed in shipyard radiography trigger enhanced oversight including pre-operational inspections, periodic compliance audits, unannounced field surveys, and incident investigation protocols. License holders face substantial penalties for violations, creating strong compliance incentives beyond inherent safety motivations.

1.3.2 International Guidance Framework

International Atomic Energy Agency Safety Standards Series provides globally recognized benchmarks codifying radiation protection principles. Safety Guide SSG-11 (revised 2016) specifically addresses industrial radiography, articulating three foundational concepts derived from

International Commission on Radiological Protection recommendations: practice justification ensuring benefits exceed detriments, protection optimization maintaining doses as low as reasonably achievable considering economic and social factors, and individual dose limitation preventing deterministic effects while restricting stochastic risk.

IAEA's Information System for Occupational Exposure in Medicine, Industry and Research underwent significant enhancement during 2024, expanding analytical capabilities while streamlining data submission workflows. This platform enables industrial radiography organizations to benchmark exposure performance against global datasets, identify exemplary practices, and implement evidence-based program improvements. Participation demonstrates regulatory commitment to continuous enhancement beyond minimum compliance.

1.3.3 United States Regulatory Model

American regulatory architecture distributes responsibility across multiple federal agencies. Nuclear Regulatory Commission exercises primary jurisdiction over radioactive materials through Title 10, Code of Federal Regulations, Part 34, which establishes detailed requirements for equipment specifications, personnel qualifications, operating procedures, and emergency response capabilities. Occupational Safety and Health Administration provides complementary worker protection mandates via Title 29 regulations, with shipyard-specific provisions (1915.57) incorporating NRC standards by reference.

Department of Transportation regulates sealed source transport under Title 49 provisions addressing packaging integrity, labeling clarity, documentation completeness, and emergency response preparedness. This multi-agency approach creates comprehensive coverage while introducing coordination challenges that licensees must navigate through careful program design and administration.

2. Radiation Physics and Biological Hazards

2.1 Ionizing Radiation Fundamentals

Ionizing radiation possesses sufficient quantum energy to disrupt atomic electron configurations, generating ion pairs and free radicals capable of damaging biological macromolecules. This distinguishes ionizing from non-ionizing radiation types (visible light, radio frequency, microwaves) lacking ionization capability. Biological consequences stem from direct ionization of critical molecules, particularly deoxyribonucleic acid, and indirect effects mediated through water radiolysis producing reactive chemical species.

Industrial radiography employs two electromagnetic radiation forms: X-rays generated through electron deceleration in electrical devices, and gamma rays originating from radioactive isotope decay. Despite differing production mechanisms, both interact identically with matter and produce equivalent biological effects at equal absorbed doses. The critical operational distinction involves controllability—X-ray production ceases when equipment powers down, whereas gamma emission continues unabated from sealed sources requiring permanent shielding.

Radiographic image formation exploits material-dependent radiation absorption. Dense materials and thick sections attenuate beam intensity more extensively than low-density or thin regions, creating transmitted radiation intensity variations detected by film or electronic sensors. Internal anomalies alter local absorption characteristics, manifesting as density variations in resulting images. Three interaction mechanisms govern this process at energies relevant to industrial applications:

Photoelectric Effect: Photons transfer complete energy to bound electrons, ejecting them from atoms. Probability increases dramatically with atomic number and decreases with photon energy, dominating at lower energies in high-Z materials. This mechanism generates excellent image contrast but limits penetration depth.

Compton Scattering: Photons interact with outer-shell electrons, transferring partial energy and deflecting from original trajectories. Predominant at moderate energies typical of industrial radiography, this mechanism creates scattered radiation that degrades image quality through background fogging while increasing personnel exposure outside primary beam paths.

Pair Production: Above 1.022 MeV threshold, photons interacting with nuclear fields generate electron-positron pairs. Relevant only for highest-energy sources, this mechanism contributes minimally to typical radiographic exposures but influences shielding design for Cobalt-60 applications.

2.2 Sealed Source Characteristics

Shipyard radiography predominantly employs two gamma-emitting isotopes selected based on material thickness, penetration requirements, and operational constraints. Understanding their distinct properties enables optimal source selection while managing safety implications.

2.2.1 Iridium-192 Applications

Reactor-produced Iridium-192 undergoes combined beta decay and electron capture to stable Platinum-192 with 73.8-day half-life. Gamma emissions spanning 0.31-0.61 MeV (average 0.38 MeV) provide optimal penetration for steel sections 10-75 mm thick. Relatively short half-life necessitates quarterly source replacement, increasing handling frequency but simplifying long-term waste management as activity decays to negligible levels within several years.

Moderate energy yields superior image contrast compared to higher-energy alternatives for appropriate thickness ranges. Compact source geometry and reduced shielding mass enhance portability, critical advantages in space-constrained shipyard environments. Equipment typically weighs 20-40 kg complete, enabling single-person transport and positioning. Lower photon energy reduces scattered radiation intensity, simplifying area control in congested locations.

Operational challenges include frequent source exchanges introducing repetitive exposure opportunities, activity decay necessitating exposure time adjustments and periodic recalibration, and penetration limitations restricting maximum inspectable thicknesses. Despite these factors, Iridium-192 remains globally predominant for general industrial applications including majority shipyard examinations.

2.2.2 Cobalt-60 Capabilities

Neutron-activated Cobalt-60 decays to stable Nickel-60 via beta emission with 5.27-year half-life, emitting dual gamma rays at 1.17 and 1.33 MeV. Superior penetration enables examination of steel sections 75-200+ mm thick, addressing heavy-section requirements in large vessel construction. Extended half-life permits multi-year source utilization, reducing replacement frequency and associated handling risks.

High photon energies demand substantially enhanced shielding—source containers typically weigh 100-200 kg compared to 20-40 kg for equivalent-activity Iridium-192 units. Controlled area boundaries extend to greater radii, potentially 50-100 meters versus 10-30 meters for Iridium-192, complicating perimeter establishment in active shipyards. Elevated scatter production increases background exposure rates requiring careful attention to reflection from nearby structures.

Regulatory oversight intensifies for typical activities exceeding 370 GBq (10 Ci), mandating semi-annual leak testing, enhanced physical security measures, and stringent transport requirements. Many facilities maintain dual-isotope inventories, deploying minimum-energy sources adequate for specific applications—practical ALARA implementation optimizing both image quality and radiation safety.

Table 1 summarizes comparative characteristics influencing source selection decisions:

Characteristic	Ir-192	Co-60	X-ray (320kV)
Decay period	73.8 days	5.27 years	Not applicable
Photon energy	0.31-0.61 MeV	1.17, 1.33 MeV	Up to 0.32 MeV
Optimal thickness	10-75 mm steel	75-200+ mm steel	5-50 mm steel
Mobility factor	High (20-40 kg)	Moderate (100-200 kg)	Variable (power needed)
Replacement cycle	Quarterly (3-4 months)	Multi-year (3-5 years)	Tube-dependent
Emission character	Continuous decay	Continuous decay	On-demand control

Table 1: Radiation source comparison for shipyard applications

2.3 Health Consequences of Exposure

Radiation energy deposition within living tissues triggers ionization cascades affecting biomolecules, particularly nuclear DNA. Cellular responses span successful repair without permanent effects, misrepair generating mutations, or lethal damage exceeding repair capacity. Outcomes depend upon absorbed dose magnitude, delivery rate, radiation quality, exposed tissue radiosensitivity, and individual factors including age and genetic predisposition.

Deterministic tissue reactions exhibit dose thresholds below which effects fail to manifest, with severity escalating above threshold levels. Massive cell depletion overwhelms tissue regenerative capacity, producing clinically observable damage. Acute radiation syndrome following whole-body exposure progresses through prodromal, latent, manifest illness, and recovery or death phases depending on dose received. Local injuries range from transient erythema through severe necrosis potentially requiring amputation, as documented in industrial radiography accidents. Cataracts, sterility, and cardiovascular effects represent additional deterministic endpoints.

Stochastic effects—primarily cancer induction—lack dose thresholds, with probability increasing proportionally to dose while severity remains independent. Linear no-threshold models adopted for regulatory purposes assume any exposure increment carries proportional cancer risk, approximately 5% per Sievert lifetime excess mortality. Global cohorts totaling 23 million occupationally-exposed workers provide epidemiological evidence bases, with comprehensive studies demonstrating statistically significant exposure-response relationships albeit modest absolute risk magnitudes at typical occupational levels. Recent investigations suggest cardiovascular disease as potential late effect, prompting dose limit reassessments.

3. Systematic Risk Assessment Approaches

Multi-methodology risk assessment integrates complementary analytical frameworks—Fine-Kinney quantitative prioritization, Fault Tree deductive failure pathway examination, and Event Tree inductive accident sequence exploration. This triangulated approach identifies radiological hazards comprehensively while guiding proportionate control measure development. Shipyard applications revealed 18 distinct hazardous scenarios: 8 intolerable (risk score >400), 8 substantial (70-400), and 2 important (20-70), with none qualifying as acceptable risk. Critical hazards encompass source jamming (R=900), inadequate perimeter control (R=540), dosimetry misuse (R=450), insufficient illumination (R=420), and protective equipment deficiencies (R=405). Each demands immediate, comprehensive intervention strategies.

4. Protection Implementation Strategies

ALARA philosophy—maintaining exposures as low as reasonably achievable—operationalizes through time minimization, distance maximization, and shielding optimization. Engineering controls including source containment, position verification, warning systems, and detection instruments provide primary safeguards. Administrative measures formalize operations through work permits, two-person requirements, area posting, and comprehensive procedures. Personal dosimetry employing TLD/OSLD legal records plus EPD real-time monitoring enables exposure tracking and intervention triggering. Synergistic implementation creates defense-in-depth architectures sustaining worker protection while enabling essential quality verification functions.

5. Workforce Competency Development

Personnel competence represents radiation safety's critical determinant. Regulatory mandates establish minimum qualifications: Radiation Safety Officers require 2,000 hours hands-on experience plus formal program management training; radiographers complete classroom instruction, examinations, and supervised on-the-job training. Comprehensive certification costs average USD 25,000-35,000 per technician, reflecting program complexity. Semi-annual refresher training maintains currency while scenario-based exercises enhance critical skill retention. Organizations investing in quality training achieve superior outcomes through knowledgeable workforces capable of executing complex procedures safely under challenging field conditions.

6. Emergency Response Capabilities

Comprehensive emergency planning addresses stuck sources, material loss, equipment damage, suspected overexposures, and transportation incidents. Initial response effectiveness during critical first minutes determines incident trajectory toward controlled resolution versus escalation. Stuck source protocols mandate immediate work cessation, area evacuation, safe perimeter establishment, alternate retraction attempts only if safe, warning sign posting, RSO notification, personnel accounting, and continuous surveillance pending recovery. Extended response encompasses careful recovery planning, timely regulatory notification, thorough root cause investigation, and corrective action implementation preventing recurrence.

7. Technological Evolution Trajectories

Digital radiography transformation captured 62% market penetration by 2024-2025, offering reduced cycle times, enhanced image manipulation, lower dose requirements, and simplified archiving versus traditional film. Computed tomography scan time reductions of 35% during 2025 expand volumetric imaging accessibility. Portable system advances replace fixed installations while automation technologies minimize personnel radiation field presence. Alternative NDT methods—phased-array ultrasonics, advanced electromagnetics, thermography—complement radiography within integrated programs optimizing defect detection while managing costs and exposures.

8. Safety Culture Foundations

Sustained safety excellence transcends technical compliance, cultivating environments wherein protective behaviors become ingrained operational norms. Leadership commitment demonstrated through resource allocation and personal involvement establishes organizational tone. Open communication channels enable proactive hazard identification and resolution before incident occurrence. Systematic experience learning through comprehensive investigations and broad lesson sharing drives continuous enhancement. ISO 45001-compliant management systems formalize requirements while audits verify effectiveness. Performance indicators balancing leading measures (training completion, equipment testing currency) and lagging metrics (actual exposures, incidents) enable objective program evaluation. Worker participation via safety committees and stop-work authority enhances both effectiveness and engagement.

9. Synthesis and Forward Recommendations

Effective shipyard radiography safety demands integrated protective element synergy: robust engineering controls, comprehensive procedures, thorough training, effective emergency capabilities, and strong safety culture. Multi-methodology risk assessment identified 18 hazardous scenarios with 8 requiring immediate intervention due to intolerable risk scores. Priority hazards span mechanical failures, human performance factors, organizational deficiencies, and systemic inadequacies.

Digital technology adoption offers substantial benefits through enhanced efficiency and reduced exposures, though implementation demands significant capital investment and workforce development. Market growth projections toward USD 4.7 billion by 2034 reflect sustained NDT demand across sectors, with shipbuilding representing substantial specialized segment confronting unique operational challenges.

Critical success factors include:

1. Training programs exceeding regulatory minima, incorporating semi-annual refreshers and realistic scenario-based exercises
2. Rigorous equipment testing protocols verifying safety system functionality including source retraction, position indication, alarms, and detectors
3. Comprehensive procedures formalized through work permit systems ensuring thorough planning and authorization
4. Dual dosimetry implementation combining legal record devices (TLD/OSLD) with real-time alarming capability (EPD)
5. Multi-methodology risk assessment explicitly addressing radiation hazards and updating assessments following operational changes
6. Detailed emergency plans addressing credible scenarios, validated through regular realistic drills
7. Safety culture cultivation via leadership commitment, communication openness, experience learning, and worker empowerment

Ultimate success depends upon people—trained operators executing procedures conscientiously, competent safety officers providing technical oversight, engaged management demonstrating authentic commitment, and effective regulators maintaining appropriate standards. Technical safeguards provide essential foundations, yet human performance determines whether protective systems function as intended. Organizations recognizing this reality while investing correspondingly in personnel development, culture enhancement, and continuous improvement achieve superior safety outcomes while realizing radiographic quality assurance benefits essential for maritime safety.

References

Emergen Research. (2024). Industrial radiography equipment market size, share & growth report [2024-2034]. *Market Research Report*. https://www.emergenresearch.com/industry-report/industrial-radiography-equipment-market

Fine, W.T. (1971). Mathematical evaluation for controlling hazards. *Journal of Safety Research*, 3(4), 157-166.

International Atomic Energy Agency. (2016). *Radiation safety in industrial radiography: Specific safety guide*. IAEA Safety Standards Series No. SSG-11 (Rev. 1). Vienna: IAEA.

International Atomic Energy Agency. (2024). IAEA upgrades online tool for radiation protection of workers in industrial radiography. *IAEA News*. Vienna: IAEA.

International Commission on Radiological Protection. (2008). *The 2007 recommendations of the International Commission on Radiological Protection*. ICRP Publication 103. Ann. ICRP 37(2-4).

Journal of Naval Architecture and Marine Technology. (2023). Risk assessment analysis of radiographic testing in shipyards. *Journal of Naval Architecture and Marine Technology*. https://jnamt.org/

MFE Inspection Solutions. (2025). Industrial radiography: An in-depth guide [New for 2025]. *Technical White Paper*. https://mfe-is.com/industrial-radiography/

Mordor Intelligence. (2025). Industrial x-ray inspection equipment and imaging software market - size, share & forecast. *Market Analysis Report*.

Occupational Safety and Health Administration. (2024). Ionizing radiation - control and prevention. *OSHA Safety Topics*. U.S. Department of Labor.

Occupational Safety and Health Administration. (2021). *Shipyard industry standards*. OSHA Publication 2268-10R. U.S. Department of Labor.

Raybloc X-Ray Protection. (2025). Radiation protection and safety in industrial radiography. *Industry Guide*. https://raybloc.com/

SafetyCulture. (2025). What you need to know about radiation safety. *Safety Resources*. https://safetyculture.com/

The EHS Daily Advisor. (2024). A guide to improving port and shipyard safety. *EHS Daily Advisor*. https://ehsdailyadvisor.com/

Turkish Atomic Energy Authority. (1982). *Law No. 2690 concerning the Turkish Atomic Energy Authority*. Official Gazette, Republic of Turkey.

Turkish Atomic Energy Authority. (2022). *Radiation protection and licensing regulation for industrial radiography*. Ankara: TAEK.

U.S. Code of Federal Regulations. (2025). Licenses for industrial radiography and radiation safety requirements. *10 CFR Part 34*. Nuclear Regulatory Commission.

U.S. Code of Federal Regulations. (2024). Standards for protection against radiation. *10 CFR Part 20*. Nuclear Regulatory Commission.

U.S. Nuclear Regulatory Commission. (2023). *Regulatory guide 8.34: Monitoring criteria and methods to calculate occupational radiation doses*. Washington, DC: NRC.

University of Maryland Baltimore. (2024). Industrial radiography permits and training. *Environmental Health and Safety Program*. https://www.umaryland.edu/ehs/

Workplace Safety North. (2023). *Industrial radiography safety program requirements*. Ontario: WSN.

Zytekno. (2025). Understanding industrial radiography: Uses, benefits & safety. *Technical Resources*. https://zytekno.com/

Chapter 8

FOOD COLORINGS AND THEIR EFFECTS ON HUMAN HEALTH

Melek Altındağ[1]

---

[1] https://orcid.org/0000-0002-8749-2196

melekilbilgi@gmail.com

Selçuk University, Food Engineering

Introduction

Food additives are widely incorporated into food products to enhance consumer appeal, extend shelf life, and ensure technological functionality during production and distribution. In general, additives are used to delay microbial and chemical spoilage, maintain product stability, preserve nutritional and sensory quality, standardize taste and appearance, and facilitate processing, packaging, storage, and transportation (Kilic-Akyilmaz, Gulsunoglu, & processing, 2015; Meeting & Organization, 2013). When applied within authorized conditions and maximum permitted levels, food additives are required to be safe for consumers and should not pose a risk to human health, as established through rigorous toxicological evaluations and risk assessment procedures conducted by regulatory authorities (Efsa, 2017).

Among the various classes of additives, food colorants play a particularly prominent role due to the strong relationship between color and consumer perception of freshness, flavor intensity, and overall product quality (Downham, Collins, & technology, 2000; Scotter, 2015). During processing, storage, and retail display, foods may experience undesirable color changes as a result of heat treatment, exposure to light and oxygen, or pH variations, which can negatively affect consumer acceptance (Scotter, 2015). To counteract these effects, colorants are used to restore color losses, enhance natural coloration, or ensure a consistent and standardized appearance across production batches(Downham et al., 2000). Importantly, both national and international regulations strictly prohibit the use of food colorants to mask spoilage or poor-quality raw materials, and their use is tightly regulated within established legal frameworks to ensure consumer protection (Efsa, 2017; Meeting & Organization, 2013).

Colorants can be classified in multiple ways (e.g. by chemical structure, solubility, source, and technological functionality). A widely used practical classification is by origin, separating colorants into natural and synthetic groups.

Regulatory context (brief overview)

Internationally, safety evaluation of additives is coordinated through the Joint FAO/WHO Expert Committee on Food Additives (JECFA), which assesses toxicological and exposure data and establishes health-based guidance values such as the Acceptable Daily Intake (ADI). These assessments inform Codex standards and support national regulatory decisions (MANUAL, 2005).

Within the European system, EFSA contributes scientific opinions and re-evaluations, and in the United States the FDA is responsible for regulating color additives and their conditions of use. In Türkiye, food additive permissions and labeling requirements are implemented through the Turkish Food Codex framework.

Natural colorants

Natural food colorants are pigments of biological origin—typically derived from plants, animals, algae, or microorganisms—and are incorporated into foods either as extracts or purified compounds. They are often preferred because, beyond visual appeal, many natural pigments are associated with bioactive properties (e.g., antioxidant potential), which can align with consumer demand for "cleaner label" products (Özcan & Bilek, 2018). Recent reviews continue to emphasize that the most important natural pigment families used in foods include anthocyanins, carotenoids, chlorophylls/chlorophyll derivatives, and betalains (Nabi et al., 2023; Wijesekara & Xu, 2024).

Common examples of natural colorants and sources used in the food industry include:

- Chlorophylls / chlorophyll derivatives (green hues)
- Carotenoids such as β-carotene and related compounds (yellow–orange hues)
- Anthocyanins (red–purple–blue hues; often pH-sensitive)
- Betalains from red beet (red–violet hues), widely used in dairy products, desserts, beverages, and some meat products (Georgiev et al., 2010)
- Curcumin from turmeric (yellow hues)
- Carmine/cochineal (E120) from insect origin (red hues)(Martins et al., 2016)

Technological advantages and limitations

Natural pigments can improve consumer acceptance and may contribute functional benefits; however, they often have lower stability than synthetic dyes under industrial conditions. Many natural colorants are sensitive to light, heat, oxygen, and pH, which can cause fading, hue shifts, or degradation. For example, some pigments may change color noticeably at low pH or during thermal treatment, limiting their use in acidic beverages or high-heat processes. These stability constraints remain a major technological driver for ongoing research, including stabilization approaches such as improved extraction/purification, formulation strategies, and protective delivery systems (e.g., encapsulation) highlighted in recent reviews (Wijesekara & Xu, 2024).

E-number recognition for selected natural pigments

Several widely used natural colorants are recognized in regulatory systems and appear with E-numbers in European-style labeling, such as:

- Anthocyanins (E163)
- Betalains (E162)
- Carotenoids(E160–E161)

  These groupings are also frequently discussed in the context of “natural colorants” adoption and industrial challenges (Martins et al., 2017; Martins et al., 2016).

Synthetic colorants

Synthetic food colorants are chemically synthesized compounds that generally do not occur in nature and are produced to deliver strong, uniform, and stable coloration in food systems (Gıda & Bakanlığı, 2013). Compared with many natural pigments, synthetic colorants typically offer important technological advantages: high tinctorial strength, good batch-to-batch reproducibility, and greater stability against heat, light, pH changes, and common food ingredients/preservatives, which helps maintain color throughout processing and the product’s shelf life (Dolan, Matulka, & Burdock, 2010; Erkmen, 2010). These features explain why synthetic dyes have historically remained widely used in processed foods despite the growing interest in natural alternatives (Amchova, Siska, & Ruda-Kucerova, 2024; Barciela, Perez-Vazquez, Prieto, & Toxicology, 2023; Martins et al., 2016)

Forms and functional classification (dyes vs. pigments/lakes)

In practice, synthetic colorants are marketed in different physical forms—powders, granules, liquids, pastes, or diluted preparations—depending on the intended application and dosing convenience (Amchova et al., 2024). Functionally, they are often discussed as:

- Dyes (water-soluble colorants): typically added after dissolving in a suitable solvent and used in beverages, confectionery syrups, gel desserts, and other high-moisture matrices.
- Pigments / lakes (water-insoluble forms): used when better performance is needed in fat-rich or low-moisture foods, and in applications where migration must be minimized (e.g., coatings). In the U.S. regulatory system, many certified colors also exist as aluminum lakes for specific use cases.

From an industrial viewpoint, the choice between dye and lake/pigment forms is guided by the food matrix (water vs. fat phase), processing conditions, and desired color uniformity (BAYDAN, SEZGİN, & Studies, 2021).

Common uses in foods

Synthetic colorants are used across a broad range of products to achieve or standardize vivid, consumer-recognizable colors—especially in confectionery, soft drinks, desserts, ice cream, sauces, jams, baked goods, instant soups, and some processed meat products (Omaye, 2004). Contemporary reviews of food dyes also emphasize that many commonly used synthetic colorants belong to the azo dye class and remain prevalent in packaged foods due to their performance and cost-effectiveness(Barciela et al., 2023).

Safety perspective and current concerns

Because synthetic colorants are deliberately added to frequently consumed processed foods, exposure management is a major public-health issue—particularly in children, who may have higher intake relative to body weight. Regulatory authorities rely on toxicological and exposure data to set guidance values such as the Acceptable Daily Intake (ADI) and to define permitted uses and maximum levels (Yurttagül & Ayaz, 2008). Recent scientific reviews continue to discuss potential adverse effects reported for some synthetic dyes in sensitive individuals—most commonly intolerance/allergy-like reactions and behavioral effects in subsets of children—while also emphasizing that risk depends on dose and real-world exposure relative to regulatory limits(Amchova et al., 2024).

In addition, newer literature highlights that safety discussions are not limited to the dye molecule itself, but may also consider impurities and contaminants that can be present at low levels depending on manufacturing and specifications(Banc et al., 2024).

Regulatory oversight (EU and U.S. examples)

In the European Union, food colors are assessed and re-evaluated within the broader food additive framework, with label declaration by name or E-number required. EFSA maintains topic pages and scientific outputs related to authorized food colors and their safety assessment (Efsa, 2017).

In the United States, the FDA states that color additives (with limited exceptions) are subject to pre-market approval, and many synthetic colors used in foods are “certified colors” that require batch certification; FDA provides public inventories and regulatory status pages for specific certified colors (e.g., FD&C Yellow No. 5/tartrazine)(FDA, 2025).

Regulatory Framework (Legal Regulations)

Food colorants, like all food additives, are subject to comprehensive legal controls to ensure they are used safely and appropriately. These regulatory systems operate at international, regional (e.g., EU), national (e.g., USA), and local (e.g., Turkey) levels, and they govern everything from safety evaluation to permitted uses, maximum levels, labeling, and enforcement.

International Standards and Safety Evaluation

At the international level, the Joint FAO/WHO Expert Committee on Food Additives (JECFA) conducts risk assessments of food additives – including colorants – based on toxicological and exposure data from animal studies and human research. JECFA establishes health-based guidance values such as Acceptable Daily Intakes (ADI), which are reference benchmarks indicating the amount of a substance that can be consumed daily over a lifetime without appreciable risk. These values are used by national and regional regulators when deciding on approval, permitted uses, and maximum levels for food colorants.

The Codex Alimentarius Commission (CAC), developed jointly by the Food and Agriculture Organization (FAO) and the World Health Organization (WHO), translates scientific evaluations (including JECFA conclusions) into international standards and guidelines for food additives, which many countries use as a basis for their own laws.

European Union Regulations

In the European Union (EU), food colorants are regulated under Regulation (EC) No 1333/2008 on food additives and related legislation. This framework requires that:

- All permitted colorants undergo rigorous safety assessment by the European Food Safety Authority (EFSA) before authorization.
- Authorized colorants must be listed in EU legislation with specified conditions of use and maximum levels in different food categories.

- Color additives must be declared on the label by either their name or E number ("Europe number"), allowing consumers to identify the presence of specific colorants in foods. An "E number" signals that a food additive has been scientifically evaluated and approved for use in the EU market (Efsa, 2017).

This system creates a harmonized regulatory environment across EU member states, and many non-EU countries (including Turkey) align their laws with EU approaches for consistency in trade and safety standards.

United States (FDA) Regulations

In the United States, the Food and Drug Administration (FDA) regulates food colorants under the Federal Food, Drug, and Cosmetic Act. Here:

- Color additives must be affirmatively approved by the FDA before they can be used in foods, drugs, or cosmetics.
- Some synthetic colorants are designated "certified color additives" (FD&C), meaning each batch must be tested and certified for compliance with specifications before use.
- Natural colorants and certain exempt substances may not require certification but still must be approved and used within regulatory conditions.
- Labels must declare color additives (e.g., "FD&C Yellow No. 5")(FDA, 2025).

The FDA continues to review the safety of colorants based on new science; for example, regulatory decisions about specific dyes change as evidence evolves.

Turkish Food Codex Regulations

In Türkiye, food colorants are regulated under the Turkish Food Codex, which incorporates international norms and draws on EU legislation (e.g., Regulation 1333/2008/EC) to establish domestic standards for food additives, including colorants. The key elements include:

- A comprehensive Food Additives Regulation (Türk Gıda Kodeksi Gıda Katkı Maddeleri Yönetmeliği) that lists permitted additives by E numbers, the foods in which they may be used, and the conditions and maximum levels for their use (TGK, 2013).
- Specific communicates and purity criteria for colorants used in foods, which outline what substances are allowed and under what conditions(TGK, 2007).

- Labeling requirements mandating that food products declare the functional class (e.g., colorant) and either the additive's name or its E number on the ingredient list (TGK, 2013).
- Recent regulatory updates have banned certain additives, such as titanium dioxide when used as a colorant, reflecting evolving safety assessments and alignment with modern food safety standards(TGK, 2023).

These regulations are enforced through official controls and inspections, and they aim to protect consumer health while maintaining fair food industry practices.

Impacts on Health of Food Colorants

The health effects of food colorants are typically discussed under two broad categories: (1) adverse reactions potentially linked to synthetic (artificial) dyes, especially in sensitive subgroups, and (2) potential health-promoting properties of certain natural pigments, when they are consumed as part of foods (not merely as trace coloring agents). Importantly, regulatory risk assessment is based on hazard + real-world exposure, and many debates focus on whether some groups (particularly children) may approach or exceed guidance values through frequent consumption of highly colored ultra-processed foods.

1) Adverse reactions associated with synthetic colorants

a) Hypersensitivity-type reactions (skin and respiratory)

A subset of individuals may experience intolerance or hypersensitivity-like reactions to specific synthetic dyes. Reported outcomes include urticaria, angioedema, eczema-like rashes, rhinitis, and asthma exacerbations, with tartrazine (E102) frequently discussed in this context (Omaye, 2004). Recent reviews similarly describe these reactions—especially urticaria and asthma symptoms—as the most commonly reported issues in sensitive individuals(Amchova et al., 2024; Banc et al., 2024). 31

It is also emphasized that such reactions appear uncommon at the population level, but clinically relevant for susceptible persons.

b) Neurobehavioral effects in children (hyperactivity/attention symptoms)

The strongest and most consistently discussed public-health concern relates to behavioral effects in some children, particularly hyperactivity-like symptoms. Your original section referenced classic findings (e.g.,(McCann et al., 2007)). More recent syntheses continue to conclude that a subset of children may show worsened attention/hyperactivity symptoms associated with synthetic food colors, though effects are generally small-to-moderate and not universal(de Oliveira et al., 2024; Nigg, Lewis, Edinger, Falk, & Psychiatry, 2012). Current interpretations often frame this as: synthetic colors do not “cause ADHD” broadly, but may aggravate symptoms in susceptible children or under certain dietary patterns.

c) Gastrointestinal and other nonspecific symptoms

Some literature reports gastrointestinal complaints, headaches/migraine-type symptoms, or other nonspecific reactions in sensitive individuals. These are harder to attribute causally because exposures often occur in complex food matrices (multiple additives plus sugar, emulsifiers, etc.). Still, reviews routinely list GI and neurological complaints among reported adverse events for certain dyes(Banc et al., 2024).

d) Toxicological signals from experimental studies (in vitro/animal)

A number of in vitro and animal studies have reported oxidative stress markers, cytotoxicity, or genotoxicity signals for particular dyes under experimental conditions. These findings are frequently cited in narrative reviews, but they do not automatically translate to human risk at regulated intake levels. Recent papers continue to explore these mechanisms (e.g., cellular assays), emphasizing the need to interpret them alongside exposure and regulatory specifications(Dos Santos et al., 2022).

2) Risk assessment and the role of ADI and exposure

Internationally, health-based guidance such as ADI is used to manage risk for approved colorants. EFSA and the European Commission note that many additives have undergone re-evaluation programs and that conditions of use may be updated if new evidence warrants it (Efsa, 2017).

A key practical point—also consistent with your original Turkish text—is that as consumption of ultra-processed, vividly colored foods increases, the chance of high cumulative exposure rises, particularly for children (higher intake per kg body weight). Recent studies continue to document the prevalence of synthetic dyes in packaged foods, supporting this exposure-based concern(Dunford, Galligan, Taillie, Musicus, & Dietetics, 2025).

3) Potential health-promoting roles of natural pigments (contextual)

Natural pigment families (anthocyanins, carotenoids, chlorophyll derivatives, betalains) are widely discussed for antioxidant and anti-inflammatory activities and potential roles in chronic disease risk modulation when consumed through pigment-rich foods (e.g., berries, beets, leafy greens). Recent reviews summarize these health-related properties and also emphasize technology/stability challenges for using them as food colorants (Magalhães et al., 2024; Novais et al., 2022).

Here, it's worth being precise in the chapter: when natural pigments are used as additives, the dose may be relatively small; the broader health benefits are more strongly supported when these pigments are consumed as part of naturally pigment-rich foods and dietary patterns.

Consumers' Perceptions and Attitudes toward Food Colorants

Consumer perception of food colorants has become an important topic in food science, nutrition, and public health, as purchasing decisions are increasingly influenced by health concerns, naturalness, and label transparency. Numerous studies indicate that colorants are among the most recognized and discussed food additives by consumers, often eliciting stronger emotional responses than less visible additives such as stabilizers or emulsifiers (Shim, Serido, & Barber, 2011; Varela & Fiszman, 2013).

Awareness and knowledge of colorants

Survey-based studies consistently show that consumers are more familiar with colorants than with many other additive categories. Colorants, sweeteners, and flavor enhancers are typically reported as the best-known food additives across different populations (Bilgin, Bayır, Türk, Uçaş, & Özkan, 2022; Shim et al., 2011). However, this familiarity does not always reflect accurate scientific knowledge. Many consumers are aware of E-numbers, yet their understanding of what these codes represent—regulatory approval rather than inherent risk—remains limited (Varela & Fiszman, 2013).

Education level has repeatedly been identified as a key determinant of knowledge. Studies conducted in Türkiye report a statistically significant association between educational status and awareness of food additives, including distinctions between natural and synthetic colorants, perceived safety, and allergenic potential (Ahsan Ansari, Siddiqui, Siddiqui, & Journal, 2019). Individuals with higher education levels are more likely to read labels carefully and to avoid products containing synthetic dyes.

Perceived health risks and trust issues

A dominant theme in consumer research is the perception of food colorants as potentially harmful, particularly synthetic ones. Multiple studies report that a substantial proportion of consumers associate colorants with cancer risk, allergic reactions, hyperactivity in children, and other chronic health problems, even when scientific evidence indicates that approved additives are safe within regulatory limits (Erdem, 2014). In Turkish consumer surveys, more than half of respondents have described colorants as a "serious health risk," and this perception tends to increase with age (Ahsan Ansari et al., 2019; Otto, Strenger, Maier-Nöth, & Schmid, 2021).

Age and gender differences are also notable. Several studies show that older consumers are less willing to purchase foods containing colorants, while women generally report higher levels of concern and greater attentiveness to ingredient lists compared with men ((Kayışoğlu & Coşkun, 2016; Şenyüz, Günaydın, Saygılı, & Karagözlü, 2023). Among parents, concerns are particularly pronounced for foods marketed to children, such as colored dairy products, confectionery, and beverages.

Natural vs. synthetic colorants: consumer preference

Across different cultural contexts, consumers consistently show a strong preference for natural colorants over synthetic alternatives. Natural colorants are commonly perceived as healthier, safer, and more "authentic", whereas synthetic dyes are often associated with artificiality and risk (Martins et al., 2016; Varela & Fiszman, 2013). This preference persists even when consumers are informed that natural colorants may have technological limitations such as lower stability or higher cost.

Recent studies emphasize that the concept of “clean label”—short ingredient lists, recognizable names, and natural sources—has significantly shaped consumer expectations. As a result, manufacturers increasingly reformulate products to replace synthetic dyes with natural pigments, sometimes highlighting this change explicitly on packaging (Martins et al., 2016; Şenyüz et al., 2023).

Role of labeling and consumer education

Food labeling plays a central role in shaping consumer attitudes toward colorants. Research indicates that consumers who regularly read food labels are more likely to avoid products containing synthetic colorants and to make purchasing decisions based on additive content (Bilgin et al., 2022). In the EU and Türkiye, mandatory declaration of additives by function and name or E-number is intended to support informed choice; however, studies suggest that label information alone is insufficient without broader nutrition and food-safety education.

Overall, the literature highlights a gap between regulatory risk assessment and consumer risk perception. While authorities evaluate colorants based on toxicological evidence and exposure limits, consumers often rely on heuristic cues such as “artificial vs. natural,” media reports, and anecdotal experiences. Consequently, improving science-based communication, increasing public understanding of regulatory frameworks, and promoting balanced dietary patterns are widely recommended to address misconceptions and support informed decision-making.

Conclusion

In contemporary food systems, the use of colorants has become nearly unavoidable due to the widespread consumption of processed and packaged foods. Food colorants play a crucial technological and sensory role by improving visual appeal, restoring or standardizing color lost during processing, and enhancing consumer acceptance. However, their use also raises important health, regulatory, and consumer-perception concerns, particularly in the context of increasing exposure among vulnerable populations such as children.

From a safety perspective, international and national regulatory authorities evaluate food colorants through structured risk-assessment frameworks based on toxicological evidence and exposure data. The establishment of Acceptable Daily Intake (ADI) values and clearly defined conditions of use ensures that authorized colorants can be consumed safely throughout a lifetime when regulatory limits are respected. Nevertheless, shifts in dietary patterns toward highly colored, ultra-processed foods may increase cumulative exposure, underscoring the need for continued surveillance, periodic re-evaluation, and evidence-based regulatory updates.

Scientific literature indicates that some synthetic colorants may be associated with adverse reactions in susceptible individuals, including hypersensitivity symptoms and behavioral effects in certain children. Although these effects are not universal and are generally observed in specific subgroups, they contribute to ongoing public concern and reinforce calls for cautious use and transparent labeling. In parallel, natural colorants have gained prominence due to consumer demand for cleaner labels and perceptions of safety, as well as their potential bioactive properties. However, technological limitations such as lower stability and higher production costs remain challenges for their broader industrial application.

Consumer studies consistently demonstrate that colorants are among the most recognized and scrutinized food additives. Perceived health risks, limited understanding of regulatory systems, and strong preferences for “natural” ingredients significantly influence purchasing behavior. This disconnect between scientific risk assessment and public risk perception highlights the importance of effective science communication, nutrition education, and clear labeling practices.

In conclusion, ensuring the safe and responsible use of food colorants requires a multidisciplinary approach that integrates robust regulatory oversight, ongoing scientific research, industry responsibility, and informed consumer choice. Promoting balanced diets, improving public awareness of additive regulations, and encouraging innovation in safer and more stable natural colorants will collectively contribute to protecting public health while meeting modern food production and consumer expectations.

References

Ahsan Ansari, M. U., Siddiqui, D. A. J. A., MUA, Siddiqui, D. (2019). Packaging features and consumer buying behavior towards packaged food items. *Glob Sci J, 7*(3), 1050-1073.

Amchova, P., Siska, F., & Ruda-Kucerova, J. (2024). Food safety and health concerns of synthetic food colors: an update. *Toxics, 12*(7), 466.

Banc, R., Filip, L., Cozma-Petruț, A., Ciobârcă, D., Miere, D. J (2024). Yellow and red synthetic food dyes and potential health hazards: A mini review. *Food Sci Tech, 81*(1), 2024.

Barciela, P., Perez-Vazquez, A., Prieto, M. (2023). Azo dyes in the food industry: Features, classification, toxicity, alternatives, and regulation. *Food Chem Toxicol, 178*, 113935.

Baydan, S., Sezgin, A. C. (2021). Gıda sanayinde kullanılan katkı maddeleri ve sağlık ilişkileri (Additives used in food industry an their relation to health). *J Tourism Gastr Stud, 9*(Special Issue 5), 527-542.

Bilgin, M. G., Bayır, A. G., Türk, S. N., Ucaş, İ., & Özkan, B. (2022). Bireylerin gıda katkı maddeleri ve etkileri konusunda bilgi ve farkındalık durumlarının değerlendirilmesi. *İstanbul Rumeli Üniversitesi Sağlık Bilimleri Dergisi, 1*(1), 1-12.

de Oliveira, Z. B., Silva da Costa, D. V., da Silva dos Santos, A. C., da Silva Júnior, A. Q., de Lima Silva, A., de Santana, R. C. (2024). Synthetic colors in food: A warning for children's health. *Int. J. Environ. Res. Public Health, 21*(6), 682.

Dolan, L. C., Matulka, R. A., & Burdock, G. A. (2010). Naturally occurring food toxins. *Toxins, 2*(9), 2289-2332.

Dos Santos, J. R., de Sousa Soares, L., Soares, B. M., de Gomes Farias, M., de Oliveira, V. A., de Sousa, N. A. B. (2022). Cytotoxic and mutagenic effects of the food additive tartrazine on eukaryotic cells. *BMC Pharm Toxicol, 23*(1), 95.

Downham, A., & Collins, P. (2000). Colouring our foods in the last and next millennium. *International Journal of Food Science and Technology, 35*, 5- 22.

Dunford, E. K., Galligan, T. M., Taillie, L. S., Musicus, A. A. (2025). All the Colors of the Rainbow: Synthetic Dyes in US Packaged Foods and Beverages in 2020. *J Acad Nutr Diet*, 1207-1217.

Younes, M., Aggett, P., Aguilar, F., Crebelli, R., Dusemund, B., Filipič, M., ... & Lambré, C. (2018). EFSA Panel on Food Additives and Nutrient Sources added to Food (ANS). *Scientific opinion on the safety of monacolins in red yeast rice. EFSA J*, *16*, 5368-73.

Erdem, N. (2014). *Tüketicilerin hazır ve yarı hazır gıdalarda kullanılan gıda katkı maddelerine yönelik görüşlerinin incelenmesi (Konya ili örneği)* (Yayımlanmış yüksek lisans tezi). Selçuk Üniversitesi, Sosyal Bilimler Enstitüsü, Konya.

Erkmen, O. (2010). Gıda kaynaklı tehlikeler ve güvenli gıda üretimi. *Çocuk Sağlığı ve Hastalıkları Dergisi, 53*(3), 220-235.

FDA. (2025). Regulatory Status of Color Additives

FD&C Yellow No. 5. Retrieved from https://hfpappexternal.fda.gov/scripts/fdcc/index.cfm?id=FDCYellow5&set=ColorAdditives&utm_source

Georgiev, V. G., Weber, J., Kneschke, E. M., Denev, P. N., Bley, T., & Pavlov, A. I. (2010). Antioxidant activity and phenolic content of betalain extracts from intact plants and hairy root cultures of the red beetroot *Beta vulgaris* L. Cv. Detroit Dark Red. *Plant Foods for Human Nutrition, 65*(2), 105-111.

Gıda, T., & Bakanlığı, H. J. R. G. T. (2013). Türk gıda kodeksi gıda katkı maddeleri yönetmeliği. (28693).

Kayışoğlu, S., & Kaptan, B. (2021). Determining the effect of gender, education level and age range on consumers' perspective on coloring additives. *II. International Ankara Multidisciplinary Studies Congress, 07.06.2021 - 08.06.2021*.

Kilic-Akyilmaz, M., & Gulsunoglu, Z. (2015). Additives and preservatives. *Handbook of vegetable preservation and processing*, 301-318.

Magalhães, D., Gonçalves, R., Rodrigues, C. V., Rocha, H. R., Pintado, M., & Coelho, M. C. (2024). Natural pigments recovery from food by-products: Health benefits towards the food industry. *Foods*, *13*(14), 2276.

Manual, P. J. T. (2005). Codex Alimentarius Commission. *9*(789251), 061473.

Martins, N., Roriz, C. L., Morales, P., Barros, L., & Ferreira, I. C. F. R. (2017). Coloring attributes of betalains: A key emphasis on stability and future applications. *Food & Function, 8*(4), 1357-1372.

31

Martins, N., Roriz, C. L., Morales, P., Barros, L., & Ferreira, I. C. F. R. (2016). Food colorants: Challenges, opportunities and current desires of agro-industries to ensure consumer expectations and regulatory practices. *Trends in Food Science & Technology, 52*, 1-15.

McCann, D., Barrett, A., Cooper, A., Crumpler, D., Dalen, L., Grimshaw, K., & Stevenson, J. (2007). Food additives and hyperactive behaviour in 3-year-old and 8/9-year-old children in the community: a randomised, double-blinded, placebo-controlled trial. *The Lancet, 370*(9598), 1560-1567.

Joint FAO/WHO Expert Committee on Food Additives. Meeting, & World Health Organization. (2013). *Evaluation of Certain Food Additives and Contaminants: Seventy-Seventh Report of the Joint FAO/WHO Expert Committee on Food Additives* (Vol. 983). World Health Organization.

N Nabi, B. G., Mukhtar, K., Ahmed, W., Manzoor, M. F., Ranjha, M. M. A. N., Kieliszek, M., ... & Aadil, R. M. (2023). Natural pigments: Anthocyanins, carotenoids, chlorophylls, and betalains as colorants in food products. *Food Bioscience*, *52*, 102403.3.

Nigg, J. T., Lewis, K., Edinger, T., & Falk, M. (2012). Meta-analysis of attention-deficit/hyperactivity disorder or attention-deficit/hyperactivity disorder symptoms, restriction diet, and synthetic food color additives. *J Am Acad Child Adolesc Psychiatry, 51*(1), 86-97.

Novais, C., Molina, A. K., Abreu, R. M., Santo-Buelga, C., Ferreira, I. C., Pereira, C., & Barros, L. (2022). Natural food colorants and preservatives: A review, a demand, and a challenge. *J Agric Food Chem*, *70*(9), 2789-2805.5.

Omaye, S. T. (2004). *Food and nutritional toxicology*: New York: CRC press.

Otto, S., Strenger, M., Maier-Nöth, A., & Schmid, M. (2021). Food packaging and sustainability–Consumer perception vs. correlated scientific facts: A review. *Journal of Cleaner Production*, *298*, 126733.

Scotter, M. J. (2015). *Colour additives for foods and beverages*: Elsevier.

S Shim, S., Serido, J., & Barber, B. L. (2011). A consumer way of thinking: Linking consumer socialization and consumption motivation perspectives to adolescent development. *Journal of Research on adolescence*, *21*(1), 290-299..

Şenyüz, Z., Günaydın, Ö. E., Saygılı, D., & Karagözlü, C. (2023). Meyveli süt ürünlerinde gıda boyası kullanımı ve tüketici davranışları: İzmir ili örneği. *Ege Üniversitesi Ziraat Fakültesi Dergisi*, *60*(4), 723-736..

TGK. (2007). Retrieved from https://faolex.fao.org/docs/pdf/tur106477.pdf?utm_source

TGK. (2013). Retrieved from https://www.tarimorman.gov.tr/GKGM/Belgeler/DB_Gida_Isletmeleri/TGK_Gida_Katki_Maddeleri_Yonetmeligi_Gida_Kategorileri_Kilavuzu.pdf?utm_source=chatgpt.com

TGK. (2023). Retrieved from https://www.resmigazete.gov.tr/eskiler/2023/10/20231013M1-1.htm

Varela, P., & Fiszman, S. M. (2013). Exploring consumers' knowledge and perceptions of hydrocolloids used as food additives and ingredients. *Food Hydrocolloids, 30*, 477-484.

Wijesekara, T., & Xu, B. (2024). A critical review on the stability of natural food pigments and stabilization techniques. *Food Research International*, *179*, 114011..

Yurttagül, M., & Ayaz, A. (2008). Katkı maddeleri: yanlışlar ve doğrular. *Hacettepe Üniversitesi Sağlık Bilimleri Fakültesi Beslenme ve Diyetetik Bölümü. Birinci Basım. Klasmat Matbaacılık. Ankara. Sağlık Bakanlığı Yayın*, *727*.

Chapter 9

THE EFFECTS OF PM2,5-BOUND PAHS ON CLIMATE CHANGE

Cihan PALOLUOĞLU[1]

---

[1] Assistant Professor, Bayburt University, Faculty of Art and Design, Interior Architecture and Environmental Design/Central Research Laboratory (BUMER), Bayburt, Turkey. cpaloluoglu@bayburt.edu.tr, ORCID: orcid.org/0000-0002-8635-8315

INTRODUCTION

PAHs associated with PM2.5 refer to the interaction between PM2.5 particles, which are fine particulate matter (PM), and PAHs (polycyclic aromatic hydrocarbons), which are highly toxic and carcinogenic, in the outdoor atmosphere in various forms. Based on this definition, it is clear how serious the situation is. Researchers with scientific studies on this subject are particularly aware of this dire situation. Furthermore, it is well known by humans and animals who suffer from the toxic, carcinogenic, and mutagenic effects that permeate their bodies after exposure to [PM2.5↔PAHs]. To elaborate further on this topic, PM2.5 particles are ultra-fine in size among PM particles and, due to their size, can easily pass through the nasal capillaries into the lungs and then reach the alveoli, the furthest point. For this reason, PM2.5 particles are highly toxic and dangerous. PAHs, on the other hand, are more toxic, carcinogenic, and mutagenic than PM2.5, and the harm they cause to humans can be seen in numerous studies throughout the literature today. These two compounds, which have quite risky effects, PM2.5 and PAHs, can easily bond by interacting in cold outdoor air. PAHs bind to the surface of PM2.5 like an adsorbent, resulting in a combination in the form of [PM2.5↔PAHs]. At the same time, because they exhibit a two-way effect in this combination, they pose a great danger to living organisms. For these reasons, [PM2.5↔PAHs] has always been a research topic under the main headings in highly current research topics.

PAHs are generally known as incomplete combustion products. Additionally, the sources of PAHs include the burning of fossil-based fuels for heating purposes in various areas. In particular, residential areas, industries, vehicles, and similar processes constitute the largest sources of [PM2.5↔PAHs]. At the same time, they are still an active subject of research due to their semi-volatile, toxic, carcinogenic, and mutagenic effects released into the atmosphere through biomass combustion (Lodovici et al., 2003; Chen et al., 2007). PM2.5s are particles within the Total Suspended Particulate Matter (TSP) group (0-100 μm) that are ultra-fine in size (2.5 μm and smaller). When PAHs fully bind to PM2.5s, they can be more easily transported over long distances in the atmosphere. Thus, the resulting [PM2.5↔PAHs] combination can be easily transported over short or long distances from their environment. Consequently, they significantly impact both all living species and climate events in the environments they reach (Baek et al., 1991; Mu et al., 2022).

The effects of PAHs on climate change will also be examined; PAHs, which are Persistent Organic Pollutants (POPs), are long-lived, persistent, and toxic. Considering the effects of PAHs on climate events solely based on these characteristics is not a very accurate approach. Furthermore, PAH compounds with high molecular weight significantly contribute to the formation mechanisms of “black carbon” and “brown carbon,” which affect the current climate systems of our era. Thus, PAHs directly increase unwanted radiative forcing effects in the atmosphere due to both their own structure and the carbon activities they generate. CO_2, one of the most effective and important known greenhouse gases, is a highly effective radiative forcing compound in the atmosphere. On the other hand, black carbon is known to be the most effective radiative forcing compound after CO_2. Due to this property, black carbon causes warming by absorbing radiation from the Sun in the atmosphere near the surface. For these reasons, PM2.5 particles that retain PAHs, or [PM2.5↔PAHs], are also defined as new climate pollutants that accelerate global warming by exhibiting greenhouse gas properties (Bond et al., 2021).

On the other hand, [PM2.5↔PAHs] acts as a catalyst in the reactions that pollutants emitted into the atmosphere from primary sources undergo to become secondary pollutants. Particularly in atmospheric environments with intense sunlight, photochemical oxidation reactions result in the formation of PAH components bound to oxygen or nitrogen. This formation increases the atmospheric oxidation capacity, triggering the rate of secondary reactions, especially the formation of ozone and secondary organic particles. As a result of the increase in these reactions, air quality is seriously damaged, disrupting the radiative balance. At the same time, they also have a significant impact on climate events and ultimately on climate change (Jariwala et al., 2021).

In addition to the primary effects of PAHs on the climate, another secondary effect mentioned is their ability to weaken the surface "albedo" (the reflection of electromagnetic radiation hitting the surface) by accumulating on glaciers or snow surfaces. Particulate matter (PM) containing PAHs, especially in regions close to glaciers or at high altitudes such as Erzurum, cause the glaciers or snow in these regions to melt faster by adsorbing the natural radiation energy on the glacier or snow surface (Sharma et al., 2020). Thanks to these black carbon mechanisms formed by PAHs with PMs, this situation can be cited as one of the causes of heat increases, particularly in places such as the Arctic region. On the other hand, climate change also significantly affects the concentrations and transport of PAHs. As a result of increased temperatures, semi-volatile PAHs heat up more than they should, leading to rapid vaporization and instantaneous changes in both their presence and concentration. Conversely, the recent increase in forest fires has led to a large release of PAHs into the atmosphere. In this case, the depletion of PAHs in the atmosphere can be effectively compensated for by the feedback system described above (Yin et al., 2023). From these perspectives, a highly reinforcing, bidirectional interaction has developed between PAHs and climate change, similar to the formation mechanism of [PM2.5↔PAHs].

As a result, [PM2.5↔PAHs] play a significant role in climate change scenarios not only due to their own properties or their conventional toxic air pollutant characteristics, but also as short-lived climate-affecting pollutants. Furthermore, numerous recent studies have shown that PAHs contribute significantly to global climate change due to their radiative forcing, aerosol optical properties, and even their melting rates on ice and snow surfaces. For this reason, regular monitoring of [PM2.5↔PAHs] is essential in the fight against climate change. At the same time, serious studies should be undertaken on what their sources are and how they can be eliminated at source. Furthermore, strategies to reduce their quantities must be implemented appropriately and in a timely manner, whether at source or in the environment where they are emitted.

Physical and Chemical Properties of [PM2.5↔PAHs]

[PM2.5↔PAHs] are KOKs, volatile compounds formed by the combination of two or more benzene rings. PAHs are also highly stable compounds with hydrophobic structures. They belong to the group of semi-volatile toxic pollutants with long half-lives, especially in atmospheric environments. Their structures contain only C and H. Furthermore, if they form rings when bonding, they belong to the aromatic compounds group. If they do not have a ring structure, they are included in the non-aromatic compounds group (Figure 1). Due to the physical formation of PAHs and the chemical bonding patterns they establish, determining both their behavior in the atmosphere and their toxicity effects is quite important (Figure 1 and Figure 2). On the other hand, PAHs are either in the gas phase or the particulate phase, depending on their molecular weight and size. Those with low molecular weights, such as naphthalene (2-3 rings), are mostly found in the gas phase. Those with high molecular weights, such as pyrene (4-7 rings), are generally found in the particulate phase (Figure 1). The group that binds most easily to PM2.5 and remains in the atmosphere for a long time is the gas phase and low-ringed ones. PAHs can remain in the atmosphere for long periods due to their chemical stability and low solubility. Furthermore, this group of PAHs readily binds to PM2.5, triggering and increasing the production of reactive oxygen species within PM2.5. Thus, they can further enhance their effects on human health and climate change (Esen et al., 2008; Zhang et al., 2020; Bandowe and Meusel, 2022; Yin et al., 2023).

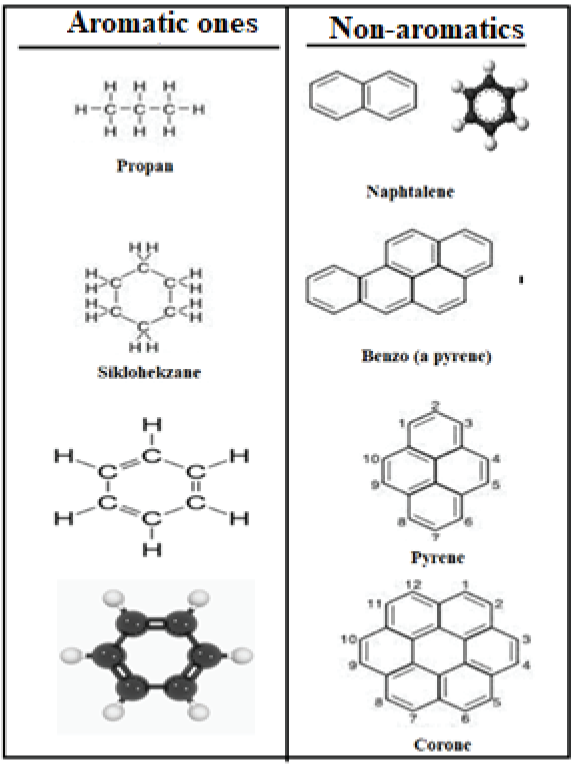

Figure 1. Chemical Properties of PAHs

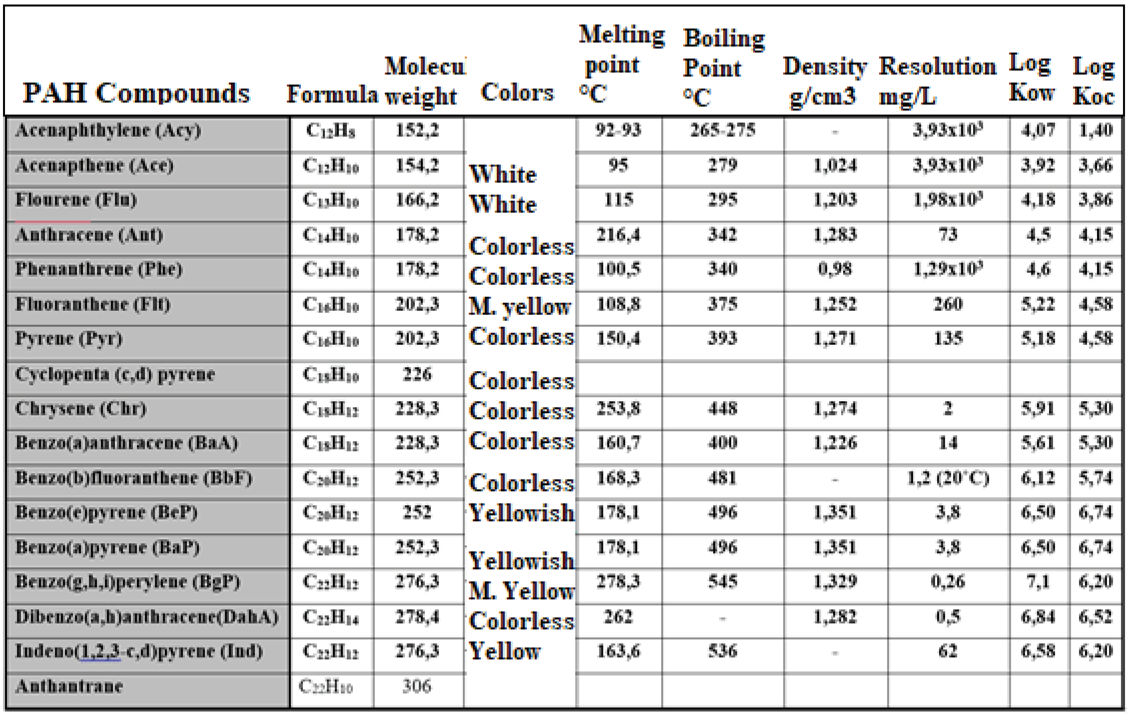

PAH Compounds	Formula	Molecul weight	Colors	Melting point °C	Boiling Point °C	Density g/cm3	Resolution mg/L	Log Kow	Log Koc
Acenaphthylene (Acy)	$C_{12}H_8$	152,2		92-93	265-275	-	3,93x10^3	4,07	1,40
Acenapthene (Ace)	$C_{12}H_{10}$	154,2	White	95	279	1,024	3,93x10^3	3,92	3,66
Flourene (Flu)	$C_{13}H_{10}$	166,2	White	115	295	1,203	1,98x10^3	4,18	3,86
Anthracene (Ant)	$C_{14}H_{10}$	178,2	Colorless	216,4	342	1,283	73	4,5	4,15
Phenanthrene (Phe)	$C_{14}H_{10}$	178,2	Colorless	100,5	340	0,98	1,29x10^3	4,6	4,15
Fluoranthene (Flt)	$C_{16}H_{10}$	202,3	M. yellow	108,8	375	1,252	260	5,22	4,58
Pyrene (Pyr)	$C_{16}H_{10}$	202,3	Colorless	150,4	393	1,271	135	5,18	4,58
Cyclopenta (c,d) pyrene	$C_{18}H_{10}$	226	Colorless						
Chrysene (Chr)	$C_{18}H_{12}$	228,3	Colorless	253,8	448	1,274	2	5,91	5,30
Benzo(a)anthracene (BaA)	$C_{18}H_{12}$	228,3	Colorless	160,7	400	1,226	14	5,61	5,30
Benzo(b)fluoranthene (BbF)	$C_{20}H_{12}$	252,3	Colorless	168,3	481	-	1,2 (20°C)	6,12	5,74
Benzo(e)pyrene (BeP)	$C_{20}H_{12}$	252	Yellowish	178,1	496	1,351	3,8	6,50	6,74
Benzo(a)pyrene (BaP)	$C_{20}H_{12}$	252,3	Yellowish	178,1	496	1,351	3,8	6,50	6,74
Benzo(g,h,i)perylene (BgP)	$C_{22}H_{12}$	276,3	M. Yellow	278,3	545	1,329	0,26	7,1	6,20
Dibenzo(a,h)anthracene(DahA)	$C_{22}H_{14}$	278,4	Colorless	262	-	1,282	0,5	6,84	6,52
Indeno(1,2,3-c,d)pyrene (Ind)	$C_{22}H_{12}$	276,3	Yellow	163,6	536	-	62	6,58	6,20
Anthantrane	$C_{22}H_{10}$	306							

Figure 2. Physical Properties of PAHs

Sources of [PM2.5↔PAHs]

[PM2.5↔PAHs] compounds, as mentioned above, are generally semi-volatile compounds resulting from incomplete combustion processes. Additionally, PAHs have known natural and anthropogenic sources (Figure 3). Natural sources of [PM2.5↔PAHs] include volcanic eruptions, storms, forest fires, petroleum and petroleum derivatives that seep naturally into the ground, and even breezes from oceans and seas. Anthropogenic sources include the combustion of fossil fuel-based solid, liquid, or gaseous substances, exhaust emissions from motor vehicles, coal used for heating in homes, thermal power plants, industrial manufacturing, raw material refineries, and gases emitted from regular landfill sites. (Figure 3). In particular, the use of low-quality diesel fuel in diesel vehicles significantly contributes to the concentrations of [PM2.5↔PAHs]. On the other hand, the most important parameters affecting the adhesion of PAHs to PM2.5 and their concentrations are: the type of fuel burned, the temperatures generated during combustion, the mixing distance in the atmosphere, and most importantly, meteorological factors. In particular, biomass burned at low temperatures can produce large amounts of PAHs with high molecular weights. Thus, PAHs with higher mass weights, originating from traffic and the combustion of fossil fuels, are released into the atmosphere in large quantities.

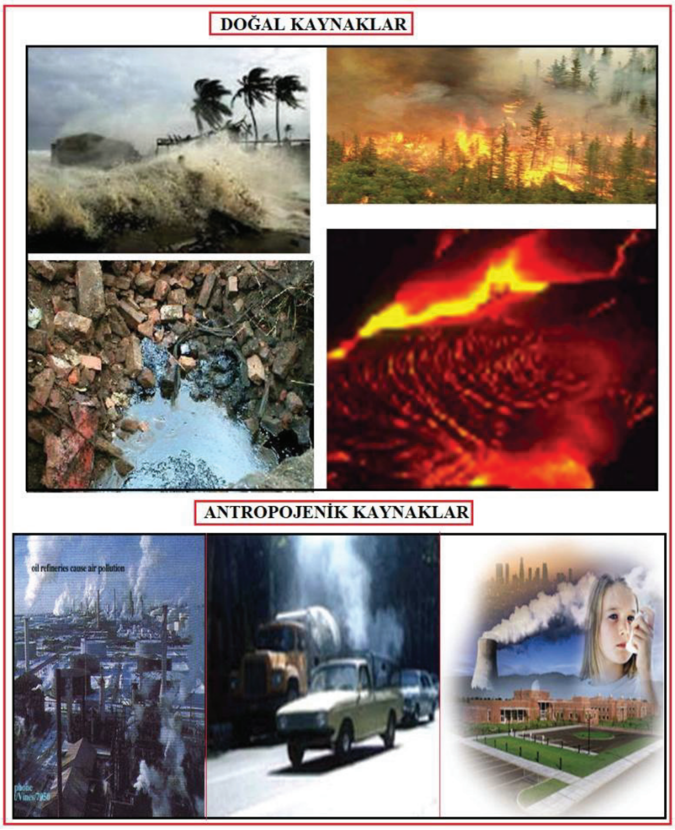

Figure 3. Sources of [PM2.5↔PAHs] Formation

Atmospheric Transport of [PM2.5↔PAHs]

[PM2.5↔PAHs] atmospheric transport events are initially a process that varies entirely depending on meteorological conditions. At the same time, it also depends on the volatile or semi-volatile properties of the [PM2.5↔PAHs] to be transported, their number of rings, molecular structures, and their binding strength to PM. Furthermore, since low molecular weight PAHs are partially in the gas phase, they can participate in photochemical oxidation or direct dispersion formation in the atmosphere. High molecular weight PAHs, on the other hand, more easily bind to PM2.5, increasing their transport and retention processes in the atmosphere. Since PM2.5 particles are very small, they can remain suspended and transported in the atmospheric environment for days, weeks, or even months, together with the PAHs bound to their surface. This also shows us that [PM2.5↔PAHs] can be transported to distances far from their release environment, even hundreds of kilometers away. However, many factors can significantly affect the transport of [PM2.5↔PAHs], such as instantaneous temperatures, changing wind speeds, and elevation changes in the mixing distance. At the same time, inversion layer formations also cause [PM2.5↔PAHs] to rise to atmospheric layers close to the surface. Furthermore, considering other factors, forest fires significantly affect their transport. At the same time, heavy traffic in cities and emissions from residential areas affect the transport of [PM2.5↔PAHs] regionally and even continentally. Thus, [PM2.5↔PAHs], which can be transported thousands of kilometers away, naturally settles on soil, water, and snow surfaces through wet or dry deposition, or by their own weight. From these environments, they either seep into groundwater and directly enter living organisms, or they directly enter the food chain and accumulate biologically from the lowest to the highest level, reaching the capillaries of living organisms. Thus, they contribute significantly to both serious diseases in humans (various cancers, mutagenic changes, etc.) and a substantial increase in the pollution load of [PM2.5↔PAHs] from an environmental perspective (Figure 4) (Sofowote et al., 2020; Mu et al., 2022; Yang et al., 2023). On the other hand, as can be seen in Figure 4, the mechanism by which [PM2.5↔PAHs] are formed is observed, with some sources of PM2.5 preceding [PM2.5↔PAHs] and PAHs being released from some sources afterwards. Subsequently, [PM2.5↔PAHs] can be easily inhaled by humans in the air environment, entering their lungs, then into the blood platelets in the capillaries, and even into the lung alveoli and bronchi. Ultimately, as shown in Figure 4, they cause a wider variety of diseases and mutagenic changes (Figure 4).

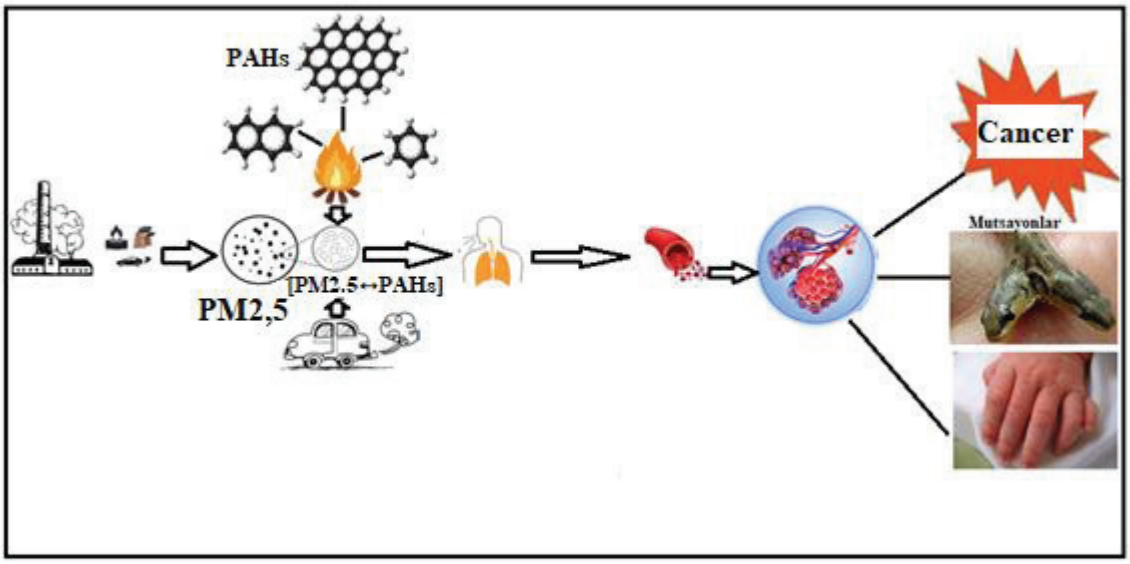

Figure 4. Formation Process, Interactions, and Some Diseases Caused by [PM2.5↔PAHs]

[PM2.5↔PAH]s' Fundamental Effects on Human Health

[PM2.5↔PAHs] are highly toxic and are only soluble in fat (lipophilic) or organic solvents, not in water. Due to these properties, they pose serious risks to human health, primarily through their accumulation in tissues or biological buildup. PM2.5 particles can easily enter the lungs through the respiratory tract and reach the alveoli due to their small size. Furthermore, [PM2.5↔PAHs] can systematically pass from the alveoli through the entire circulatory system. Thus, they cause both acute diseases and various chronic disorders. The most dangerous known effects of PAHs are their carcinogenic, mutagenic, and toxic properties (Taşdemir and Payan, 1999; Castellano et al., 2003; Gaga, 2004). Furthermore, high-ring benzo[a]pyrene (BaP) and similar PAHs can damage cellular repair systems in the human body. At the same time, these high molecular weight PAHs damage the helical structure of DNA, causing systemic mechanisms to malfunction. Furthermore, [PM2.5↔PAHs] that accumulate biologically in the body can increase the risk of lung cancer, skin cancer, and bladder cancer in humans over long periods (Figure 4) (Boström et al., 2020; Zhao et al., 2021). Furthermore, exposure to [PM2.5↔PAHs] affects the respiratory systems of humans, causing a gradual decline in respiratory function. At the same time, it triggers asthma disorders and negatively affects the development of children's lungs.

[PM2.5↔PAHs] are not only dangerous to the respiratory system or cancer-related disorders; limiting their harmful effects in this manner is not the correct approach. [PM2.5↔PAHs] can also affect the body from head to toe, including cardiovascular disorders, neurological disorders, and reproductive failure, as well as the urological system (Figure 5). In fact, if you look closely at Figure 5, it depicts the different intravascular changes that can occur over time with the entry, accumulation, and concentration of [PM2.5↔PAHs] in human blood vessels. It would be wrong to quickly dismiss this as simply clotting. Clotting is one of the most dangerous and insidious reactions in the body. It is a risky process that can suddenly lead to collapse scenarios in humans, ranging from the best-case scenario of stroke, shock, and vegetative state to the worst-case scenario of sudden death.

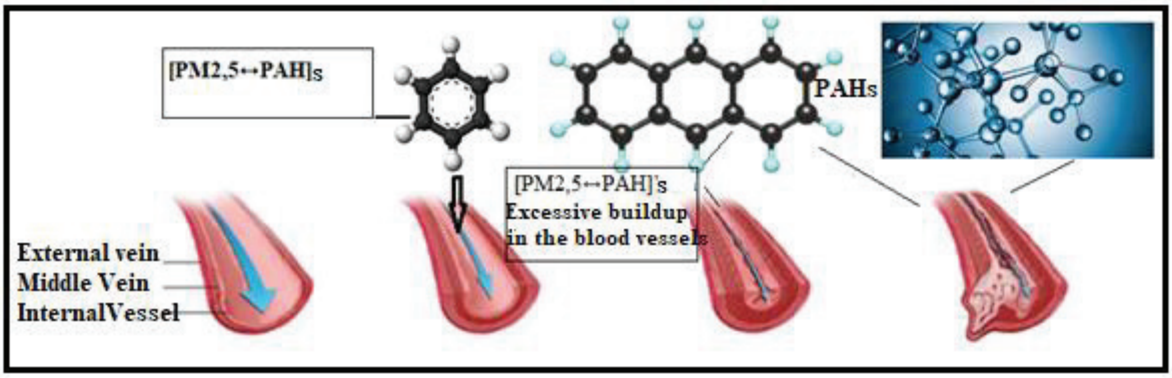

Figure 5. Accumulation of [PM2.5↔PAHs] in Human Blood Vessels and Potential Harmful Effects Based on Quantity

On the other hand, if we revisit the effects of [PM2.5↔PAHs] on the urological system, the primary concern is the retardation of fetal growth in the womb. It also increases the risk of low birth weight. Furthermore, due to hormonal imbalances, there is almost no part of the body that is unaffected. In addition to this information, if mothers are heavily exposed to [PM2.5↔PAHs] during pregnancy (e.g., excessive smoking, prolonged exposure to traffic), it can seriously damage the DNA structure that naturally forms in the baby in the womb. Depending on the severity of this damage, it can lead to health problems that are quite difficult to treat and repair, either in the short term or over a long period of time (Perera et al., 2022; Xiong et al., 2023). Due to all these harmful risks associated with [PM2.5↔PAHs], these harmful pollutants can be considered a critical threat to human health. They must be monitored regularly, especially in large cities and areas with heavy traffic and industry. At the same time, control mechanisms must be developed, and mitigation policies must be rapidly implemented in all areas of life.

Meteorological Factors Affecting [PM2.5↔PAHs]

[PM2.5↔PAHs] are significantly affected not only by the concentrations of their emissions in the environment where they are released, but also by all meteorological parameters individually. Parameters such as wind speed, precipitation, and relative humidity, especially temperatures, significantly affect both the gas/particle phase changes of [PM2.5↔PAHs] and can also determine their long-term residence and transport in the atmosphere. Furthermore, PAHs can often transition to the particulate phase at low temperatures, increasing their concentration on PM2.5. Conversely, on hot summer days, they can shift to the gas phase, accelerating atmospheric photooxidative degradation reactions. Particularly during winter months when temperatures are at their lowest and inversion layers are present, PAH and PM2.5 accumulations increase in urban areas, raising [PM2.5↔PAHs] concentrations to maximum levels (Bari et al., 2020; Mu et al., 2022). For these reasons, seasonal interactions with meteorological factors should also be considered in PAH studies. This allows for a more accurate interpretation of both seasonal conditions and long-term trends.

Determination of [PM2.5↔PAHs] Concentrations

1. Sampling Procedures

Sampling is both the first and most important step in determining the atmospheric concentrations of [PM2.5↔PAHs]. In sampling studies, either active or passive sampling methods are selected. If active sampling is to be performed, i.e., in processes involving both the device and an electrical charge, three types of devices are generally used: either a high-volume air sampler (Hi-Vol), a medium-volume air sampler (Mid-Vol), or a low-volume air sampler (Low-Vol). To capture [PM2.5↔PAHs] with any of these devices, a PM2.5 cap is attached to the devices. This allows only particles of PM2.5 size, 2.5 micrometers and below, and the associated PAHs to be collected on quartz (glass fiber filter: GFF) or PTFE filters. The air sampling flow rate used also varies depending on the suction power of the devices. Some devices have an air intake of 16.7 L min^{-1} (USEPA), while others have an air intake of 1-1.4 m^3 min^{-1} (Paloluoğlu, 2008). The sampling period is usually set to 24 hours so that the effects of daily meteorological factors can be determined. In addition, prior to sampling, all materials and equipment, especially the filters, undergo conditioning procedures for 24 or 48 hours. Subsequently, the initial weights are recorded, and the masses of the net [PM2.5↔PAHs] retained on the filter after sampling can be calculated in milligrams or micrograms. If only PM2.5 were present, gravimetric methods could be used for weighing, and then the concentrations per cubic meter of air could be quickly determined by comparing them to the air flow rates of the device. However, when [PM2.5↔PAHs] are involved, and due to the volatile nature of PAHs, they must be wrapped in protective aluminum foil, transported to the sampling point in a storage container, brought back to the laboratory environment with the same precision immediately after sampling, and stored in a refrigerator at a minimum temperature of -18 ^{0}C [PM2.5↔PAHs] emissions must be prevented and preserved until experimental procedures (Zhang et al., 2020; Bari et al., 2020). In passive sampling methods, in addition to electrical devices, Tischler, precipitation samplers, containers, Teflon caps, and many different types of materials can be used. As it is not possible to go into too much detail here, Figure 6 below shows images of both active and passive sampling devices of different types and characteristics;

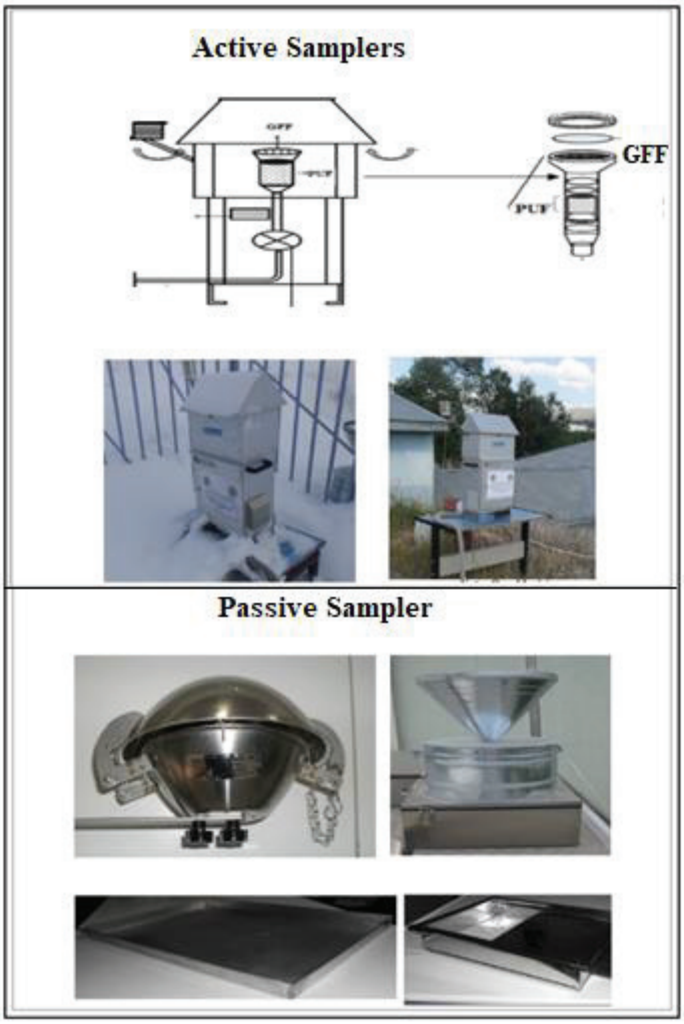

1. **Figure 6.** Some Active and Passive Samplers

2. Laboratory Procedures - Extraction Experiments

In order for [PM2.5↔PAHs] to be analyzed using a GC-MS device, extraction experiments must first be performed to transfer PAHs trapped in the PM2.5 filter from a solid medium to a liquid medium using organic solvents such as hexane or acetone. Before proceeding to extraction experiments, an extractor is used according to the phases. For example, for the particulate phase, the solid-liquid phase extraction method is selected. The extractor is an ultrasonic bath. For the liquid-liquid phase method, a vacuum filtration extractor is used. Finally, for the gas-liquid phase extraction method, a Soxhlet extractor is used (Paloluoğlu, 2016). Organic solvents such as dichloromethane, hexane, and acetone are generally preferred as solvents in extraction processes. In extractor processes, the extracted sample undergoes a series of steps to reduce its volume. At the same time, PAH samples with reduced volume in the Rotari device are then enriched with hexane in nitrogen gas 2 or 3 times, and each time they are depleted, the final volume is collected in 1 mL vials from 40 mL, labeled, and stored in the refrigerator until analysis. (Gaga, 2004; Bandowe and Meusel, 2022; Shen et al., 2022). Furthermore, the solid-liquid phase extraction method, which briefly summarizes the extraction steps, is presented in Figure 7 below (Paloluoğlu, 2008).

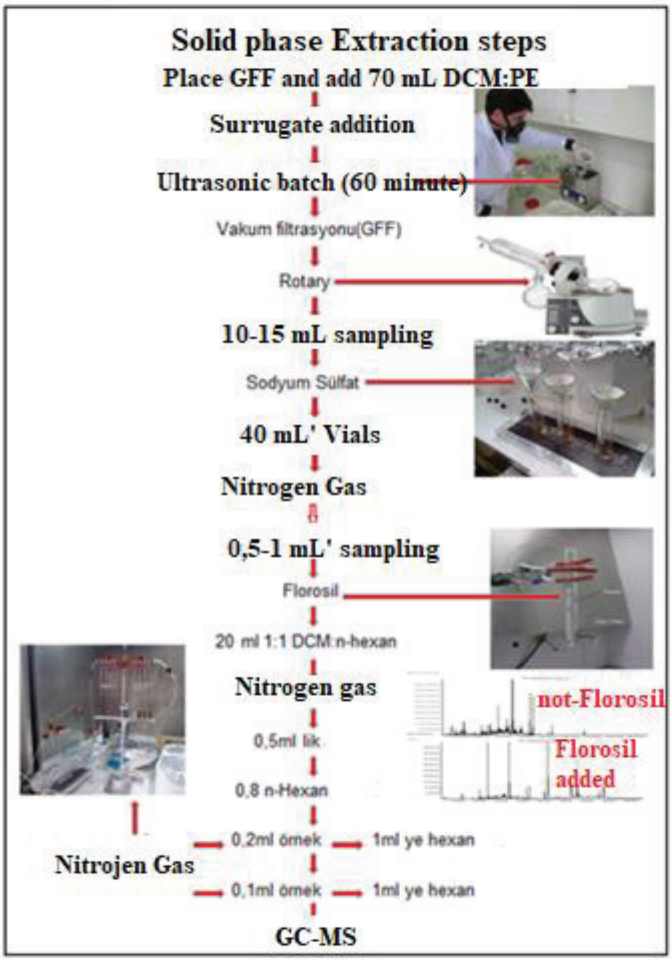

Figure 7. Solid-Liquid Phase Extraction Steps

1. Analysis Procedures with GC-MS Device

In gas chromatography-mass spectrometry devices, the presence of PAHs is usually identified through library scanning, and their numerical concentration values can be determined at the nano-gram or micro-gram levels. In addition, the GC-MS instrument can operate with very high sensitivity in the detection and identification of volatile and semi-volatile trace organic compounds. The most commonly used modes in analysis are either electron ionization (EI) or selective ion monitoring (SIM). When working in SIM mode, PAHs can generally be detected with higher sensitivity under low atmospheric conditions. HP-5MS capillary columns are preferred as the MS column. The widespread use of this column, which is most commonly used in PAH analyses, has also been documented in the literature. First, calibration curves are calculated on the device. This is done using PAH mixes set at predetermined concentrations, ensuring that the r^2 values are close to 1 and have at least 4 decimal places after 0 (0.9999). Furthermore, for more accurate and realistic results, blank studies are also performed using deuterium-labeled internal PAH standards at the working steps (Gaga, 2004; Paloluoğlu 2008; Yang et al., 2023; Zhao et al., 2021). Furthermore, Table 1 below presents the sample GC-MS working parameters used by Paloluoğlu in his 2008 and 2016 master's and doctoral theses. Figure 8 also shows the first PAH-mix reading screen in GC-MS by the same researcher, along with the screen peak images of 19 PAH concentrations read from a real PAH sample immediately below it;

Table 1. General Operating Parameters for GC-MS

GC column	30 m x 250 µm x 0.25 µm nominal film thickness, 5% Phenyl Methyl Siloxane, HP 5MS, capillary column
Liner	Deactivated glass wool Splitless glass liner (Agilent Technologies)
Carrier gas	Ultra-pure Helium, 99.999%, 1 mL/min
Injection type	Splitless
Injection port temperature	280°C
Oven temperature	70°C (4 min), 7°C/min to 250°C (5 min), 5°C/min to 300°C (8 min)
Injection volume	1 µL
Mass spectrometer	Electron impact, 70 eV
Mass spectrometer quadrupole temperature	150 °C
Mass spectrometer source temperature	230 °C

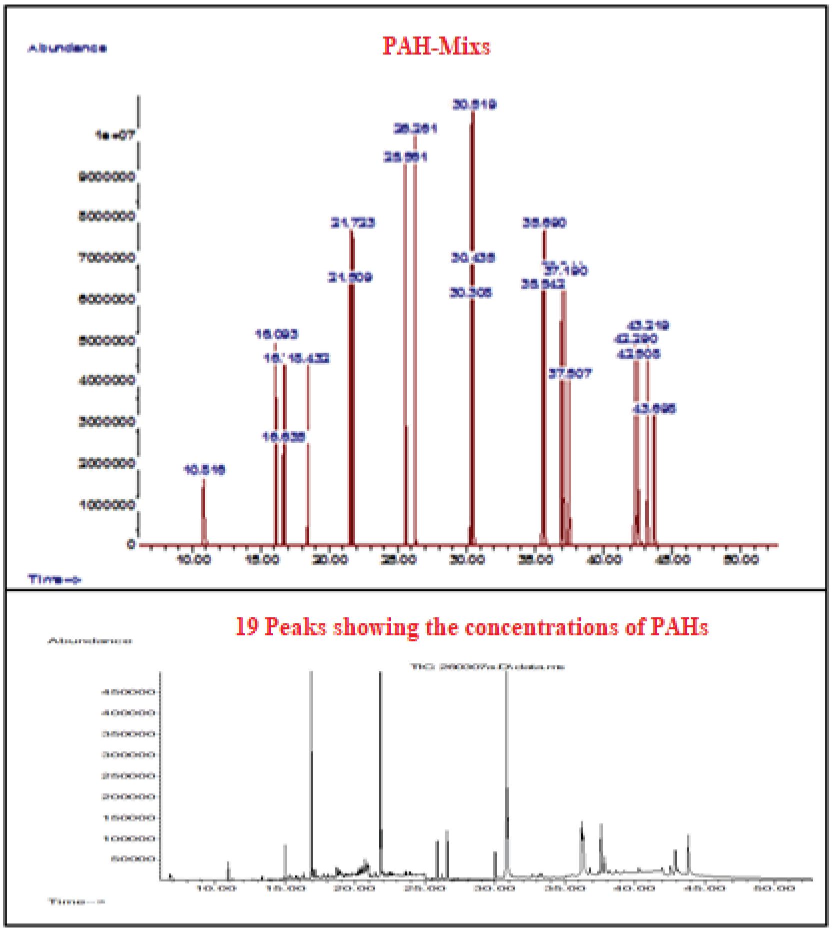

Şekil 8. PAH-Mix Okutma Ekranı – 19 Adet PAH'ın Konsantrasyon Pikleri

The preceding section aimed to provide a better understanding of the properties, effects, and concentration detection of [PM2.5↔PAHs] by utilizing a series of visuals. The following section will attempt to explain the presence and effects of [PM2.5↔PAHs] on climate change, which is the subject of current research, and will connect to the conclusions with comments.

The Effects of [PM2.5↔PAHs] on Climate Change

[PM2.5↔PAHs] do not have a direct effect on climate change like greenhouse gases (CO_2, N_2O, CH_4, CFC, water vapor, etc.), but they have indirect yet quite powerful effects. PAHs with high molecular weight, together with black carbon or brown carbon, can completely alter light reflection in the atmosphere, i.e., the radiative balance. After combining with black or brown carbon, PAHs trap the radiant light coming from the Sun. Thus, they increase heat formation in the lower part of the troposphere. At the surface, they cause cooling. As a result, they significantly alter the conditions of the atmospheric mixture components by disrupting the vertical temperature balance in the atmospheric layer where this combination is found. Ultimately, they can create a complex area that triggers climate change by causing a series of undesirable reactions (Zhao et al., 2019; Bon et al., 2021; Yang et al., 2023).

One of the effects of [PM2.5↔PAHs] on the climate system is on clouds and aerosols. [PM2.5↔PAHs], in combination with carbon compounds, affects the structure and properties of cloud condensation nuclei (CCN) due to the surface characteristics of carbon PM. This situation can lead to changes in the area covered by clouds, their distribution lifetimes, and their albedo, directly causing climate changes through short and long wavelength radiation (Jariwala et al., 2021).

On the other hand, [PM2.5↔PAHs] can cause losses in the albedo of ice and snow surfaces. In particular, when [PM2.5↔PAHs] combine with black or brown carbon and are transported over long distances to glaciers or cold regions, they almost completely eliminate the reflectivity of snow and ice surfaces in these areas. Thus, more heat and light from the Sun is retained, accelerating the melting of snow and ice. Consequently, glacial melting processes are accelerated in terms of climate change (Sharma et al., 2020). Furthermore, there are two-way interactions between climate change and [PM2.5↔PAHs]. In this case, climate change increases the emissions of [PM2.5↔PAHs], and [PM2.5↔PAHs] also accelerates some processes of climate change, creating feedback mechanisms (Mu et al., 2022; Yin et al., 2023).

Measures and Precautions to Reduce the Climate Change Impacts of [PM2.5↔PAHs]

The most effective measure that can be taken is the source reduction method, which is also the first method applied to other air pollutants. In addition, fuels must be converted from fossil content to fossil-free renewable energy forms. At the same time, technological improvement methods must be regulated. Of course, in order to fully implement these in the country, political and social policies must be reorganized. On the other hand, the use of coal and low-quality fuels must be completely eliminated as part of the fuel transition. By switching to cleaner or renewable energies (such as natural gas, electricity, heat pumps) instead, the binding of PAHs to black carbon can be minimized (Bond et al., 2021). In particular, the transition from diesel fuel or similar heavy fuels in motor vehicles to electric or hybrid vehicles must be encouraged through incentives. These measures would significantly reduce the concentrations of [PM2.5↔PAHs].

Following fuel conversions, the second measure is to control the indiscriminate burning of biomass in open areas. Burning all kinds of household or recycled materials, including various plastics, whether in rural areas or on mountain tops, means that [PM2.5↔PAHs] from these burning materials are released into the atmosphere and carried to different areas hundreds or even thousands of kilometers away. This situation directly triggers changes in the climate system. In this regard, in addition to clean stove technologies, closed combustion systems must be promoted, and a transition must be made from biomass to modern combustion systems and composting systems appropriate for the times. This will result in significant reductions in [PM2.5↔PAHs] emissions (Yin et al., 2023).

Another method, the third one, is the development and implementation of advanced flue gas treatment technologies. In such chimneys, emissions of [PM2.5↔PAHs] will be significantly reduced using electrostatic filters, bag filters, cyclone systems, and activated carbon methods (Khan et al. 2021). The fourth and final prevention method is the urgent updating and implementation of air quality policies to combat climate change. Looking at the situation in Turkey in terms of these measures to be taken, it is not sufficient to consider [PM2.5↔PAHs] only in terms of their toxic properties or air quality. When considered together with the change and growth processes of cities, policies to be organized for the climate, and energy transformation efforts, they can be prevented and are also a comprehensive environmental problem.

CONCLUSIONS AND RECOMMENDATIONS

[PM2.5↔PAHs] are multifaceted pollutants that have critical effects on everything from human health to ecosystems and climate systems. Due to their physical and chemical properties, PAHs are semi-volatile, insoluble in water and soluble only in organic solvents, and have long half-lives, giving them a strong ability to bind with PM2.5. In this case, both their toxic effects and their combined interactive effects are significantly increased. Furthermore, PM2.5 increases the chances of PAHs being transported to more distant regions. Due to their ability to bind with black carbon or brown carbon, as described above, PAHs can have an indirect yet equally powerful effect on climate change, similar to greenhouse gases.

[PM2.5↔PAHs] can also penetrate deep into cloud cores and easily alter their working mechanisms, as detailed further in the preceding sections. It has even been explained that they can readily cause the rapid melting of snow surfaces and ice in cold regions with glacial structures, such as the Arctic. Here again, due to the strong bonds they form with black carbon, they can directly intervene in and influence such climate changes. This situation also demonstrates once again that [PM2.5↔PAHs] do not confine themselves to regional sources. Conversely, they demonstrate and prove that they possess a significant and, in their own way, globalized impact mechanism due to their long-range transport.

Looking specifically at our own country; The burning of solid and fossil-based fuels such as coal, especially in cold regions during the winter months, the increase in traffic emissions in these regions, and the development of industrial activities cause the presence and concentration of [PM2.5↔PAHs] to increase significantly, especially during the winter months. Looking at the micro scale in addition to these macro images; cigarette smoke burned indoors, excessive use of fossil-based biomass indoors, inadequate ventilation systems in small industrial or business areas, and, in addition, the burning of agricultural waste increase the ratio of [PM2.5↔PAHs] in indoor and outdoor air. [PM2.5↔PAHs] levels in both indoor and outdoor air. Thus, as detailed above regarding the harmful effects of [PM2.5↔PAHs], they continue to increase the risks to human health and their contribution to climate change day by day. In this regard, scientific studies conducted in Turkey are not limited to a single perspective. At the same time, they take many factors into account and use them to obtain numerical results and to demonstrate studies on finding measures on how to combat them. In this respect, the harms, toxic, carcinogenic, and mutagenic effects of [PM2.5↔PAHs] are not considered one-sidedly. Along with these, the sustainability of methods to combat and prevent [PM2.5↔PAHs] in cities and the serious need to address energy use, whether cyclical or transformational, are highlighted. Climate change impacts are also addressed to a significant extent. In this context, the fundamental recommendations that can be offered to reduce the effects of [PM2.5↔PAHs] on climate change are listed below in order;

1- Efforts to transition to clean energy should be increased by reducing waste disposal methods at the source,

2- Emissions controls required in the energy and industrial sectors should be regularly increased,

3- The open burning of biomass in open areas should be brought under control,

4- [PM2.5↔PAHs] levels must be monitored regularly at the national level and controls must be tightened,

5- Low-emission zones must be created in urban areas of large cities, and planning policies must be strengthened,

6- Coordination efforts must be made to address both climate conditions and air quality.

In general, it can be concluded that [PM2.5↔PAHs] compounds have a highly dynamic structure in terms of toxicity and can establish a multifaceted interactive relationship involving carcinogenicity, mutagenicity, health risks, influencing atmospheric conditions, and contributing to climate change. For these reasons, PAHs must be eliminated at the source and their emissions reduced. This should not be seen merely as an effort to improve air quality. At the same time, they are taking firm steps toward becoming a highly strategic climate policy tool by reducing the rate of global warming and ensuring compatibility with climate systems. To minimize this issue from every angle, the number of comprehensive studies must be increased, and decisive actions must be taken swiftly. The steps to be taken and the measures to be implemented in this regard will remain among the most important determining factors in the transition to healthier and more sustainable atmospheric systems, whether globally or for those living in Turkey or anywhere else in the world.

REFERENCES

Bandowe, B. A. M., & Meusel, H. (2022). Atmospheric polycyclic aromatic hydrocarbons and their transformation products: Properties, occurrence, and fate. Environmental Pollution, 292, 118300.

Bari, M. A., Kindzierski, W. B., & Cho, S. (2020). A review of seasonal variation and sources of PM2.5-bound PAHs in urban environments. Science of the Total Environment, 737, 140308.

Baek, S., O., Field, R., A., Goldstone, M., E., Kirk, P., W., Lester, J., N., Perry, R., 1991. "A review of atmospheric polycyclic aromatic hydrocarbons: Sources, fate and behavior", Water, Air and Soil Pollution, 60 (3-4), 279-300.

Bond, T. C., Xu, Y., & Wang, H. (2021). Climate forcing of black carbon and organic aerosols: Advances and remaining uncertainties. Nature Climate Change, 11(7), 607-615.

Boström, C. E., Gerde, P., Hanberg, A., Jernström, B., Johansson, C., Kyrklund, T., ... & Törnqvist, M. (2020). Polycyclic aromatic hydrocarbons: Cancer risks and mechanisms. Environmental Health Perspectives, 128(9), 096001.

Castellano, A.V., Cancio, J.L., Aleman, P.S., Rodriguez, J.S., 2003. Polycyclic Aromatic Hydrocarbons In Ambient Air Particles In The City Of Las Palmas de Gran Canaria. Environment International, 29, 475-480.

Esen, F., Vardar, N., et al. (2008). Atmospheric concentrations of PAHs, their possible sources and gas-to-particle partitioning at a residential site of Bursa, Turkey. Atmospheric Research, 88(3-4), 243-255. Uludağ Üniversitesi

Gaga, E., O., 2004, "Investigation of Polycyclic Aromatic Hydrocarbon (PAH) Deposition in Ankara, The Graduate School of Natural and Applied Sciences, Middle East Technical University, Doktora Tezi, Ankara.

Jariwala, N., Patel, J., & Gajjar, P. (2021). Atmospheric transformation of PAHs and their radiative impacts: A review. Science of the Total Environment, 778, 146132.

Khan, M. B., Ding, X., & He, Q. (2021). Source apportionment of PM2.5-bound PAHs from anthropogenic and natural emissions: Implications for air quality and health risks. Environmental Pollution, 279, 116898.

Kılıç E. (2008). Bayburt İli Hava Kalitesinin Değerlendirilmesi. Atatürk Üniversitesi Fen Bilimleri Enstitüsü, Yüksek Lisans Tezi, Erzurum, Türkiye.

Khan, M. B., Ding, X., & He, Q. (2021). Particle-bound PAHs: Atmospheric measurement, source apportionment and implications for health. Environmental Pollution, 279, 116898.

Mu, Q., Zhang, Y., & Xu, H. (2022). Long-range transport and atmospheric fate of particle-bound PAHs: Implications for air quality and climate. Environmental Pollution, 311, 119962.

Lodovici, M., Venturini, M., Marini, E., Grechi, D., Dolara, P., "Polycyclic aromatic hydrocarbons air levels in Florence, Italy, and their correlation with other air pollutants", Chemosphere, 50, 377-382, 2003

Perera, F., Wang, S., Vishnevetsky, J., Zhang, B., Cole, K. J., Tang, D., ... & Rauh, V. (2022). Prenatal exposure to airborne PAHs and child development: Updated evidence from cohort studies. Environmental Science & Technology, 56(7), 4232-4240.

Paloluoğlu C. (2016). Erzurum'da Çeşitli Örnekleme Yöntemleri Kullanılarak Farklı Ortamlarda Poliklorlu Bifenillerin (PCB'ler) Konsantrasyonlarının Belirlenmesi. Doktora Tezi, Atatürk Üniversitesi Fen Bilimleri Enstitüsü, Erzurum, Türkiye.

Paloluoğlu C. (2008). Erzurum şehir merkezinde polisiklik aromatik hidrokarbonların (PAH'ların) konsantrasyonlarının alansal dağılımı, Atatürk Üniversitesi Fen Bilimleri Enstitüsü, Yüksek Lisans Tezi, Erzurum, Türkiye, 2008.

Sharma, S., Chylek, P., & Andrews, E. (2020). Black carbon deposition and its role in Arctic surface warming: Interactions with PAH-rich aerosols. Atmospheric Chemistry and Physics, 20(15), 9103-9120.

Shen, G., Tao, S., Wang, R., & Yang, Y. (2022). Emission and analytical characteristics of PAHs from combustion sources. Environmental Science & Technology, 56(3), 1512-1523.

Sofowote, U., Su, Y., & Krysik, M. (2020). Regional and long-range atmospheric transport of particulate PAHs: Evidence from receptor modeling. Atmospheric Environment, 229, 117452.

Taşdemir, Y., ve Payan F. 1999. Atmosferik çökelme örneklerinin toplanması. Türkiye' de Çevre Kirlenmesi Öncelikleri Sempozyumu cilt.1., 552-560.

Xiong, Q., Li, X., Zhou, Y., & Zhang, Y. (2023). PM2.5-bound PAHs exposure and epigenetic alterations during pregnancy: Implications for maternal-fetal health. Science of the Total Environment, 858, 160036.

Yang, Y., Lee, S. C., & Choi, S. D. (2023). Transboundary movement of PM2.5-bound PAHs and their deposition in remote environments. Environmental Science & Technology, 57(12), 4821-4830.

Yang, L., Wang, X., & Zhang, Y. (2021). Exposure to atmospheric particulate matter-bound polycyclic aromatic hydrocarbons and associated health risks. International Journal of Environmental Research and Public Health, 18(4), 2177. MDPI

Yin, H., Li, X., & Lu, S. (2023). Wildfire-driven emissions of PAHs under a warming climate: Trends and implications. Environmental Science & Technology, 57(4), 2143-2152.

Zhang, Y., Mu, Q., & Xu, H. (2020). Particle-gas partitioning of PAHs and its implications for atmospheric transformation processes. Atmospheric Environment, 224, 117316.

Zhao, Y., Chen, G., Zhang, Z., & Liu, W. (2021). Oxidative stress and DNA damage induced by particle-bound PAHs: A mechanistic review. Chemosphere, 271, 129540.

Zhao, G., et al. (2019). Role of black carbon mass size distribution in the direct aerosol radiative forcing. Atmospheric Chemistry and Physics, 19(20), 13175-13192. ACP

Chapter 10

SMART MILITARY GARMENTS

Makbule FİDAN[1], *Mihriban KALKANCI* [2]

---

[1] Graduate School of Natural and Applied Sciences, Department of Advanced Technologies, Pamukkale University, Turkey. ORCID: https://orcid.org/0009-0004-0134-9527

[2] Denizli Vocational School of Technical Sciences, Pamukkale University, Turkey, (ORCID: https://orcid.org/0000-0003-3287-1428)

1. Introduction

The evolving structure of contemporary military operations, coupled with increasingly technology-driven threat environments, has rendered traditional equipment inadequate for ensuring the operational efficiency and survivability of security forces. Modern battlefields demand not only physical resilience but also rapid, data-supported decision-making capabilities. Accordingly, military uniforms are no longer expected to function merely as protective garments; rather, they are transforming into multifunctional platforms integrated with advanced sensors, communication modules, and data-transfer infrastructures. Building upon the conceptual model titled "Smart Military E-Outfit of the Future," this study provides a comprehensive examination of wearable technologies employed in military applications, focusing on their technical architecture, operational roles, advantages, limitations, and developmental trajectory in Türkiye. Supported by recent scholarly research, the analysis aims to elucidate the emerging strategic importance of smart textile systems in future military doctrines [1–3].

The transformation underway in the defense sector has not been limited to heavy weaponry or air-defense systems; it has also initiated a significant paradigm shift in individual soldier equipment. The relevance of wearable technologies in military contexts has increased in parallel with the growing emphasis on information sharing, physiological monitoring, and situational awareness in modern warfare. Smart textiles, incorporating microsensors, conductive fibers, embedded microprocessors, and advanced energy-management components, enable seamless interaction with the surrounding environment and facilitate data-driven operational behavior [4].

Projects such as the "Smart Military E-Outfit of the Future" exemplify the potential of these systems to enhance the effectiveness, protection, and decision-making capabilities of military personnel. Current literature increasingly addresses issues such as system design principles, field-level performance evaluations, ergonomic optimization, and cost-effectiveness analyses, reflecting the expanding role of such technologies in national defense strategies [5]. In Türkiye, the development of military wearable systems has accelerated through sustained R&D investments by defense industry organizations, strengthening the country's technological capacity in this domain [6].

Military smart garments represent an advanced class of technological textiles designed to enhance soldier survivability and operational adaptability in modern combat environments. These garments are integrated with power management units, enabling prolonged operation under low-energy conditions. The strategic potential of such systems is expected to expand significantly in both national and international defense frameworks [1].

Equipped with high-precision sensors, smart garments monitor a range of physiological and positional parameters, including body temperature, heart rate, and spatial location. Empirical studies indicate that the integration of these systems enhances individual soldier resilience and contributes to real-time command-and-control decision-making processes [5]. Data collected by these sensors are transmitted wirelessly to centralized platforms, allowing continuous monitoring of personnel status. Despite these advantages, challenges such as high production costs, limited battery endurance, and vulnerability to environmental stressors remain significant constraints [2]. Furthermore, ensuring data security is critical for the broader operational deployment of these systems [3].

In Türkiye, defense industry leaders such as ASELSAN are actively developing indigenous solutions and striving to integrate them into existing military frameworks [6]. Collaborative initiatives with academic institutions have facilitated the convergence of advanced design, health monitoring, and communication technologies into cohesive wearable platforms, demonstrating both technological feasibility and operational relevance [7,8].

2. Smart Garments

Smart garments are textile products equipped with electronic components that can interact with the user, sense environmental conditions, and respond accordingly. These garments typically incorporate sensors capable of monitoring physical parameters such as temperature, pressure, and humidity, communication modules for data transmission, and, in some cases, actuators that provide feedback or responses [4].

In a military context, smart garments are defined as wearable systems that continuously monitor soldiers' health status, positional information, and environmental threats, transmitting this data to centralized command centers in real time [1]. The primary goal of these systems is to ensure maximum comfort and safety for the user while enhancing operational effectiveness. Most smart garments are textile-based, offering lightweight, flexible structures that do not restrict mobility and can be worn over extended periods without compromising comfort [5].

The integration of such technologies into military apparel enables real-time monitoring of soldiers' physiological conditions, which allows for faster intervention in life-threatening situations and improved overall mission performance [2]. By combining wearable sensors, communication modules, and ergonomic textile design, smart military garments represent a significant advancement in modern soldier systems, bridging the gap between protection, situational awareness, and operational support.

The development of smart textile technologies began in the 1980s, driven by the miniaturization of electronic circuits and the proliferation of mobile communication systems. In the initial stages, these technologies were largely experimental in the fields of medicine and sports, with simple wearable sensors designed to measure physiological data being developed as prototypes [3].

By the 1990s, specialized projects for military applications began to emerge. During this period, the U.S. military initiated research on sensor-integrated uniforms, with institutions such as DARPA serving as early investors in this field [4]. From the 2000s onward, rapid technological advancements diversified smart textile applications. Integrated systems in garments evolved from simple monitoring functions to active roles, including alerting and defensive capabilities. For instance, impact-resistant fabrics, thermal sensors, and wireless communication modules were progressively incorporated into military uniforms [2].

In recent years, these technologies have become more accessible through collaborations between civilian and defense industries, with countries increasingly focusing on domestic production through intensive R&D activities. In Türkiye, institutions such as ASELSAN and TÜBİTAK have supported the development of indigenous military smart garment prototypes [6,7].

3. Technical Aspects of Smart Military Garments

Smart military garments are highly specialized uniforms that integrate a variety of sensors designed to collect both physiological and environmental data from soldiers in real time. These garments continuously monitor vital signs such as heart rate, body temperature, and positional information, transmitting the collected data via wireless systems to centralized command centers for immediate analysis. This continuous monitoring enables commanders to assess the health status and operational readiness of soldiers, as well as to respond promptly to emerging threats or environmental hazards [1].

Some advanced smart military garments are also equipped with additional functionalities, including the detection of chemical, biological, radiological, or nuclear (CBRN) hazards, as well as energy harvesting capabilities, which allow the garments to partially self-sustain their power needs. By integrating these technologies, smart military garments go far beyond the protective and functional capabilities of traditional uniforms, providing real-time data acquisition, analysis, and communication functions that are critical for enhancing operational effectiveness and soldier safety.

Figure 1 provides a detailed representation of protective smart textiles employed in military applications, highlighting the integration of multiple functional components within a single garment. Embedded **physiological sensors**, strategically positioned throughout the fabric, continuously monitor vital signs such as heart rate, respiration, body temperature, and muscle activity, enabling commanders to assess soldiers' health and readiness in real time. **Environmental sensors** are also embedded to detect external threats, including toxic gases, radiation levels, humidity, temperature extremes, and other hazardous conditions that may compromise mission safety.

The figure also illustrates the use of **conductive fibers and interwoven circuits**, which facilitate seamless data transmission from sensors to integrated communication modules without restricting mobility or comfort. These fibers act as both signal pathways and power conduits, connecting energy sources such as **flexible batteries or energy-harvesting modules** that convert solar, kinetic, or thermal energy into usable power for the garment's electronics. Some garments additionally incorporate **actuators or haptic feedback devices**, which can provide real-time alerts to the wearer, such as vibration warnings in response to environmental hazards or physiological anomalies.

Collectively, these integrated components demonstrate the multifunctional nature of modern smart military textiles. They exemplify how advanced material design, electronic integration, and ergonomic considerations converge to create uniforms that are not only protective but also enhance situational awareness, operational decision-making, and overall soldier performance [11].

Figure 1. Protective Smart Textiles [13]

3.1. Energy Management and Power Sources

The electronic components used in smart garments require reliable energy sources, which are typically provided by integrated batteries and renewable energy systems. Solar panels and kinetic energy harvesting mechanisms convert soldiers’ movements into usable power, thereby extending the operational lifespan of the garments [2]. However, energy storage capacities remain limited, and environmental factors such as extreme temperatures, humidity, and dust can negatively affect battery performance. Therefore, the optimization of energy management systems is critical to ensuring the field effectiveness of smart garments [5].

3.2. Data Security and Privacy

Data security is of paramount importance in military operations. If information transmitted wirelessly from smart garments falls into the wrong hands, operational security may be compromised [1]. To mitigate these risks, encryption algorithms, secure communication protocols, and data anonymization techniques are employed. Additionally, preventive measures against cyberattacks ensure both the privacy of soldiers and the integrity and accuracy of operational data [2].

3.3. Integration and System Compatibility

Smart military garments are designed to operate as part of a broader military communication and control infrastructure. This integration enables real-time transmission of health, positional, and environmental data to command centers [5]. Compatibility with multiple systems ensures continuous information flow during operations, enhances coordination among field personnel, and supports rapid decision-making and risk mitigation [1].

3.4. User Experience and Ergonomics

Smart military garments must be designed to maximize comfort and mobility. Lightweight, flexible, and breathable materials prevent fatigue during extended use [2]. The placement of sensors and electronic components must avoid restricting movement or causing discomfort. Ergonomic design not only improves operational efficiency but also enhances user satisfaction and adoption [5].

3.5. Future Perspectives and Research Directions

Future developments in smart military garments are expected to include AI-assisted data analysis, advanced biomedical sensors, and nanotechnology-based materials [5]. Research is increasingly focused on autonomous energy generation, wireless charging systems, and self-healing fabrics. These innovations will enhance soldier safety while significantly improving operational flexibility [2].

3.6. Application and Training Processes

Effective deployment of smart military garments requires that personnel are fully trained in the use of these technologies. Therefore, specialized training programs and field trials are conducted [1]. Training encompasses technical operation of the garments, sensor utilization, and data security protocols. Practical exercises and simulations are also organized to ensure seamless integration into operational scenarios, maximizing the effectiveness of the technology in real-world conditions [2].

4. Examples of Smart Military Garments

- **Smart Military E-Outfit of the Future**: This garment is equipped with sensors that monitor body functions and wireless communication systems. Its solar-powered battery enables extended operation, while real-time data are transmitted to command centers, allowing continuous monitoring of soldiers’ status [1].

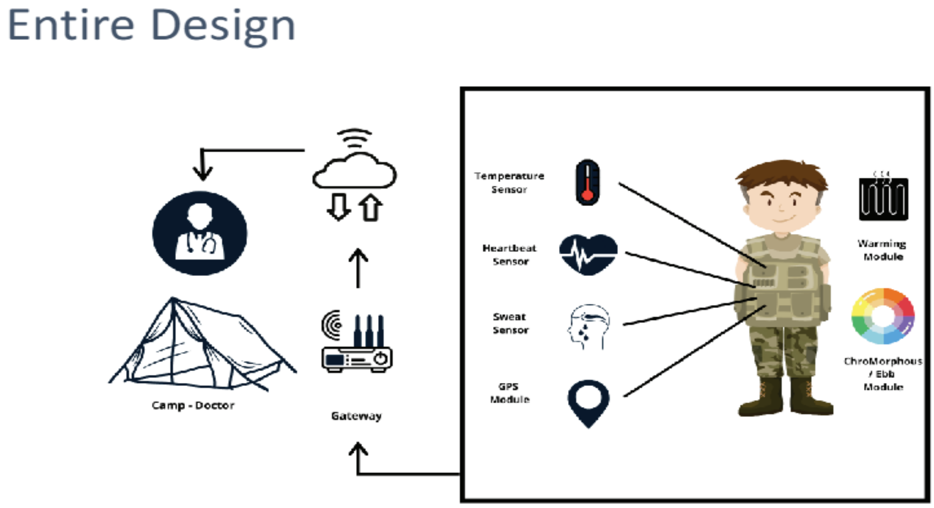

Figure 2. Smart Military E-Outfit of the Future Design [12].

- **FELIN (France)**: Developed by France, this system includes specialized helmets, uniforms, and communication equipment for soldiers. Health data, environmental information, and tactical data are collected and integrated into a unified platform.

- **ASELSAN Smart Uniform**: Developed by ASELSAN, this smart garment measures soldiers' biometric data such as heart rate, body temperature, and humidity, transmitting the information to command centers via wireless networks and providing alerts in critical situations [6]. Additionally, the **CENKER Soldier System** has been developed to integrate with smart garments, offering wearable military technology that combines command and control, communications, reconnaissance-surveillance, and situational awareness capabilities in a single platform. This system provides soldiers with real-time tactical information and enhanced battlefield awareness [9].

Figure 3. ASELSAN CENKER [6,9]

- **NATO Soldier System Integration (SSI)**: NATO's SSI integrates helmet, vest, and communication devices into a single uniform, enabling real-time monitoring of soldiers' status.
- **U.S. Army Smart Garments**: The U.S. Army is developing smart uniforms that monitor health and provide ballistic protection. Some prototypes also include advanced features such as wound detection and drug delivery.

Figure 4. U.S. Army Smart Jacket [11].

5. Advantages and Operational Challenges of Smart Military Garments

Smart military garments provide the capability to monitor soldiers' health and environmental conditions in real time. This enables immediate detection of critical situations and rapid response, creating life-saving effects [1]. Additionally, these garments enhance operational efficiency; environmental hazards such as toxic gases or radiation can be detected early, minimizing associated risks [2]. Integrated energy sources allow prolonged usage, supporting operational continuity. Communication and location-tracking features further improve coordination and soldier safety [5]. These technologies also reduce the equipment burden on soldiers, enhancing mobility and overall mission performance.

However, the high costs of smart garments may limit their widespread adoption [2]. The complexity of technological components increases maintenance and repair requirements. Electronic components are sensitive and may fail under harsh field conditions, such as extreme temperatures, humidity, or mechanical shocks [1]. Energy sources are limited, making continuous long-term operation challenging, particularly for renewable energy systems like solar power, which depend on environmental conditions. Furthermore, concerns regarding privacy and data security are critical. Wireless communication systems can be vulnerable to cyberattacks, potentially compromising operational security [5].

6. Smart Military Garments in Türkiye

Turkey has made substantial investments in smart military garment technologies as part of a strategic initiative to reduce foreign dependency in the defense industry and to enhance domestic production capabilities. This approach not only aims to strengthen technological self-sufficiency but also to bolster national defense and security capabilities. ASELSAN, as one of the leading institutions in this field, develops advanced smart garment systems specifically designed to meet the operational requirements of soldiers in the field. These systems integrate critical functionalities such as health monitoring, environmental surveillance, situational awareness, positional tracking, and communication into a unified platform, thereby significantly improving soldier safety and operational effectiveness [9]. For instance, under the *Smart Soldier Uniform* project, garments equipped with biometric sensors continuously monitor vital signs including heart rate, body temperature, and movement patterns, transmitting this information in real time to command centers. This enables commanders to track the health and operational status of soldiers instantaneously and to implement rapid interventions in critical situations.

Research and development activities in Turkey have extended beyond sensor and communication technologies to include the enhancement of textile materials used in these garments. Nanotechnology-reinforced fabrics, which are lightweight, durable, and resistant to harsh environmental conditions, have been a primary focus [10]. These materials not only provide physical protection against external threats but also offer additional operational support functionalities, such as thermal regulation, impact resistance, and integrated energy management systems. Smart garments provide significant advantages for units engaged in tactical operations, including ground forces, special operations units, and security teams. Moreover, applications are being explored for civilian defense, disaster response, and border security teams, demonstrating the versatility and strategic value of these technologies.

Overall, Turkey's technology-oriented approach and investment in domestic production have enhanced the country's defense industry autonomy while contributing to broader strategic security objectives. Indigenous smart military garment systems directly improve the effectiveness of national defense policies, ensuring that soldiers on the field are better protected and operationally empowered. Looking ahead, the integration of nanotechnology, artificial intelligence-enabled data analytics, and advanced energy management solutions is expected to further expand the functional capacity and strategic impact of smart military garments in Turkey [9,10].

7. Conclusion

In the defense industry, smart military garments are critical technological innovations developed to enhance soldier safety and operational efficiency in modern combat environments. Equipped with advanced sensors and communication systems, these garments allow real-time monitoring of soldiers' health, location, and environmental risks, transmitting data instantaneously to command centers. This capability enables rapid field response and effective coordination, positively influencing mission success.

However, factors such as high costs, limited energy resources, environmental challenges, and data security concerns present significant limitations to widespread deployment. In Türkiye, R&D efforts by ASELSAN and other domestic defense industry organizations have achieved substantial progress, with locally produced smart garment projects contributing to the reduction of foreign dependency. Innovations such as nanotechnology-reinforced durable materials and integrated energy management systems ensure prolonged field performance. Future integration of AI-assisted analysis systems, self-healing materials, and autonomous energy generation is expected to further enhance the functionality of smart military garments.

In conclusion, smart military garments exemplify a tangible application of technological advancements in defense, playing a critical role in safeguarding soldiers' lives and improving operational effectiveness. Continued investment and technological development in this area will facilitate broader adoption of these systems within national and international security strategies.

REFERENCES

1. Scataglini, S., Andreoni, G., Gallant, J. (2018, June). Smart clothing design issues in military applications. In International Conference on Applied Human Factors and Ergonomics (pp. 158-168). Cham: Springer International Publishing.
2. Karpagam, K. R., Saranya, K. S., Gopinathan, J., Bhattacharyya, A. (2017). Development of smart clothing for military applications using thermochromic colorants. The Journal of The Textile Institute, 108(7), 1122-1127.
3. Mondal, S., Adak, B., Mukhopadhyay, S. (2023). 11 Functional and smart textiles for military and defence applications. Smart and functional textiles, 397.
4. Stoppa, M., & Chiolerio, A. (2014). Wearable electronics and smart textiles: A critical review. Sensors, 14(7), 11957–11992.
5. Jadhav, R., Deshmukh, S., & Kale, P. (2023). Wearable military smart clothing: An overview. Defence Technology Review, 17(3), 212–229.
6. ASELSAN. (2021). Akıllı Asker Üniforması Projesi. https://www.aselsan.com.tr/
7. Sahin, O., Kayacan, O., Bulgun, E. Y. (2005). Smart textiles for soldier of the future. Defence Science Journal, 55(2), 195.
8. Krishnaswamy, S., Nambissan, V. D., Jeyaraj, A., Raguraman, K. G., & Gummadi, S. N. (2024). A multifunctional smart fabric based on reduced graphene oxide for next generation military couture. Diamond and Related Materials, 150, 111669.
9. ASELSAN. (2022). https://www.aselsan.com.tr/
10. Kara, Ş., Yeşilpınar, S., Arslan, M. (2021). A survey and design study of a protective cycling top wear. Fibres and Textiles in Eastern Europe, 28(1), 31–45.
11. Kiron, M. I. (2021). *Applications of smart textiles for protective purposes*. Textile Learner. https://textilelearner.net/applications-of-smart-textiles-for-protective-purposes/
12. M. S. H, D. N and A. M, "Smart Military E-Outfit of the Future," *2022 IEEE Delhi Section Conference (DELCON)*, New Delhi, India, 2022, pp. 1-7, doi: 10.1109/DELCON54057.2022.9752954.
13. https://www.maxim.com/gear/ceradyne-ihps-ballistic-helmet-2018-3/?utm_source

Chapter 11

THE EFFECT OF SUPERCRITICAL WATER CONDITIONS IN UPGRADING OF OPIUM ALKALOID WASTEWATER

Nihal Cengiz[1], *Levent Ballice*[2] , *Mehmet Sağlam*[3]

---

[1] Ege University, Engineering Faculty, Department of Chemical Engineering, 35100 Bornova, İzmir, Turkey, E-mail address: nihal.cengiz@ege.edu.tr, ORCID: 0000-0002-6572-7046

[2] Ege University, Engineering Faculty, Department of Chemical Engineering, 35100 Bornova, İzmir, Turkey

E-mail address: levent.ballice@ege.edu.tr, ORCID: 0000-0002-3137-1352

[3] Ege University, Engineering Faculty, Department of Chemical Engineering, 35100 Bornova, İzmir, Turkey

E-mail address: mehmet.saglam@ege.edu.tr

Ege University Graduate School Of Natural And Applied Sciences

Title of the Thesis: Treatment Of Industrial Wastewaters By Utilizing In Energy (CH4/H2) Production Via Hydrothermal Gasification

Author: Nihal Cengiz

Supervisor: Prof. Dr. Levent Ballice,

Co-Supervisor: Prof. Dr. Mehmet Sağlam

Department of Chemical Engineering

Bornova, İzmir, 2017

1. Introduction

Alkaloid definition made by Pelletier is given as "Alkaloid is a cyclic compound containing a nitrogen in a negative oxidation state which is of limited distribution in living organisms (S.W. Pelletier, 1996)." Alkaloids are produced from various types of plants but most common, opium poppy capsule is used since it has high content and variety of alkaloids. Opium poppy plant (Papaver somniferum) is processed to obtain, opium and poppy straw as raw materials. Morphine is extracted with water-lime solution then with organic solvents and acid. Wastewater is generated at an amount of 27.5 m^3/h during the recovery of the toluene, alcohol groups, etc (Özdemir, 2006).

Alkaloids such as morphine, thebaine, codeine and oripavine are extracted from opium and poppy straw basicly. (INGB, 2016). Approximately 12,000 known alkaloids, depending on their biological activity, are used as pharmaceuticals, stimulants, narcotics and poisons (Gürkök, T., Parmaksız İ., Boztepe G., 2010). Turkey is one of the leader country in alkaloid manufacturing sector and Australia, Spain, France, Hungary, India are the other largest manufacturers. Opium processing wastewater from Afyon/Turkey plant were characterized by some researchers, treatment plant authorities and characteristics were given in Table 1. This dark-brown and resistant to biodegradation wastewater has some non-extracted alkaloids in its raw form according to GC-MS analysis (Cavit B. Bural, 2008) and has some compounds in addition to alkaloids of morphine, codeine, 7 aminoclonezepam, Diltiazem and THC-COOH (Cengiz et al., 2017). It has high COD that is mainly soluble and includes acetic acid as major, high BOD contents and low pH value (Aydin et al., n.d.). Aniline, toluol (Kaçar et al., 2003), phytin, cellulose and wax type materials (Aydin et al., 2010) were the compounds reported as pollutants in this wastewater. Two-stage activated sludge treatment unit of alkaloid factory did not operated properly shortly after installation due to unrestrained temperature rise in the aeration tank (Koyuncu, 2003). Wastewater generated has been discharged by dilution into Lake of Eber near the plant and caused a serious environmental problem with other factories in the region.

In Marmara Research Center, TÜBITAK, (H. Kınlı, 1994) treatability studies of the pretreated form of opium processing wastewater were done by adsorption with activated carbon, diatomite and perlite in 1994, but not considerable results were obtained. They also investigated coagulation of pollutants with $Al_2SO_4.18H_2O$ (alum), $FeCl_3$, $Fe_2(SO_4)_3$ and $FeSO_4.7H_2O$ and best removal efficiencies were achieved with alum, $Fe_2(SO_4)_3$ and $FeCl_3$. Effluent COD was lowered to 550-600 ppm from initial COD of 1000 ppm by 40-45% efficiency which is not much effective (Turkish Atomic Energy Authority, 2011). Wet air oxidation is proposed as a pretreatment in the study of Kaçar et al. (Kaçar et al., 2003) and they investigated operating conditions such as temperature, pressure, pH, etc. Experimental finding shows that 26% COD removal was obtained at 150°C and 0.65 MPa with 2.0 h of reaction time. Catalytic wet air oxidation (CWAO) was used in the study of Aytimur et al. (Aytimur & Atalay, 2004) as chemical treatment and activated sludge technique as biological treatment for alkaloid wastewater. In CWAO, the catalyst used was $FeCl_2.4H_2O$ (Ridel—de Haén). Anaerobic processes were preferred by some researchers to raw wastewater (Aydin et al., 2010; Kunukcu & Wiesmann, 2004; Sevimli et al., 1999) due to COD content of this wastewater is soluble and biodegradable in a high ratio as reported. Bural et al. (Cavit B. Bural, 2008) applied aerobic biological treatment after an anaerobic pretreatment of wastewater since it has organic substances in a significant amount and aerobic process cannot achieve treatment directly, alone. Kunukçu et al. compared aerobic and anaeorobic digestion and dissolved oxygen demand are measured to observe the removal efficiencies and they are found that aerobic biological treatment is more efficient with 75.3 % and anaerobic digestion and WAO process have lower degradation activity (39.7 % and 25.7% COD removals, respectively) (Kunukcu & Wiesmann, 2004). Özdemir used diluted forms of Afyon alkaloids wastewater with COD contents of 2400, 6000 and 9600 mg/L. The highest anaerobic treatment efficiency of 77% was achieved in BM included (biochemical methane) reactor with the inlet COD content of 9600 mg/L. The effect of gamma rays was also investigated and the treatment speed was found higher with irradiated wastewater has an initial COD of 25 g/L (Özdemir, 2006).

In the study of Koyuncu (Koyuncu, 2003), Ultrafiltration (UF), Nanofiltration (NF) and Reverese osmosis (RO) experiments were done with the effluent of opium processing wastewater treatment plant with a COD content of 1900-2000 mg/L and 950 mg/L. Complete color removal and high COD and conductivity removals were accomplished with all types of NF and RO membranes and they suggest this method as advanced treatment of this wastewater. Gasification/oxidation of wastewaters in supercritical water medium is a new option in treatment purpose. Various industrial wastewaters such as black liquor (Sricharoenchaikul, 2009), olive mill wastewater (Casademont et al., 2017; Kıpçak & Akgün, 2017), chemical plant wastewater (Lee & Ihm, 2010; Shin et al., 2009), copper wastewater (Chen et al., 2018), coking wastewater (Jiang et al., 2017), and organic industrial wastewaters (García Jarana et al., 2008) are commonly investigated to produce biofuel such as hydrogen/methane and to destruct organic pollutant constituents.

All of the studies show that enough level of treatment of this wastewater from Afyon Alkaloids Plant was hard because of its complex structure and high resistant to treatment. Possibly for this reason, by disregarding the polluting of the environment, discharge COD limit in 1995 is excessively increased in 2004 regulation from 250 to 1500 ppm (Ministry of Environment and Forestry, 2004) as shown in Table 2. There was no research reported in literature on the utilization of this wastewater, from Afyon Alkaloids Plant which is a specific industry, for energy production. Hydrogen and methane which are used as clean energy sources will be produced by upgrading of alkaloid wastewater via supercritical water gasification as the first time.

2. Materials and Methods

2.1 Feedstock and catalyst

Wastewater obtained from the Opium Alkaloids Plant in Afyon, Türkiye, was used as the feedstock. The influent wastewater had a COD of 35,000 mg O_2/L and a TOC of 15,000 mg/L, as determined by in-house analyses. Prior to use, the samples were only mixed to ensure homogeneity and reproducibility, without any filtration. Potassium carbonate (K_2CO_3, 99.0% purity, Sigma-Aldrich) was employed as the catalyst.

Experimental Procedure

Supercritical water gasification (SCWG) experiments were conducted in a stainless-steel batch autoclave reactor equipped with an electric heater. The reactor, previously described in detail elsewhere, has an internal volume of 100 cm^3 and is designed to operate at temperatures up to 650°C and pressures up to 50.0 MPa. Experiments were performed at 400, 500, and 600°C under corresponding pressures of 23.0–46.0 MPa. For each run, 15 mL of wastewater was loaded into the reactor, and K_2CO_3 was added in amounts ranging from 0.125 to 0.625 g.

After sealing, the reactor was purged with nitrogen to remove air and heated at a rate of 8–10 K/min to the target temperature, which was maintained for 1 h using a PID controller. Upon completion, the reactor was cooled to ambient temperature using electric fans. The produced gas volume was measured with a gasometer and sampled using gas-tight syringes for chromatographic analysis. The reactor contents were washed with water to collect aqueous and solid products, which were then separated by filtration. The aqueous phase was acidified to pH ≈ 2 using concentrated sulfuric acid to suppress organic acid ionization, while the solid residue was dried at 105°C for 24 h prior to weighing.

Product Analysis

The gaseous products (H_2, CO_2, CO, CH_4, and C_2–C_4 hydrocarbons) were analyzed using gas chromatography with TCD and FID detectors, achieving a standard deviation of ±2%. Calibration was performed using a certified standard gas mixture.

The TOC and COD contents of the raw wastewater and aqueous products were determined using a TOC analyzer and standard COD analysis methods. Additionally, LC/MS-MS analyses were conducted on the raw wastewater and aqueous products (without catalyst) to identify compounds degraded during gasification, following solvent extraction and sample preparation procedures reported previously.

The TOC content of the solid residues was measured using the solid sample module of the TOC analyzer.

Carbon gasification efficiency (CGE, %) = $\dfrac{\sum_i n_i C_i \dfrac{PV_{gas}}{RT} M}{V_{feed}\, TOC_{ww}} x100$

Total Organic Carbon Removal Efficiency (TOCRE, %) = $\dfrac{TOC_{ww} - TOC_{aq}}{TOC_{ww}} x100$

Chemical Oxygen Demand Removal Efficiency (CODRE, %) = $\dfrac{COD_{ww} - COD_{aq}}{COD_{ww}} x100$

3. Results

SCWG experiments were carried out with and without K_2CO_3 catalyst at temperatures between 400 and 600°C and pressures of 23.5–45.5 MPa. The effects of reaction temperature and catalyst loading on gas yields, product distributions, carbon gasification efficiency (CGE), total organic carbon removal efficiency (TOCRE), and chemical oxygen demand removal efficiency (CODRE) were systematically investigated. All experiments were conducted in triplicate to ensure accuracy and reproducibility.

Table 1. Discharge limits for opium alkaloid production plants (WPCR, 2004)

Parameter	Unit	Composite Sample (24h)
COD	mg/L	1.500
TKN	mg/L	15
TSS	mg/L	200
pH	-	6-9

Table Hata! Belgede belirtilen stilde metne rastlanmadı**..** Technical specifications taken from the authorities of the wastewater treatment plant (Afyon Alkaloids Plant, 2017, oral interview).

BOD (Biological Oxygen Demand)	7000-17000 mg/L
COD	25000-45000 mg/ L
Temperature	Summer:35-50°C Winter: 26-40°C
TSS (mg/L)	250-3900 mg/L
pH	4-6,5
Total Kjeldahl Nitrogen (TKN-N)	400-850 mg/L
NH_4-N	54-280 mg/L
TP	6-8 mg/L
Sulphate (SO_4)	7000-14000 mg/L
Volatile fatty acid	7000-15000 mg/L
Total hardness	1000-1200 mg $CaCO_3$/L
Ca hardness	1000 mg $CaCO_3$/L
Conductivity	24.0000-30.000 µS/cm
TDS	26.000-33.000 mg/L
Na	4000-7000 mg/L
K	4000-6000 mg/L
Alkalinity	1500-5000 mg/lt ($CaCO_3$)

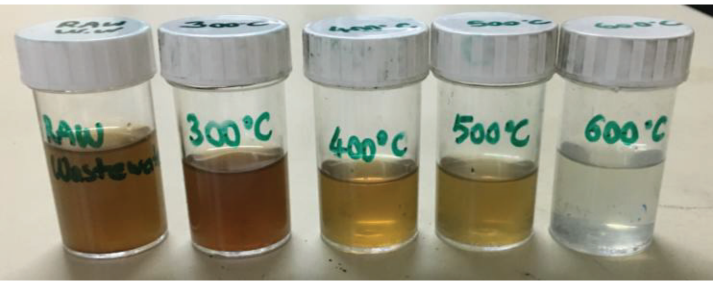

Figure 1. Effect of reaction temperature on the visual appearance of wastewater after SCWG.

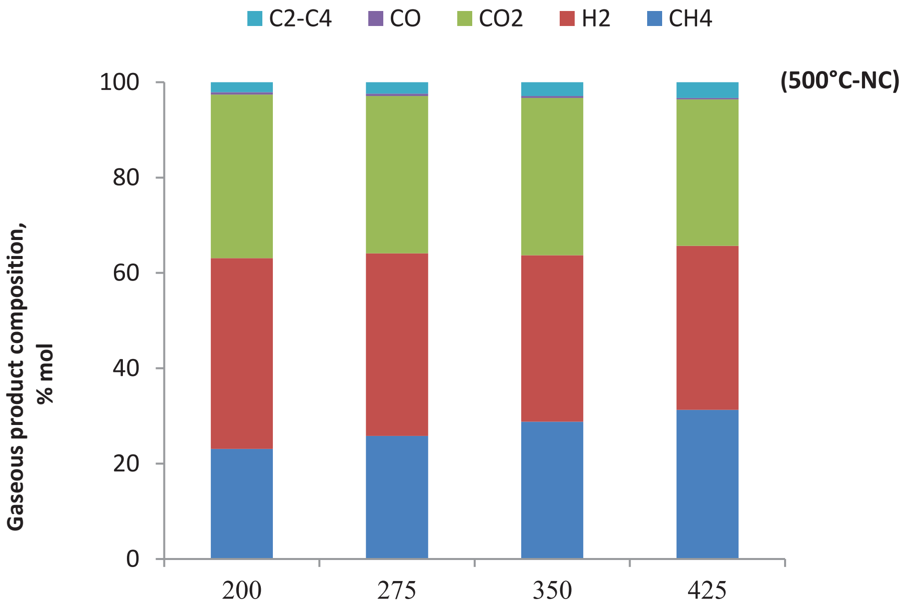

Figure 2. Effect operating pressure on gaseous product distribution in hydrothermal gasification of alkaloid wastewater at 500°C without catalyst.

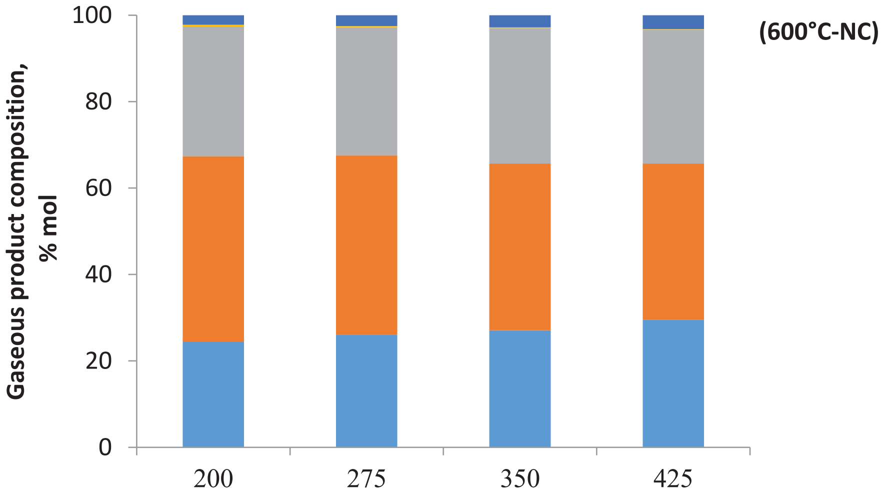

Figure 3. Effect operating pressure on gaseous product distribution in hydrothermal gasification of alkaloid wastewater at 600°C without catalyst.

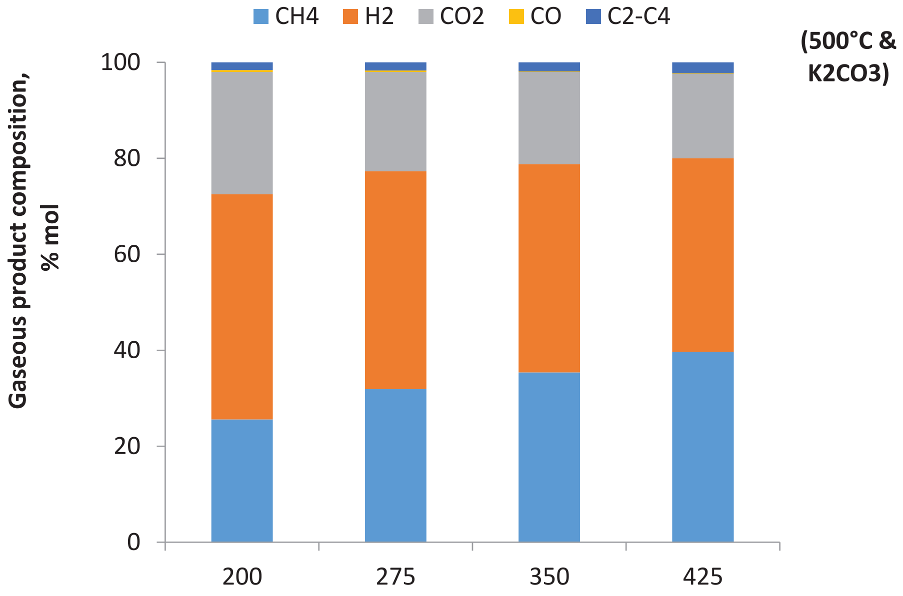

Figure 4. Effect operating pressure on gaseous product distribution in hydrothermal gasification of alkaloid wastewater at 500°C with K_2CO_3 catalyst.

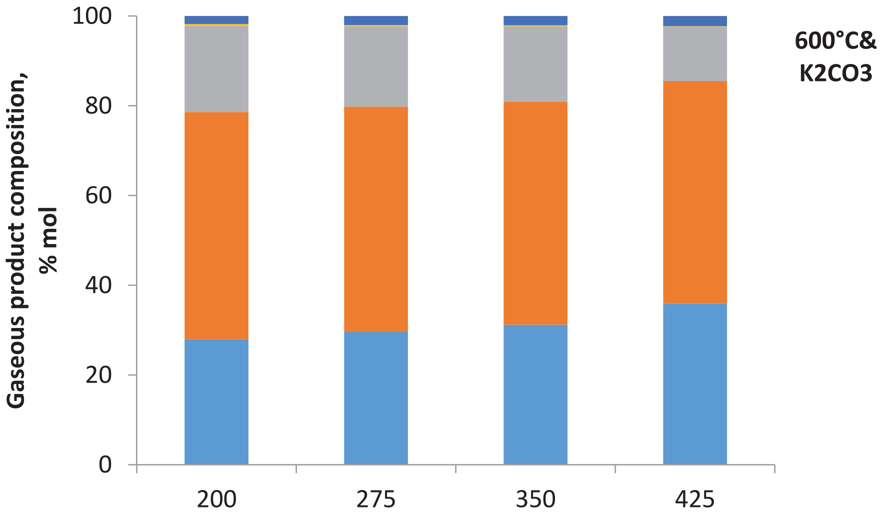

Figure 5. Effect operating pressure on gaseous product distribution in hydrothermal gasification of alkaloid wastewater 600°C with K_2CO_3 catalyst.

Table 3. Reaction conditions and experimental results

Exp Code	***T, °C***	***P, bar***	***Set Pressure, bar***	***Catalyst***	***Volume of wastewater/ catalyst amount***	***Gas product yield (mol gas/kg C in ww)***
AF-T5-P1	500	198	200	-	10 mL/-	76.1
AF-T5-P2	500	270	275	-	12.5mL/-	71.3
AF-T5-P3	500	345	350	-	15mL/-	66.6
AF-T5-P4	500	420	425	-	20mL/-	65.2
AF-T5K-P1	500	198	200	K_2CO_3	10 mL/-	117.2
AF-T5K-P2	500	270	275	K_2CO_3	12.5mL/0.416g	112.1
AF-T5K-P3	500	345	350	K_2CO_3	15mL/0.560g	105.1
AF-T5K-P4	500	420	425	K_2CO_3	20mL/0.666g	96.6
AF-T6-P1	600	209	200	-	8mL/-	97.8
AF-T6-P2	600	270	275	-	10mL/-	94.3
AF-T6-P3	600	372	350	-	12.5mL/-	88.2
AF-T6-P4	600	430	425	-	15mL/-	83.6
AF-T6K-P1	600	197	200	K_2CO_3	8mL/0.266g	140.0
AF-T6K-P2	600	270	275	K_2CO_3	10mL/0.333g	137.5
AF-T6K-P3	600	355	350	K_2CO_3	12.5mL/0.416g	135.2
AF-T6K-P4	600	425	425	K_2CO_3	15mL/0.500g	132.9

4. Discussion

CGE, %	TOC_{RE}, %	COD_{RE}, %
57.7	75.9	71.9
55.9	75.1	76.7
55.5	74.4	80.1
55.1	71.3	83.1
78.0	93.1	83.7
77.0	92.5	81.4
74.9	91.6	88.6
73.1	89.9	89.3
70.8	88.1	84.8
70.3	87.8	90.3
69.4	87.2	89.1
68.7	85.6	87.7
87.5	94.3	86.9
87.2	94.0	91.9
86.8	93.4	93.0
85.8	92.8	95.8

4.1 Influence of Pressure on Gasification of Opium Alkaloid Wastewater

The effect of reaction temperature and pressure on CGE, CLE, gaseous product distribution and yields, TOC, COD content of aqueous product is investigated and given in Table 3. The studied conditions are the pressure range of 200-425 bar, reaction temperatures of 500ºC and 600°C for both catalytic (K_2CO_3) and non-catalytic experiments. The gaseous product yields were given in Fig 2-5. The volume of wastewater and the catalyst amounts were determined to maintain the objected reaction pressures. Pre-experiments were done to provide pressures with a maximum deviation of ±0.5MPa.

Carbon gasification efficiency is slightly decreased by a ratio within 2-3% as increasing pressure while the carbon liquefaction efficiency is increased (3-4%) at 500°C and non-catalytic runs. Similarly, at 600°C pressure enhance liquefaction efficiency and reduced gasification efficiency very slightly. In catalytic pressure effect experiments, trends are similar as in non-catalytic experiments, that pressure effect at 500°C is little more apparent than at 600°C. Temperature increment from 500 to 600°C and catalyst addition promoted gasification and the highest CGE value is reached as 87.5% at 600°C and 200 bars with K_2CO_3. The catalyst use improved CGE from 57.7 to 78% at 500 °C, and at 600°C, 70.8 to 87.5% while it decreased CLE values from 24% to 7% at 500°C and from 11.9 to 5.7% at 600°C at 200 bars. At the other operated pressures, similar variations are observed. The effect of temperature is seen stronger than pressure from the point of gasification. Madenoglu et al. (2013) studied with glucose to determine the best conditions to obtain high valuable gaseous and aqueous products yields and minimum residue. They concluded that CGE increases at high temperatures and low pressures while the temperature is more effective than the effect of pressure on the gaseous product composition. It is explained by dielectric constant of water is significantly lower at high temperatures as it is a little higher at high pressures (Madenoğlu et al. 2013).

In the formation of gaseous and aqueous product, the ionic and radical mechanisms are responsible due to change of density and ionic product. At elevated temperature, decrease in density cause less ionic product and the radical mechanism is enhanced (Dinjus and Kruse 2004). The total produced gas amount is promoted as the temperature goes up from 500 to 600°C from 875 to 1125 mmol/liter while it decreased as the pressure goes up from 200 to 425 bar slightly, 750 mmol/liter at 500°C, 961 mmol/liter at 600°C. The increasing pressure reduced the amount of the produced gas and CGE (by 4-5%) while it promoted CLE at slightly at 500 and 600°C in a previous work of us done with real biomass samples of wood residues (Cengiz et al. 2016). The highest CGE and produced gas was obtained in the HTG of pine tree sawdust at 80.9% and 1238.0 g gas/kg biomass, at 600°C and 20.0 MPa in the presence of K_2CO_3.

Based on literature, K_2CO_3 is one of the most effective catalysts in supercritical water gasification studies. The catalyst enhanced the total gaseous product yield significantly at the ratios of 54% at 500°C and 43% at 600°C. The pressure increase caused a small reduction in the total produced gas amount for catalytic runs also. Chakinala et al. (2010) studied glycerol and microalgae gasification in batch (quartz capillaries) and continuous flow reactors and investigated (Chakinala et al. 2010). They reported that the addition of K_2CO_3 promoted the glycerol gasification efficiency and results higher hydrogen yields catalyzing the water-gas shift reaction.

The gaseous product obtained is mainly composed of H_2, CO_2, CH_4, and a little CO, and C_2–C_4 in HTG of opium alkaloid wastewater at all studied conditions. The molar percentages of the gaseous product (mole/kg C in wastewater) for all cases are given in Figs 2-5. The molar percentage of CH_4 is changed from 23.1 to 31.3% at 500°C and from 24.4 to 29.5% at 600°C in the absence of catalyst as the pressure increases within 200-425 bar range. H_2 molar percentage is varied from 34.4 to 40.0 % at 500°C and 36.2% to 43.0 at 600°C in non-catalytic runs. It shows us, the pressure enhanced methanation reactions while decreasing H_2 formation. Ionic product, Kw affects the reaction mechanism in supercritical water medium and it increases with the increasing pressure or the decreasing temperature. At high K_w values (higher than 10-14), ionic mechanism (hydrolysis) is dominated due to increase of pressure while increasing temperature promotes the pyrolysis (free-radical) reaction. H_2 yield decreases with increasing pressure, but using catalyst increases the H_2 yield from 30.4 to 50.9 mol/kg C in wastewater at 500°C and 200 bars and at 600°C, yield of H_2 increases similarly. The trend is as expected due to supercritical water properties variation as mentioned above.

There is limited number of study on the effect of pressure in hydrothermal gasification of biomass/wastewater. The effect of pressure may be changed according to the studied temperature and the levels of pressure. Since the density variation of free radical and ionic reactions are opposite, the free radical reaction rate decrease with pressure while that of the ionic reactions are promoted with pressure because of higher ionic products at higher densities as shown in Fig. 6 (Basu and Mettanant 2009).

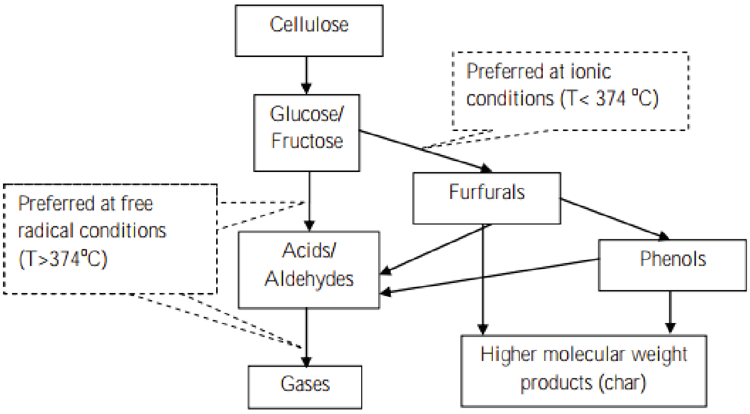

Figure 6. Reaction mechanisms depending on the conditions (Basu and Mettanant 2009).

Demirbas (2004) investigated hydrogen production from fruit shell within 650-750 K and 23-48 MPa, and found that increase in pressure and temperature cause higher hydrogen yields (Demirbas 2004). In contrast, Hao et al. found that hydrogen is slightly higher as the pressure decrease in 0.1 M of glucose gasification (Hao et al. 2003). We found that the pressure has a negative effect on hydrogen yields in the gasification of wood residues within the studied conditions which are same with this experimental part. The highest yields of hydrogen obtained in the presence of K_2CO_3 at 600°C was 27.0 mol/kg for pine tree sawdust and 24.7 mol/kg for fir tree sawdust at the lowest reaction pressures of 20.5 MPa and 20.3 MPa, respectively. Madenoglu et al. (Madenoğlu et al. 2013) stated that the hydrogen and carbon dioxide yields decrease with increasing pressure at constant temperature while methane yield increase. Lu et al. investigated the effect of process parameters (teperature, pressure, and residence time and feedstock concentration) by using orthogonal experimental design method within 3 levels for each parameter. They found that the increasing pressure, H_2 yield, CH_4 yield and CGE have a tendency to increase, and then decreases.

The catalyst addition promoted formation of both CH_4 and H_2 and the sum of the molar percentage of H_2 and CH_4 from 65.8 to % 80.0 % at 425 bar & 500°C and from 65.7 to 85.5% at 425 bar & 600°C. At the same time, CH_4 yield slightly increases by increasing pressure at 500°C using catalyst and without catalyst. CH_4 yield remains almost constant without catalyst as the temperature rises while in catalytic runs it decreases. For maximum H_2 yield, 500°C, 200 bar and K_2CO_3 addition should be selected and to maximize CH_4, 600°C, 425 bar and non-catalytic run should be selected.

Carbon dioxide yields are lowered by the increase of pressure and increased from 500 to 600°C slightly. K_2CO_3 addition has also reduced the CO_2 yield at 600°C while the effect of catalyst at 500°C is not clear, since at 20.0 MPa, it is higher that catalytic run but at 42.5 MPa, it is seen as decreased. CO and C_2-C_4 hydrocarbons yields are very low comparing to H_2, CH_4 and CO_2. The yields of CO are slightly increased by increasing pressure and catalyst addition while the yields of C_2-C_4 hydrocarbons are decreased at high pressures. Temperature is not much effective on C_2-C_4 hydrocarbons yields, slightly decrease with increasing temperature in non-catalytic runs and slightly increase in catalytic runs.

Some valuable researches have been done to evaluate the importance of the parameter in supercritical water gasification (Lu et al. 2006; Madenoğlu et al. 2013; Reddy et al. 2014; Kang et al. 2016). Lu et al. (2006) ordered parameters which effect the gaseous product formation especially hydrogen yields as temperature > pressure > feedstock concentration > residence time. Kang (2016) has investigated different parameters and reported that the order of importance for hydrogen production is: temperature > catalyst loading > catalyst type > biomass type.

4.2 Variation of TOC and COD Removal Efficiencies

TOC (11500 mg/L) and COD (32050 mg/L) content of wastewater lowered by hydrothermal gasification technique successfully in both non-catalytic and catalytic runs at 500 and 600°C and are shown in Table 3. COD removals varied between 71.9-95.8% in this experimental part of the thesis. COD content in the aqueous product decreases with increasing temperature and pressure but temperature is more effective in COD removal. COD decreased from 9000 to 4875 mg/L with 100°C temperature increment at 200 bars while, COD lowered to 5400 mg/L as pressure increases from 20.0 to 42.5 MPa. Catalyst use has a substantial effect since COD is reduced from 9000 to 5225 mg/L at 500°C but this effect is less at 600°C. In the point of process economy, K2CO3 addition provides COD removals at 500°C as high as in 600°C non-catalytic runs and to prefer catalyst addition instead of temperature increase will be reasonable. COD content removal achieved at 95.8% as maximum at 600°C and 42.5 MPa in the presence of K_2CO_3.

TOC content of the aqueous product destructed with a ratio between 71-94% in the studied range of temperature, pressure in non-catalytic and catalytic runs. TOC removal increased at elevated temperatures and lower pressures. The most significant parameter is catalyst addition at 500°C while catalyst promoted TOC removal at 600°C, too. Temperature is also effective and TOC content is lowered from 2770 to 1370 mg/L as the temperature increases from 500 to 600°C and improved removal by a ratio of %12 at 200 bars. At higher pressures, same tendency was observed. The highest TOC removals were reached at 600°C and in the presence of K_2CO_3, pressure effect is not seen clearly in this case but lowest pressure, 20.0 MPa, may be given as the best condition within studied pressure range.

5. Conclusion

- ✓ CGE is slightly decreased as the pressure increasing from 200-425 bar at 500°C and 600°C, and both in non-catalytic and catalytic runs which are carried out in the presence of K_2CO_3.
- ✓ Temperature increment in pressure effect experiments from 500 to 600°C and catalyst addition enhanced gasification and the highest CGE value is reached as 87.5% at 600°C and 200 bar with K_2CO_3.
- ✓ The pressure promoted methanation reactions while affect H_2 formation negatively. H_2 yield decreases with increasing pressure, but using catalyst increases amount of H_2 produced at 500°C and 600°C.
- ✓ For maximum H_2 yield, 500°C, 200 bars and K_2CO_3 addition should be chosen while to maximize CH_4, 500°C, 425 bar and catalytic run should be selected.
- ✓ Carbon dioxide yields are lower at lower pressures and increased slightly as increasing temperature. K_2CO_3 addition has also reduced the CO_2 yield at 600°C while the effect of catalyst at 500°C is not clear.
- ✓ CO and C_2-C_4 hydrocarbons yields are very low comparing to H_2, CH_4 and CO_2. The yields of CO are slightly increased by increasing pressure and catalyst addition while the yields of C_2-C_4 hydrocarbons are decreased at high pressures. Temperature is not much effective on C_2-C_4 hydrocarbons yields.
- ✓ Chemical oxygen demand of the aqueous product lessens at high temperatures and pressures while the effect of temperature is stronger on COD removal.
- ✓ Catalyst use has a substantial effect since COD is reduced from 9000 to 5225 ppm at 500°C and 200 bars with addition of K_2CO_3, but this effect is less at 600°C.
- ✓ In terms of operation cost, catalyst (K_2CO_3) addition provides COD removals at 500°C as high as in 600°C non-catalytic runs. Catalyst addition should be chosen instead of temperature increase to obtain similar treatment efficiency.

Acknowledgments
We gratefully appreciate the financial support of Ege University -Aliye Üster Vakfı and Ege University-EBILTEM (Project No: 16 MÜH 133).

Nomenclature

Ci	concentration of component ‘i’ in the gas product (vol.%)
HTG	hydrothermal gasification
ni	number of carbon atoms of component ‘i’ in the gas product
m	weight of biomass in feed (g)
M	molar mass of carbon (g mol−1)
P	pressure (Pa)
R	universal gas constant. 8.3143 J mol−1 K−1
T	temperature (K)
Vgas	volume of gas product under ambient conditions (L)

TOCaq	total organic carbon content of the aqueous product (g L−1)
TOCww	total organic carbon content of raw alkaloid wastewater (g L−1)
CODww	chemical oxygen demand raw alkaloid wastewater (g L−1)
TOCaq	chemical oxygen demand of the aqueous product (g L−1)

References

Aydin, A. F., Ersahin, M. E., Dereli, R. K., Sarikaya, H. Z., & Ozturk, I. (n.d.). Long-term anaerobic treatability studies on opium alkaloids industry effluents Long-term anaerobic treatability studies on opium alkaloids industry effluents. *Journal of Environmental Science and Health , Part A : Toxic / Hazardous Substances and Environmental*, *April 2013*, 37–41. https://doi.org/10.1080/10934520903429865

Aydin, A. F., Ersahin, M. E., Dereli, R. K., Sarikaya, H. Z., & Ozturk, I. (2010). Long-term anaerobic treatability studies on opium alkaloids industry effluents. *Journal of Environmental Science and Health. Part A, Toxic/Hazardous Substances & Environmental Engineering*, *45*(2), 192–200. https://doi.org/10.1080/10934520903429865

Aytimur, G., & Atalay, S. (2004). Treatment of an Alkaloid Industry Wastewater by Biological Oxidation and / or Chemical Oxidation. *Energy Sources*, *26:7*(April 2013), 661–670. https://doi.org/10.1080/00908310490445607

Casademont, P., García-Jarana, M. B., Sánchez-Oneto, J., Portela, J. R., & Martínez de la Ossa, E. J. (2017). Hydrogen production by catalytic conversion of olive mill wastewater in supercritical water. *The Journal of Supercritical Fluids*. https://doi.org/https://doi.org/10.1016/j.supflu.2017.11.033

Cavit B. Bural. (n.d.). AEROBIC BIOLOGICAL TREATMENT OF OPIUM ALKALOID WASTEWATER - EFFECT OF GAMMA RADIATION AND FENTON'S OXIDATION AS PRETREATMENT. In *THE GRADUATE SCHOOL OF NATURAL AND APPLIED SCIENCES OF MIDDLE EAST TECHNICAL UNIVERSITY*. https://doi.org/10.1017/CBO9781107415324.004

Cavit B. Bural. (2008). *AEROBIC BIOLOGICAL TREATMENT OF OPIUM ALKALOID WASTEWATER - EFFECT OF GAMMA RADIATION AND FENTON'S OXIDATION AS PRETREATMENT*. *August*.

Cengiz, N. Ü., Sağlam, M., Yüksel, M., & Ballice, L. (2017). Treatment of high-strength opium alkaloid wastewater using hydrothermal gasification. *The Journal of Supercritical Fluids*, *130*(February), 301–310. https://doi.org/10.1016/j.supflu.2017.07.003

Chen, Q., Yang, J., Jin, H., & Wang, Y. (2018). Simultaneous treatment of copper wastewater and biomass waste in supercritical water. *The Journal of Supercritical Fluids*, *138*, 143–146. https://doi.org/https://doi.org/10.1016/j.supflu.2018.04.014

García Jarana, M. B., Sánchez-Oneto, J., Portela, J. R., Nebot Sanz, E., & Martínez de la Ossa, E. J. (2008). Supercritical water gasification of industrial organic wastes. *Journal of Supercritical Fluids*, *46*, 329–334. https://doi.org/10.1016/j.supflu.2008.03.002

Gürkök, T., Parmaksız İ., Boztepe G., ve K. E. (2010). Haşhaş (Papaver somniferum L.) Bitkisinde Alkaloid Biyosentez Mekanizması. *BiyoTeknoloji Elektronik Dergisi.*, *1(2)*, 31–45.

H. Kınlı. (1994). *The report of treatability studies of biological wastewater treatment plant effluent of TMO Opium Alkaloids Plant*.

INGB, N. D. T. R. (2016). *Narcotic Drgus*.

Jiang, D., Wang, Y., Zhang, M., Zhang, J., Li, W., & Han, Y. (2017). H2 and CO production through coking wastewater in supercritical water condition: ReaxFF reactive molecular dynamics simulation. *International Journal of Hydrogen Energy*, *42*(15), 9667–9678. https://doi.org/https://doi.org/10.1016/j.ijhydene.2017.03.164

Kaçar, Y., Alpay, E., & Ceylan, V. K. (2003). Pretreatment of Afyon alcaloide factory's wastewater by wet air oxidation (WAO). *Water Research*, *37*(5), 1170–1176. https://doi.org/Pii S0043-1354(02)00448-7\rDoi 10.1016/S0043-1354(02)00448-7

Kıpçak, E., & Akgün, M. (2017). Biofuel production from olive mill wastewater through its Ni/Al 2 O 3 and Ru/Al 2 O 3 catalyzed supercritical water gasification. *Renewable Energy*, 1–10. https://doi.org/10.1016/j.renene.2017.06.075

Koyuncu, I. (2003). An advanced treatment of high-strength opium alkaloid processing industry wastewaters with membrane technology: pretreatment, fouling and retention characteristics of membranes. *Desalination*, *155*(3), 265–275. https://doi.org/Pii S0011-9164(03)00304-7\rDoi 10.1016/S0011-9164(03)00304-7

Kunukcu, Y. K., & Wiesmann, U. (2004). Activated Sludge Treatment and Anaerobic Digestion of Opium Alkaloid Factory. *World Water Congress 2004*.

Lee, I. G., & Ihm, S. K. (2010). Hydrogen Production by SCWG Treatment of Wastewater from Amino Acid Production Process. *Industrial & Engineering Chemistry Research*, *49*, 10974–10980. https://doi.org/Doi 10.1021/Ie100469n

Ministry of Environment and Forestry. (2004). Water Pollution Control Regulation. *Official Newspaper*.

Özdemir, R. T. (2006). *Anaerobic Treatment of Opium Alkaloid Wastewater and Effect of Gamma-Rays on Anaerobic Treatment* (Issue September).

S.W. Pelletier. (1996). *Alkaloids: Chemical and Biological Perspectives*.

Sevimli, M. F., Aydin, A. F., Sarikaya, H. Z., & Ozturk, I. (1999). Characterization and treatment of effluent from opium alkaloid processing wastewater. *Water Science and Technology*, *40*(1), 23–30. https://doi.org/Doi 10.1016/S0273-1223(99)00359-5

Shin, Y. H., Shin, N. C., Veriansyah, B., Kim, J., & Lee, Y. W. (2009). Supercritical water oxidation of wastewater from acrylonitrile manufacturing plant. *Journal of Hazardous Materials*, *163*(2–3), 1142–1147. https://doi.org/10.1016/j.jhazmat.2008.07.069

Sricharoenchaikul, V. (2009). Assessment of black liquor gasification in supercritical water. *Bioresource Technology*, *100*(2), 638–643. https://doi.org/10.1016/j.biortech.2008.07.011

Tülay Güngören, Mehmet Sağlam, Mithat Yüksel, Hakan Madenoğlu, Rahim İşler, İsmail H. Metecan, Ahmet R. Özkan, and L. B. (2007). Near-Critical and Supercritical Fluid Extraction of Industrial Sewage Sludge. *Ind. Eng. Chem. Res.*, 1051–1057.

Turkish Atomic Energy Authority. (2011). *Türkiye atom enerjisi kurumu*.

Chapter 12

CURRENT STUDIES ON ION REMOVAL USING PISTACHIO SHELLS

Hasan Kıvanç YEŞİLTAŞ[1], *Güray KILINÇÇEKER*[2]

---

[1] Hasan Kıvanç YEŞİLTAŞ, Research Assistant Dr., Cukurova University Engineering Faculty Environmental Engineering Department Adana Turkey, ORCID ID: 0000-0003-3331-3209

[2] Güray KILINÇÇEKER, Prof. Dr., Cukurova University Faculty of Arts and Sciences Chemistry Department Adana Turkey, ORCID ID: 0000-0003-3030-4518

1) ION REMOVAL FROM WATER AND WASTEWATER

When wastewater from domestic and industrial activities is discharged into ecosystems without treatment or with insufficient treatment, it causes irreversible ecological damage in receiving water environments. This pollution, mixing with aquatic ecosystems, reduces the light penetration of water, leading to a decrease in dissolved oxygen levels and negatively impacting biodiversity (Kaya and Şahin, 2022; Şentürk and Alzein, 2020). In particular, toxic substances in the aquatic food chain accumulate in living organisms, reaching higher-level consumers and posing serious risks to the health of humans, the organisms at the bottom of the food chain (Andal et al., 2018; Seymen et al., 2025; Yetilmezsoy and Demirel, 2008). Therefore, protecting water resources and ensuring that wastewater discharges meet standards are extremely important for environmental sustainability, the environment, and public health (Kaya and Şahin, 2022; Yetilmezsoy and Demirel, 2008).

One of the most important parameters determining water quality is the ionic components dissolved in the water. Although the presence of some ions such as calcium and magnesium within certain limits in drinking and utility water is necessary for health; The presence of nitrate (NO^{3-}), phosphate (PO_4^{3-}), fluoride (F^-), and various heavy metal ions (ionic forms of Pb^{2+}, Cd^{2+}, Cr^{6+}, etc.) creates toxic effects (Abraham et al., 2025; Kursunoglu and Demir, 2022; Yetilmezsoy and Demirel, 2008). In particular, the excessive accumulation of nutrients such as nitrogen and phosphorus, originating from agricultural fertilizers and domestic waste, in water sources leads to eutrophication. Eutrophication causes algal blooms, depleting oxygen in the aquatic environment and making life impossible for other organisms (Al-sareji et al., 2024; Kayranli et al., 2022).

Heavy metal ions from industrial wastewater cause persistent pollution in nature because they are not biodegradable. These metals in ionic form, along with other inorganic anions such as sulfates and chlorides, seep into groundwater and surface water sources, polluting drinking water reservoirs (Moreno-Virgen et al., 2024; Shaikhiev et al., 2023). Therefore, effectively removing these harmful ions from water and wastewater is a priority for researchers, both to maintain ecosystem balance and to safeguard public health (Al-sareji et al., 2024; Kursunoglu and Demir, 2022; Yetilmezsoy and Demirel, 2008).

Many different treatment methods are applied to remove ions from water and wastewater (Figure 1), including chemical precipitation, coagulation-flocculation and sedimentation, membrane filtration techniques, and electrochemical treatment (Bazrafshan et al., 2016; Moreno-Virgen et al., 2024; Turan and Mesci, 2011). Among these treatment methods, chemical sedimentation treatment techniques have led researchers to seek more sustainable and economical alternatives due to the high amount of sludge generated by traditional methods and/or the high operating and energy costs of membrane processes (Bazrafshan et al., 2016; Yetilmezsoy and Demirel, 2008). In this context, physicochemical methods stand out, particularly because they provide high selectivity and efficiency in removing low concentrations of pollutants, minimize waste, and allow for pollutant recovery (Al-Awadhi et al., 2023; Kumar et al., 2021; Moreno-Virgen et al., 2024). Among these methods, adsorption and ion exchange processes are noteworthy as the most common and effective applications in water and wastewater treatment, both in terms of ease of operation and cost-effectiveness (Al-sareji et al., 2024; Kayranlı et al., 2022; Morcalı et al., 2013).

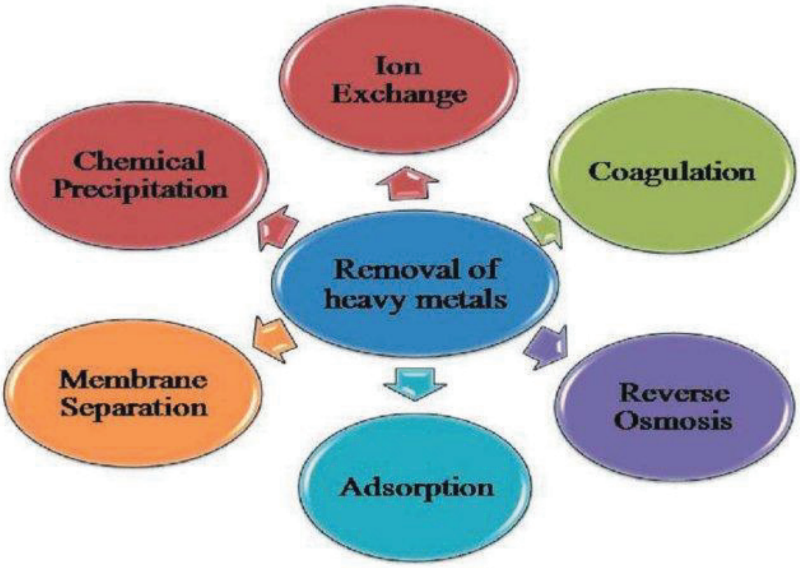

Figure 1. Methods used for ion removal from water and wastewater (Chakraborty ve ark., 2022)

2) ADSORPTION AND ION EXCHANGE METHOD

Adsorption refers to the process of achieving treatment by attaching the targeted pollutant to a solid material called an adsorbent (Figure 2). Technically defined as the transfer of a substance from the gas or liquid phase to the surface of a solid material, this process can occur permanently or temporarily through physical or chemical interactions. In temporary adsorption (physical adsorption), the attached substance can be recovered, and the adsorbent can be reused through regeneration. Activated carbon is the most commonly used adsorbent and is frequently used in adsorption processes today, produced by carbonization from biomass materials such as tree bark and fruit seeds. These materials can be modified with elements such as iron, or given magnetic properties, and are also used in water and wastewater treatment. The adsorption process is not limited to organic materials but is also carried out with high efficiency using composite structures made of inorganic salts or minerals (Tchobanoglus et al., 2003; Amen et al., 2020; Dias and Fontes, 2020; Alka et al., 2021; Weerasundara et al., 2021).

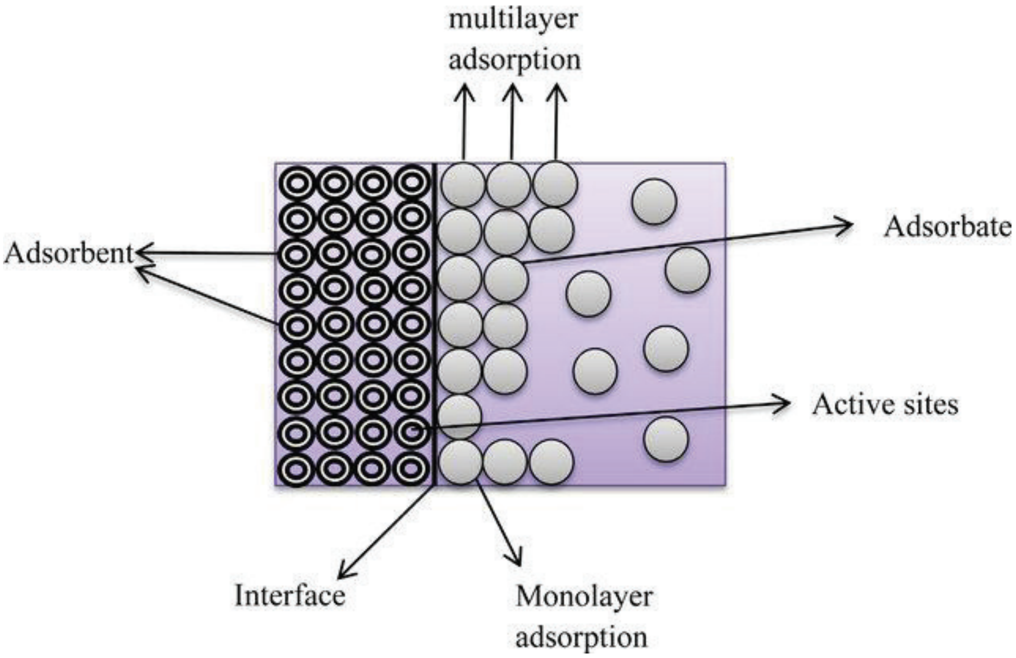

Figure 2. Image of the adsorption method. (Soliman and Moustafa, 2020).

The ion exchange method is based on the principle of reversible exchange of ions in the liquid phase with similarly charged ions on the ion exchanger through the influence of electrostatic forces. In this process, no permanent physical change occurs in the structure of the solid material. Similar to the adsorption process, synthetic polymeric resins as well as natural inorganic materials such as zeolites and clays are widely used in the ion exchange process (Helfferich, 1962; Crittenden et al., 2012). With this method, anions such as phosphorus, nitrate, and arsenic can be removed from water and wastewater; Toxic cations such as lead, nickel, chromium, and cadmium can also be removed with high efficiency. Treatment efficiency varies depending on the functional groups of the material used and its selectivity (affinity) to the target pollutant (Clifford, 1999; Bashir et al., 2019). Ion exchange materials that reach saturation can be reactivated through regeneration; this allows for the recovery of valuable substances, as in adsorption, and also enables the reuse of the material while reducing operating costs (Zagorodni, 2006; Daud et al., 2019).

3) THE CONCEPT OF BIOMATERIALS, THEIR USE AND IMPORTANCE IN WATER AND WASTEWATER TREATMENT

The term biomaterial commonly refers to natural or modified substances obtained from agricultural waste of plant origin and with a lignocellulosic structure (Barbu et al., 2020; Shaikhiev et al., 2023; Şentürk and Alzein, 2020). Biomass sources such as pistachio shells mainly consist of components such as cellulose, hemicellulose, and lignin. Pistachio shells contain rich functional groups such as hydroxyl, carboxyl, and phenolic groups that can trap pollutants on their surface (Şentürk and Alzein, 2020; Dönmez et al., 2016; Şentürk and Alzein, 2019). Pistachio shells, which are produced as a result of agricultural activities, can be re-evaluated as renewable and sustainable natural resources that do not harm the ecosystem. (Al-sareji et al., 2024; Shaikhiev et al., 2023; Kursunoglu and Demir, 2022).

In order to synthesize adsorbent and ion exchange materials from biomaterials, in addition to washing and grinding the raw material, chemical activation and modification processes are carried out with organic components such as acids (H_2SO_4, HCl, HNO_3), bases (NaOH, KOH) or citric acid (Kaya, 2022; Kaya, 2021; Seymen et al., 2025; Parlayıcı, 2024; Mohammed et al., 2020). Furthermore, producing high surface area activated carbons from these wastes through pyrolysis and carbonization methods, or synthesizing composite materials with metal oxide nanoparticle coatings, are among the most common production methods (Al-sareji et al., 2024; Baytar et al., 2018; Nejadshafiee and Islami, 2020; Mohammed et al., 2020; Saghir et al., 2022). In water and wastewater management, the use of these materials is critically important due to their low cost compared to commercial activated carbons, their support for circular economy principles, and their high effectiveness in removing a wide range of pollutants such as heavy metals and dyes (Şentürk et al., 2020; Kursunoglu and Demir, 2022; Armagan and Toprak, 2015; Şentürk and Alzein, 2019).

4) ION REMOVAL STUDIES USING PISTACHIO SHELLS

In the research conducted by Moreno-Virgen et al. (2024), the removal of Ni(II) and Pb(II) ions was achieved using pistachio shells (PS) that were washed, dried at 70°C, and ground to a size of 0.50–0.84 mm; adsorption capacities of 14.8 mg/g for Ni(II) and 6.3 mg/g for Pb(II) were reached. Yetilmezsoy et al. (2008) obtained 99% efficiency and a maximum capacity of 27.1 mg/g in Pb(II) removal using pistachio shells passed through a 1 mm sieve, and found that the data fully conformed to the Langmuir isotherm.

Al-Awadhi et al. (2023), in their study with powdered peanut shells (PPS) with a size of 0.063-0.500 mm, removed Pb(II) and Al(III) ions with capacities of 36.63 mg/g and 12.77 mg/g, respectively; they reported that the process was described by the Langmuir isotherm and pseudosecond-order kinetic model. Magnetic active carbon nanocomposites (H2NSO3-MAC NCs) developed by Nejadshafiee et al. (2020) and modified with sulfamic acid offered a very high capacity of 277.77 mg/g in Cu(II) removal and proved that the data were consistent with the Langmuir isotherm and pseudosecond-order kinetics. Kavranli et al. Abraham et al. (2022), in their study with raw pistachio shells, obtained a capacity of 72.46 mg/g for Ni(II) and 36.73 mg/g for Pb(II); they stated that the Freundlich model was valid for nickel ions and the Langmuir model for lead ions.

Abraham et al. (2025) increased the Pb(II) removal efficiency to 88.9% (52.63 mg/g) by modifying pistachio shells with potassium hydroxide (KOH) and determined that this process followed the Freundlich isotherm and pseudosecond-order kinetic models. Morcali et al. (2013) investigated the removal of platinum (Pt) with pistachio shells carbonized at 1000°C in an argon atmosphere (CPNS) and obtained results consistent with the Langmuir isotherm and pseudosecond-order kinetic models with a capacity of 38.31 mg/g. Kumar et al. A nanocomposite (ZVC@PS) prepared by immobilizing zero-valent copper nanoparticles on peanut shells (2021) removed Cr(VI) ions with a capacity of 110.9 mg/g. Similarly, Banerjee et al. (2018), working on Cr(VI) removal, reported an adsorption capacity of 27.95 mg/g with peanut shell powder ground to a size of 250-350 µm. Finally, Turan et al. (2011), in their study with peanut shells dried at 373 K and reduced to a size of 0.5 mm, achieved a 96% removal efficiency of Zn(II) ions and showed that the experimental data fit the pseudosecond-order kinetic model with high correlation. Table 1 contains summaries of various studies found in the literature.

Table 1. Summary of Studies on Ion Removal Using Pistachio Shells

Material and Modification	**Preparation Procedures**	**Removed Ion**	**Removal Capacity / Efficiency**	**Isotherm and Kinetic Model**
Pistachio Shell (PS)	Washing, drying at 70°C, grinding to 0.50–0.84 mm size.	Ni(II) Pb(II)	Ni(II): 14.8 mg/g Pb(II): 6.3 mg/g.	-
Antep Pistachio Shells	Washing, drying at 80°C, sieving through 1 mm.	Pb(II)	27.1 mg/g 99% removal.	Langmuir isotherm.
Precursor PS (PPS)	Washing, drying at 110°C, grinding to powder (0.063-0.500 mm size).	Pb(II) Al(III)	Pb(II): 36.63 mg/ Al(III): 12.77 mg/g.	Langmuir isotherm Pseudo-second-order kinetic.
H_2NSO_3-MAC NCs	Carbonization at 750°C, functionalization with Fe_3O_4 and sulfamic acid.	Cu(II) Fe(II) Zn(II) Ni(II)	Cu(II): 277.77 mg/g.	Langmuir isotherm Pseudo-second-order kinetic.
Pistachio Shell	Washing, drying at 105°C, grinding, and sieving.	Ni(II) Pb(II)	Ni(II): 72.46 mg/g Pb(II): 36.73 mg/g.	Freundlich (Ni(II) Langmuir (Pb(II)) Pseudo-second-order.

KOH Modified PS	Immersion in KOH solution (24 h), drying at 80°C.	Pb(II)	52.63 mg/g 88.9% efficiency.	Freundlich isotherm Pseudo-second-order kinetic.
CPNS (Carbonized shell)	Activation in Argon atmosphere at 1000°C, sizing to 250 µm.	Platinum (Pt)	38.31 mg/g.	Langmuir isotherm Pseudo-second-order kinetic.
ZVC@PS (Nanocomposite)	Immobilization of zero-valent copper nanoparticles onto PS.	Cr(VI)	110.9 mg/g.	-
Pistachio Shell Powder	Washing, drying at 100°C, grinding to 250-350 µm size.	Cr(VI)	27.95 mg/g.	-
Pistachio Shells (PS)	Washing, drying at 373 K, grinding to 0.5 mm size.	Zn(II)	96% removal.	Pseudo-second-order kinetic.

5) CONCLUSION AND RECOMMENDATIONS

This evaluation revealed that pistachio shells, widely accessible due to agricultural activities, possess significant potential as a sustainable and low-cost adsorbent for removing toxic ions from water and wastewater. The evaluated literature studies showed that pistachio shells, in both processed and unprocessed forms, are effective in removing various heavy metals such as lead, nickel, copper, chromium, zinc, and platinum. However, modification processes such as acid/base activation, carbonization, or nanocomposite synthesis significantly increased the adsorption capacity by increasing the surface area and functional group diversity of the material. When the studies in the literature were evaluated using kinetic models, it was understood that they were commonly explained by the pseudo-second-order kinetic model, with chemical interactions being dominant, while the adsorption equilibrium isotherm data mostly conformed to the Langmuir isotherm, which indicates single-layer adhesion on homogeneous surfaces. Therefore, the reuse of this waste biomass contributes to the circular economy by providing agricultural waste management and also constitutes an economical alternative compared to expensive commercial activated carbon. In addition to studies obtained at the laboratory scale, a large part of the current literature focuses on batch systems and synthetic solutions; therefore, emphasis should be placed on continuous flow column studies to determine the performance of the material under real industrial wastewater conditions and its competitive adsorption behavior in the presence of other ions. Furthermore, detailed examination of desorption and regeneration cycles to determine the economic life of the adsorbent, development of safe methods for the disposal or recovery of metal-laden waste adsorbent, and comprehensive techno-economic analyses to prove the commercial viability of the process are critical for translating academic knowledge in this field into practical application.

REFERENCES

Abraham, N. M., Pawels, R., & Madhu, G. (2025). Removal of lead ions from aqueous solution using potassium hydroxide modified natural adsorbents. *Indian Journal of Chemical Technology, 32*(2), 254-260.

Al-Awadhi, M. M. H., Bashnaini, M. S. A., & Akl, M. A. (2023). Biosorption of Lead (II) and Aluminum (III) from real water samples onto precursor pistachio shells: Adsorption characteristics, kinetics and thermodynamic studies. *Egyptian Journal of Chemistry, 66*(10), 259-268.

Alka, S., Shahir, S., Ibrahim, N., Ndejiko, M. J., Vo, D. V. N., & Abd Manan, F. (2021). Arsenic removal technologies and future trends: A mini review. *Journal of Cleaner Production, 278*, 123805.

Al-sareji, O. J., Al-Samarrai, S. Y., Grmasha, R. A., Meiczinger, M., Al-Juboori, R. A., Jakab, M., ... & Hashim, K. S. (2024). A novel and sustainable composite of L@PSAC for superior removal of pharmaceuticals from different water matrices: Production, characterization, and application. *Environmental Research, 251*, 118565.

Amen, R., Bashir, H., Bibi, I., Shaheen, S. M., Niazi, N. K., Shahid, M., ... & Rinklebe, J. (2020). A critical review on arsenic removal from water using biochar-based sorbents: The significance of modification and redox reactions. *Chemical Engineering Journal, 396*, 125195.

Andal, N. M., Vivithabharathi, K., & Devi, N. S. (2018). Virtual screening of treated pistachio vera shell powder as a potential sorbent in sequestering ubiquitous divalent metal ions from aqueous matrices. *Oriental Journal of Chemistry, 34*(1), 352-361.

Banerjee, M., Bar, N., Basu, R. K., & Das, S. K. (2018). Removal of Cr (VI) from its aqueous solution using green adsorbent pistachio shell: A fixed bed column study and GA-ANN modeling. *Water Conservation Science and Engineering, 3*(1), 19-31.

Barbu, M. C., Sepperer, T., Tudor, E. M., Petutschnigg, A., Antov, P., & Kristak, L. (2020). Walnut and hazelnut shells: Untapped industrial resources and their suitability in lignocellulosic composites. *Applied Sciences, 10*(18), 6340.

Bashir, A., Malik, L. A., Ahad, S., Manzoor, T., Bhat, S. A., Dar, G. N., & Pandith, A. H. (2019). Removal of heavy metal ions from aqueous system by ion-exchange and adsorption methods: A review. *Environmental Chemistry Letters, 17*(2), 729-754.

Bazrafshan, E., Alipour, M. R., & Mahvi, A. H. (2016). Textile wastewater treatment by application of combined chemical coagulation, electrocoagulation, and adsorption processes. *Desalination and Water Treatment, 57*, 9203-9215.

Chakraborty, R., Asthana, A., Singh, A. K., Jain, B., & Susan, A. B. H. (2022). Adsorption of heavy metal ions by various low-cost adsorbents: a review. *International Journal of Environmental Analytical Chemistry*, *102*(2), 342-379.

Clifford, D. A. (1999). Ion exchange and inorganic adsorption. In R. D. Letterman (Ed.), *Water quality and treatment: A handbook of community water supplies* (5th ed., pp. 9.1-9.91). New York, NY: McGraw-Hill.

Crittenden, J. C., Trussell, R. R., Hand, D. W., Howe, K. J., & Tchobanoglous, G. (2012). *MWH's water treatment: Principles and design* (3rd ed.). Hoboken, NJ: John Wiley & Sons.

Daud, Z., Awang, H., Latiff, A. A. A., Nasir, N., Ridzuan, M. B., & Ahmad, Z. (2019). Suspended solid, color, COD and oil and grease removal from biodiesel wastewater by coagulation and flocculation processes. *International Journal of Integrated Engineering, 11*(1), 214-221.

Dias, A. C., & Fontes, M. P. F. (2020). Arsenic (V) removal from water using hydrotalcites as adsorbents: A critical review. *Applied Clay Science, 191*, 105615.

Dönmez, İ. E., Selçuk, S., Sargın, S., & Özdeveci, H. (2016). Kestane, fındık ve antepfıstığı meyve kabuklarının kimyasal yapısı. *Turkish Journal of Forestry, 17*(2), 174-177.

Enache, A.-C., Cojocaru, C., Samoila, P., Ciornea, V., Apolzan, R., Predeanu, G., & Harabagiu, V. (2023). Adsorption of Brilliant Green dye onto a mercerized biosorbent: Kinetic, thermodynamic, and molecular docking studies. *Molecules, 28*(10), 4129.

Helfferich, F. G. (1962). *Ion exchange*. New York, NY: McGraw-Hill.

Kaya, A., & Şahin, S. A. (2022). Acid Orange 7 adsorption onto quaternized pistachio shell powder from aqueous solutions. *Biomass Conversion and Biorefinery, 12*, 6015-6032.

Kayranli, B., Gok, O., Yilmaz, T., Gok, G., Celebi, H., Seckin, I. Y., & Mesutoglu, O. C. (2022). Low-cost organic adsorbent usage for removing Ni2+ and Pb2+ from aqueous solution and adsorption mechanisms. *International Journal of Environmental Science and Technology, 19*, 3547-3564.

Kumar, S., Brar, R. S., Babu, J. N., Dahiya, A., Saha, S., & Kumar, A. (2021). Synergistic effect of pistachio shell powder and nano-zerovalent copper for chromium remediation from aqueous solution. *Environmental Science and Pollution Research, 28*(44), 63422-63436.

Kursunoglu, S., & Demir, I. (2022). The potential of pistachio shell-based activated carbons for metal removal from aqueous solutions: A review. *Energy Sources, Part A: Recovery, Utilization, and Environmental Effects, 44*(4), 8572-8590.

Morcali, M. H., Zeytuncu, B., Aktas, S., Yucel, O., & Gulluoglu, A. N. (2013). Platinum adsorption from chloride media using carbonized biomass and commercial sorbent. *Minerals & Metallurgical Processing, 30*(2), 129-136.

Moreno-Virgen, M. R., Rodríguez-García, K. A., Bonilla-Petriciolet, A., Reynel-Ávila, H. E., Villalobos-Delgado, F. J., Mendoza-Castillo, D. I., ... & Ortiz-Lozano, J. A. (2024). A circular economy-based valorization of agricultural residues to remove heavy metals from water: Adsorption and final disposal strategy. *Adsorption Science & Technology, 42*, 1-24.

Nejadshafiee, V., & Islami, M. R. (2020). Intelligent-activated carbon prepared from pistachio shells precursor for effective adsorption of heavy metals from industrial waste of copper mine. *Environmental Science and Pollution Research, 27*(2), 1625-1639.

Seymen, S. T., Eroğlu, H. A., Kadıoğlu, E. N., Umar, M., Hamid, A., Khan, H., ... & Akbal, F. (2025). Comprehensive study on efficient diclofenac sodium removal using walnut and pistachio shell activated carbon: ANN, kinetics, isotherms, thermodynamics and DFT calculations. *Biomass and Bioenergy, 202*, 108216.

Shaikhiev, I. G., Kraysman, N. V., & Sverguzova, S. V. (2023). Review of pistachio (Pistacia) shell use to remove pollutants from aqua media. *Biointerface Research in Applied Chemistry, 13*(4), 389.

Soliman, N. K., & Moustafa, A. F. (2020). Industrial solid waste for heavy metals adsorption features and challenges; a review. *Journal of Materials Research and Technology*, *9*(5), 10235-10253.

Şentürk, İ., & Alzein, M. (2019). H_2SO_4 ile aktive edilen fıstık kabuğu kullanılarak sürekli sistem kolonda sucul çözeltiden asidik boya giderimi. *Afyon Kocatepe Üniversitesi Fen ve Mühendislik Bilimleri Dergisi, 19*(3), 697-708.

Şentürk, İ., & Alzein, M. (2020). Adsorptive removal of basic blue 41 using pistachio shell adsorbent - Performance in batch and column system. *Sustainable Chemistry and Pharmacy, 16*, 100254.

Tchobanoglous, G., Burton, F. L., & Stensel, H. D. (2003). *Wastewater engineering: Treatment and reuse* (4th ed.). New York, NY: McGraw-Hill.

Turan, N. G., & Mesci, B. (2011). Use of pistachio shells as an adsorbent for the removal of Zinc(II) ion. *Clean – Soil, Air, Water, 39*(5), 475-481.

Weerasundara, L., Ok, Y. S., & Bundschuh, J. (2021). Selective removal of arsenic in water: A critical review. *Environmental Pollution, 268*, 115668.

Yetilmezsoy, K., & Demirel, S. (2008). Artificial neural network (ANN) approach for modeling of Pb(II) adsorption from aqueous solution by Antep pistachio (Pistacia Vera L.) shells. *Journal of Hazardous Materials, 153*(3), 1288-1300.

Zagorodni, A. A. (2006). *Ion exchange materials: Properties and applications*. Amsterdam: Elsevier.

Zhang, Y., Jin, Y., Li, S., Wu, H., & Luo, H. (2024). Preparation of pistachio shell-based porous carbon and its adsorption performance for low concentration CO_2. *Particuology, 95*, 103-114.

Chapter 13

SUPERPIXEL BASED INDIVIDUAL TREE CROWN SEGMENTATION: METHODS, APPLICATIONS, AND CHALLENGES

Sude Gül YEL[1], Esra TUNÇ GÖRMÜŞ[2]

---

[1] Lecturer, Artvin Çoruh University, Artvin Vocational School, Department of Land Registry and Cadastre. Email: sudegyildiz@artvin.edu.tr ORCID: 0000-0001-9975-8345

[2] Assoc. Prof. Dr., Karadeniz Technical University, Faculty of Engineering, Department of Geomatics Engineering. Email: etuncgormus@ceng.ktu.edu.tr ORCID: 0000-0002-3334-2061

1. Introduction

Individual tree crown (ITC) segmentation plays a key role in obtaining and managing forest inventories, carrying out sensitive forestry activities such as ecosystem conservation, forest health and heterogeneity, and monitoring the effects of global climate change on forests at the individual tree level (Calders et al., 2020; Kattenborn et al., 2021; Weinstein et al., 2021). With ITC segmentation; by determining the location, size, and crown parameters of each tree, ecosystem services such as timber production, carbon storage capacity, and the water cycle can be addressed (Wan Mohd Jaafar et al., 2018; Liu et al., 2023). Forests are under the influence of climate originated stresses such as drought and shifts in seasonal dates. The analysis of tree responses to this situation and the measures that can be taken becomes possible thanks to segmentation methods at the ITC level.

In the literature, in segmentation studies conducted at the individual tree crown level; optical images and lidar data reflecting the structure of the crown are used separately or together. Although data fusion is quite effective in capturing the topology of the tree, it is more costly and tiring compared to multispectral images alone (Ke & Quackenbush, 2011; Dersch et al., 2024; Yang et al., 2024; Wang et al., 2025). By using correct segmentation methods, studies conducted with RGB or multispectral images have also succeeded in obtaining high accuracies (Modica et al., 2020; Martins et al., 2021; Buchner et al., 2025). Especially high resolution optical images facilitate crown separation at the individual level (Xiao et al., 2019). However, increasing spatial resolution causes an increase in image size (Stutz et al., 2018; Achanta et al., 2012). A large number of pixels representing an individual crown increases computational cost (Ibrahim & El-kenawy, 2020). In this sense, superpixel based approaches that divide the image into spectrally homogeneous and spatially consistent regions provide a strong intermediate representation for ITC segmentation (Crommelinck et al., 2017; Martins et al., 2021). Superpixel representations instead of pixels are hardware friendly. While superpixels reduce pixel level noise inside the crown, by providing a partitioning that is more sensitive to crown boundaries, they produce more meaningful analysis units for both classical machine learning and deep learning based methods (Achanta et al., 2012; Crommelinck et al., 2017). In recent years, superpixel based ITC approaches; from rule and threshold based methods to graph and optimization based models, from object based classification schemes to deep learning integrations, have been addressed in a wide methodological spectrum and have produced successful results in different forest types (Martins et al., 2019; Martins et al., 2021; Deluzet et al., 2022).

Traditional segmentation approaches such as watershed segmentation, region growing algorithms, and classical techniques such as geometric modeling are valuable, however, they often remain insufficient in structurally complex forests where overlapping crowns, variable light conditions, topography, and inter species spectral similarity are intense (Deluzet et al., 2022). While these methods also need a large number of parameters that vary from forest to forest, as a result of the parameters not being adjusted correctly, they frequently lead to over or under segmentation in heterogeneous covers (Buchner et al., 2025). These constraints of traditional methods have required the investigation of more adaptable and data oriented segmentation paradigms.

Superpixel segmentation; divides the image into meaningful regions by grouping spectrally homogeneous pixels with strong neighborhood relationships. Since it segments the image by taking into account not only the pixel but also the neighborhood relationship, it preserves object boundaries much better compared to pixels and, thanks to this feature, appears as a strong alternative method in segmentation (Achanta et al., 2012; Franklin et al., 2022). Instead of directly processing millions of pixels found in high dimensional remote sensing images, it reduces complexity and lowers computational cost by grouping them. By preventing noisy pixels at the tree crown boundary from causing erroneous calculations, it produces more sharply bounded crown pieces; in this way, by providing intermediate representations that are smaller than full crown objects but richer in information than a single pixel, it both reduces noise and provides a solid basis for neighborhood based or classification based algorithms (Zhou et al., 2020; Wang et al., 2023). Multispectral images, thanks to additional spectral information such as NIR and red edge bands they contain, facilitate the separation of crown and background, support species separation, and with the ability to capture fine spectral changes inside the crown, work compatible with superpixel segmentation methods (Martins et al., 2021; Liu et al., 2023; Buchner et al., 2025).

When these advantages are considered, superpixel based ITC segmentation is gradually gaining wider acceptance in the literature. This book chapter explains in a comprehensive manner the theoretical bases of superpixel use on multispectral images, the main algorithms, application examples in different forest ecosystems, and the opportunities it offers for future research.

2. Overview of Superpixel Segmentation Techniques (ITC Relevant)

The concept of superpixel was first proposed by Ren & Malik (2003), based on the reasoning that pixels do not correctly reflect real object curvatures and that the natural curved structure of objects cannot be represented by pixels alone. In this way, the idea that superpixels with perceptual integrity should take the place of the pixel, which is accepted as the building block of the image, has attracted great interest in the literature.

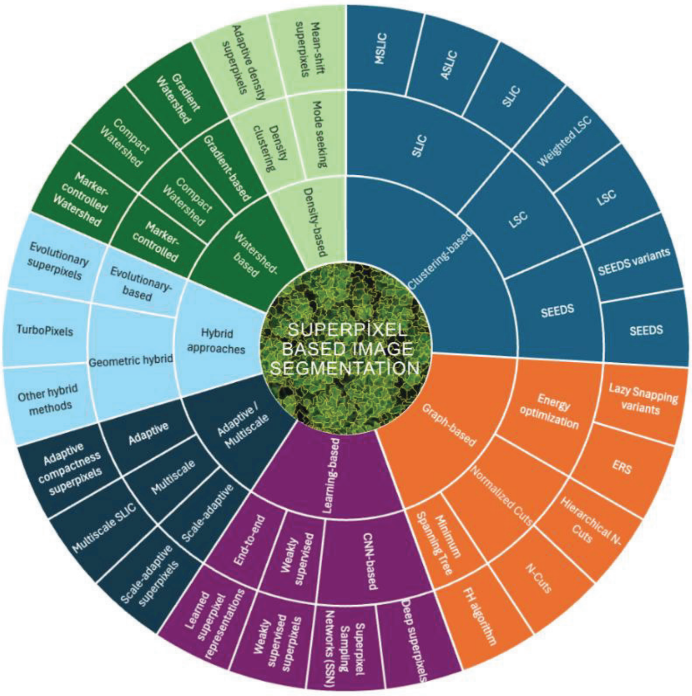

Figure 1. Hierarchical taxonomy of superpixel based image segmentation methods. The diagram summarizes classical clustering, graph, watershed, density, and hybrid based superpixel approaches alongside recent advances in learning based, adaptive, and multiscale superpixel generation. The taxonomy highlights the methodological evolution from hand crafted segmentation strategies to data driven and scale adaptive frameworks, providing a conceptual foundation for their application in multispectral remote sensing and individual tree crown segmentation.

At the same time, seeing these structures as the first step of segmentation increased their popularity and led to the development of new superpixel based methods (Crommelinck et al., 2017; Cong et al., 2018; Ibrahim & El-kenawy, 2020; Yang et al., 2020; Ng et al., 2023). Superpixel based image segmentation methods cover a very wide area in the literature (Figure 1). In this section, superpixel techniques used in ITC segmentation are addressed.

2.1. Clustering based Method

They are methods that cluster image pixels according to color, feature similarity and spatial proximity, and produce scalable and fast pre segmentation. The most widely used class of this method is the Simple Linear Iterative Clustering (SLIC) family (Achanta et al., 2012).

Simple Linear Iterative Clustering (SLIC)

SLIC; is an algorithm created by a k means clustering method customized to the proximity of pixels in color space (CIELAB); in terms of color and spatial closeness. In this method, pixels are assigned to certain centers at each iteration and the clusters are updated. By avoiding the scattered computation of the classical k means method, it is faster because it performs the search in a limited region around the superpixel center. Due to these properties, SLIC produces fast results by making computation efficient even on large images compared to other algorithms (Achanta et al., 2012). Thanks to the parameter it offers to the user to produce the desired number of superpixels, it allows the size smoothness ratio to be adjusted flexibly (Figure 2).

Figure 2. Images segmented using SLIC into superpixels of size different pixels (Achanta et al.,2012)

Adaptive SLIC (ASLIC); is an algorithm that dynamically calculates the fixed compactness factor, which is manually determined by the user in the classical SLIC algorithm, for each superpixel cluster. At each iteration, it calculates the compactness factor within that cluster according to its texture and automatically updates it. In this way, it produces more regular and larger superpixels in flat areas, and in complex areas (generally at object boundaries) superpixels that adhere more tightly to the edge (Achanta et al., 2012; Boemer et al., 2018).

Manifold SLIC (MSLIC); is an algorithm that calculates the spatial distance computed by SLIC not in a 5D Euclidean space, but by projecting it onto a 2D Manifold surface area that is sensitive to image content. MSLIC accepts the color differences and intensities in the image as a manifold surface, and calculates the distance between pixels in a geodesic manner (Liu et al., 2016). In detecting the boundaries of very similar objects such as two trees of the same type, it achieves high success in separating objects by calculating complex boundaries more sharply.

Superpixels Extracted via Energy Driven Sampling (SEEDS)

SEEDS; adopts an iterative improvement approach based on energy optimization while performing superpixel segmentation. In this method, the image is initially divided into regular parts in the form of a regular grid, then these parts are iteratively rearranged, modified, and the energy is attempted to be reduced. In the energy function, color similarity between neighboring regions and intra region consistency are included. At each iteration, region assignments of pixels are updated with small changes until the total energy decreases. The algorithm operates at different hierarchical levels, gradually refining superpixel boundaries. This multi scale approach allows obtaining both fast convergence and quality segment boundaries. SEEDS stands out as a method that offers high speed and satisfactory segmentation accuracy, especially in real time applications (Bergh et al., 2012).

Linear Spectral Clustering (LSC)

LSC; performs spectral clustering with a linear approach. This method carries out the calculations over a weighted distance metric by evaluating the color and position features of each pixel together. Since this weighted k means based clustering linearly approximates the optimization criterion of spectral segmentation, the method is named linear spectral. While being fast like SLIC, it brings superpixel boundaries closer to the real object boundaries in the image. Since this method establishes a good balance between quality and speed, it has become an effective tool in the segmentation of high resolution images (Li & Chen, 2015).

2.2. Graph Based Superpixel Segmentation

It is a method in which pixels are defined as nodes, and the similarities between them and their neighbors are defined as edge weights. By minimizing a cost function defined on the graph, it segments pixels through clustering. As a result, superpixels are a minimum tension tree structure composed of the most similar pixels within itself. By producing superpixels with irregular sizes and shapes, it has a structure that naturally adapts to object boundaries (Wu et al., 2018).

Energy Optimization

In this method, the segmentation problem is formulated as a labeling task. The image is divided into overlapping small patches, and only one label is assigned to each pixel. Superpixels are created by minimizing an energy function that encourages pixels with the same label to be grouped with neighbors (Peng et al., 2015). ERS; defines an objective function based on optimizing the entropy rate of a random walk on an image graph. The objective function aims to keep the internal homogeneity of superpixel regions at low entropy, while also aiming to control the total number of regions. The algorithm ensures that each superpixel has a similar pixel intensity distribution and a compact shape (Liu et al., 2011). Although the segmentation quality of this method is good, the computation of the cost function it optimizes is costly. Still, if the goal is to produce balanced and consistent superpixels, this will provide a strong theoretical basis.

Normalized Cuts (N-cuts)

N cuts; iteratively divides the graph of pixels into parts by using contour and texture features. While it is optimized with a cost function, boundary adherence is lower compared to other methods and it has a complex structure (Wang et al., 2017).

Minimum Spanning Tree

In this method, the pixels forming the superpixel are brought together with a prediction definition by calculating the shortest path in an undirected graph using the Dijkstra algorithm. It is not cumbersome in terms of computation (Felzenszwalb et al., 2004).

2.3. Learning Based

A prediction map is produced to learn the centers to which pixels are assigned for learning based, and then this map is converted into superpixel regions. The training of the model is guided by a loss function based on criteria such as boundary accuracy and regional consistency, in order to make the superpixel segmentation compatible with the target outputs.

Superpixel Sampling Networks (SSN)

SSN; is a model that makes superpixel segmentation end to end learnable. Each pixel is softly assigned to multiple candidate superpixels and is represented with a differentiable assignment matrix. It operates with a loss function that minimizes the distances between the centers of superpixels and the learned representations of the pixel such as color and position. In this way, the network learns to create semantically meaningful superpixel clusters by using task oriented, spatial position, and segments the image into superpixels. It offers a superpixel production process that is more flexible, sensitive, and compatible with learning based systems compared to traditional methods (Jampani et al., 2018).

Evolutionary Neural Networks (CNN)

CNN based superpixel segmentation method; is a deep learning based approach. It is a learning based network that provides higher accuracy and flexibility in superpixel production compared to traditional algorithms. The model learns whether neighboring pixels should be within the same superpixel based on similarity measures learned by the CNN architecture. Instead of producing superpixels directly, the network creates a superpixel map through a post processing step based on the learned similarities (Ilyas et al., 2020).

Many methods developed in the field of superpixel segmentation have provided important contributions in dividing images into regions with perceptual integrity. However, not all of these methods have been used in the context of individual tree crown segmentation (ITC). In the future recommendations section, methods that are not described here but are important for ITC segmentation will be mentioned. At this point, it will be more meaningful to focus on superpixel algorithms that are directly integrated into ITC applications, which is the focus of this section.

For this reason, in the following part, superpixel based methods used especially in the separation of individual tree crowns from high resolution multispectral or UAV images and how these methods are integrated with different segmentation approaches (CHM analysis, region growing, deep learning etc.) will be systematically addressed.

3. Superpixel Based ITC Segmentation

Superpixel segmentation is at the center of contemporary approaches aimed at extracting individual tree crowns (ITC) from multispectral images and significantly facilitates segmentation processes by reducing the spatial and spectral complexity in high resolution images. Especially in high resolution images, increasing pixel numbers cause the prolongation of traditional pixel based analyses and an increase in computation and memory requirements (Chen et al., 2020). Superpixel based segmentation techniques, unlike pixel based methods, facilitate object creation at the crown level with an intermediate representation approach by dividing the image into homogeneous, boundary compatible regions and by increasing spatial sensitivity. In pixel based methods, in forests consisting of multi layered, overlapping crowns containing shadows, factors such as spectral similarity of crowns and texture heterogeneity reduce segmentation accuracy. In this context, superpixels provide a very suitable basis for subsequent algorithms in ITC segmentation by producing basic units that preserve crown boundaries, are computationally efficient, and biologically meaningful.

3.1. Application Case Studies

Due to factors such as crown morphology, canopy closure degree, and the complexity of surrounding objects in different ecosystem types, superpixel based ITC segmentation methods show different performances (Li et al., 2020; Adhikari et al., 2020; Wang et al., 2025). For this reason, superpixel based approaches have concentrated on different application areas such as natural mixed forests, regular plantations, and urban trees (Liu et al., 2023; Subedi et al., 2025). Applications of superpixel based individual tree crown segmentation in different forest and land types are summarized in Table 1. Below, these three main application areas are summarized in terms of the data types used, methodological preferences, and the outputs obtained (Jiao & Deng, 2016; Firoze et al., 2023).

Table 1. Study area types in which superpixel based individual tree crown segmentation has been applied.

Article Title	**Forest / Land Cover Type**	**Citation**
Individual Building Rooftop and Tree Crown Segmentation from High-Resolution Urban Aerial Optical Images	Urban tree cover	(Jiao & Deng, 2016)
Image Segmentation and Classification with SLIC Superpixel and Convolutional Neural Network in Forest Context	Temperate mixed forest	(Martins et al., 2019)
Quantifying Understory and Overstory Vegetation Cover Using UAV-Based RGB Imagery in Forest Plantation	Temperate mixed forest	(Li et al., 2020)
An Integrated Object and Machine Learning Approach for Tree Canopy Extraction from UAV Datasets	Natural forest	(Adhikari et al., 2020)
Machine Learning and SLIC for Tree Canopies Segmentation in Urban Areas	Urban forest	(Martins et al., 2021)
Monitoring Leaf Phenology in Moist Tropical Forests by Applying a Superpixel-based Deep Learning Method to Time-series Images of Tree Canopies	Tropical forest	(Song et al., 2022)
Tree Instance Segmentation with Temporal Contour Graph	Temperate mixed forest	(Firoze et al., 2023)

Article Title	Forest / Land Cover Type	Citation
Individual Tree Segmentation and Tree-counting Using Supervised Clustering	Plantation	(Wang et al., 2023)
Very high resolution images and superpixel-enhanced deep neural forest promote urban tree canopy detection	Temperate mixed forest	(Liu et al., 2023)
A Hierarchic Method of Individual Tree Canopy Segmentation Combing UAV Image and LiDAR	Temperate mixed forest	(Wang et al., 2025)
Automated Individual Tree Crown Detection and Segmentation using Simple Non-Iterative Clustering (SNIC) Algorithms and High-Resolution LiDAR	Plantation	(Subedi et al., 2025)

3.1.1. Temperate Mixed Forests

In temperate mixed forests, superpixel ITC segmentation contains a high degree of overlap and boundary ambiguity due to species diversity and irregular crown shapes (Li et al., 2020; Wang et al., 2023). In such forest scenes, the superpixel approach provides over segmentation, producing small and compact units that are sensitive to crown boundaries (Adhikari et al., 2020). For this purpose, the outputs of SLIC or alternative algorithms are combined with learning based classifiers, enabling the model to re merge individual tree crowns (Martins et al., 2019). In addition, in order to separate overlapping tree crowns in such forests, the integration of superpixel based 2D segments with LiDAR or SfM based height information has been recommended (Xiao et al., 2019; Wang et al., 2025). These studies show that in structurally complex natural forests, superpixel based approaches produce more reliable results especially with multi source data integration (Li et al., 2020).

3.1.2. Urban Tree Crowns

In urban areas, ITC detection is a much different problem than forest scenes. In urban area images, due to building roofs, asphalt roads, and heterogeneous textures remaining in the ITC background, the segmentation process becomes much more complex (Jiao & Deng, 2016; Csillik et al., 2018; Liu et al., 2023). Superpixel based methods, by increasing boundary consistency, enable a more accurate representation of urban tree crowns compared to pixel based segmentation (Liu et al., 2023). Superpixel regions produced from very high resolution satellite or aerial images contribute to improving tree structure separation by their sharp boundaries when combined with deep learning or machine learning based models (Jiao & Deng, 2016; Liu et al., 2023). In addition, it has been reported that superpixel based pre segmentation provides high accuracies in images such as urban trees containing different classes by reducing edge blurring and classification noise in CNN or graph based methods (Jiao & Deng, 2016; Martins et al., 2019; Firoze et al., 2023; Liu et al., 2023). In mixed class forest scenarios such as concrete, asphalt, tree crown, superpixel based methods stand out as a strong pre processing step (Liu et al., 2023).

3.1.3. Plantation/Orchard Use Cases

In regular planting systems such as plantations and orchards, superpixel based ITC segmentation generally offers higher accuracies due to homogeneous crown structures and regular spacing (Adhikari et al., 2020; Subedi et al., 2025). Superpixel algorithms such as SLIC or SNIC facilitate the automatic segmentation of individual trees by producing regions that represent compact and similarly sized crowns (Adhikari et al., 2020; Subedi et al., 2025). In plantation areas, superpixel based methods show stable performance across different crown densities and species groups (Li et al., 2020; Subedi et al., 2025). With these properties, superpixel based ITC approaches offer scalable and operational solutions for precision forestry and agricultural inventory applications (Adhikari et al., 2020).

3.2. Common Remote Sensing Platforms and Sensors

In superpixel based ITC segmentation, the selection of the data source directly determines both the visual separability of crown boundaries and the reliability of the features to be produced (color texture 3D structure), due to differences in spatial and spectral resolutions. The reviewed studies are mainly grouped into two main platform classes, UAV based systems, and airborne and satellite based platforms (Table 2).

Table 3. Remote sensing platforms, sensors, and spectral information used in superpixel based individual tree crown segmentation studies.

Study	Platform	Sensor	Spectral Information
Jiao & Deng (2016)	Manned Airborne Platform	RGB camera	RGB
Martins et al. (2019)	UAV	RGB camera	RGB
Xiao et al. (2019)	Satellite	Optical stereo	RGB + 3D structural information
Li et al. (2020)	UAV	RGB camera	RGB
Adhikari et al. (2021)	UAV	RGB camera	RGB
Martins et al. (2021)	UAV	RGB camera	RGB
Wang et al. (2023)	UAV	RGB + MS camera	RGB, MS (Blue, Green, Red, Red edge,NIR)
Firoze et al. (2023)	UAV	RGB camera	RGB
Liu et al. (2023)	Satellite	Multispectral	PAN + MS (Blue, Green, Red, NIR)
Wang et al. (2025)	UAV	RGB camera + LiDAR	RGB + structural

3.2.1. Unmanned Aerial Vehicle (UAV) Based Platforms

In most superpixel based ITC segmentation studies, UAV platforms are preferred (Martins et al., 2019; Li et al., 2020; Martins et al., 2021; Adhikari et al., 2021; Wang et al., 2023; Firoze et al., 2023; Wang et al., 2025). The main reason for this is that the centimeter level spatial resolutions provided by UAV platforms allow detailed evaluation of individual tree crown boundaries. The most common sensor type is RGB cameras (Martins et al., 2019; Adhikari et al., 2021; Wang et al., 2023). These sensors are more economical, accessible, and meet the color level expectations of superpixel algorithms such as SLIC, showing high conformity to crown boundaries (Martins et al., 2019; Adhikari et al., 2021; Wang et al., 2023).

In some studies, multispectral cameras are used in addition to RGB sensors. Multispectral (MS) sensors contribute especially to vegetation ground separation and the separation of overlapping crowns with the spectral information they contain such as Red edge and NIR that represent vegetation well (Wang et al., 2023). Superpixel based approaches both reduce computational cost in these high resolution UAV images and produce more consistent crown objects compared to pixel based methods (Martins et al., 2021; Subedi et al., 2025).

3.2.2. Airborne and Satellite Based Platforms

The use of airborne and satellite based platforms at the individual tree level is less compared to UAV. The main reason for this is that the spatial resolution of airborne and satellite based platforms is limiting for individual crown segmentation in dense forest cover. Nevertheless, very high resolution satellite images and optical data obtained from airborne platforms are successfully applied with superpixel based approaches, especially in open crown or urban tree covers (Xiao et al., 2018; Xiao et al., 2019; Liu et al., 2023).

3.3. Spectral Features Used for Superpixel Generation

The quality of the partitioning obtained in superpixel production is a critical pre processing step for the workflow in ITC segmentation, since it directly affects the success of subsequent clustering, merging, and classification stages. Spectral features are used alone or together with spatial and structural constraints depending on the sensor type, platform, and the targeted forest structure. A common characteristic observed in studies performing superpixel based ITC segmentation is that mostly raw RGB bands have been used. Superpixel production through auxiliary calculations such as vegetation indices is quite limited. The main reason for this is that superpixel algorithms aim to produce low level representations. Local spectral variations can be suppressed through the homogenizing effect of indices, weakening crown boundary adherence. Therefore, in studies using multispectral data, indices have been used not directly in superpixel production, but as features that increase the discriminative power of spectral bands (Liu et al., 2023; Wang et al., 2023).

3.3.1. RGB Based Spectral Features

The largest part of superpixel based ITC studies is based on RGB images obtained from UAV platforms (Martins et al., 2019; Li et al., 2020; Adhikari et al., 2021; Martins et al., 2021; Firoze et al., 2023). Superpixel algorithms such as SLIC and SNIC detect similarity between pixels by calculating the spectral distance between visible bands with distance formulas such as Euclidean. Spectral reflectance differences between the sunlit top parts of tree crowns and shaded branches, and local spectral gradients caused by leaf arrangement, contribute to the preservation of crown boundaries even without using an additional vegetation index. In this way, superpixel algorithms show high conformity to tree crown boundaries even with only RGB bands. Indeed, Martins et al. (2019) and Adhikari et al. (2021) showed that RGB based superpixel segmentation adjusted with appropriate compactness parameters can successfully represent fine scale crown geometry. It has been observed that rather than using RGB bands alone, color differences between bands create strong spectral gradients at crown boundaries and increase the boundary adherence of superpixel algorithms (Martins et al., 2019; Firoze et al., 2023).

However; difficulties are sometimes experienced in separating two crowns of the same species, similar health conditions, and under the same light direction. These difficulties, especially in forests with dense and overlapping crown structures, lead to problems such as excessive fragmentation of superpixel partitioning or merging of neighboring crowns. In such cases, additional steps such as supervised clustering or hierarchical merging following superpixel production become mandatory (Li et al., 2020; Firoze et al., 2023).

3.3.2. Multispectral Based Spectral Features

In some of the studies, multispectral bands are used in order to strengthen superpixel production. In this way, by going beyond the geometric and textural information provided by RGB data, an additional spectral separation sensitive to plant biochemical and physiological properties is provided (Wang et al., 2023). Thanks to red edge and NIR bands, the contrast between spectrally close neighboring crowns is increased and the within crown homogeneity of superpixel segments is improved. Red edge and NIR being sensitive to leaf density and chlorophyll content contribute to the separation of neighboring crowns that appear spectrally similar. Although the spatial resolution of satellite data is lower compared to UAV images, multi band spectral information has provided an important compensation mechanism in crown ground separation and the separation of overlapping crowns. Liu et al. (2023) presented a feature set that strengthens both spatial and spectral separation in superpixel production by using band combinations of pan sharpened multispectral data obtained from the Gaofen 2 satellite.

3.4. Superpixel Level Feature Representation

In superpixel based ITC analysis, after superpixels are produced and before entering classification or clustering algorithms, each superpixel needs to be represented with a numerical vector. Merging or clustering algorithms calculate whether superpixels belong to the same crown by computing the similarities between these feature vectors. For this reason, the feature vector needs to be enriched with color, texture, shape and structural components, and when necessary, superpixel boundaries need to be corrected with refinement. The aim here is to reduce pixel complexity and to produce more stable surfaces at the crown level (Jiao & Deng, 2016).

3.4.1. Vegetation Indices and Spectral Band Combinations

The Normalized Difference Vegetation Index (NDVI) has been used mostly for ground tree separation rather than for superpixel production. In workflows, vegetation area extraction is carried out before segmentation. NDVI values above a certain level indicate the presence of trees there and allow working on the real vegetation area. This NDVI value is an adaptable threshold according to the study area, tree species and tree health. Xiao et al., (2019) determined the NDVI threshold as 0.3. In this way, by narrowing the search space before superpixel production, it prevents the model from producing erroneous crowns in non tree areas.

During the feature embedding stage into superpixels, some studies directly use raw RGB bands, while studies performing segmentation with multispectral data also benefit from the distance values between bands (Xiao et al., 2019). In a study using Gaofen 2 multispectral satellite images, pan sharpening is performed by fusing the PAN band with the MS image. While PAN carries spatial detail, MS bands carry spectral differences between objects. In this way, by enriching the features of superpixels, crown separation is sharpened (Liu et al., 2023).

3.4.2. Texture Based Descriptors for Superpixel Representation

The conducted studies show that texture information is used at two different levels in superpixel based ITC analysis. In the first approach, after superpixel production, each superpixel is represented with a numerical feature vector through various texture descriptors, and this vector is used in classification or separation processes. In the second approach, texture and edge information are included directly in the decision mechanism in order to improve the superpixel geometry, that is, at the stage of rearranging the boundaries (refinement). Separating these two usage forms is of critical importance for correctly interpreting the function of texture information in ITC segmentation.

Martins et al. (2021) represented the superpixels produced with the SLIC algorithm with a multidimensional feature set consisting of color, texture, shape and gradient. As texture features, Gray Level Co occurrence Matrix (GLCM), texture descriptors based on Gabor filters, and Local Binary Patterns (LBP) were used. GLCM based textures calculate structural order differences between spectrally similar looking regions by producing second order statistics based on spatial neighborhood relationships of pixel intensities. Especially in transition regions such as crown and grass or crown and shadow, GLCM based homogeneity, contrast and entropy measures play a distinctive role. Gabor filters, thanks to their multiscale and orientation sensitive band passing structures, represent the dominant frequency and orientation components of leaf and crown textures. In this way, they facilitate the separation of tree crowns from other surfaces that exhibit more regular and oriented textures. LBP based textures, by encoding local micro patterns, ensure that the texture signature is preserved in a more stable manner, especially in UAV images where illumination and shadow changes are intense.

The second usage form of texture information is the superpixel boundary improvement approach proposed by Jiao & Deng (2016). With this approach, texture and edge information are used not only for the grouping of algorithms such as superpixel based classification or clustering, but also for the direct arrangement of superpixel geometry. In this process, the standard deviation of pixel intensities is calculated for each superpixel and a threshold value is determined. In cases where the standard deviation exceeds the threshold value, the related superpixel is labeled as having high complexity. Such superpixels are accepted as regions assumed to have boundary ambiguity and are directed to the refinement stage. In the refinement process, the Canny edge detector is used and it is assumed that strong gradient points inside the superpixel represent real object boundaries. Here, the threshold value is experimentally determined in a way suitable for the study area. Thanks to this approach, texture and edge information are used not only as a part of the feature vector, but directly embedded into the decision rule. In the context of ITC segmentation, the main gain of this strategy is that in regions where crown boundaries are complex or ambiguous, it prevents the superpixel from remaining as a single piece and enables the boundaries to better conform to the real crown geometry.

3.5. Technical Workflows for Superpixel Based ITC Segmentation

3.5.1. Superpixel Based Rule Driven and Heuristic Workflows

Superpixel based ITC segmentation literature, one of the earliest and conceptually simplest approaches, is deterministic, rule and threshold based workflows. Studies belonging to this class aim to distinguish individual tree crowns through superpixels with the help of predefined rules, without using learning based models or global optimization schemes (Jiao & Deng, 2016).

After the superpixel is produced, it is represented with a multi component feature vector (for detailed information see Section 3.4: Superpixel Level Feature Representation). What differentiates this type of workflow is the refinement stage based on texture and edge information it contains. At this stage, the standard deviation of pixel intensities (σ_i) is calculated in order to determine the internal complexity of superpixels. If the σ_i value is greater than a predefined threshold value, it is labeled as having high complexity. Pixels with high complexity mean that they are located at the place where the tree crown intersects with another object. For these reasons, the information they contain is unreliable. The threshold value is determined experimentally.

At the refinement stage, the Canny edge detector is activated for such complex superpixels. The edge information obtained with the Canny algorithm is used in redrawing superpixel boundaries. In this way, a complex labeled superpixel that is initially in one piece but actually contains more than one object is divided into regions, producing sub segments that better conform to crown boundaries.

The most prominent advantage of such rule based workflows is interpretability and reproducibility. Each decision step used (σ_i calculation, threshold value, Canny edges) is clearly defined, and model parameters can be directly controlled by the user. However, the fact that the success of the methods largely depends on parameters and may vary in different scenarios puts the user in a difficult position. Still, such methods show that even without using learning in superpixel based ITC segmentation, meaningful and competitive results can be obtained through carefully designed heuristic rules (Jiao & Deng, 2016).

3.5.2. Superpixel Based Graph Workflows

The second important workflow type in superpixel based ITC segmentation is those built on graph representations and energy distance optimization. In such graphic approaches, the superpixel is considered as a structural element defined through node or core and neighbor relationships (Xiao et al., 2019). This method presents frameworks in which decisions about which crown the superpixel belongs to are made based on global or semi global optimization results rather than singular rules.

First, the neighborhood relationship between superpixels is established with graph methods. Each superpixel is defined as a graph node. The edges between these nodes are defined with weighted relationships that include not only spatial adjacency, but also multiple criteria such as spectral similarity, height difference, and spatial distance. In this way, the superpixel set becomes a multidimensional graph representing the crown structure. In such approaches, the decision making path is based on clustering or a relationship model with a weighted similarity function. A cost function defining the relationship between superpixels is prepared. The function includes spectral difference, spatial distance, and if available height difference obtained from DSM with different weights. The weights are used to balance the contribution of different information sources to the decision process. For example, it plays a determining role in separating spectrally similar but spatially distant crowns. The final crown segmentation is obtained through superpixel combinations that provide the global or local minimum of this cost function (Xiao et al., 2019). In this study, it is noteworthy that threshold values are not the decision itself but a part of the optimization process.

The most important advantage of these graph based workflows in terms of ITC segmentation is making local decisions consistent within a global context. Especially in forests with dense cover or overlapping crown structures, graph based approaches explicitly include the relationship of the superpixel with its surroundings into the model. In this way, crown boundaries are determined in a more balanced and geometrically consistent manner.

3.5.3. Superpixel Based Object Classification Pipelines

The third basic approach in superpixel based ITC segmentation is workflows that accept superpixels as basic objects and label them through supervised classification. In this framework, the superpixel is evaluated neither only as an intermediate partition nor as a node of an optimization graph. On the contrary, it is an independent sample that is represented with a feature vector and can be assigned to a class.

The common starting point of these workflows is the over segmentation of high resolution forest images at the superpixel level with the SLIC algorithm. Then, each superpixel is represented with a multidimensional feature vector and carried to the supervised classification stage. Martins et al. (2019) separated superpixels into tree and non tree classes by using classical machine learning algorithms such as Random Forest (RF) and Support Vector Machine (SVM). In this approach, each superpixel is used as a labeled sample during the training stage. The classifier learns discriminative patterns among color, texture, and shape features. Tree based methods such as RF provide relative robustness against high dimensional texture features. SVM can define decision boundaries between classes more sharply.

Martins et al. (2021) carried learning one step further. It integrates superpixel based representation with deep learning. In this approach, the superpixel is used as a direct input or an input mask for the CNN.

3.5.4. Superpixel Based Deep Learning Workflows

Superpixel based deep learning workflows redefine the role of the superpixel in ITC segmentation. In this approach, the superpixel is not only a pre processing or partitioning tool. On the contrary, it is positioned as a direct component of the learning architecture. The common reason for the emergence of workflows in this class is the high computational cost of CNNs operating at the pixel level and their sensitivity to noise. Superpixels produced with algorithms such as SLIC significantly reduce the size of the network input compared to pixels. Thus, the deep network learns over a superpixel based representation instead of millions of pixels. This situation not only increases computational efficiency; at the same time, it enables learning to take place over higher level semantic contexts.

In one study, superpixel production was used as a mandatory step before CNN. Superpixels obtained with SLIC were either given to the CNN directly as region based inputs or spatial consistency was ensured by using superpixel boundaries as masks on pixel based CNN inputs. This design allowed the CNN to evaluate pixels located within the same crown in a consistent context. As a result, the superpixel has become not only a data reduction tool for CNN but also a building block that determines the spatial organization of learning (Martins et al., 2019).

In a different study, superpixel based deep learning workflows were expanded with the temporal dimension (Firoze et al., 2023). In this study, superpixels produced from multi temporal RGB images are tracked as consistent regions across successive time steps and the deep learning model learns these superpixel based time series. The superpixel approach undertakes two critical functions here: the first is to reduce temporal noise by grouping pixels that change over time under homogeneous regions. The second is to enable the CNN or sequential network structures to learn region level change patterns. In this way, the model can capture structural and spectral changes at the crown level instead of temporary variations in individual pixels.

3.6. Evaluation Metrics for Superpixel Based ITC Segmentation

Superpixel based individual tree crown (ITC) segmentation studies use evaluation metrics that vary depending on the output level targeted by the methods and the type of data used. According to the reviewed studies; it is not possible for different segmentation methods to represent their performance with a single accuracy metric. Instead, a pixel and object based evaluation approach is adopted.

3.6.1. Pixel Level Accuracy Metrics

The most common evaluation approach in superpixel based ITC segmentation studies is the pixel level comparison of the produced segmentation outputs with reference mask data (Martins et al., 2019; Li et al., 2020; Martins et al., 2021; Wang et al., 2023; Liu et al., 2023). The accuracy of superpixel or CNN based outputs is quantitatively measured based on whether the pixel matches the reference label or not. This approach provides a direct and repeatable framework for comparing the overall performance of methods, especially in cases where ground truth data are available in raster form.

In these studies, Overall Accuracy (OA) is the most basic performance indicator. OA expresses the ratio of correctly classified pixels to all pixels. It provides a quick summary of the overall performance of the methods. However, since class distribution is generally imbalanced in the ITC context, OA alone has not been sufficient. In most of these studies, OA has been evaluated together with class sensitive metrics such as Precision, Recall and F1 score. Precision shows how many of the pixels labeled as crown by the model are actually crown, while Recall reveals how many of the reference crown pixels can be correctly captured. F1 score reflects the balance between these two measures and is used especially to evaluate the trade off between false positives and false negatives.

Another group of metrics that stand out in pixel level evaluation are overlap based measures (Martins et al., 2019; Martins et al., 2021; Wang et al., 2023). Metrics such as Intersection over Union (IoU) and Dice coefficient have been used. IoU measures the ratio of the intersection between the predicted segmentation mask and the reference mask to their union, expressing the spatial agreement of the segmentation. The Dice coefficient similarly evaluates overlap and can provide a more sensitive measurement especially in areas where small crowns are present. In terms of ITC segmentation, these metrics reflect not only correct class information but also how accurately crown areas are represented spatially. A common characteristic of the studies under this subheading is that the outputs of superpixel or CNN based methods are produced directly in raster format or converted into this format. This situation has made the application of pixel level metrics a natural and practical option.

3.6.2. Object Level (Crown Based) Evaluation Metrics

Some studies have used crown based accuracy analyses (Jiao & Deng, 2016; Xiao et al., 2019; Wang et al., 2025). A common characteristic of these studies is that they evaluate the success of segmentation outputs based on correctly detected individual crowns rather than the number of correctly classified pixels. In these studies, one of the most commonly used metrics is the crown detection rate. It quantitatively expresses how many of the reference crowns can be successfully detected by the method. In one study, crown candidates obtained after superpixel refinement were matched one by one with reference crowns and correct detection rates were calculated (Jiao & Deng, 2016).

These metrics are combined with matching based F1 score in most studies. This metric reflects the balance between Precision and Recall over correctly matched crowns and can consider both over segmentation and under segmentation situations at the same time. While evaluating the success of superpixel based methods, a one to one crown matching approach has been adopted, where each reference crown is matched with only one predicted crown (Xiao et al., 2019).

4. Comparative Evaluation of Superpixel Based ITC Methods

The comparison of superpixel based ITC segmentation studies cannot be performed over a single accuracy metric due to the diversity of data types used and validation metrics. In the reviewed studies, performance has been reported through pixel level classification accuracy, object level crown detection, mask overlap, and instance based metrics. This situation shows that comparison is meaningful only within the same metric family.

In studies using pixel level evaluation, the highest accuracies were obtained in UAV based approaches where superpixel representations were combined with supervised learning. In particular, Adhikari et al. (2021) reported 98.8 percent OOB accuracy, while Martins et al. (2021) reported 0.932 accuracy and F1 score with deep learning integration. In satellite based studies, accuracy levels remained more limited; Liu et al. (2023) reached an overall accuracy value of 0.89 with a superpixel supported deep network approach.

In object and instance level evaluations, overlap and detection performance come to the forefront instead of pixel accuracy. Firoze et al. (2023), with a deep learning approach using temporal superpixel representations, obtained AP = 74.6 and 91.5 percent tree counting accuracy, showing that superpixel representations are effective in object based and temporal tasks. In general, the comparative evaluation reveals that the highest accuracies are obtained in scenarios where high resolution UAV data, rich feature representation, and learning based methods are used together.

5. Challenges and Limitations

Superpixel based individual tree crown (ITC) segmentation, although it offers important advantages in high resolution remote sensing data, has some structural limitations that are clearly observed in the literature. At the beginning of these, there is the fact that the parameters used in superpixel production (for example superpixel number, compactness) are highly dependent on the scene and the sensor. In most studies, these parameters are determined experimentally, and there is no generally applicable adjustment strategy between different forest types.

Another basic limitation appears in dense and homogeneous canopy structures. Models have difficulty separating spectrally similar neighboring crowns in superpixel representations created based only on optical images. Naturally, this situation leads to under segmentation errors. Although it has been shown that structural data (DSM, LiDAR) can reduce this problem, the fact that such data are not accessible for every study area limits the applicability of the method.

Finally, the diversity and lack of standardization in evaluation metrics make the direct comparison of methods difficult. Reporting high pixel level accuracies does not always mean high success at the individual crown level. This situation makes it difficult to interpret the real performance of superpixel based ITC methods.

6. Future Directions

The first prominent direction for future studies is the development of adaptive superpixel production approaches. Instead of fixed parameter algorithms, dynamic superpixel representations that take into account the spectral and structural complexity of the scene may provide more consistent results across different forest conditions.

The second important direction is the tighter integration of superpixel representations with graph and deep learning architectures. Approaches in which the superpixel is considered not only as a pre processing step but as a basic unit of learning have the potential to increase contextual consistency, especially in scenes with complex crown interactions.

In addition, multi source data fusion (RGB, multispectral, DSM, LiDAR) is one of the main factors that increase the accuracy of superpixel based ITC segmentation. In this direction, flexible frameworks that combine different data types under a common region based representation have critical importance for future applications. Finally, the development of standard evaluation protocols that consider pixel, object and structural metrics together will make an important contribution to the maturation of the field. The fact that the number of studies performing superpixel based ITC segmentation in the literature is not very high, and the high performances shown by the existing ones, gives the impression that research in this area should be increased.

7. Conclusion

This book chapter focuses on superpixel-based individual tree crown segmentation methods applied to remote sensing data. The theoretical foundations of superpixel segmentation techniques, application examples in the ITC context, and different workflows have been examined comprehensively. The literature shows that superpixel based methods provide more efficient, crown boundary sensitive, and biologically meaningful representations compared to pixel based approaches. Especially learning based approaches and approaches using multi source data reach the highest accuracy levels. On the other hand, parameter sensitivity, uncertainties originating from spectral similarity, and the lack of evaluation standards are among the current limitations of the method. In general, superpixel based ITC segmentation offers a strong and flexible methodological framework for precision forestry, ecosystem monitoring, and environmental analyses at the individual tree level. In the future, it is predicted that this method will be further strengthened in terms of accuracy and generalizability with approaches based on adaptive superpixel production and graph based deep learning integration.

Acknowledgement

The authors acknowledge the EU COST (European Cooperation in Science and Technology) ant its Actions CA17134 “Optical Synergies For Spatiotemporal Sensing of Scalable Ecophysiological traits” (SENSECO) and Action CA22136 “Pan-European Network of Green Deal Agriculture and Forestry Earth Observation Science” (PANGEOS) for providing a platform for scientific networking and knowledge exchange related to this work.

References

Achanta, R., Shaji, A., Smith, K., Lucchi, A., Fua, P., & Süsstrunk, S. (2012). SLIC superpixels compared to state-of-the-art superpixel methods. *IEEE transactions on pattern analysis and machine intelligence*, *34*(11), 2274-2282.

Adhikari, A., Kumar, M., Agrawal, S., & S, R. (2021). An integrated object and machine learning approach for tree canopy extraction from UAV datasets. *Journal of the Indian Society of Remote Sensing*, *49*(3), 471-478.

Boemer, F., Ratner, E., & Lendasse, A. (2018). Parameter-free image segmentation with SLIC. *Neurocomputing*, *277*, 228-236.

Buchner, L., Eisen, A. K., & Jochner-Oette, S. (2025). How precise is precise enough? Tree crown segmentation using high resolution close-up multispectral UAV images and its effect on NDVI accuracy in Fraxinus excelsior L. trees. *Journal of Forestry Research*, *36*(1), 137.

Calders, K., Adams, J., Armston, J., Bartholomeus, H., Bauwens, S., Bentley, L. P., ... & Verbeeck, H. (2020). Terrestrial laser scanning in forest ecology: Expanding the horizon. *Remote Sensing of Environment*, *251*, 112102.

Crommelinck, S., Bennett, R., Gerke, M., Koeva, M. N., Yang, M. Y., & Vosselman, G. (2017). SLIC superpixels for object delineation from UAV data. *ISPRS Annals of the Photogrammetry, Remote Sensing and Spatial Information Sciences*, *4*, 9-16.

Chen, Z., Guo, B., Li, C., & Liu, H. (2020, September). Review on superpixel generation algorithms based on clustering. In *2020 IEEE 3rd international conference on information systems and computer aided education (ICISCAE)* (pp. 532-537). IEEE.

Cong, L., Ding, S., Wang, L., Zhang, A., & Jia, W. (2018). Image segmentation algorithm based on superpixel clustering. *IET Image Processing*, *12*(11), 2030-2035.

Csillik, O., Cherbini, J., Johnson, R., Lyons, A., & Kelly, M. (2018). Identification of citrus trees from unmanned aerial vehicle imagery using convolutional neural networks. *Drones*, *2*(4), 39.

Deluzet, M., Erudel, T., Briottet, X., Sheeren, D., & Fabre, S. (2022). Individual tree crown delineation method based on multi-criteria graph using geometric and spectral information: Application to several temperate forest sites. *Remote Sensing*, *14*(5), 1083.

Dersch, S., Schöttl, A., Krzystek, P., & Heurich, M. (2024). Semi-supervised multi-class tree crown delineation using aerial multispectral imagery and lidar data. *ISPRS Journal of Photogrammetry and Remote Sensing*, *216*, 154-167.

Felzenszwalb, P. F., & Huttenlocher, D. P. (2004). Efficient graph-based image segmentation. *International journal of computer vision*, *59*(2), 167-181.

Firoze, A., Wingren, C., Yeh, R. A., Benes, B., & Aliaga, D. (2023). Tree instance segmentation with temporal contour graph. In *Proceedings of the IEEE/CVF Conference on Computer Vision and Pattern Recognition* (pp. 2193-2202).

Ibrahim, A., & El-kenawy, E. S. M. (2020). Image segmentation methods based on superpixel techniques: A survey. *Journal of Computer Science and Information Systems*, *15*(3), 1-11.

Ilyas, T., Khan, A., Umraiz, M., & Kim, H. (2020). Seek: A framework of superpixel learning with cnn features for unsupervised segmentation. *Electronics*, *9*(3), 383.

Jampani, V., Sun, D., Liu, M. Y., Yang, M. H., & Kautz, J. (2018). Superpixel sampling networks. In *Proceedings of the European Conference on Computer Vision (ECCV)* (pp. 352-368).

Jiao, J., & Deng, Z. (2016). Individual Building Rooftop and Tree Crown Segmentation from High-Resolution Urban Aerial Optical Images. *Journal of Sensors*, *2016*(1), 1795205.

Kattenborn, T., Leitloff, J., Schiefer, F., & Hinz, S. (2021). Review on Convolutional Neural Networks (CNN) in vegetation remote sensing. *ISPRS journal of photogrammetry and remote sensing*, *173*, 24-49.

Ke, Y., & Quackenbush, L. J. (2011). A review of methods for automatic individual tree-crown detection and delineation from passive remote sensing. *International Journal of Remote Sensing*, *32*(17), 4725-4747.

Liu, Y. J., Yu, C. C., Yu, M. J., & He, Y. (2016). Manifold SLIC: A fast method to compute content-sensitive superpixels. In *Proceedings of the IEEE conference on computer vision and pattern recognition* (pp. 651-659).

Liu, M. Y., Tuzel, O., Ramalingam, S., & Chellappa, R. (2011, June). Entropy rate superpixel segmentation. In *CVPR 2011* (pp. 2097-2104). IEEE.

Liu, Y., Zhang, H., Cui, Z., Lei, K., Zuo, Y., Wang, J., ... & Qiu, H. (2023). Very high resolution images and superpixel-enhanced deep neural forest promote urban tree canopy detection. *Remote Sensing*, *15*(2), 519.

Li, Z., & Chen, J. (2015). Superpixel segmentation using linear spectral clustering. In *Proceedings of the IEEE conference on computer vision and pattern recognition* (pp. 1356-1363)..

Li, L., Chen, J., Mu, X., Li, W., Yan, G., Xie, D., & Zhang, W. (2020). Quantifying understory and overstory vegetation cover using UAV-based RGB imagery in forest plantation. *Remote Sensing*, *12*(2), 298.

Martins, J., Junior, J. M., Menezes, G., Pistori, H., Sant, D., & Gonçalves, W. (2019, July). Image segmentation and classification with SLIC Superpixel and convolutional neural network in forest context. In *IGARSS 2019-2019 IEEE International Geoscience and Remote Sensing Symposium* (pp. 6543-6546). IEEE.

Martins, J. A. C., Menezes, G., Goncalves, W., Sant'Ana, D. A., Osco, L. P., Liesenberg, V., ... & Junior, J. M. (2021). Machine learning and SLIC for Tree Canopies segmentation in urban areas. *Ecological informatics*, *66*, 101465.

Modica, G., Messina, G., De Luca, G., Fiozzo, V., & Praticò, S. (2020). Monitoring the vegetation vigor in heterogeneous citrus and olive orchards. A multiscale object-based approach to extract trees' crowns from UAV multispectral imagery. *Computers and Electronics in Agriculture*, *175*, 105500..

Ng, T. C., Choy, S. K., Lam, S. Y., & Yu, K. W. (2023). Fuzzy superpixel-based image segmentation. *Pattern Recognition*, *134*, 109045.

Peng, J., Shen, J., Yao, A., & Li, X. (2015). Superpixel optimization using higher order energy. *IEEE Transactions on Circuits and Systems for Video Technology*, *26*(5), 917-927.

Song, G., Wu, S., Lee, C. K., Serbin, S. P., Wolfe, B. T., Ng, M. K., ... & Wu, J. (2022). Monitoring leaf phenology in moist tropical forests by applying a superpixel-based deep learning method to time-series images of tree canopies. *ISPRS Journal of Photogrammetry and Remote Sensing*, *183*, 19-33.

Ren, & Malik. (2003, October). Learning a classification model for segmentation. In *Proceedings ninth IEEE international conference on computer vision* (pp. 10-17). IEEE.

Stutz, D., Hermans, A., & Leibe, B. (2018). Superpixels: An evaluation of the state-of-the-art. *Computer Vision and Image Understanding*, *166*, 1-27.

Subedi, P. B., Zurqani, H. A., Blazier, M. A., Yáñez, M., & Cunningham, K. (2025, April). Automated Individual Tree Crown Detection and Segmentation using Simple Non-Iterative Clustering (SNIC) Algorithms and High-Resolution LiDAR. In *2025 IEEE Conference on Technologies for Sustainability (SusTech)* (pp. 1-8). IEEE.

Van den Bergh, M., Boix, X., Roig, G., De Capitani, B., & Van Gool, L. (2012, October). Seeds: Superpixels extracted via energy-driven sampling. In *European conference on computer vision* (pp. 13-26). Berlin, Heidelberg: Springer Berlin Heidelberg.

Wan Mohd Jaafar, W. S., Woodhouse, I. H., Silva, C. A., Omar, H., Abdul Maulud, K. N., Hudak, A. T., ... & Mohan, M. (2018). Improving individual tree crown delineation and attributes estimation of tropical forests using airborne LiDAR data. *Forests*, *9*(12), 759.

Wang, Y., Yang, X., Zhang, L., Fan, X., Ye, Q., & Fu, L. (2023). Individual tree segmentation and tree-counting using supervised clustering. *Computers and Electronics in Agriculture*, *205*, 107629.

Wang, M., Liu, X., Gao, Y., Ma, X., & Soomro, N. Q. (2017). Superpixel segmentation: A benchmark. *Signal Processing: Image Communication*, *56*, 28-39.

Wang, R., Hu, C., Han, J., Hu, X., Zhao, Y., Wang, Q., ... & Xie, Y. (2025). A Hierarchic Method of Individual Tree Canopy Segmentation Combing UAV Image and LiDAR. *Arabian Journal for Science and Engineering*, *50*(10), 7567-7585.

Weinstein, B. G., Marconi, S., Bohlman, S. A., Zare, A., Singh, A., Graves, S. J., & White, E. P. (2021). A remote sensing derived data set of 100 million individual tree crowns for the National Ecological Observatory Network. *Elife*, *10*, e62922.

Wu, X., Liu, X., Chen, Y., Shen, J., & Zhao, W. (2018). A graph based superpixel generation algorithm. *Applied Intelligence*, *48*(11), 4485-4496.

Xiao, C., Qin, R., Huang, X., & Li, J. (2018, July). Individual tree detection from multi-view satellite images. In *IGARSS 2018-2018 IEEE International Geoscience and Remote Sensing Symposium* (pp. 3967-3970). IEEE.

Xiao, C., Qin, R., Xie, X., & Huang, X. (2019). Individual tree detection and crown delineation with 3D information from multi-view satellite images. *Photogrammetric Engineering & Remote Sensing*, *85*(1), 55-63.

Yang, J., Gan, R., Luo, B., Wang, A., Shi, S., & Du, L. (2024). An improved method for individual tree segmentation in complex urban scenes based on using multispectral LiDAR by deep learning. *IEEE Journal of Selected Topics in Applied Earth Observations and Remote Sensing*, *17*, 6561-6576.

Yang, F., Sun, Q., Jin, H., & Zhou, Z. (2020). Superpixel segmentation with fully convolutional networks. In *Proceedings of the IEEE/CVF conference on computer vision and pattern recognition* (pp. 13964-13973).

Zhou, Y., Wang, L., Jiang, K., Xue, L., An, F., Chen, B., & Yun, T. (2020). Individual tree crown segmentation based on aerial image using superpixel and topological features. *Journal of applied remote sensing*, *14*(2), 022210-022210.

Chapter 14

SUSTAINABILITY AND ADSORPTION APPLICATIONS IN ADSORBENT PRODUCTION

Çiğdem SARICI ÖZDEMİR[1]

---

[1] Prof. Dr. Inonu University, Faculty of Engineering, Department of Chemical Engineering, Malatya, Turkey, https://orcid.org/0000-0003-2129-3044

1. INTRODUCTION

Earth, home to numerous civilizations and many endangered species, faces a grave threat brought on by technological innovations. This threat is climate change. The causes of climate change include increasing human needs due to a growing population, new technologies developed to meet these needs, a mindset focused on consumption rather than production, and the resulting pollution. This pollution poisons humanity through three different pathways: air, soil, and water. The air we breathe, the fruits and vegetables we eat, and the water we drink, along with numerous toxicological factors, contribute to an increase in diseases.

Adsorption, defined as the retention of gases and liquids on solid surfaces, eliminates these effects. Adsorption, which can occur physically or chemically, can be classified based on the equilibrium between solid, liquid, and gas molecules. One of the fundamental elements in adsorption is the solid to which the contaminant adheres, namely the adsorbent. The porous structure of adsorbents plays a major role in retaining contaminants. Differently sized pores can retain or trap molecules of different sizes. The primary factor determining the surface properties of an adsorbent is the raw material from which it is produced. When these raw materials are examined, they can be classified into three different types: agricultural waste, industrial waste, and biological waste. When we consider adsorbent production as a waste utilization process, it also appears to have an economic contribution. The crucial factor is the continuity, or sustainability, of this production [1,2].

The dictionary definition of sustainability conveys the meaning of continuity. Economically, sustainability refers to the efficient and balanced use of resources to meet the needs of present and future generations. Therefore, recycling waste and repurposing it for different purposes will also contribute to sustainability. Different methods are used in adsorbent production. These methods for activating the surface of raw materials can be diversified into physical activation, chemical activation, and photocatalyst. Methods such as Frourier Transform Infrared Spectroscopy (FTIR), Scanning Electron Microscopy (SEM), X-Ray Diffraction (XRD), and BET (Brunauer–Emmett–Teller) are used in the characterization of the resulting adsorbent. Adsorption equilibrium studies provide information about the adsorption isotherm type, and kinetic studies can determine the reaction mechanism and thermodynamic expressions [3-4]. This topic will discuss the effective parameters in adsorbent production and their impact on adsorption applications.

2. ADSORBENT AND PRODUCTION METHODS

Many raw materials are used in the production of adsorbents, which are the structures on which unwanted contaminants form the solid phase during the adsorption process. These raw materials generally consist of waste. When these wastes are classified:

Agricultural wastes: Agricultural wastes are considered wastes and residues resulting from the production, consumption, or processing of plant and animal products. The amount and composition of solid wastes produced are influenced by various conditions, such as the socio-economic characteristics of communities or societies, their traditional structures, dietary habits, geography, occupations, and climate. It is crucial that these wastes be recycled and utilized for the national economy. Examples include fruit peels, seeds, and pulp[5].

Biological wastes: Materials that are naturally decomposed by microorganisms such as bacteria, algae, or fungi are called biological wastes. Biological wastes include shells, sediments, leaves, food scraps, eggshells, and grass clippings. In addition, waste activated sludge from activated sludge systems and algae collected from the sea are used as inexpensive and high-capacity adsorbents for various heavy metals and dyes. Molds used in the production of various enzymes also play an important role in the adsorption of toxic substances[6].

Industrial wastes: Byproducts or intermediate products generated during industrial production processes can be considered industrial wastes. These wastes generally cannot be consumed or processed over time and form as slag. Geopolymer, a thermal power plant waste, is an example of industrial waste. In addition, process wastes such as blast furnace slag from iron and steel production, polymeric waste from plastic and resin production, and oil and heavy metal sludge are also included among industrial wastes[6].

Table 1 shows adsorbents produced using different raw materials and their adsorption capacities. An examination of the table reveals that adsorption capacity changes depending on dye concentration in studies using the same dye. Adsorption rates on the solid surface varied depending on the functional groups of the adsorbents, the variety of production methods, and the changes in porosity caused by pretreatment.

Table1 Adsorbents produced using different raw materials and their adsorption capacities

Adsorbents	Dye (methylene blue) concentration (mg/L)	Adsorption capacity (mg/g)	Reference
Papaya seeds	10	120,48	[7]
Apricot seeds	80	19,1	[8]
Cedrela odorata seeds	100	158,7	[9]
Orange seeds	25	38	[10]
Olive black seeds	50	476,2	[11]
Avacado seeds	10	67,57	[12]
Textural waste	100	64,30	[6]
Peanut shell	100	67,57	[5]
Activated carbon	100	66,56	[13]

When producing adsorbents with desired surface properties using different types of waste, physical activation, chemical activation, and photocatalytic activation methods can be used.

In the physical activation method, the waste is activated under an inert atmosphere at different temperatures. As a result of this activation, changes begin to occur on the waste surface, opening pores and creating new pores. Changes in channels and cracks create new areas for the molecules to be removed. This results in a scavenging of the solid surface area[14].

In the chemical activation method, the waste is pretreated with a chemical ($ZnCl_2$, H_3PO_4, KOH, NaOH, etc.). The optimum conditions for this process in terms of time, quantity, and temperature can be determined. Physical activation is performed under an inert atmosphere to ensure the reactivation of the pores that have opened and filled after the chemical treatment[15].

In the photocatalytic activation process, the waste is activated with a suitable photocatalyst. Among these photocatalysts, TiO_2 and ZnO are widely used. In photocatalytic treatment studies, TiO_2 is widely used as a catalyst for the photocatalytic removal of pollutants due to its non-toxicity, wide band gap, affordability, ability to operate under atmospheric pressure and at room temperature, and rapid electron transfer during the process[16].

Studies show that the surface area of the adsorbent varies depending on the raw material used and the activation method used (Table2). Chemical activation will increase the pores, and physical activation will remove chemicals that have filled these opened pores. Physical activation alone can achieve the desired surface area and pore properties. The activation temperature may vary depending on the decomposition temperature of the chemicals or raw materials. To fully open the pores and achieve the smallest pores, the optimum time must be calculated. Depending on the bond breaking energy and intermolecular forces, variables such as gas flow rate, raw material amount, chemical concentration, temperature and time in the activation method can be determined. While physical activation is generally used for agricultural waste, chemical activation is preferred for industrial waste. This is primarily because industrial waste undergoes a formation process and is exposed to various types of chemicals during this process. Removing these chemicals from the structure and promoting pore development may not be possible through physical activation alone; chemical activation is also used in conjunction.

Table2 Surface area changes depending on adsorbent and production methods

Adsorbents	Activation/Temperature	Surface Area (m^2/g)	Reference
Tea Branches	Pyrolysis/600ºC	176	[15]
Paddy Straw	Pyrolysis/700ºC	311	[14]
Carbon Nanotube	Catalytic chemical vapor deposition	180,9	[17]
Fe-MgO nanocomposite	Chemical coprecipitation	199,78	[18]
eggshell/starch/Fe_3O_4		35,648	[19]

3. ADSORPTION MECHANISM

Dipole-dipole, induced dipole, hydrogen bonding, chemical bonding, and ion exchange interactions between the adsorbed material and the porous solid represent the various interactions of the adsorption mechanism. Depending on whether the adsorbed material is cationic or anionic, the surface properties of the solid, and the diffusion pattern, adhesion occurs through chemical adsorption or physical adsorption. Lignin, cellulose, and hemicellulose are found in most agricultural wastes. These structures, particularly in cationic dyes, form hydroxy groups through hydrogen bonding or electrostatic forces. Furthermore, depending on the acidic or basic nature of the chemical used in adsorbent production through chemical activation, various chemical bonds, including aromatic groups, can be observed between the dye and the adsorbent. Electrostatic interactions occur between charged particles. If the adsorbent surface and the dye surface are charged differently, attraction occurs; if they are charged equally, repulsion occurs. The pore size between the adsorbed material and the adsorbent also affects the adsorption mechanism. If the size of the organic molecule is smaller than the pore size of the adsorbent, the adsorbent pores will fill over time. In studies evaluating industrial wastes as adsorbents, adsorption occurs in the active sites via ion exchange, complexation, or electrostatic attraction. Complexation is the most acceptable mechanism for the retention of toxic substances. The alkaline properties of industrial wastes and the π bonds in the C=C structure cause both physical and chemical adsorption on the modified surface as a result of H-bonding and van der Waals attraction. In addition, the inorganic and organic structures of the adsorbed substance mean different adsorption efficiencies and different adsorption mechanisms. While inorganic toxicants are primarily adsorbed via H-bonding, precipitation, ion exchange, and electrostatic interaction, the adsorption mechanism of organics generally involves complexation, y-electron donor-acceptor interactions, and van der Waals attraction [20].

4. ADSORPTION ISOTHERMS

Adsorption, which occurs by adsorption on a solid surface, is mathematically expressed as the amount of substance adsorbed on a unit adsorbent. The amount of substance adsorbed per unit mass of adsorbent is a function of temperature, concentration, pressure, or equilibrium pressure. When the temperature is held constant, this function can be expressed by the following equation.

$$q_e = \frac{(C_0 - C_e)\,V}{m}$$

q_e = Amount of substance adsorbed on unit adsorbent (mg/g)

C_0 = Initial dye concentration of the solution (mg/L)

C_e = Concentration of dye remaining in the solution after adsorption (mg/L)

V = Volume of the solution (L)

m = Weight of the adsorbent (g)

Various models are used to determine the mechanism by which the adsorption process occurs and to determine the relationship between the adsorbed substance and the solid. The Langmuir isotherm [21] is a process in which physical and chemical adsorption are observed simultaneously. The Freundlich isotherm [22], which advocates a heterogeneous adsorption mechanism, also demonstrates the formation of different types of active centers. The Redlich-Peterson [23] equation, where the ideal monolayer approach is not accepted, is also related to the Freundlich equation. The Toth [24] isotherm, where surface heterogeneity is prominent, appears as an isotherm with three unknowns. A combination of the Langmuir and Freundlich isotherms is the Sips isotherm [25]. The relationship between thermodynamic relations, heat of adsorption, and adsorption surface coverage is given by the Temkin isotherm [26]. The Dubinin-Radushkevich [27] isotherm describes the multilayer adsorption of molecules involving Wanderwaals forces on a porous solid surface. Another isotherm based on determining the pore structure of a solid is the Dubinin-Astakhov [28] isotherm. These equations and equations, derived by taking into account the basic approaches of the adsorption mechanism, are given in Table 3. This table shows the nonlinear equation and linear equation for each equation. Information is also given about the values to be applied in graphical calculations. In the Langmuir equation, Q_o represents the maximum adsorption capacity (mg/g), and b (L/mg) represents the Langmuir constant. Calculations for the feasibility of adsorption can be made with the b value.

While the K_f value is the Freundlich constant, the 1/n value can vary between 0 and 1. When it is 1, linear adsorption occurs. For the D-R equation; k_{ad} (mol^2/kJ^2) is the activity coefficient depending on the average free energy, and ε (kJ/mol) is the Polonyi potential. In the D-A isotherm model, E_{DA} and n_{DA} are size constants. In the calculation of the heat of adsorption, b_T represents the Temkin constant, and A_T (L/mg) represents the equilibrium constant. K_R is the Redlich-Peterson coefficient, and β is a dimensionless R-P constant varying between 0 and 1. In the Sips equation, which is an equation derived to complete the Freundlich isotherm based on the assumptions made, K_S (L/mg) represents the equilibrium constant, β_s parameter represents the dimensionless quantity, and a_S (mg/g) represents the maximum adsorption capacity. In the Toth isotherm, where surface heterogeneity is effective, K_T (mg/g) is a constant indicating surface heterogeneity, and a_T is the Toth constant, which increases with temperature. The t parameter is independent of temperature and defines the degree of adsorption heterogeneity.

5. ADSORPTION KINETIC

Kinetic approaches, which express the time-varying evolution of adsorption outside of equilibrium, can provide insight into the mass transfer steps and the properties of the adsorbent. Models created in adsorption kinetics are defined as reaction-dependent, mass transfer-dependent, and reaction-diffusion-based equations. When examining the mechanism of kinetics, four steps are identified. The first step involves the transport of liquid molecules to the hydrodynamic boundary layer around the adsorbent; the second step involves the adsorbate passing through the fluid film within the adsorbent; the third step involves internal diffusion, pore diffusion, and surface diffusion; and finally, the molecules adsorb onto active sites on the solid surface. Because the first and fourth steps are so rapid, the second and third steps determine the rate of reaction. Resistance plays a significant role in determining the rate of adsorption. If the resistance created during adsorption increases, the concentration difference will also increase to overcome it.

If adsorption occurs chemically as a surface reaction, models based on reaction kinetics are used based on experimental data. These models, which ignore mass transfer mechanisms, are presented in Table 3. The pseudo-order equations are analyzed differently depending on the adsorption process. Adsorption kinetic data cover the period from the initial equilibrium stage to the final equilibrium stage. However, the time required for adsorption to reach equilibrium is quite long. In this case, many studies have reported that the pseudo-second-order equation actually fits the adsorption equation incorrectly. To eliminate these problems, a definition called a mixed-order model can be developed. This definition incorporates both pseudo-first-order and pseudo-second-order kinetic models.

Table 3 Isotherm equations

Isotherm	Nonlinear form	Linear form	Plot
Langmuir	$q_e = \frac{Q_o b C_e}{1 + bC_o}$	$\frac{C_e}{q_e} = \frac{1}{bQ_o} + \frac{C_e}{Q_o}$	$\frac{C_e}{q_e}$ vs C_e
Freundlich	$q_e = K_F C_e^{1/n}$	$\ln q_e = \ln K_f + \frac{1}{n} \ln C_e$	$\ln C_e$ vs $\ln q_e$
Dubinin-Radushkevich	$q_e = (q_m) \exp(-k_{ad} \varepsilon^2)$	$\ln q_e = \ln q_m - k_{ad} \varepsilon^2$	$\ln q_e$ vs ε^2
Temkin	$q_e = \frac{RT}{b_T} \ln A_T C_e$	$q_e = \frac{RT}{b_T} \ln A_T + \left(\frac{RT}{b_T} \right) \ln C_e$	Q_e vs $\ln C_e$
Dubinin-Astakhov	$q_e = (q_{mDA}) \exp\left(\frac{-\varepsilon}{E_{DA}} \right)^{n_{DA}}$	$\ln q_e = \ln q_{mDA} - n_{DA} \frac{-\varepsilon}{E_{DA}}$	$\ln q_e$ vs ε^2
Redlich-Peterson	$q_e = \frac{K_R C_e}{1 + a_R C_e^{\beta}}$	$\ln\left(K_R \frac{C_e}{q_e} - 1 \right) = \beta \ln(C_e) + \ln(a_R)$	$\ln\left(K_R \frac{C_e}{q_e} - 1 \right)$ vs $\ln C_e$
Sips	$q_e = \frac{K_s a_s C_e^s}{1 + a_s C_e^s}$	$s \ln(C_e) = -\ln\left(\frac{K_s}{q_e} \right) + \ln a_s$	$\ln\left(\frac{K_s}{q_e} \right)$ vs $\ln C_e$
Toth	$q_e = \frac{K_T C_e}{(a_T + C_e^t)^{1/t}}$	$\ln\left(\frac{q_e}{K_T} \right) = \ln(C_e) - \frac{1}{t} \ln(a_T + C_e)$	$\ln\left(\frac{q_e}{K_T} \right)$ vs $\ln C_e$

Unlike chemical adsorption, ion exchange and ionic bond formation reactions are not very common. Mass transfer and diffusion-based models are used in adsorption mechanisms where such features occur. When examining reaction kinetics in models, the absence of chemical adsorption is assumed. In mass transfer, defined as the movement of molecules from a high-concentration to a low-concentration environment, physical adsorption, ionic exchange, and bond formation are considered more significant when examined within the context. These models are not as straightforward to solve as kinetic-based models. They may require specialized solutions based on boundary and equilibrium conditions using various numerical methods.

If a chemical reaction occurs during adsorption, reaction-diffusion models must be considered. These analyses also assume an irreversible first-order reaction. They assume a stable solid phase, fluid film diffusion, and pore diffusion.

6. CONCLUSION

As a result, it appears that there are many factors influencing the adsorption process, the primary of which is the adsorbent. The usability of an adsorbent in the adsorption process depends on its suitability for surface properties and its ability to be obtained in an economically sustainable manner. Adsorbents of agricultural, industrial, and biological origin can be produced using various physical and chemical methods. The pore properties of the resulting adsorbent are used in various areas of adsorption studies. Using the equilibrium and kinetic data obtained during the activation of the adsorption mechanism, optimum conditions are calculated using the relevant equations.

Table 4 Kinetics equations

Models	Reference
Reaction kinetics-based models	
Pseudo-first to nth-order model	[29]
Elovich model	[30]
Avrami (Bangham) model	[31]
Ritchie’s model	[32]
Largitte double step model	[33]
Generalized kinetic model	[34]
Exponential kinetic mode	[35]
Hyperbolic tangent model	[36]
Statistical rate theory model	[37]
Langmuir kinetics model	[21]
Mass transfer diffusion-based models	
Boyd-Reichenberg’s intraparticle diffusion model	[38]
Vermeulen model	[39]
Weber–Morris model	[40]
Linear driving force model	[41]
Mathews-Weber mode	[42]
Furusawa-Smith model	[43]
Boyd’s external diffusion model.	[38]
Langmuir external diffusion model	[44]
Reaction-diffusion based models	
Multi-mechanism model	[45]
Fractal-like kinetic model	[46]

REFERENCES

[1] Loura N, Rathee K, Dhull R, Singh M, Dhull V. (2024) Carbon nanotubes for dye removal: A comprehensive study of batch and fixed-bed adsorption, toxicity, and functionalization approaches Journal of Water Process Engineering 67 :106193

[2] Herrera-Gonz´ alez A M, Caldera-Villalobos M, Pelaez-Cid AA (2019) Adsorption of textile dyes using an activated carbon and crosslinked polyvinyl phosphonic acid composite, J. Environ. Manag. 234 :237–244.

[3] Kaur M , Krishnan U, Sharma P, Kaur K, Sharma R, Kumarf A (2025) MXenes in action: Adsorption strategies for environmental contaminants Journal of Alloys and Compounds 1034:181350.

[4] Saleh TA. (2022) Isotherm models of adsorption processes on adsorbents and nanoadsorbents. in: Interface Science and Technology, Elsevier B.V:99–126.

[5] Sarıcı-Özdemir Ç, Kılıç F (2016) Experimental and modeling studies of methylene blue adsorption onto particles of peanut shell, Particulate Science And Technology 34:658–664

[6] Sarıcı Özdemir Ç (2012) Adsorption and desorption kinetics behaviour of methylene blue onto activated carbon, Physicochem. Probl. Miner. Process. 48:441−454

[7] Jong T S, Yoo C Y, Kiew P L (2020) Feasibility study of methylene blue adsorption using magnetized papaya seeds, Prog. energy Environ. 1–12.

[8] Kavci E, Erkmen J, Bingol MS, (2023) Removal of methylene blue dye from aqueous solution using citric acid modified apricot stone, Chem. Eng. Commun. 210:165–180.

[9] Subratti A, Vidal J L, Lalgee L J, Kerton F M, Jalsa N K (2021) Preparation and characterization of biochar derived from the fruit seed of Cedrela odorata L and evaluation of its adsorption capacity with methylene blue, Sustain. Chem. Pharm. 21:100421.

[10] Botrel B M C, Magriotis Z M, Saczk A A, Coelho S M, De Sales P F (2015) Removal of methylene blue by orange and uvaia seeds J. Adv. Agric. 3:237–253.

[11] Al-Ghouti M A, Al-Absi R S (2020) Mechanistic understanding of the adsorption and thermodynamic aspects of cationic methylene blue dye onto cellulosic olive stones biomass from wastewater, Sci. Rep. 10:1–18

[12] Dominguez MP, Mendoza J, Hechenleitner R (2025) Continuous and batch methylene blue removal using avocado seed carbon: performance evaluation and kinetic analysis, Bioresour. Technol. Reports 102071

[13] Sarıcı-Özdemir Ç (2017) Examination of the adsorption for methylene blue using different adsorbents Desalination and Water Treatment 90:311–319

[14] Wang W, Wang P, Wu C, Zhang L, Mao L, Zhu L, Jiang H, Zheng Y, Liu X, (2024) Adsorption of acetochlor-contaminated water systems using novel P-doped biochar: Effects, application, and mechanism, Chemosphere 350:141027

[15] Xu H, Zhou Q, Yan T, Jia X, Lu D, Ren Y, He J, (2024) Enhanced removal efficiency of Cd^{2+} and Pb^{2+} from aqueous solution by H_3PO_4–modified tea branch biochar: Characterization, adsorption performance and mechanism, J. Environ. Chem. Eng. 12:112183,

[16] Miyah Y , Messaoudi N , Benjelloun M , El-Habacha M, Georgin J , Angeles GH , Knani S (2025) Comprehensive review on advanced coordination chemistry and nanocomposite strategies for wastewater microplastic remediation via adsorption and photocatalysis Surfaces and Interfaces 72:106955

[17] Machado F M, Bergmann C P, Fernandes T H M, Lima E C, Royer B, Calvete T, Fagan SB (2011) Adsorption of reactive red M-2BE dye from water solutions by multiwalled carbon nanotubes and activated carbon, J. Hazard. Mater. 192: 1122–1131,

[18] Gubin S P, Koksharov Y A, Khomutov G B, Yurkov G Y (2005) Magnetic nanoparticles: preparation, structure and properties, Usp. Khim. 74:539–574

[19] Hosseini S S, Hamadi A, Foroutan R, Peighambardoust S J, Ramavandi B, (2022) Decontamination of Cd^{2+} and Pb^{2+} from aqueous solution using a magnetic nanocomposite of eggshell/starch/Fe_3O_4, J. Water Process Eng. 48: 102911.

[20] Mondal S , Cho S, Lee J (2025) Material innovations and challenges in adsorption-based nanoplastic removal for water purification: A comprehensive review of efficacy, mechanisms, performance factors, and future perspectives Journal of Environmental Chemical Engineering 13:117503

[21] Langmuir I (1918) The adsorption of gases on plane surfaces of glass, mica and platinum, J. Am. Chem. Soc. 40 :1361–1368.

[22] Freundlich H M F (1906) Über die adsorption in iösungen, Phys. Chem., 57:385–470.

[23] Redlich O, Peterson D I (1959) A useful adsorption isotherm, J. Phys. Chem., 63:1024–1026.

[24] Toth J (1971) State equations of the solid gas interface layer, Acta Chem. Acad. Hung., 69:311–317.

[25] Sips R (1948) Combined form of Langmuir and Freundlich equations, J. Chem. Phys., 16 :490–495.

[26] Temkin M J, Pyzhev V, (1940) Recent modifications to Langmuir isotherms, Acta Physiochim. Chem. USSR, 12 271–279.

[27]. Dubinin M M, Radushkevich L V, (1947) The equation of the characteristic curve of the activated charcoal, Proc. Acad. Sci. USSR Phys. Chem. Sect. 55 331–337.

[28] Cheng P., Hu Y.H., (2016) Dubinin-Astakhov model for acetylene adsorption on metalorganic frameworks, Appl. Surf. Sci. 377 :349–354

[29] Tran H N (2022) Differences between chemical reaction kinetics and adsorption kinetics: fundamentals and discussion. J. Tech. Educ. Sci. 33–47.

[30] Elovich S Y, Larionov O G (1962) Theory of adsorption from nonelectrolyte solutions on solid adsorbents. Russ. Chem. Bull. 11:191–197.

[31] Cerný S, Ponec V, Hl adek L (1970) Analogue simulation of adsorption calorimetry. J. Chem. Therm. 2:391–397.

[32] Ritchie A G (1977) Alternative to the Elovich equation for the kinetics of adsorption of gases on solids. J. Chem. Soc., Faraday Trans. 1:1650–1653.

[33] Largitte L, Pasquier R, (2016) New models for kinetics and equilibrium homogeneous adsorption. Chem. Eng. Res. Des. 112:289–297.

[34] Hu Q, Chen N, Feng C, Hu W, (2016) Kinetic studies for nitrate adsorption on granular chitosan–Fe(III) complex. Desalination Water Treat. 57:27783–27793.

[35] Haerifar M, Azizian S (2013) An exponential kinetic model for adsorption at solid/ solution interface. Chem. Eng. J. 215: 65–71.

[36] Eris S, Azizian S (2017) Analysis of adsorption kinetics at solid/solution interface using a hyperbolic tangent model. J. Mol. Liq. 231:523–527.

[37] Ward C A, Findlay R D, Rizk M (1982) Statistical rate theory of interfacial transport. I. Theoretical development. J. Chem. Phys. 76:5599–5605

[38] Boyd G E, Adamson A W, Myers Jr, L S (1947) The exchange adsorption of ions from aqueous solutions by organic zeolites. II. Kinetics. J. Am. Chem. Soc. 69: 2836–2848.

[39] Vermeulen T (1953) Theory for irreversible and constant-pattern solid diffusion. Ind. Eng. Chem. 45:1664–1670.

[40] Wang J, Guo X (2022) Rethinking of the intraparticle diffusion adsorption kinetics model: interpretation, solving methods and applications. Chemosphere 309:136732.

[41] Glueckauf E (1955) Theory of chromatography. Part 10.—formulæ for diffusion into spheres and their application to chromatography. Trans. Faraday Soc. 51:1540–1551.

[42] Mathews A R, Weber A W J, (1984) Modeling and parameter evaluation for adsorption in slurry reactors. Chem. Eng. Commun. 25:157–171.

[43] Furusawa T, Smith JM (1973) Fluid-particle and intraparticle mass transport rates in slurries. Ind. Eng. Chem. Fund. 12:197–203

[44] Yao C, Chen T (2017) A film-diffusion-based adsorption kinetic equation and its application. Chem. Eng. Res. Des. 119, 87–92

[45] Yao C, Zhu C (2021) A new multi-mechanism adsorption kinetic model and its relation to mass transfer coefficients. Surface. Interfac. 26:101422

[46] Kopelman R (1988) Fractal reaction kinetics. Science 241:1620–1626

Chapter 15

STRATEGIC ROLE OF ENVIRONMENTAL CRITERIA IN THIRD-PARTY LOGISTICS SELECTION

Ayfer ERGİN[1]

---

[1] Assoc. Prof. Dr. İstanbul University-Cerrahpaşa, Faculty of Engineering, Maritime Transport Management Engineering Department, Avcilar Campus, İstanbul, Türkiye

Mail: ayfersan@iuc.edu.tr

ORCID ID: 0000-0002-6276-4001

1. Introduction

The transportation and logistics sector constitutes a critical infrastructure that underpins the uninterrupted functioning of the global economy. As noted by (May, 2005), “transport is the lifeblood of the twenty-first-century economy.” The expansion of global production networks, increasing supply chain complexity, and growing expectations for rapid delivery have positioned logistics activities as an indispensable component of modern economic systems. However, these developments have simultaneously intensified environmental sustainability challenges. Transportation activities contribute significantly to air pollution, ecosystem degradation, carbon emissions, noise, traffic congestion, and climate change (Murphy et al., 1995, Wu and Dunn, 1995). According to the World Economic Forum (2009), the transportation sector is responsible for approximately 20% of global carbon dioxide (CO_2) emissions, highlighting its substantial environmental footprint (World Economic Forum, 2009).

In contemporary supply chains, a significant share of logistics operations is outsourced to specialized service providers. Within this context, third-party logistics service providers (3PLs) have evolved into strategic partners in supply chain design and operational management. The literature defines 3PLs as professional organizations that offer integrated logistics services, including transportation, warehousing, distribution, inventory management, order processing, customs clearance, reverse logistics, and customer-oriented supply chain solutions (Hertz and Alfredsson, 2003, Halldórsson and Skjøtt-Larsen, 2006).

Empirical research indicates that the environmental impact of logistics activities is considerably greater than commonly perceived. Freight transportation and warehousing operations are estimated to account for nearly 10% of global energy consumption and energy-related emissions (Marchant and Baker, 2010, Maas et al., 2014). Given that approximately 80% of industrial firms outsource their logistics activities to 3PL providers (Wallenburg, 2009), these organizations occupy a pivotal position in global environmental sustainability efforts. Maas et al. (2014) emphasize that, due to their scale, infrastructure, and process management capabilities, 3PL providers possess a substantially higher potential to drive environmental improvements compared to smaller, local transport operators (Maas et al., 2014).

Despite this potential, the absence of comprehensive international regulations directly limiting the carbon emissions of 3PL providers has resulted in environmental strategies being largely shaped by voluntary initiatives and customer-driven expectations. Following the implementation of the Kyoto Protocol, carbon reduction and environmental reporting practices have become more visible, accompanied by increasing regulatory and sectoral pressures (Evangelista et al., 2018). This shift has encouraged 3PL providers to adopt carbon accounting systems, energy efficiency programs, green transportation solutions, and sustainable operational practices.

Studies focusing on medium-sized European 3PL providers demonstrate that environmental sustainability has increasingly become a source of competitive differentiation, corporate reputation, and sectoral legitimacy (Fürst and Oberhofer, 2012). Nevertheless, a notable mismatch persists in practice: although many 3PL customers demand detailed environmental performance data, such information often plays a limited role in 3PL selection decisions (Maas et al., 2014). This gap points to a significant theoretical and practical shortcoming regarding how environmental criteria should be structured and operationalized within purchasing and outsourcing processes.

Key challenges in assessing environmental performance within the logistics sector include inconsistencies in measurement methodologies, insufficient integration of environmental considerations into information management systems, and the lack of standardized environmental reporting frameworks (Evangelista et al., 2017). These limitations hinder the objective and comparable evaluation of environmental criteria in 3PL selection processes.

Against this backdrop, 3PL providers have emerged as decisive actors in supply chain performance not only in terms of cost efficiency and service quality but also with respect to energy efficiency, carbon reduction, environmental management systems, and sustainable service design. Consequently, the systematic, measurable, and strategic integration of environmental criteria into 3PL selection has become an essential component of sustainable supply chain management.

Against this background, the increasing strategic relevance of third-party logistics service providers necessitates a systematic examination of the environmental and sustainability criteria used in 3PL selection. Understanding how these criteria are defined, structured, and operationalized constitutes a critical step toward integrating sustainability considerations into logistics outsourcing decisions.

2. Environmental and Sustainability Criteria in 3PL Selection

The growing complexity of global value chains has led firms to restructure their logistics activities through outsourcing, thereby transforming the selection of third-party logistics service providers (3PLs) into a strategic decision domain (Marchet et al., 2017). In this context, traditional performance indicators such as cost, speed, and reliability are no longer sufficient on their own. Increasing regulatory pressure, corporate sustainability commitments, and rising stakeholder expectations have elevated environmental sustainability criteria to a central position in 3PL selection processes (Marchet et al., 2017).

The environmental performance of 3PL providers has become a critical evaluation dimension, as it directly influences firms' ability to align logistics operations with sustainability-oriented supply chain strategies (Gürler, 2025, Raut et al., 2018). Accordingly, integrating environmental criteria into the 3PL selection process extends beyond mitigating the environmental impacts of logistics activities. It requires the holistic alignment of outsourced logistics services with broader corporate sustainability objectives (Hamdan and Rogers, 2008).

Among the environmental criteria considered in 3PL selection, indicators related to energy efficiency, emission management, and the adoption of alternative fuels have gained particular prominence (Gardas et al., 2019, Ergin and Ergin, 2023). The technical characteristics of vehicle fleets, the systematic calculation of carbon footprints, and transparent reporting practices based on standardized metrics directly shape firms' environmental risk profiles. Although maritime transport is widely regarded as the most energy-efficient and environmentally favorable mode in terms of emissions per unit of cargo transported (Sandal and Ergin, 2023, Ergin and Sandal, 2023, Yasa et al., 2016, Ergin and Ergin, 2021), its dominant role in global trade also positions it among the largest contributors to total emission volumes (Ergin and Ergin, 2023). This paradox underscores the need for 3PL providers to adopt not only operational improvements but also strategic environmental management approaches that account for modal emission balances across multimodal logistics networks.

Despite the increasing importance of these indicators in 3PL evaluation processes, energy efficiency in logistics is still frequently approached as a narrow operational performance metric focused primarily on cost reduction or service quality (Halldórsson and Kovács, 2010). In contrast, energy efficiency plays a critical role in reducing the environmental footprint of logistics activities that remain heavily dependent on non-renewable energy sources. The literature increasingly emphasizes that energy efficiency should be understood not merely as an operational output, but as a strategic domain that supports sustainable development objectives (Erandika et al., 2024).

The presence of formal environmental and energy management systems also constitutes a key determinant in 3PL selection. Compliance with internationally recognized standards such as ISO 14001 and ISO 50001 indicates that environmental sustainability is addressed at the level of corporate governance rather than being limited to isolated operational initiatives. From a warehousing and facility management perspective, the energy-intensive nature of logistics facilities further highlights the importance of energy efficiency, resource utilization, and waste management as core indicators of a 3PL provider’s environmental performance (Wehner et al., 2022).

In line with circular economy principles, the scope and effectiveness of reverse logistics practices have gained increasing relevance in 3PL selection decisions. Efficient management of product returns, repair, reuse, and recycling processes plays a strategic role in reducing the environmental impacts of logistics activities. Within this framework, packaging optimization, the use of reusable packaging systems, and the environmentally compliant management of waste logistics represent key components that strengthen the sustainability performance of 3PL providers (Mavi et al., 2017).

The effective evaluation and comparability of these processes are increasingly facilitated by digitalization, which functions not merely as an operational tool but as a structural enabler. Digital technologies enhance the traceability and comparability of environmental data, thereby supporting the systematic integration of environmental criteria into 3PL selection processes (Moreira and Rodrigues, 2023). Finally, when environmental criteria are assessed alongside social sustainability and corporate governance dimensions, a holistic ESG (Environmental–Social–Governance) approach becomes essential for comprehensive 3PL evaluation (Moreira and Rodrigues, 2023).

Overall, addressing environmental and sustainability criteria within a comprehensive framework has become a fundamental requirement for sustainable supply chain management in 3PL selection. The criteria set presented in Table 1 encompasses the most frequently emphasized environmental dimensions in the literature and provides a structured basis for systematically evaluating the sustainability capabilities of 3PL providers.

Table 1. Key Environmental and Sustainability Criteria in 3PL Selection.

Criterion	Definition and Scope (3PL Perspective)	Key References
Energy efficiency	Practices aimed at reducing energy consumption per unit of logistics service in transportation and warehousing operations, including route optimization, eco-driving, and the use of energy-efficient equipment	Centobelli et al. (2017); Wehner et al. (2022); Gupta et al. (2022); Moreira & Rodrigues (2023); Cheng et al. (2023); Evangelista et al. (2017); Evangelista (2014); Wolf & Seuring (2010)
Carbon emission measurement and reporting	Systematic calculation, monitoring, and reporting of CO_2 and other greenhouse gas emissions associated with logistics activities	Moreira & Rodrigues (2023); Cheng et al. (2023); Evangelista (2014); Wolf & Seuring (2010)
Low-carbon transportation and alternative fuel use	Adoption of low-carbon transportation solutions through the use of electric, biofuel-powered, or hybrid vehicles	Cheng et al. (2023); Gupta et al. (2022)
Environmental and energy management systems (ISO	Systematic management of environmental and energy performance within the framework of internationally recognized standards	Wehner et al. (2022); Moreira & Rodrigues (2023); Evangelista et al. (2017); Evangelista (2014)

14001, ISO 50001)		
Corporate environmental governance	Establishment, monitoring, and integration of environmental objectives at the top management level into corporate policies and decision-making processes	Moreira & Rodrigues (2023); Evangelista & Durst (2015); Evangelista et al. (2017); Gupta et al. (2022); Evangelista (2014)
Green transportation and warehousing infrastructure	Availability of energy-efficient warehouses, environmentally friendly equipment, low-emission vehicle fleets, and sustainable operational infrastructure	Singh et al. (2018); Wehner et al. (2022); Gupta et al. (2022); Evangelista (2014)
Sustainable network and route optimization	Planning of distribution networks and transportation routes in a manner that minimizes environmental impacts	Cheng et al. (2023); Gupta et al. (2022)
Environmental data monitoring and digitalization	Use of digital tools such as carbon footprint calculators, energy monitoring systems, telematics, and digital reporting platforms to track environmental performance	Moreira & Rodrigues (2023); Singh et al. (2018); Wehner et al. (2022); Evangelista & Durst (2015); Gupta et al. (2022); Evangelista (2014); Singh Bhatti et al. (2010)
Environmental transparency and reporting	Accuracy, traceability, and disclosure of environmental performance data to stakeholders	Moreira & Rodrigues (2023); Singh et al. (2018); Evangelista & Durst (2015); Evangelista (2014); Wolf & Seuring (2010)
Reverse logistics capability	Environmentally compliant management of product returns, recycling, reuse, and remanufacturing processes	Mavi et al. (2017); Evangelista (2014); Chen et al. (2022)
Packaging and waste management	Use of reusable packaging systems, waste reduction initiatives, and sustainable waste logistics practices	Mavi et al. (2017)
ESG-based evaluation approach	A holistic evaluation framework in which environmental criteria are assessed in conjunction with social and governance dimensions	Moreira & Rodrigues (2023); Evangelista & Durst (2015); Evangelista et al. (2017); Evangelista (2014)

The manner in which operational capabilities, corporate governance, and digital infrastructure jointly converge to generate strategic value is summarized in the holistic framework presented in Figure 1.

Figure 1. A Holistic Evaluation Framework for Sustainable 3PL Selection.

While the identification of environmental and sustainability criteria provides a foundational basis for 3PL evaluation, their strategic significance extends beyond operational assessment. The following section examines how these criteria influence competitive positioning, regulatory alignment, and corporate legitimacy within logistics outsourcing decisions.

3. Strategic Role of Environmental Criteria in 3PL Selection

For many years, environmental criteria in the selection of third-party logistics service providers (3PLs) were regarded as secondary considerations that complemented traditional operational performance indicators such as cost efficiency, speed, and service reliability. However, the intensification of global climate policies, the expansion of regulatory frameworks targeting carbon emissions, and the widespread adoption of ESG (Environmental–Social–Governance)–oriented corporate reporting have fundamentally altered this perspective. Environmental criteria have increasingly evolved into a strategic decision dimension in 3PL selection. Recent studies demonstrate that environmental performance is not merely a mechanism for mitigating ecological impacts, but also a key determinant of competitive advantage, corporate reputation, and supply chain resilience (Moreira and Rodrigues, 2023).

3.1 Strategic Positioning from the Perspectives of Competition, Reputation, and Regulation

The strategic relevance of environmental criteria is particularly evident in the competitive positioning of 3PL providers. Investments in energy efficiency, low-carbon transportation solutions, and formal environmental management systems enable 3PLs not only to improve their environmental performance, but also to enhance operational efficiency and generate long-term economic value. From this perspective, environmental sustainability initiatives should not be interpreted as cost-intensive compliance burdens; rather, when effectively managed, they constitute strategic investments that strengthen market differentiation and competitive advantage (Moreira and Rodrigues, 2023, Wehner et al., 2022).

Within this strategic transformation, transportation mode choice emerges as a critical decision area in which environmental performance becomes operationally visible. The literature consistently identifies maritime transport as a comparatively environmentally favorable mode in terms of energy consumption and carbon emissions per unit of cargo, particularly when compared with road and air transport (Ergin and Ergin, 2018). Nevertheless, this environmental advantage is not solely attributable to the transport mode itself. It is strongly conditioned by the 3PL provider's capability for multimodal integration, network and route optimization, and effective operational coordination across logistics systems.

Recent developments in maritime transport, particularly the increasing deployment of vessels powered by alternative fuels such as LNG, methanol, biofuels, and synthetic fuels, further reinforce the environmental performance potential of 3PL providers. These fuel technologies align closely with the International Maritime Organization's (IMO) targets for reducing carbon intensity and greenhouse gas emissions in shipping (Bask and Rajahonka, 2017, Ergin and Ergin, 2023). In this context, 3PL providers are transitioning from conventional transport intermediaries to strategic partners that actively support their clients' compliance with environmental regulations and decarbonization objectives.

At the same time, customers, investors, and regulatory authorities are demanding higher levels of transparency and accountability regarding the environmental impacts of logistics activities. The adoption of environmental and energy management systems such as ISO 14001 and ISO 50001, together with systematic carbon emission measurement and reporting practices, has become a central indicator of a 3PL provider's regulatory compliance capacity and corporate responsibility (Moreira and Rodrigues, 2023, Wehner et al., 2022, Evangelista et al., 2017, Evangelista, 2014). Consequently, environmental criteria are increasingly perceived not as voluntary initiatives, but as strategic necessities for maintaining corporate legitimacy and ensuring long-term regulatory alignment.

While the strategic importance of environmental criteria in 3PL selection is increasingly evident in terms of competitiveness, regulatory alignment, and corporate legitimacy, their full strategic value becomes more apparent when examined through the lenses of supply chain resilience and risk management. Environmental performance is not only associated with compliance and reputation, but also with a firm's capacity to anticipate, absorb, and adapt to environmental, regulatory, and market-related disruptions. In this respect, the integration of environmental criteria into 3PL selection serves as a critical mechanism for enhancing long-term value creation by strengthening the robustness and adaptability of supply chain structures.

3.2 Resilience, Risk Management, and Long-Term Value Creation

The strategic role of environmental criteria becomes even more pronounced when examined from the perspectives of supply chain resilience and risk management. Volatility in energy prices, the introduction of carbon taxation mechanisms, and uncertainty surrounding environmental regulations constitute significant sources of risk for logistics operations (Song et al., 2024, Feng and Kou, 2025). Within this context, 3PL providers characterized by high energy efficiency, optimized resource utilization, and low-carbon operational structures contribute substantially to enhancing the resilience of supply chains against environmental and economic shocks (Moreira and Rodrigues, 2023).

Energy efficiency and carbon-reduction capabilities enable 3PL providers to mitigate exposure to cost fluctuations associated with fuel price volatility and regulatory compliance. By proactively investing in low-carbon technologies and environmentally efficient processes, 3PLs are better positioned to anticipate regulatory tightening and adapt to evolving policy environments. Consequently, environmental performance emerges as a strategic risk-mitigation mechanism rather than a reactive compliance response.

Maritime transportation, when supported by alternative fuel technologies, represents a particularly salient example of how environmental strategies can reinforce supply chain resilience. Investments in vessels powered by liquefied natural gas (LNG), methanol, biofuels, and synthetic fuels reduce long-term carbon costs while enhancing compliance with international decarbonization targets (Ergin and Ergin, 2023). Such investments enable 3PL providers to manage regulatory uncertainty more effectively and to offer more stable and predictable logistics solutions to their clients (Psaraftis, 2016).

In parallel, the growing adoption of circular economy principles has further expanded the strategic scope of environmental criteria in 3PL selection. Reverse logistics capabilities, packaging optimization, and sustainable waste management practices have become complementary mechanisms for improving both environmental performance and operational resilience. Efficient management of return flows and material recovery processes reduces resource dependency and operational disruptions, thereby contributing to long-term supply chain stability (Chen et al., 2022, Mavi et al., 2017).

Taken together, environmental criteria in 3PL selection extend beyond short-term operational considerations and function as strategic enablers of long-term value creation. When integrated with transportation mode choices, fuel technology investments, and corporate governance capacities, these criteria support the development of logistics systems that are not only environmentally sustainable but also economically resilient and strategically robust. This integrated perspective underscores the role of environmental sustainability as a permanent strategic orientation rather than a transient managerial trend in 3PL selection.

4. Conclusion

This chapter has examined the growing strategic importance of environmental and sustainability criteria in the selection of third-party logistics service providers (3PLs) through a comprehensive review of the relevant literature. Increasing complexity in global value chains, intensifying climate change mitigation efforts, and the rising expectations associated with corporate sustainability agendas have fundamentally reshaped 3PL selection processes. In this evolving context, 3PL providers have moved beyond their traditional role as operational service executors to become strategic partners that play a critical role in achieving sustainable supply chain objectives.

The analysis presented throughout the chapter identifies energy efficiency, carbon emission measurement and reporting, environmental and energy management systems, green operational infrastructure, digital traceability, and reverse logistics capabilities as the core environmental criteria shaping 3PL selection decisions (Chen and Chen, 2022, Mavi et al., 2017). These criteria enhance the measurability and comparability of environmental performance, thereby enabling more objective, transparent, and systematic supplier selection processes. The literature clearly indicates that environmental sustainability is no longer confined to reducing ecological impacts alone, but has become closely intertwined with long-term competitiveness, corporate reputation, and strategic positioning.

Transportation mode choice emerges as a particularly critical dimension through which the environmental performance of 3PL providers becomes operationally visible. Maritime transportation offers significant environmental advantages in terms of energy consumption and carbon emissions per unit of cargo when compared to road and air transport. However, the effective realization of these advantages depends on 3PL providers' capabilities in multimodal integration, network and route planning, and operational coordination. The increasing adoption of vessels powered by alternative fuels further enhances the environmental performance of maritime transport and strengthens the role of 3PL providers as strategic enablers of their clients' decarbonization and regulatory compliance efforts.

When evaluated from the perspectives of supply chain resilience and risk management, the strategic relevance of environmental criteria becomes even more pronounced. Fluctuations in energy prices, the introduction of carbon pricing mechanisms, and uncertainty surrounding environmental regulations pose significant risks to logistics operations. In this regard, 3PL providers characterized by high energy efficiency, low-carbon operations, and institutionally embedded environmental management practices contribute to the development of supply chains that are more resilient to environmental, regulatory, and economic shocks.

In conclusion, the systematic, measurable, and strategic integration of environmental and sustainability criteria into 3PL selection has become a fundamental requirement of sustainable supply chain management. Energy and emission management, environmental governance structures, green operational infrastructure, effective utilization of the environmental potential of maritime transport, and robust reverse logistics capabilities constitute the core components of 3PL sustainability performance. Integrating these criteria into supplier selection processes not only supports the reduction of environmental impacts, but also enables firms to achieve long-term competitive advantage and to build more resilient and future-oriented supply chains.

From a research perspective, future studies may extend the present framework by empirically testing the relative importance of environmental, social, and governance criteria in 3PL selection across different industries and geographical contexts. Quantitative decision-making models integrating ESG indicators with operational performance metrics could further enhance the practical applicability of the proposed framework. Longitudinal studies examining how environmental criteria influence long-term supplier relationships and supply chain resilience would also provide valuable insights.

From a policy perspective, the findings underscore the need for more standardized environmental reporting requirements and harmonized regulatory frameworks for logistics service providers. Policymakers may play a critical role by promoting transparency in carbon accounting, incentivizing low-carbon logistics investments, and supporting the diffusion of digital monitoring technologies. Such policy interventions could facilitate the systematic integration of environmental sustainability into 3PL selection practices and accelerate the transition toward more resilient and sustainable supply chains.

References

BASK, A. & RAJAHONKA, M. 2017. The role of environmental sustainability in the freight transport mode choice: A systematic literature review with focus on the EU. *International Journal of Physical Distribution & Logistics Management,* 47**,** 560-602.

CHEN, L., DUAN, D., MISHRA, A. R. & ALRASHEEDI, M. 2022. Sustainable third-party reverse logistics provider selection to promote circular economy using new uncertain interval-valued intuitionistic fuzzy-projection model. *Journal of Enterprise Information Management,* 35**,** 955-987.

CHEN, L. T. & CHEN, S. Q. 2022. Volunteer multi-person multi-task optimization dispatch method considering two-sided matching. *Soft Computing,* 26**,** 3837-3861.

ERANDIKA, T., PALLAWALA, T., WIJESINGHE, A., PERERA, D., KARUNARATHNA, N. & KALANSURIYA, N. 2024. Investigation of the Carbon Offsetting Targets Towards Sustainability: A Focus on 3PL Companies.

ERGIN, A. & ERGIN, M. F. 2018. Reduction of Ship Based CO2 Emissions from Container Transportation. *International Journal of Computational and Experimental Science and Engineering,* 4**,** 1-4.

ERGIN, A. & ERGIN, M. F. 2021. The role of antifouling coating in the marine industry. *In:* KALKANCI, M. & GÜNDAY, A. (eds.) *Research Reviews in Engineering.* Istanbul: Gece Kitapligi.

ERGIN, A. & ERGIN, M. F. 2023. Alternative Fuels In The Future Of The Maritime Industry. *In:* ÖZALP, C. & BARDAK, S. (eds.) *International Theory, Research And Reviews In Engineering.* Ankara: Serüven Yayınevi.

ERGIN, A. & SANDAL, B. 2023. Mobbing among seafarers: Scale development and application of an interval type-2 fuzzy logic system. *Ocean Engineering,* 286**,** 115595.

EVANGELISTA, P. 2014. Environmental sustainability practices in the transport and logistics service industry: An exploratory case study investigation. *Research in Transportation Business & Management,* 12**,** 63-72.

EVANGELISTA, P., COLICCHIA, C. & CREAZZA, A. 2017. Is environmental sustainability a strategic priority for logistics service providers? *Journal of environmental management,* 198**,** 353-362.

EVANGELISTA, P., SANTORO, L. & THOMAS, A. 2018. Environmental sustainability in third-party logistics service providers: A systematic literature review from 2000–2016. *Sustainability,* 10**,** 1627.

FENG, L. & KOU, Q. 2025. The role of logistics provider's carbon tax in a supply chain. *International Journal of Systems Science: Operations & Logistics,* 12**,** 2482617.

FÜRST, E. & OBERHOFER, P. 2012. Greening road freight transport: evidence from an empirical project in Austria. *Journal of Cleaner Production,* 33**,** 67-73.

GARDAS, B. B., D. RAUT, R. & NARKHEDE, B. E. 2019. Analysing the 3PL service provider's evaluation criteria through a sustainable approach. *International Journal of Productivity and Performance Management,* 68**,** 958-980.

GÜRLER, H. E. 2025. ÜÇÜNCÜ TARAF LOJİSTİK (3PL) SAĞLAYICILARININ SÜRDÜRÜLEBİLİRLİK PERSPEKTİFİNDEN DEĞERLENDİRİLMESİ: FUCOM

TEMELLİ ENTEGRE BİR YAKLAŞIM. *Ömer Halisdemir Üniversitesi İktisadi ve İdari Bilimler Fakültesi Dergisi,* 18**,** 1-31.

HALLDÓRSSON, Á. & KOVÁCS, G. 2010. The sustainable agenda and energy efficiency: Logistics solutions and supply chains in times of climate change. *International Journal of Physical Distribution & Logistics Management,* 40**,** 5-13.

HALLDÓRSSON, Á. & SKJØTT-LARSEN, T. 2006. Dynamics of relationship governance in TPL arrangements–a dyadic perspective. *International Journal of Physical Distribution & Logistics Management,* 36**,** 490-506.

HAMDAN, A. & ROGERS, K. J. 2008. Evaluating the efficiency of 3PL logistics operations. *International journal of production economics,* 113**,** 235-244.

HERTZ, S. & ALFREDSSON, M. 2003. Strategic development of third party logistics providers. *Industrial marketing management,* 32**,** 139-149.

MAAS, S., SCHUSTER, T. & HARTMANN, E. 2014. Pollution prevention and service stewardship strategies in the third-party logistics industry: Effects on firm differentiation and the moderating role of environmental communication. *Business Strategy and the Environment,* 23**,** 38-55.

MARCHANT, C. & BAKER, P. 2010. Reducing the environmental impact of warehousing. *Green Logistics: Improving the environmental sustainability of Logistics***,** 167-192.

MARCHET, G., MELACINI, M., SASSI, C. & TAPPIA, E. 2017. Assessing efficiency and innovation in the 3PL industry: an empirical analysis. *International Journal of Logistics Research and Applications,* 20**,** 53-72.

MAVI, R. K., GOH, M. & ZARBAKHSHNIA, N. 2017. Sustainable third-party reverse logistic provider selection with fuzzy SWARA and fuzzy MOORA in plastic industry. *The international journal of advanced manufacturing technology,* 91**,** 2401-2418.

MAY, G. H. 2005. Transport in Europe: where are we going? *Foresight,* 7**,** 24-38.

MOREIRA, O. J. & RODRIGUES, M. C. M. 2023. Sourcing third party logistics service providers based on environmental, social and corporate governance: a case study. *Discover Sustainability,* 4**,** 36.

MURPHY, P. R., POIST, R. F. & BRAUNSCHWEIG, C. D. 1995. Role and relevance of logistics to corporate environmentalism: anempirical assessment. *International Journal of Physical Distribution & Logistics Management,* 25**,** 5-19.

PSARAFTIS, H. N. 2016. Green maritime logistics: the quest for win-win solutions. *Transportation Research Procedia,* 14**,** 133-142.

RAUT, R., KHARAT, M., KAMBLE, S. & KUMAR, C. S. 2018. Sustainable evaluation and selection of potential third-party logistics (3PL) providers: An integrated MCDM approach. *Benchmarking: An International Journal,* 25**,** 76-97.

SANDAL, B. & ERGIN, A. 2023. NAVIGATING UNCERTAINTY: FROM TYPE-1 TO INTERVAL TYPE-2 FUZZY LOGIC IN DECISION MAKING. *Academic Studies in Engineering***,** 79.

SONG, J., XU, C. & WANG, C. 2024. Impacts of the carbon tax on green shipping supply chain under the port competition. *Expert Systems,* 41**,** e13229.

WALLENBURG, C. M. 2009. Innovation in logistics outsourcing relationships: proactive improvement by logistics service providers as a driver of customer loyalty. *Journal of supply chain management,* 45**,** 75-93.

WEHNER, J., TAGHAVI NEJAD DEILAMI, N., ALTUNTAS VURAL, C. & HALLDORSSON, A. 2022. Logistics service providers' energy efficiency initiatives for environmental sustainability. *The international journal of logistics management,* 33**,** 1-26.

WORLD ECONOMIC FORUM, M. Supply chain decarbonization: The role of logistics and transport in reducing supply chain carbon emissions. 2009. World Economic Forum Geneva, Switzerland.

WU, H. J. & DUNN, S. C. 1995. Environmentally responsible logistics systems. *International journal of physical distribution & logistics management,* 25**,** 20-38.

YASA, H., ERGIN, M. F., ERGIN, A. & ALKAN, G. 2016. Importance of Inert Gases for Chemical Transportation. *Proceedings Book* 825.

Chapter 16

URBANIZATION AND CLIMATE CHANGE: THE COST OF UNCONTROLLED DEVELOPMENT

Meral KORKMAZ

1. Introduction

- *Global Climate Change Context*

Global climate change and its associated destructive impacts have long constituted one of the central topics of scientific inquiry and international debate (Fourier, 1824; Esper et al., 2013; Ramanauskas et al., 2024). In recent years, the increasing frequency and intensity of heatwaves, extreme precipitation events leading to floods, hurricanes, storms, wildfires, and disasters causing large-scale loss of life have been widely reported as tangible manifestations of disruptions within the climate system (Laino & Iglesias, 2023; McBean & Ajibade, 2009).

In addition, recent global pandemics, escalating geopolitical tensions and the risk of armed conflict, radiation-related threats, rising levels of air pollution, and other environmental pressures exceeding the carrying capacity of ecosystems have rendered climate change–related risks increasingly complex and multidimensional (Chirico, 2021; Gameiro et al., 2023). These developments indicate that the global ecological balance is approaching a critical and potentially irreversible tipping point.

In this context, it has become evident that approaches focusing solely on post-disaster response are insufficient to address the challenges posed by climate change. Instead, integrated strategies encompassing sustainable land use, climate-sensitive urbanization, ecosystem-based planning, and robust legal and institutional frameworks must be pursued simultaneously. Today, climate change is no longer perceived merely as an environmental transformation, but rather as a structural crisis exerting profound and multifaceted impacts on urban policies, social life, economic systems, and public health (Türkeş, 2008; İğci & Çobanoğlu, 2019). The rapid accumulation of greenhouse gases in the atmosphere since the Industrial Revolution—driven by fossil fuel consumption, deforestation, intensive urbanization, and inappropriate land-use decisions—has resulted in rising global mean temperatures, disrupted precipitation regimes, and an increased occurrence of extreme weather events (Baş & Partigöç, 2022).

- *The Role of Cities in Climate Change*

Within this process, cities have emerged as both key drivers of climate change and the spatial contexts in which its impacts are most intensely experienced (Tuğaç, 2018). In a world where more than half of the global population resides in urban areas, emission-intensive activities related to energy consumption, transportation, industry, and housing are predominantly concentrated in cities. Conversely, climate-related risks such as floods, heatwaves, air pollution, and infrastructure stress are also most acutely felt in urban environments (Tuğaç, 2018; Şen & Özer, 2018).

- *Uncontrolled Urban Development, UHI, and LST Dynamics*

Uncontrolled urban development, in particular, has become a critical accelerating mechanism within the climate change framework. Unplanned urban expansion, the proliferation of impervious surfaces, the loss of green and blue spaces, the reduction of carbon sinks, and the increasing use of heat-retaining construction materials not only intensify global warming but also strengthen the urban heat island (UHI/SUHI) effect. Recent studies employing land use/land cover (LULC) change analysis, land surface temperature (LST) metrics, and vegetation and built-up indices (e.g., NDVI and NDBI) clearly demonstrate that increasing building density is associated with higher LST values, while declining vegetation cover exacerbates the intensity of UHI effects (Mohamed et al., 2025; Yavuz & Ünlütürk, 2025).

- *Aim and Scope of the Study*

Against this backdrop, the aim of this study is to examine the impacts of uncontrolled urban development on global warming and climate change by integrating mechanisms such as land-use transformation, rising surface temperatures, disruptions in the carbon cycle, and increasing urban vulnerability through a literature-based synthesis. Furthermore, based on insights derived from recent empirical research, the study seeks to evaluate scientifically grounded mitigation and adaptation strategies relevant to urban planning and local governance.

Existing research indicates that in many countries, sustainable land-use and climate adaptation policies have not been assessed in a comprehensive and integrated manner at the national scale. International organizations often provide generalized recommendations based on selected environmental and regional indicators; however, they frequently fail to examine, in sufficient detail, the institutional, legal, and implementation gaps that hinder progress toward sustainable development goals at the country level. Although more comprehensive national assessments of sustainable land use and climate adaptation have been conducted in some contexts, these efforts largely remain confined to strategic frameworks and policy recommendations, while a globally binding and actionable set of solutions addressing increasingly complex challenges has yet to be developed.

These shortcomings contribute to the emergence of a self-reinforcing cycle of climate-related risks. Growing population pressure, combined with the unplanned and inefficient use of energy and water resources, leads to increased greenhouse gas emissions, thereby accelerating climate change and intensifying the frequency and severity of heatwaves, floods, inundations, wildfires, and other extreme weather events. In the aftermath of such disasters, many countries tend to implement short-term, climate-insensitive urbanization practices, including the covering of riverbeds, the development of floodplains, and the enforcement of zoning decisions that disregard natural thresholds and ecological constraints.

In recent years, the rapid increase in the proportion of concrete surfaces relative to soil and green areas particularly within gated residential developments has further disrupted the natural hydrological cycle and expanded the extent of impervious surfaces. This process accelerates surface runoff during precipitation events, increasing flood risk while simultaneously intensifying the urban heat island effect. Moreover, the failure to replace trees removed under development pressure weakens the carbon sequestration capacity of cities and undermines the buffering function of ecosystems against climate change. Consequently, unplanned and uncontrolled urbanization emerges not only as an outcome of climate change but also as one of its fundamental structural drivers, deepening and perpetuating its impacts.

2. Materials and Methods

In this section, the studies selected within the scope of the review were evaluated using a thematic synthesis approach. The synthesis was structured around the following analytical axes: (i) shared mechanisms explaining the relationship between uncontrolled urbanization and climate change, (ii) the use of UHI/SUHI–LST–LULC indicators, (iii) similarities and differences observed across different geographical contexts, and (iv) methodological trends, including remote sensing, numerical modeling, and emerging predictive tools. Within this framework, the key findings emphasized in the literature are integrated and synthesized below.

Recent studies demonstrate that the relationship between uncontrolled urbanization and climate change manifests through similar dynamics across different geographical contexts. The review conducted by Yavuz and Ünlütürk (2025) indicates that, after 2015, UHI-related research has predominantly concentrated on highly urbanized regions of the Northern Hemisphere, with satellite imagery such as Landsat and MODIS, alongside indicators including LST, NDVI, and NDBI, serving as the primary analytical tools. These studies consistently report positive relationships between increasing building density, impervious surface ratios, and surface temperatures, while vegetation-related indicators exhibit negative correlations. Accordingly, uncontrolled urban development is confirmed to generate a climatically measurable risk that is not only theoretical but also quantitatively observable through remote sensing and numerical modeling techniques (Yavuz & Ünlütürk, 2025).

In interpreting these findings, studies explaining the historical and spatial background of urbanization were employed as contextual references. From a historical perspective, urbanization processes driven by population movements, economic concentration, and spatial expansion are known to exert substantial development pressure on natural areas. Ayodeji (2009) emphasizes that the alterations induced by intensive urban development in energy balance, hydrological cycles, and thermal regimes have transformed urban ecosystems into systematic drivers accelerating global warming. This observation helps explain why UHI effects are more pronounced in cities experiencing unplanned development.

Within the scope of this review, studies revealing long-term trends were comparatively evaluated based on their temporal coverage. Research conducted between 2004 and 2024 consistently demonstrates a stable global relationship between urbanization and rising surface temperatures. In developing countries, rapid population growth, limited planning capacity, and uncontrolled development lead to higher UHI intensities, whereas in developed countries, green infrastructure, high-albedo materials, and climate-sensitive planning policies partially mitigate these effects (Mohamed et al., 2025).

From the perspective of geographical diversity, findings from case studies selected from rapidly urbanizing regions were examined together with their spatial expansion and vulnerability dimensions. Rapidly growing African cities provide some of the most visible examples of these dynamics. Li et al. (2021) show that in Kampala, built-up areas more than doubled between 1995 and 2017, resulting in a significant increase in both the intensity and spatial extent of SUHI effects. The contraction of green and blue spaces, expansion of impervious surfaces, and proliferation of informal settlements contributed to the emergence of new heat islands, particularly in the northern and eastern parts of the city. One of the key contributions of this study is the identification of thermal environmental degradation as a factor that simultaneously intensifies socio-economic vulnerability (Li et al., 2021).

From a methodological standpoint, analytical tools and data sources used in the literature were classified as evidence-generation approaches within this review. Remote sensing technologies have become the primary instruments for assessing the urbanization–LST relationship. While Landsat data are widely used for long-term analyses in tropical and temperate climates, MODIS data are preferred in polar regions due to their high temporal resolution. In recent years, 3D urban models and artificial intelligence–based prediction algorithms have enabled more precise identification of the spatial distribution of LST, offering new opportunities for modeling urban climate risks (Mohamed et al., 2025).

As a result of this thematic synthesis, the common mechanism identified across the reviewed studies is presented as an integrative explanatory framework. Although the impacts of uncontrolled urban development on global warming and climate change vary according to regional conditions, the literature consistently converges around the following mechanism:

"Increase in impervious surfaces + decrease in green areas + rising building density = LST increase and deepening of UHI/SUHI effects."

Accordingly, the existing body of academic evidence indicates that urbanization policies need to be fundamentally reconsidered within the context of climate change.

2.1. Core Dynamics of Uncontrolled Urban Development

The fundamental dynamics driving uncontrolled urban development exhibit a multilayered structure in which socio-economic, demographic, and spatial processes operate simultaneously (Aksöz & Çelik, 2023; Mavi, 2025). Key drivers include rapid population growth, intense rural-to-urban migration, economic growth pressures, and the resulting increase in housing demand. The inability of planning systems to adapt to this rapid transformation leads to the proliferation of unregulated land-use decisions and the accelerated conversion of natural ecosystems under development pressure. Particularly in metropolitan areas, spatial expansion trends intensify urban sprawl, accelerating the conversion of agricultural lands, forests, and wetlands into built-up areas (Çiftçi et al., 2013; Koç, 2023).

Within this context, ecological footprint and biocapacity indicators serve as critical measures for understanding the environmental background of uncontrolled urbanization. In Türkiye, while the per capita ecological footprint remained below biocapacity during the 1960s, a pronounced biocapacity deficit emerged after the 1980s as consumption levels exceeded the regenerative capacity of ecosystems. A similar trend is observed globally, where since the 1970s, the ecological footprint has surpassed global biocapacity, establishing a persistent regime of overconsumption. Consequently, increasing production and consumption patterns across sectors such as energy, transportation, industry, and agriculture, combined with urbanization pressures, have exponentially intensified the burden on the climate system (Baş & Partigöç, 2022).

Another determining dynamic of uncontrolled urban development is unplanned land-use change. The replacement of natural surfaces with concrete, asphalt, and other impervious materials results in the loss of ecosystem services, disruption of precipitation regimes, and deterioration of urban microclimatic conditions. The fragmentation of green spaces, reduction of carbon sinks, and decline in biodiversity collectively increase both ecological and climatic vulnerability in urban areas. In addition, zoning amnesties, inadequate enforcement mechanisms, and market-driven development models represent structural factors that further promote uncontrolled urbanization (Şen & Özer, 2018; Mavi, 2025).

These processes lead to disruptions in urban energy balance, increased heat accumulation, and pronounced alterations in urban microclimate conditions. Factors such as rising building density, expansion of impervious surfaces, use of low-albedo construction materials, and restricted air circulation constitute the primary physical and morphological mechanisms underlying the formation of the Urban Heat Island (UHI) effect (Figure 1). In this regard, uncontrolled urban development should be considered not merely as a spatial planning issue, but as a structural environmental risk that both amplifies climate change and increases urban climatic vulnerability (Baş & Partigöç, 2022).

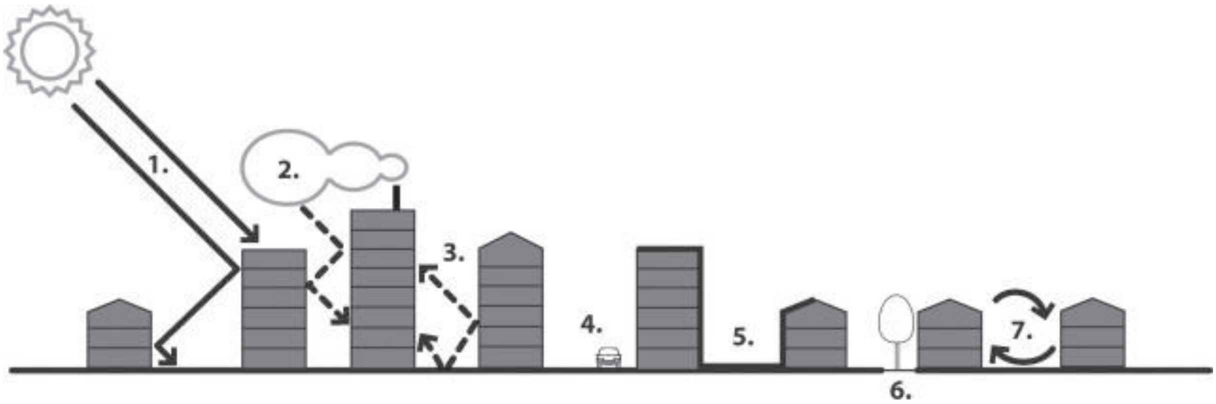

Figure 1. Key physical and morphological processes leading to the formation of the Urban Heat Island (UHI) effect in urban areas as a result of uncontrolled development (Kleerekoper, Van Esch & Salcedo, 2012).

As illustrated in Figure 1, the absorption of solar radiation and trapping of heat by low-albedo surfaces (1), the retention of longwave radiation due to atmospheric pollution (2), and the reduction of nocturnal heat loss associated with increased building density (3) significantly accelerate temperature increases in urban areas. In addition, anthropogenic heat emissions (4), increased heat storage capacity of building materials (5), weakened evaporation processes (6), and reduced turbulent heat transport resulting from lower wind speeds (7) constitute the principal mechanisms reinforcing the urban heat island effect.

2.2. The Relationship Between Uncontrolled Urban Development and Global Warming: The LULC–LST–UHI Axis

With the acceleration of urbanization, the replacement of natural surfaces by impervious materials leads to significant transformations in land use/land cover (LULC) patterns, which in turn cause systematic increases in land surface temperatures (LST) in urban areas. Empirical studies demonstrate that reductions in vegetation cover, shrinkage of water bodies, and increasing building density generate higher LST values compared to rural areas, constituting core components of urban heat island (UHI) formation (Mohamed et al., 2025). These findings indicate that uncontrolled urban development functions as a spatially explicit process that intensifies global warming.

The widespread expansion of impervious surfaces increases the thermal storage capacity of urban areas. Heat absorbed during daytime hours is gradually released into the atmosphere at night, causing urban centers to remain warmer than their rural surroundings. This phenomenon represents not only a microclimatic deviation but also produces secondary effects by increasing energy demand and fossil fuel consumption. Consequently, uncontrolled urbanization directly affects both local thermal environments and global warming dynamics (Ayodeji, 2009).

Another major outcome of uncontrolled urbanization is the reduction of carbon sinks (Sütçüoğlu et al., 2022). The contraction of forested areas and the conversion of agricultural land into built-up environments weaken the carbon sequestration capacity of ecosystems, while the replacement of natural habitats with concrete surfaces increases greenhouse gas accumulation in the atmosphere (Ayodeji, 2009). As a result, urbanization exerts dual pressure on both energy balance and ecosystem services.

Although the impacts of LULC changes on LST vary across climatic zones, the general trend remains consistent. In tropical and semi-arid regions, vegetation loss is the most significant driver of LST increase; in temperate regions, seasonal variability influences the magnitude of warming; and in polar regions, the expansion of low-albedo surfaces and permafrost thawing intensify UHI effects (Mohamed et al., 2025). This pattern suggests that uncontrolled urban development generates a globally consistent warming tendency.

The urban heat island effect is not limited to temperature increases alone; it also produces significant consequences for public health, energy consumption, and urban vulnerability. High concentrations of heat-retaining materials, limited green space availability, and heat accumulation associated with transportation systems increase respiratory and cardiovascular health risks during heatwaves, elevate mortality rates, and place additional stress on energy infrastructure (Baş & Partigöç, 2022). These impacts are particularly pronounced in areas with high concentrations of low-income populations.

Increasing building density and the expansion of impervious surfaces further reinforce UHI effects by delaying the release of heat stored during the day into the atmosphere during nighttime hours. Yavuz and Ünlütürk (2025) emphasize that reduced vegetation cover, rising concrete and asphalt ratios, and intensive energy consumption establish a reciprocal feedback relationship between UHI and global warming. Accordingly, uncontrolled urban development should be regarded not merely as a local temperature anomaly, but as a structural risk that contributes to global-scale greenhouse gas accumulation.

UHI and surface urban heat island (SUHI) effects are particularly pronounced in tropical regions. A study conducted in Kampala demonstrates that increasing impervious surfaces, declining albedo values, and the loss of green and blue spaces raised LST by up to 5–6°C, with impacts extending toward urban peripheries (Li et al., 2021). These findings reveal that uncontrolled urbanization disrupts surface energy balance, generating both spatial and socio-economic vulnerability.

Finally, urbanization-driven increases in traffic density, vehicle ownership, household energy demand, and industrial activities lead to elevated emissions of CO_2 and NO_x, thereby intensifying the global warming process simultaneously through atmospheric composition and surface temperature pathways (Ayodeji, 2009).

2.3. Impacts of Uncontrolled Urban Development on Climate Change

Climate change is defined as statistically significant long-term variations in the mean state or variability of the climate system. Since the Industrial Revolution, accelerated fossil fuel consumption, deforestation, and unplanned urbanization have increased greenhouse gas concentrations in the atmosphere, leading to rising global temperatures and destabilization of the climate system. During this process, the influence of human activities on climate has become increasingly evident, while climate change–related disasters have generated critical risks for both natural environments and human settlements (Baş & Partigöç, 2022).

Uncontrolled urbanization emerges as a fundamental process that both accelerates climate change and increases vulnerability to its impacts. The replacement of natural surfaces with concrete, asphalt, and other impervious materials strengthens the urban heat island (UHI) effect, while increased heat absorption and storage capacities fundamentally alter urban temperature regimes. Rising LST values result in ecosystem degradation, habitat loss, declining biodiversity, and weakened hydrological cycles. These changes increase the risk of sudden flooding in some regions while intensifying drought tendencies in others (Mohamed et al., 2025).

Rising urban temperatures produce not only ecological impacts but also direct consequences for human health (Deniz, 2009; Bayram et al., 2006). In cities where UHI effects are pronounced, elevated ozone concentrations during heatwaves increase mortality rates associated with respiratory and cardiovascular diseases. Increased energy demand for cooling purposes further stimulates fossil fuel consumption, leading to higher greenhouse gas emissions and creating a new feedback loop that reinforces global warming (Mohamed et al., 2025).

One of the key components of urban vulnerability is the rapid transformation of natural surfaces and the increasing proportion of impervious areas (Karakoç & Kovancı, 2022). Dependence on fossil fuels in transportation, inadequate infrastructure, loss of green spaces, and rising building density render cities more vulnerable to extreme weather events. These conditions elevate flood risks, deteriorate air quality, and accelerate biocapacity losses in urban environments (Baş & Partigöç, 2022).

Another critical consequence of climate change is sea-level rise, which increases risks such as flooding, coastal erosion, saltwater intrusion, and land loss, particularly in coastal cities (Aksay et al., 2005). In artificial environments with high proportions of impervious surfaces, these impacts are more severe, and island states and low-lying coastal regions are increasingly identified as among the most vulnerable areas to future climate-induced migration (Baş & Partigöç, 2022).

Trends in climate-related disasters further indicate an escalation of risk. According to CRED data, disaster frequency and associated mortality have increased significantly over the past two decades compared to the 1980–1999 period. Climate-driven hazards such as floods and storms have intensified both economic and social devastation, particularly in developing countries (Baş & Partigöç, 2022).

The elevation of nighttime temperatures due to the urban heat island effect further contributes to the persistence of climate risks. Yavuz and Ünlütürk (2025) highlight that delays in the nocturnal release of heat stored in high-thermal-mass building materials cause sustained temperature differentials in urban centers. This condition transforms UHI into both a direct public health risk and a critical feedback mechanism that reinforces climate change.

The social dimensions of UHI and SUHI processes are also significant. Li et al. (2021) demonstrate that the highest SUHI intensities in Kampala are concentrated in areas characterized by inadequate infrastructure and socio-economic vulnerability. Low-quality building materials, limited green spaces, and insufficient ventilation increase susceptibility to heat stress, particularly among vulnerable groups such as the elderly and children. These findings reveal that irregular urbanization transforms climate change into not only an environmental issue but also a social problem that exacerbates inequality.

Uncontrolled urban development also leads to habitat fragmentation and biodiversity loss, while the reduction of forested areas disrupts ecological cycles and weakens the buffering capacity of cities against climate change (Ayodeji, 2009). Air pollution generated by industrial activities and dense traffic further amplifies the impacts of rising temperatures and increases health risks for urban residents. The accumulation of particulate matter and ozone, when combined with high temperatures, significantly reduces urban quality of life (Ayodeji, 2009).

In conclusion, the contribution of uncontrolled urbanization to climate change extends far beyond temperature increases alone. It represents a multidimensional process affecting ecosystem integrity, public health, socio-economic inequality, and disaster risk simultaneously. Therefore, urbanization dynamics must be addressed within a holistic and interdisciplinary framework in the context of climate change.

3. Synthesized Findings: Urban Mitigation and Adaptation Approaches

Considering the impacts of climate change on cities, it has become imperative to address both mitigation and adaptation policies simultaneously within an integrated and long-term framework. IPCC reports clearly demonstrate that the cost of initiatives aimed at reducing greenhouse gas emissions and strengthening adaptive capacity is substantially lower than the total damages expected from climate change. Accordingly, the adoption of renewable energy sources, energy-efficient building designs, sustainable transportation systems, green infrastructure applications, and disaster-oriented planning strategies has emerged as a set of fundamental approaches for both emission reduction and vulnerability mitigation in urban areas (Baş & Partigöç, 2022).

The sustainable urbanization paradigm highlights the need for a multidimensional transformation that includes the protection of natural areas, enhancement of urban green spaces, promotion of public transportation, and the widespread implementation of ecosystem-based planning practices. Afforestation, shading elements, conservation of water bodies, permeable surface applications, and the use of environmentally friendly building materials play a critical role in mitigating the urban heat island (UHI) effect (Ayodeji, 2009).

In parallel, the discipline of urban planning has moved beyond traditional growth models that neglect climate change, adopting new approaches centered on sustainability, resilience, and ecological integrity. Contemporary planning paradigms such as eco-cities, compact cities, carbon-neutral cities, smart cities, and resilient cities require the reconsideration of multiple processes, including land use, energy management, transportation planning, and green infrastructure development. The effective implementation of this transformation necessitates interdisciplinary collaboration among urban planners, engineers, climate scientists, ecologists, and social scientists (Baş & Partigöç, 2022).

The literature addressing the reduction of urban thermal risks consistently identifies green infrastructure as one of the most effective mitigation mechanisms across all climate zones. Parks, afforestation initiatives, green roofs, vertical gardens, and corridor-based green spaces can generate cooling effects ranging between 2 and 5°C within urban environments, providing significant benefits for both public health and energy consumption. Water bodies, high-reflectance (high-albedo) materials, permeable surfaces, and morphological designs focused on shading and wind corridors also represent effective intervention areas for reducing surface temperatures. In addition, remote sensing technologies, three-dimensional urban models, and artificial intelligence–based LST prediction tools enable the monitoring of thermal risks at the urban scale and support spatially targeted planning decisions (Mohamed et al., 2025).

The effectiveness of green infrastructure and material-based solutions is consistently supported by international literature. According to Yavuz and Ünlütürk (2025), green roofs, vertical gardens, increased park areas, afforestation, and permeable surface applications significantly reduce both surface and air temperatures, thereby decreasing cooling energy demand and improving energy efficiency. High-albedo roof and façade coatings, as well as reflective asphalt and concrete surfaces, reduce heat accumulation by reflecting a greater portion of incoming solar radiation, ultimately limiting UHI intensity. These findings demonstrate that climate adaptation strategies must address not only new urban developments but also the transformation of existing urban fabric (Yavuz & Ünlütürk, 2025).

Evidence supporting the indispensable role of nature-based solutions in climate adaptation also includes studies conducted in rapidly urbanizing African cities. Li et al. (2021) show that the preservation of water bodies and green corridors is decisive in reducing SUHI intensity, while planned urbanization strengthens bluespace–greenspace connectivity and limits urban thermal risks. This approach is of particular strategic importance for cities experiencing rapid population growth and intense pressure from unregulated urban expansion.

Local governments have also emerged as central actors in the fight against climate change. Given the unique spatial, ecological, and socio-economic characteristics of cities, a “one-size-fits-all” climate policy approach is insufficient; instead, locally tailored strategies are required. In this context, climate action plans that define greenhouse gas inventories, mitigation targets, and sector-specific adaptation measures have become increasingly widespread. Participation of local governments in international networks such as ICLEI, the Covenant of Mayors, and C40 provides significant opportunities for accessing financial resources, building institutional capacity, and sharing best practices (Baş & Partigöç, 2022).

Overall, reducing the impacts of uncontrolled urbanization in the context of climate change is not merely a technical planning issue; it requires a multidimensional transformation encompassing land-use policy reform, ecosystem conservation, disaster risk reduction, social justice enhancement, and the strengthening of urban resilience. The expansion of green and blue infrastructure, mitigation of UHI effects, development of sustainable transportation options, and implementation of participatory planning processes constitute the fundamental building blocks of climate-resilient cities (Baş & Partigöç, 2022).

4. Conclusions

This study examines the impacts of uncontrolled urbanization on global warming and climate change within a multidimensional framework, providing an integrated assessment of the ecological, thermal, socio-economic, and health-related consequences of urbanization dynamics. The findings indicate that rapid and unplanned urban growth triggers interrelated processes such as rising surface temperatures, loss of natural habitats, exceedance of ecological carrying capacity, increasing air pollution levels, and deepening urban vulnerability to climate-related disasters. The literature consistently confirms that increases in land surface temperature (LST) resulting from LULC changes represent both a local manifestation of global warming and a feedback mechanism that amplifies the impacts of climate change (Mohamed et al., 2025; Li et al., 2021; Yavuz & Ünlütürk, 2025).

The study further demonstrates that uncontrolled urbanization poses significant risks not only to the physical environment but also to the health, quality of life, and socio-economic security of urban populations. The disproportionate exposure of older adults, children, and low-income groups to high temperatures and increased air pollution highlights how climate change intersects with social inequalities, creating compounded vulnerability. This finding underscores the need for urbanization policies that integrate ecological considerations while simultaneously promoting social justice.

The results also reveal that mitigation and adaptation strategies cannot be treated as separate pathways in managing climate change at the urban scale. Solutions such as green infrastructure, permeable surfaces, high-albedo materials, protection of green and blue corridors, and compact, carbon-neutral urban models provide effective tools for both reducing UHI effects and preserving ecosystem integrity. Moreover, the integration of remote sensing technologies, AI-based LST prediction models, and 3D urban simulations into planning processes offers valuable insights for monitoring risks and targeting interventions more effectively.

In conclusion, the relationship between uncontrolled urbanization and climate change extends beyond an environmental issue and constitutes a complex challenge that must be addressed across planning, public health, economic development, social policy, and governance domains. Reorganizing urbanization processes in accordance with sustainability principles is critical not only for reducing current climate risks but also for building resilient cities capable of withstanding future climate-related disasters. By synthesizing existing literature within a comprehensive analytical framework, this study provides a strong theoretical foundation supporting the necessity of sustainable urbanization policies.

References

Aksay, C. S., Ketenoğlu, O., & Kurt, L. (2005). Küresel Isınma ve İklim Değişikliği. *Selçuk Üniversitesi Fen Fakültesi Fen Dergisi*, *1*(25), 29-42.

Aksöz, F., & Çelik, A. (2023). Küresel iklim değişikliğine karşı dirençli kent yönetişimi. *Uluslararası Sosyal Siyasal ve Mali Araştırmalar Dergisi*, *3*(2), 75-85.

Ayodeji, O. (2009). *Urbanisation and the incidence of urban heat island: Implications for climate change and global warming.* REAL CORP 2009 Proceedings, 960–965.

Baş, E., & Partigöç, N. S. (2022). İklim değişikliğine uyum sürecinde kent planlamanın rolü. *Resilience*, *6*(1), 127-143.

Bayram, H., Dörtbudak, Z., Fişekçi, F. E., Kargın, M., & Bülbül, B. (2006). Hava kirliliğinin insan sağlığına etkileri, dünyada, ülkemizde ve bölgemizde hava kirliliği sorunu" paneli ardından. *Dicle Tıp Dergisi*, *33*(2), 105-112.

Chirico, F. (2021). *Spirituality to cope with COVID-19 pandemic, climate change and future global challenges*. Journal of Health and Social Sciences, 6, 151–158.

Çiftçi, Ç., Dursun, Ş., Levend, S., & Kunt, F. (2013). Topoğrafik yapı, iklim şartları ve kentleşmenin Konya'da hava kirliliğine etkisi. *Avrupa Bilim ve Teknoloji Dergisi*, *1*(1), 19-24.

Deniz, M. (2009). Sanayileşme perspektifinde kentleşme ve çevre ilişkisi. *Journal of Geography*, (19), 95-105.

Esper, J., Smerdon, J. E., Anchukaitis, K. J., Allen, K., Cook, E. R., D'Arrigo, R., Guillet, S., Ljungqvist, F. C., Reinig, F., Schneider, L., *et al.* (2013). *The IPCC's reductive Common Era temperature history*. Communications Earth & Environment, 5, 222. https://doi.org/10.xxxx

Fourier, J. (1824). *Remarques générales sur les températures du globe terrestre et des espaces planétaires*. Annales de Chimie et de Physique, 27, 136–167. (Original work archived in 2020). Available online: https://www.academie-sciences.fr/pdf/dossiers/Fourier/Fourier_pdf/Mem1827_p569_604.pdf (accessed on 27 January 2024). *(In French)*

Gameiro, F., Ferreira, P., & Faria, M. (2023). *Association between social and emotional competencies and quality of life in the context of war, pandemic and climate change*. Behavioral Sciences, 13, 249. https://doi.org/10.xxxx

İğci, T., & Çobanoğlu, N. (2019). İklim değişikliğinin ve iklim değişikliğiyle ilgili küresel anlaşmaların çevre etiği bakımından değerlendirilmesi. *Ankara Üniversitesi Çevrebilimleri Dergisi*, *7*(2), 130-146.

Karakoç, D. Y., & Kovancı, E. (2022). İklim Değişikliğine Uyum Çabalarında Kentsel Yeşil Alan Yönetimi: İstanbul, Ankara ve İzmir Örnekleri. *Vizyoner Yönetim*, 53.

Kleerekoper, L., Van Esch, M., & Salcedo, T. B. (2012). How to make a city climate-proof, addressing the urban heat island effect. Resources, Conservation and Recycling, 64, 30-38.

Koç, V. (2023). Küresel kentsel gelişimin çevresel etkileri üzerine bir inceleme. *JOEEP: Journal of Emerging Economies and Policy*, *8*(1), 421-433.

Laino, E., & Iglesias, G. (2023). *Extreme climate change hazards and impacts on European coastal cities: A review*. Renewable and Sustainable Energy Reviews, 184, 113587. https://doi.org/10.xxxx

Li, X., Stringer, L. C., Chapman, S., & Dallimer, M. (2021). How urbanisation alters the intensity of the urban heat island in a tropical African city. *PLoS One*, *16*(7), e0254371.

Mavi, İ. (2025). Küresel Kentleşme Sürecinde Sosyolojik Dönüşümler ve Türkiye'de Çarpık Kentleşme Gerçeğinde Sürdürülebilir Kentleşme. *Nişantaşı Üniversitesi Sosyal Bilimler Dergisi*, *13*(1), 13-14.

McBean, G., & Ajibade, I. (2009). *Climate change, related hazards and human settlements*. Current Opinion in Environmental Sustainability, 1, 179–186.

Mohamed, A., Lorestani, N., & Shabani, F. (2025). *Impact of urbanization on land surface temperature: A global perspective.* Current Research in Environmental Sustainability, 10, 100315.

Ramanauskas, E., Bukantis, A., Dringelis, L., Kaveckis, G., & Jonkutė-Vilkė, G. (2024). *Climate change and cities of Lithuania: Threats, problems and prerequisites for solution*. Urban Science, 8(4), 186.

Sütçüoğlu, G. G., Demirkol, A. K., Zamani, A., & Önaç, A. K. (2022). Kent Ormanlarının Karbon Yakalama Potansiyeli. 6th International Students Science Congress Proceedings. İzmir Katip Çelebi University.

Şen, G., & Özer, Y. E. (2018). Üniversite öğrencilerinin iklim değişikliği ve çevre sorunları konusundaki farkındalıklarının değerlendirilmesi: Dokuz Eylül Üniversitesi kamu yönetimi örneği. *Bitlis Eren Üniversitesi Sosyal Bilimler Dergisi*, *7*(2), 667-688.

Tuğaç, Ç. (2018). Türkiye için iklim değişikliğine dayanıklı kentsel planlama modeli önerisi: Eko-kompakt kentler. *Atatürk Üniversitesi İktisadi ve İdari Bilimler Dergisi*, *32*(4), 1047-1068.

Türkeş, M. (2008). Küresel iklim değişikliği nedir? Temel kavramlar, nedenleri, gözlenen ve öngörülen değişiklikler. *İklim Değişikliği ve Çevre*, *1*(1), 26-37.

Yavuz, E., & Ünlütürk, M. S. (2025). The Impact of Cities on Climate Change: A Literature Review on Urban Heat Island. *International Journal of Environment and Geoinformatics*, *12*(2), 80-93.

Chapter 17

PERFORMANCE COMPARISON OF PID AND PD CONTROLLERS FOR QUADROTOR STABILIZATION UNDER SIMULATED WIND FORCES

Okan DUYMAZLAR [1]

---

[1] Lecturer, Ege University, Ege Vocational School, Mechatronics, okan.duymazlar@ege.edu.tr, ORCID:0000-0002-1327-7493.

1. INTRODUCTION

PID and PD controllers are the most widely used feedback control techniques in engineering and have especially turned into standard solutions for position-velocity control in industrial processes, autonomous vehicles, robotic arms, and drone and mobile robots (Alavandar & Nigam, 2008; Engin & Engin, 2012, 2018; Salih, Moghavvemi, Mohamed, & Gaeid, 2010). PD controllers can quickly and steadily produce a response using the system's instantaneous error (P) and rate of change of error (D); therefore, they provide good damping in transient regimes but may not fully reach the target point in steady-state error conditions. In contrast, the PID controller eliminates the error accumulated over time by adding an integral (I) term to the PD structure, bringing the steady-state error close to zero (Bolandi, Rezaei, Mohsenipour, Nemati, & Smailzadeh, 2013; Engin & Engin, 2014; Okasha, Kralev, & Islam, 2022; Subudhi & Ezhilarasi, 2018). However, if the integral effect is incorrectly tuned, it can cause excessive accumulation (windup), resulting in delayed and oscillatory behavior. Therefore, while PID control offers better accuracy, PD control provides faster response and more stable behavior. The different characteristics of these two control structures become particularly evident in dynamic applications such as drone position control under the influence of disruptive forces.

In particular, this study aims to provide a comprehensive comparison of the two fundamental feedback methods commonly employed in quadrotor position control – PID and PD controllers. In the experimental setup established on AirSim, two drones were subjected to the same flight scenario, each attempting to maintain its target position using a different control strategy (Microsoft Research, 2021). Due to the disruptive forces (wind effect) applied in random directions and magnitudes during flight, both the transient regime responses and stability characteristics of the controllers were examined in depth. This comparison experimentally examined the PID controller's advantage in steady-state error compensation and the PD controller's ability to respond more stably and quickly to high-frequency disturbances.

2. MATERIAL AND METHOD

In this study, the comparison of drone position control algorithms was performed on Microsoft AirSim. AirSim is an open-source simulation platform that realistically simulates physics-based flight dynamics, sensor modeling, and environmental disturbances (Madaan et al., 2019; Microsoft Research, 2021).

The simulation environment was controlled via the Python API through the AirSim client. Instead of applying torque directly to the drone motors, AirSim's high-level control interface was used, and drone movement was achieved using the move_by_velocity_async(vx, vy, vz) command. With this approach, the PID/PD outputs generated by the controller are directly converted into body-referenced velocity commands for the drone, thus ensuring a fair comparison of different control algorithms on the same dynamics.

Figure 1 *Drone models used to test the controllers*

In the simulation, two drones with identical physical models, as shown in Figure 1, were used. One drone was operated with a PID controller, and the other with a PD controller. Both drones were directed to a specified target location, and wind effects were modeled by applying random external forces to the environment simultaneously. These forces were applied periodically using AirSim's set_external_force([Fx, Fy, Fz]) function, and the response behavior of both controllers to the disruptive effects was observed.

During the simulation, the instantaneous position, axis-based error values, and control commands (Vx, Vy, Vz) from the drones were saved, and the results were stored in CSV format. With this data flow, the stability, accuracy, and recovery performance of the PID and PD controllers became directly comparable.

2.1. Overall Structure of Controllers

In controllers, it is only the x-y-z position information and linear velocity of the drone that are used. To elaborate for a single axis: the target position is defined as x_ref, the measured position as x(t), and the error as e(t) = x_ref - x(t). In clearer terms, as shown in the following equation, the controller functions as a position-to-velocity converter.

$$u(t) = v_{\mathrm{cmd}}(t)$$

AirSim receives commands in the form of linear velocity parameters, as shown in the formula below.

$$[v_x, v_y, v_z] = u(t)$$

Therefore, the PID does not directly generate torque/thrust for the drone dynamics; it only provides a speed target to AirSim's low-level motor controller.

The classic PID controller is in the form shown in the following formula:

$$u(t) = K_p e(t) + K_i \int_0^t e(\tau)\, d\tau + K_d \frac{de(t)}{dt}$$

The same equation is used in discrete time (within the simulation cycle) as shown below:

$$u[k] = K_p e[k] + K_i I[k] + K_d \frac{e[k] - e[k-1]}{\Delta t}$$

The integral update is performed at the Δt step, which is predetermined and used as 0.01 seconds in this simulation study.

$$I[k] = I[k-1] + e[k]\Delta t$$

The three axes of the drone's position have been controlled separately and an independent PID/PD controller has been implemented for each axis. The controller output has been sent to AirSim as a speed command.

$$u_x(t), u_y(t), u_z(t) \; \& \; \left(v_{x}, \, v_{y}, \, v_z\right)$$

Simulations were performed on both controllers using the same time steps and discrete integral. The only difference between the controllers is whether they include the integral coefficient.

2.2. Modeling and Application of Disruptive Effects

In a real flight environment, external factors such as wind impacts, turbulence, sudden air currents, or vibration of the platform directly affect the drone's stability. Therefore, to evaluate the performance of control algorithms more realistically in the simulation environment, disturbance forces were applied to the system at specific intervals. These disturbances were modeled as short-term external force impacts that suddenly and unexpectedly change the drone's position and velocity dynamics.

These external forces ensured that the control algorithms could be tested in sudden and non-ideal scenarios that closely resemble real flight conditions, rather than just under nominal conditions. The robustness, recovery speed, and damping characteristics of the controllers could be quantitatively evaluated by observing the system's response immediately after each disturbance. Such an approach provides a more reliable assessment of controller performance, particularly in terms of stability preservation and trajectory recovery under realistic environmental uncertainties.

In the simulation, disturbing effects were generated in random directions and within a specific magnitude range. Force components (Fx, Fy, Fz) were selected in both positive and negative directions to force the system in different directions. Thus, not only the target tracking performance of the control algorithms but also their stability, recovery time, and resilience to disturbance effects could be analyzed. Some of the instantaneous results of the disturbance effects on both drones are shown in Figure 2.

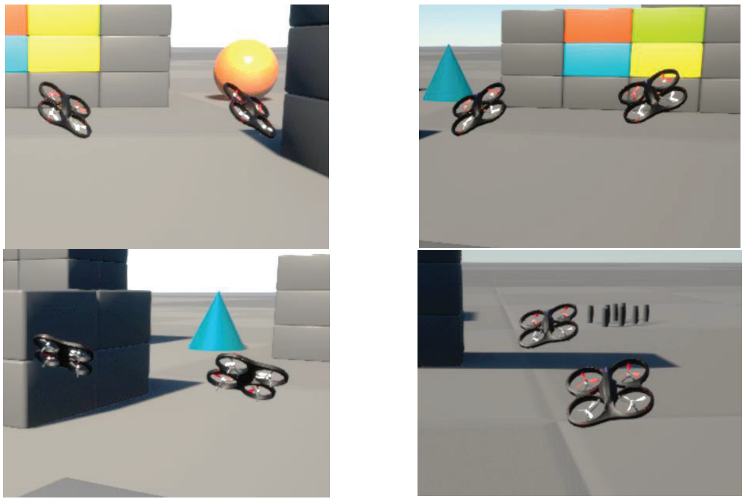

Figure 2 The effects of disruptive factors on both drones

The duration of the disruptive effect in the initial simulations lasts for 0.5 seconds, successfully replicating the instantaneous and impulsive nature of wind. The short duration of the effect is critical for evaluating how quickly and smoothly the control system can recover its stability in response to sudden disturbances.

A specific time window has been established for the drones to regain balance after each disturbance pulse. In this study, the interval between two pulses was set to 5 seconds. This duration was chosen to clearly observe the controller's recovery behavior, reveal the transient response differences between PD and PID algorithms, and prevent excessive accumulation of disturbance effects on the system. The amplitude range of the disturbances was set to ±30 Newton. This range was selected to be compatible with the natural dynamics of the drone platform used in the simulation and to ensure that the control algorithms create realistic loading without approaching their boundary conditions. Forces applied at this magnitude can disturb the drone's position simultaneously in three axes, not just one; this provides a significant advantage in evaluating the multi-axis correction performance of the control algorithms.

For systematic and reproducible evaluation, the disturbance injection strategy has been designed in a controlled and parameterized manner. Instead of adding random or steady-state noise, disturbances were applied as discrete impulse-like forces at predefined times, allowing for clear isolation and analysis of the system response. This methodology eliminates uncertainty in performance evaluation by directly linking every deviation in position, velocity, and attitude to a known external disturbance. When disturbances are configured in such a way, each controller is exposed to the same disturbance conditions, making the simulations a fair and transparent environment for comparing different control strategies. Furthermore, these configurations make it possible to examine in detail how quickly and effectively controllers suppress transient errors and how quickly and effectively they regain stability before the next disturbance is added, providing a clear basis for quantitative performance metrics such as settling time, overshoot, and residual oscillations.

In this context, structuring the disruptive impact framework also serves to address the gap between simulated idealized conditions and the inherent uncertainty of real-world flight conditions. Through clearly defining the timing, magnitude, and form of each disruptive impact, it maintains simulation experimental control while also revealing non-ideal effects that challenge controller dynamics. Balancing these factors is crucial to avoid overly optimistic performance assessments that could arise from purely nominal simulations. Furthermore, the use of impulse-like disturbance effects provides a clear distinction between the forced response caused by the disturbance and the natural response managed by the controller and system dynamics. Thus, the transient behavior observed after each disturbance can be attributed primarily to the control algorithm itself rather than superimposed or accumulated external effects. This design choice ensures that variations in system response are both meaningful and interpretable, enhancing the reliability of subsequent comparisons between different controller configurations and disturbance impact scenarios.

Disturbance effects were applied at different amplitudes and durations, and the expected duration for impulse intervals was also defined as an additional parameter. The performance of the models was examined in detail using different scenarios based on the three parameters mentioned.

As a result, this approach made it possible to objectively compare the behavior of both PD and PID control strategies under sudden disruptive effects. Sudden impacts, with their short duration and repetitive cyclical structure, created powerful test scenarios that represent real flight dynamics.

2.3. PID and PD Controller Coefficients

Across the two control strategies, the controller structures were deliberately kept as similar as possible throughout the study to ensure a fair and controlled comparison. Both controllers were implemented within the same dynamic model, subjected to the same reference trajectories, and exposed to the same disruptive shock impacts defined in the simulation environment. This design choice eliminates potential bias arising from differences in tuning procedures or controller complexity and allows for a clearer focus on the observed performance variations being directly attributable to structural differences in the control laws. In this way, the standardization of experimental conditions establishes a clear and interpretable framework for evaluating how different feedback mechanisms affect system behavior under external disturbances. Otherwise, even minor differences in controller configuration, particularly when analyzing disturbance response performance, can lead to misleading results if not properly isolated.

In the controller designs in this study, the P (Proportional) and D (Derivative) gains for both controllers were set to fixed values determined experimentally(He & Zhao, 2014). The only parameter that distinguishes the PID (Proportional-Integral-Derivative) controller from the PD (Proportional-Derivative) controller is the I (Integral) gain. The main objective of this study is to investigate the significant effect of the integral parameter on the system response against unpredictable external disturbance effects.

In this comparative framework, only one of the two controllers incorporates integral effect, while both controllers have the same proportional and derivative gain values. The P, I, and D parameters used in the results are shared along with the response signals. By keeping the P and D parameters completely identical, any observed difference in the system response can be attributed solely to the presence or absence of the integral term. Intentionally isolating the integral effect prevents confounding effects from other tuning parameters and ensures the comparison remains methodologically sound. Consequently, the integral component's role in compensating for accumulated errors, rejecting steady-state disturbances, and improving steady-state accuracy may be evaluated clearly and objectively, without interference from changes in proportional or derivative behavior.

3. RESULTS

Within the scope of this study, along with the Kp, Ki, and Kd coefficients in the simulation environment, wind force representing the disturbing effect, wind application duration, and the waiting time between two disturbing effects were also used as experimental parameters. Different combinations were tested within the scope of the design parameters; for example, in some scenarios, the wind effect duration was kept short, but the wind strength (force randomly generated in three axes) was increased. In another variation of the same experiment, the wind force and effect duration were kept constant, and the waiting time between disturbing effects was changed.

In all scenarios, the Kp and Kd coefficients of both controllers were kept constant, and the integral gain Ki in the PID controller was tested with different values under the same experimental conditions. Thus, a comprehensive analysis was performed by creating a wide pool of experimental parameters.

The most critical point of this study is that both drones have exactly the same characteristics except for their initial reference positions and are exposed to wind forces of the same magnitude during the same runtime throughout the simulation. This allowed for a fair and objective comparison of the performance of the PID and PD control algorithms.

The results obtained were evaluated based on position errors in the x–y–z axes and are presented in Figures 3–8.

Figure 3 Short impact duration and long recovery time results (Kp:2, Ki:0.2, Kd:0.8, Force: 0.5N, Interval: 10s)

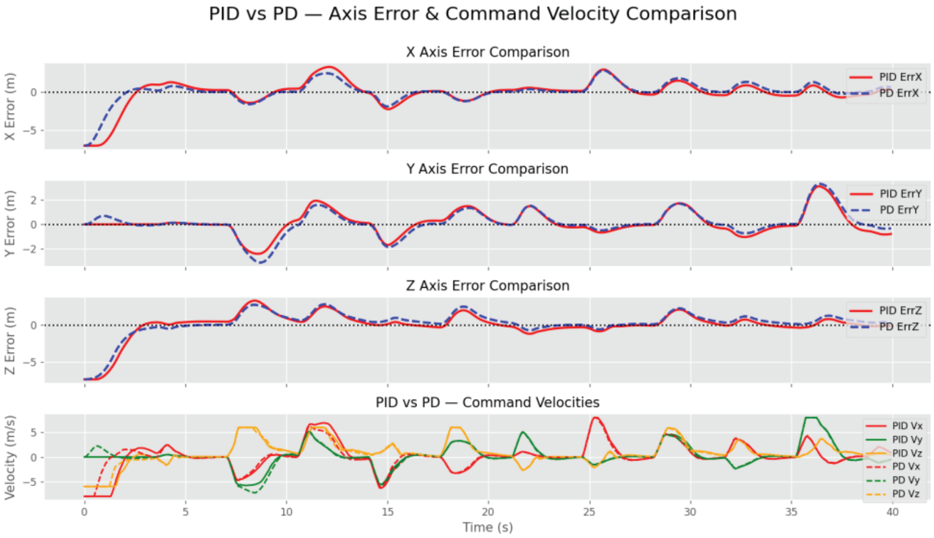

Figure 4 Short impact duration and short recovery time results (Kp:2, Ki:0.2, Kd:0.8, Force: 0.5N, Interval: 5s)

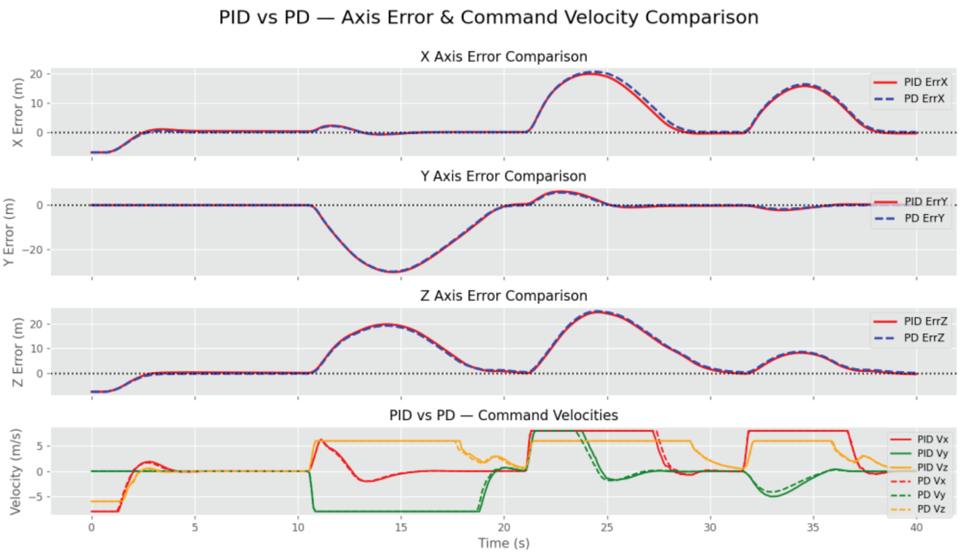

Figure 5 Strong wind impact and long recovery time results (Kp:2, Ki:0.2, Kd:0.8, Force: 15N, Interval: 10s)

In the subsequent experimental parameters, the Kp and Kd coefficients of the controllers were used identically, but the integral coefficient of the PID controller was changed.

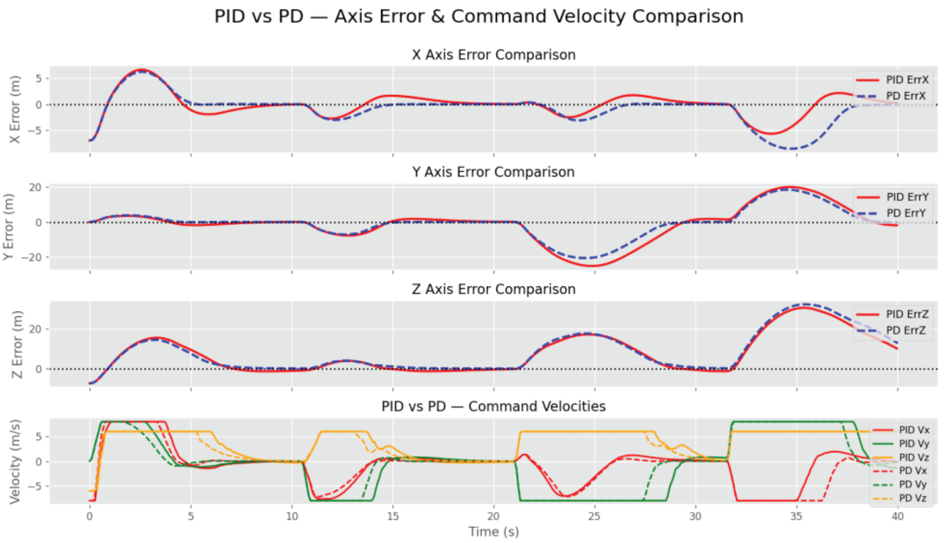

Figure 6 Strong wind impact and bigger integral const.
(Kp:2, Ki:0.8, Kd:0.8, Force: 15N, Interval: 5s)

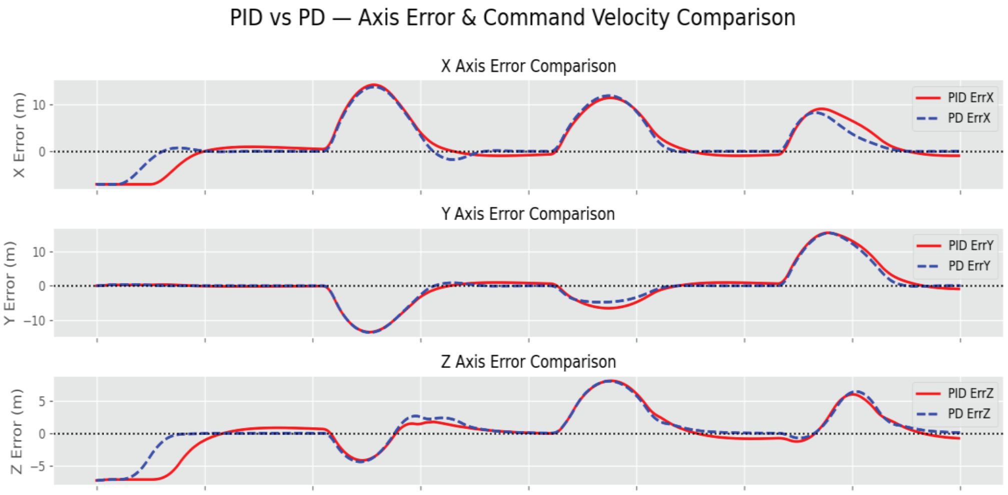

Figure 7 Strong wind impact and bigger integral const.
(Kp:2, Ki:1.8, Kd:0.8, Force: 15N, Interval: 10s)

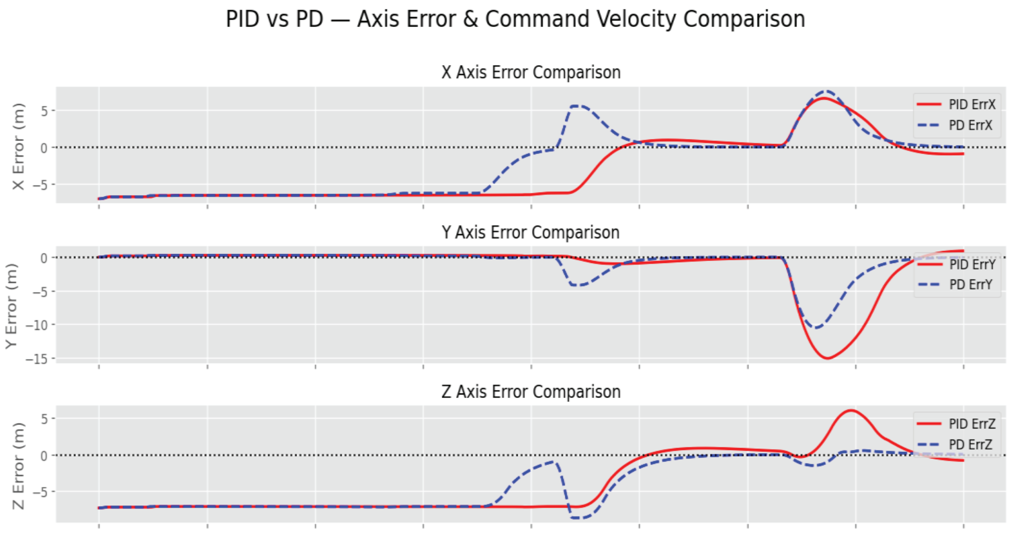

Figure 8 Strong wind impact and bigger integral const.
(Kp:2, Ki:2.8, Kd:0.8, Force: 30N, Interval: 10s)

The results presented in Figures 3–8 comparatively demonstrate how PID and PD controllers behave under wind simulation. First, in experiments using low wind intensity and long recovery times (Figures 3 and 4), both controllers were able to reduce position error in a stable manner, but the PID controller showed smoother recovery, especially on the X and Y axes, due to its integral effect. The PD controller, on the other hand, produced a more aggressive speed command immediately after the impact, but in the long run, it could not reach as low a steady-state error level as the PID controller.

In scenarios where wind intensity was increased (Figure 5), the error of both the PID and PD controllers increased significantly, with amplitudes increasing dramatically, especially on the Y and Z axes, due to the force impact. In this case, although the integral effect of the PID helps to stabilize the system, it also exhibits a more delayed correction behavior compared to the PD controller. In other words, when the wind force is very high, the integral term can delay the response rather than improving the system's behavior.

Therefore, the effect of different Ki values was also investigated. As seen in Figures 6–8, increasing the integral gain (Ki = 0.8, 1.8, and 2.8) significantly changed the system behavior. Although the PID controller became more stable against shocks and had lower long-term error as the Ki value increased, the short-term overshoot amount increased, and the system occasionally produced more aggressive correction commands due to excessive integral accumulation. In the same experiments, the PD controller produced less oscillation but ultimately did not achieve as low a steady-state error level as the PID.

When all results are evaluated together, under wind-simulated disturbance effects:

- PD controller offered a more stable solution with a quick response to short disturbances and low wind levels.
- PID controller was more successful in situations requiring long-term recovery and where steady-state error was significant.
- Increasing the integral term did not always improve performance; in some cases, it led to excessive responses.
- Comparison was fair and consistent since both controllers were exposed to the same external force profile.

As a resılt, while the difference between the two controllers was quite small at low wind levels (Figures 3–4), at high wind speeds (Figures 5–8), the integral parameter of the PID controller became the most critical factor determining performance. Thus, the study clearly demonstrates that gain settings in PID/PD selection under wind effects in quadrotor simulation directly affect flight stability.

REFERENCES

Alavandar, S., & Nigam, M. J. (2008). Fuzzy PD+I control of a six DOF robot manipulator. *Industrial Robot*. Retrieved from https://doi.org/10.1108/01439910810854610

Bolandi, H., Rezaei, M., Mohsenipour, R., Nemati, H., & Smailzadeh, S. M. (2013). Attitude Control of a Quadrotor with Optimized PID Controller. *Intelligent Control and Automation*. Retrieved from https://doi.org/10.4236/ica.2013.43039

Engin, M., & Engin, D. (2012). Path planning of line follower robot. In *EDERC 2012 - Proceedings of the 5th European DSP in Education and Research Conference*. Retrieved from https://doi.org/10.1109/EDERC.2012.6532213

Engin, M., & Engin, D. (2014). Design of real time embedded PID controller for sun tracking robot manipulator. In *IEEE/ASME International Conference on Advanced Intelligent Mechatronics, AIM*. Retrieved from https://doi.org/10.1109/AIM.2014.6878156

Engin, M., & Engin, D. (2018). PID CONTROL OF A PARALLEL MECHANISM SUN TRACKING SYSTEM BY MICROCONTROLLER. In *SOLARTR 2018 Proceedings*.

He, Z., & Zhao, L. (2014). A simple attitude control of quadrotor helicopter based on Ziegler-Nichols rules for tuning pd parameters. *Scientific World Journal*. Retrieved from https://doi.org/10.1155/2014/280180

Madaan, R., Gyde, N., Vemprala, S., Brown, M., Nagami, K., Taubner, T., … Kapoor, A. (2019). AirSim Drone Racing Lab. In *Proceedings of Machine Learning Research*.

Microsoft Research. (2021). AirSim.

Okasha, M., Kralev, J., & Islam, M. (2022). Design and Experimental Comparison of PID, LQR and MPC Stabilizing Controllers for Parrot Mambo Mini-Drone. *Aerospace*. Retrieved from https://doi.org/10.3390/aerospace9060298

Salih, A. L., Moghavvemi, M., Mohamed, H. A. F., & Gaeid, K. S. (2010). Flight PID controller design for a UAV quadrotor. *Scientific Research and Essays*.

Subudhi, C. S., & Ezhilarasi, D. (2018). Modeling and Trajectory Tracking with Cascaded PD Controller for Quadrotor. In *Procedia Computer Science*. Retrieved from https://doi.org/10.1016/j.procs.2018.07.082

Chapter 18

VEGETATION INDICES FOR MONITORING FOREST PHENOLOGY

Sude Gül YEL[1], *Esra TUNÇ GÖRMÜŞ*[2]

---

[1] Lecturer, Artvin Çoruh University, Artvin Vocational School, Department of Land Registry and Cadastre. Email: sudegyildiz@artvin.edu.tr ORCID: 0000-0001-9975-8345

[2] Assoc. Prof. Dr., Karadeniz Technical University, Faculty of Engineering, Department of Geomatics Engineering. Email: etuncgormus@ceng.ktu.edu.tr ORCID: 0000-0002-3334-2061

1. Introduction

Forest phenology defines the annual life cycle stages that cover the processes from the budding of trees together with early spring, to leaf expansion and flowering processes that reach photosynthetic saturation in late spring and early summer, and up to the senescence and dormancy periods with autumn (Berra & Gaulton, 2021; Dronova & Taddeo, 2022). These seasonal processes reflect ecosystem functioning and climatic variability (Gray & Ewers, 2021; Zheng et al., 2022). However, the factors of phenological change are not only these. Anthropogenic pressures resulting from urbanization (Hu et al., 2024), topographic difficulties in mountainous regions (Orusa et al., 2023), differences in forest species (Guo et al., 2024), and temperature anomalies imposed by global climate change (Zheng et al., 2022) also take place among the factors shaping phenological dynamics.

In forests; photosynthetic activity, structural changes, and changes occurring in pigments as a result of seasonality can be measured through remote sensing technologies (Liu et al., 2022; Guo et al., 2024; Yan et al., 2025). The use of remote sensing in phenology studies provides ease thanks to high temporal resolution and the possibility of monitoring over large areas (Misra et al., 2020). Phenological dynamics are observed from stand level to tree level with optical sensors located on satellites and aerial platforms (Kleinsmann et al., 2023). However, data sources are not limited to these. In narrow areas, continuous monitoring methods such as Flux towers and PhenoCams are also used (Thapa et al., 2021). Especially in cloudy regions or times when obtaining optical images is difficult, SAR images are used (Li et al., 2023). Thanks to the high spatial resolution offered by nano satellite constellations such as PlanetScope, monitoring forest phenology at the tree level has become possible (Wu et al., 2021).

Vegetation indices are derived from formulas that combine different spectral bands of remote sensing imagery. In this way, the phenological states of forests are expressed numerically and can be used in analyses. The start and end times of phenological phases can be detected with the help of indices (Yan et al., 2025). The Normalized Difference Vegetation Index (NDVI) has been the most widely used metric in determining long term seasonal trends (Aktürk, 2024). However, this index remains insufficient in sensitively monitoring photosynthetic efficiency and stress conditions. In order to monitor more sensitively, physiological based indices such as the Photochemical Reflectance Index (PRI) have been developed (Liu et al., 2022). In addition, for RGB sensors with limited spectral band width, the Green Chromatic Coordinate (GCC) index, which is based on color changes in visible bands, has become the standard of phenological monitoring (Thapa et al., 2021).

The success of these developed indices is directly related to how the raw data are processed. When recent period studies are examined (2020–2025), it is seen that the harmonic regression (Maxwell et al., 2023) method is used in the analysis of index time series, and that traditional methods have left their place to deep learning algorithms such as ‘PhenoFormer’ (Katal et al., 2022; Sainte Fare Garnot et al., 2024). As a platform, it is seen that cloud based platforms such as Google Earth Engine (GEE) have taken the place of traditional desktop applications (Orusa et al., 2023).

In this section, in the light of the mentioned technological developments, based on the current literature published during the 2020–2025 period, the basic and innovative indices used in forest phenology will be addressed.

2. Spectral Basis of Vegetation Phenology

Vegetation indices help to monitor the changes shown by the interaction of forests with solar radiation during seasonal processes. In the time interval from leaf emergence to leaf fall, different physiological changes occur in the leaves of trees. We observe these changes with leaves that green in early spring and leaves that redden and yellow in autumn. The main reason for these color changes is the change in the amount of water and chlorophyll in the leaf and the biophysical changes occurring in the canopy structure. These changes create distinct differences in the visible (VIS) and near-infrared (NIR) bands. Vegetation indices make it possible to numerically represent phenological stages by increasing the contrast of these changes observed in the bands.

2.1 Vegetation Reflectance Characteristics Across Phenological Stages

Forests pass through different stages during phenological phases. Especially in deciduous forests, leaves appear green due to the high chlorophyll pigment content in spring and summer months. With autumn, when photosynthetic activity decreases, while the amount of chlorophyll in tree leaves decreases, carotenoid and anthocyanin become dominant. While carotenoid pigments cause leaves to appear yellow and orange in color, anthocyanin pigments cause the leaf to redden (Figure 1).

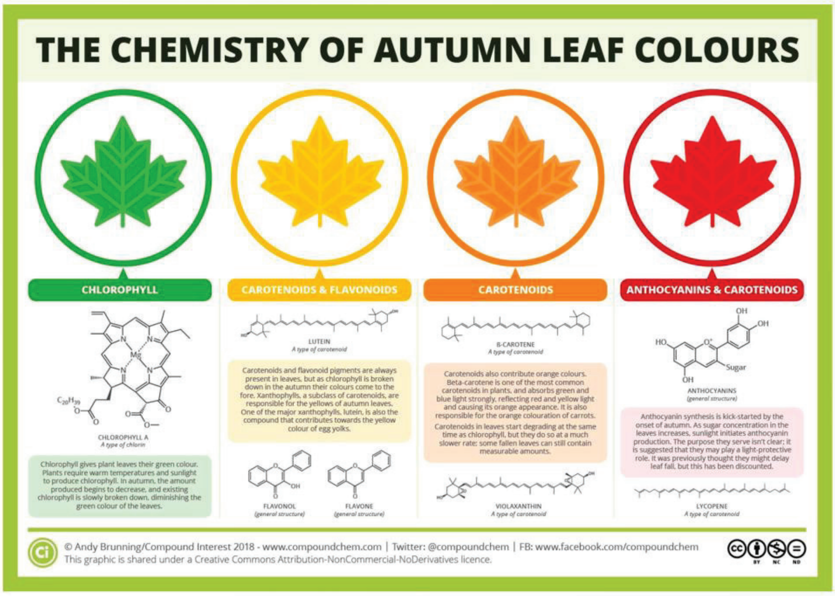

Chlorophyll gives plant leaves their green colour. Plants require warm temperatures and sunlight to produce chlorophyll. In autumn, the amount produced begins to decrease, and existing chlorophyll is slowly broken down, diminishing the green colour of the leaves.

Carotenoids and flavonoid pigments are always present in leaves, but as chlorophyll is broken down in the autumn their colours come to the fore. Xanthophylls, a subclass of carotenoids, are responsible for the yellows of autumn leaves. One of the major xanthophylls, lutein, is also the compound that contributes towards the yellow colour of egg yolks.

Carotenoids also contribute orange colours. Beta-carotene is one of the most common carotenoids in plants, and absorbs green and blue light strongly, reflecting red and yellow light and causing its orange appearance. It is also responsible for the orange colouration of carrots.

Carotenoids in leaves start degrading at the same time as chlorophyll, but they do so at a much slower rate: some fallen leaves can still contain measurable amounts.

Anthocyanin synthesis is kick-started by the onset of autumn. As sugar concentration in the leaves increases, sunlight initiates anthocyanin production. The purpose they serve isn't clear; it is suggested that they may play a light-protective role. It was previously thought they might delay leaf fall, but this has been discounted.

© Andy Brunning/Compound Interest 2018 - www.compoundchem.com | Twitter: @compoundchem | FB: www.facebook.com/compoundchem
This graphic is shared under a Creative Commons Attribution-NonCommercial-NoDerivatives licence.

Figure 1. Changes in leaf pigment chemistry depending on phenological stages (Buddenbaum & Hill, 2020). Figure credit: Andy Brunning / *Compound Interest* (CC BY 4.0).

These chemical processes occurring in leaves are reflected to sensors as different spectral signatures. Along with this, factors such as disease conditions of trees and water stress also affect these reflectance characteristics (Figure 2).

If we evaluate these changes according to phenological stages;

The Start of Season (SOS) stage is the period when leaves start to grow after budding. In this period, leaf area and the amount of chlorophyll in its content start to increase. While the increase in chlorophyll increases absorption in visible red channels, it starts to decrease reflectance values (Yan et al., 2025). Along with this, an increase begins in NIR reflectance values. The most critical change in the spectral curve occurs in the red edge region. The transition curve from red to NIR band becomes sharper. For this reason, the most sensitive regions in SOS determination are red, red edge, and NIR bands (Thapa et al., 2021). Since the leafing process continues and chlorophyll pigments do not reach their peak, SWIR bands show lower sensitivity.

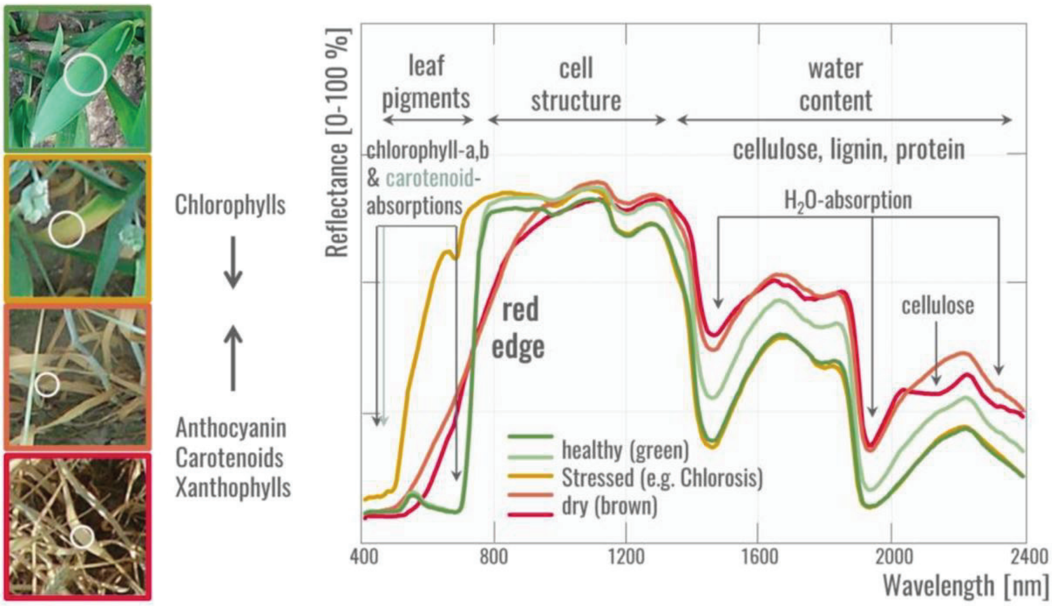

Figure 2. Figure 2. A schematic that conceptually shows the spectral reflectance behavior of vegetation in visible, near-infrared, and shortwave infrared bands; the changes depending on leaf pigments, cellular structure, water content, and physiological stress conditions (Buddenbaum & Hill, 2020). Photos courtesy of Theres Küster; spectra courtesy of Hermann Kaufmann.

Green-up / Leaf Expansion is the period when leaf area and chlorophyll content increase rapidly. After SOS, the expansion of leaf area causes an increase in photosynthetic activity. This increases NIR reflectance while strengthening absorption in the visible bands. In this stage, the most useful bands are still the NIR and red edge bands.

Peak of Season (POS) is the stage when photosynthetic activity reaches its peak and the densest leaf area is observed. In this stage, trees have the highest chlorophyll content and the most distinct crowns.

NIR reflectance remains at the highest level. However, in dense and closed canopies, the NDVI index calculated with NIR reaches saturation. In this period, even under the highest biomass conditions, red edge bands still have the best reflectance characteristics. SWIR bands in this stage mainly provide information about water content (Xu et al., 2021; Maxwell et al., 2023).

Mid-season / Maturity Phase is the period when spectral signals are the most stable. In this period, leaf area and chlorophyll content stabilize, and the spectral signature gains a plateau character. While no significant changes occur in VIS and NIR bands, fluctuations in water status can be observed in the SWIR band. For this reason, in time series, the maturity phase is evaluated as a stable phase (Gray & Ewers, 2021; Dronova & Taddeo, 2022).

The Senescence Onset stage is the stage when stability is disrupted due to changes in pigment composition as a result of chlorophyll degradation. While an increase in reflectance is observed in red and green bands, NIR band reflectance values decrease. These changes become particularly evident at the leaf and crown levels. Due to the relative effect of anthocyanins and carotenoids, visible bands have critical importance for monitoring phenological transitions at this stage (Wu et al., 2021; Guo et al., 2024). The onset of the aging process also causes a backward shift in the red edge region.

In the End of Season (EOS) stage, leaves have completely fallen. The replacement of chlorophyll by carotenoid and xanthophyll pigments shifts the reflectance spectrum toward yellow and orange wavelengths (Liu et al., 2022). However, before leaves begin to fall, narrowband green channels (526–536 nm) can be a precursor of activity decline (Liu et al., 2022). The cessation of photosynthetic activity reduces NIR reflectance to a minimum. In VIS bands, soil and woody surface effects are observed. In this period, SWIR bands reflect the effect of residual moisture content and structural components. In this way, they provide complementary information in determining EOS (Misra et al., 2020; Thapa et al., 2021; Orusa et al., 2023). Trees complete photosynthetic activity before leaf fall. Even if photosynthetic activity ends, leaves may still continue to appear green. Measurements made with optical channels can be misleading in EOS calculation here. However, SIF can clearly calculate the EOS date when photosynthetic activity stops, even before the tree shows a physical response to this.

2.2 Spectral Sensitivity of Optical Bands To Phenological Processes

The sensitivity of phenological signals to spectral bands varies depending on the leaf morphology of the species and the degree of seasonal structural change. In evergreen species, structural changes according to season are limited. For this reason, phenology is monitored through physiological channels. Structural indices show almost no change according to the phenological cycle. Narrow green bands (526–536 nm), which are used to capture changes in the xanthophyll cycle and pigment pool rather than chlorophyll amount, are used in the detection of phenological cycles (Liu et al., 2022). These channels can capture seasonal changes in the size of the internal pigment pool even if the external appearance of the plant remains green.

A conducted study has proven that MODIS ocean bands (especially Band 11, 526–536 nm) are much more sensitive than structural indices in monitoring terrestrial vegetation phenology. Especially in evergreen species, while optical channels remain insufficient in calculating EOS, the high accuracy of these bands has been surprising. This situation shows the underestimated importance of carotenoid pigments in monitoring plant seasonality (Liu et al., 2022).

3. Key Vegetation Indices for Forest Phenology

In monitoring phenological processes with remote sensing, vegetation indices transform multi-band spectral information into single metrics. In this form, instead of multi-band spectral information, they are used as indicators that facilitate and summarize temporal analyses. The phenology sensitivity at the spectral band level discussed in the previous section shows that each band becomes sensitive at different stages. Thanks to these band combinations, indices allow finer details to be captured according to specific phenological stages. Vegetation indices used in forest ecosystems are divided into three groups according to the type of phenological signal they capture: greenness-based, chlorophyll and pigment sensitive, and senescence- and stress-focused.

Figure 3. Sunburst representation of vegetation indices used according to phenological stages in forest ecosystems and the spectral bands to which these indices are sensitive. The inner ring shows phenological stages, the middle ring shows the related indices, and the outer ring shows the spectral bands on which the indices are based. Colors were selected to reflect seasonal transitions.

3.1 Greenness Based Indices

Greenness Based Indices are the main reference point in monitoring forest phenology (Aktürk, 2024). They characterize the structural properties of vegetation, the amount of green biomass, and the leaf area index (LAI) at the spectral level. The greenness-based indices discussed in this section are summarized in Table 1 together with the spectral bands they use and their basic characteristics.

The most fundamental index in this category is NDVI. It measures vegetation density and photosynthetic activity by using the contrast between red and near-infrared bands. This index mostly succeeds in capturing photosynthetic capacity and the SOS date (Rouse et al., 1974; Tucker, 1979; Zheng et al., 2022). The reason we state "mostly" is that this index reaches early saturation at the Peak of Season (POS) stage. In addition, it is also highly affected by background noise. Indices such as EVI and EVI2, which was produced for sensors without a blue band, are more resistant to these noises (Huete et al., 2002; Jiang et al., 2008; Kleinsmann et al., 2023).

One of the most remarkable innovations especially in recent years is the NIRv index. This innovation strengthens the relationship between vegetation structure and gross primary productivity (GPP) by combining near-infrared reflectance with NDVI. It has become a valuable index for the literature by minimizing noise especially in complex land cover types (Badgley et al., 2017; Yan et al., 2025). SAVI is known for its sensitivity to canopy structure. OSAVI, derived from SAVI, produces stable results even in sparse vegetation by normalizing soil reflectance (Huete, 1988; Kleinsmann et al., 2023; Yan et al., 2025).

kNDVI is a modern approach that models nonlinear relationships sensitively and overcomes the saturation effect by combining machine learning techniques with spectral analysis (Camps-Valls et al., 2021; Yan et al., 2025). GCC and ExG indices, which reveal millimetric color changes in the canopy through VIS bands, can quantify species-based phenological signals (Sonnentag et al., 2012; Hufkens et al., 2012; Thapa et al., 2021). IPVI is used in monitoring forest structure with its strong correlation with LAI (Toomey et al., 2015).

Indices such as GCC and NDVI mostly focus on the greenness level at the SOS stage. Unlike these, RCC can produce more sensitive results compared to other indices especially in determining the EOS period. The examined studies have revealed that while GCC increases with leaf development in spring, RCC generally shows an opposite trend, and these values show characteristic changes with leaf senescence in autumn (Klosterman & Richardson, 2017).

These Greenness Based Indices allow us to understand not only the greenness level of forest ecosystems, but also how species-based phenological patterns change thanks to the combination of spatial resolution and temporal continuity (Xu et al., 2021; Dronova & Taddeo, 2022).

Table 1. Greenness based vegetation indices commonly used in forest phenology studies, including their standard abbreviations, full names, literature references, and mathematical formulations.

Index	**Index name**	**Reference(s)**	**Formula**
NDVI	Normalized Difference Vegetation Index	(Rouse et al., 1974; Tucker, 1979)	(NIR − Red) / (NIR + Red)
kNDVI	Kernelized Normalized Difference Vegetation Index	(Camps-Valls et al., 2021)	$\tanh((2\sigma(\text{NIR} - \text{Red}))^2)$
NIRv	Near-Infrared Reflectance of Vegetation	(Badgley et al., 2017)	NIR × NDVI
IPVI	Infrared Percentage Vegetation Index	(Crippen, 1990)	NIR / (NIR + Red)
DVI	Difference Vegetation Index	(Richardson & Wiegand, 1977)	NIR − Red
SR	Simple Ratio Index	(Jordan, 1969)	NIR / Red
EVI	Enhanced Vegetation Index	(Huete et al., 2002)	G × (NIR − Red) / (NIR + C1 × Red − C2 × Blue + L)
EVI2	Two-band Enhanced Vegetation Index	(Jiang et al., 2008)	2.5 × (NIR − Red) / (NIR + 2.4 × Red + 1)
SAVI	Soil-Adjusted Vegetation Index	(Huete, 1988)	(NIR − Red) / (NIR + Red + L) × (1 + L)
OSAVI	Optimized Soil-Adjusted Vegetation Index	(Rondeaux et al., 1996)	(1 + 0.16) × (NIR − Red) / (NIR + Red + 0.16)
PPI	Plant Phenology Index	(Jin & Eklundh, 2014)	−K × ln((DVI − DVIsoil) / (DVImax − DVI))
VIgreen	Green–Red Normalized Difference Vegetation Index	(Rouse et al., 1974)	(Green − Red) / (Green + Red)
GCC	Green Chromatic Coordinate	(Sonnentag et al., 2012)	Green / (Red + Green + Blue)
RCC	Red Chromatic Coordinate	(Toomey et al., 2015)	Red / (Red + Green + Blue)
ExG	Excess Green Index	(Hufkens et al., 2012)	2 × Green − (Red + Blue)

3.2 Chlorophyll and Pigment Sensitive Indices

Chlorophyll and pigment sensitive indices are defined as advanced spectral parameters that monitor internal biochemical processes regulating photosynthetic activity and changes in pigment pools (chlorophyll, carotenoid, anthocyanin, and xanthophyll ratios), rather than structural changes of vegetation (leaf area or biomass) in forest phenology studies (Liu et al., 2022; Yan et al., 2025). Chlorophyll and Pigment Sensitive Indices are summarized in Table 2 together with the spectral bands they use and their basic characteristics. The most fundamental index of this category is PRI. This index directly reflects changes in the xanthophyll cycle and light use efficiency (LUE) (Gamon et al., 1992; Zhang et al., 2017).

Scaled PRI (sPRI), derived from MODIS ocean bands, is one of the innovations in the literature. The main feature that distinguishes these bands from other terrestrial bands is that they have a narrow band range (especially Band 11: 526–536 nm). Thanks to this feature, weak pigment signals that are lost in broad bands can be captured. sPRI can detect the xanthophyll cycle, which is an instantaneous defense mechanism against light stress, even at the satellite scale. In this way, it enables monitoring of invisible physiological phenology in evergreen forests with fixed LAI (Liu et al., 2022; Gamon et al., 2016).

CCI can track seasonal shifts in the ratio of chlorophyll to carotenoids. It is an index that provides important contributions in monitoring dormancy processes of conifers (Gamon et al., 2016; Yan et al., 2025). Indices such as CIre and NDRE capture the delay in chlorophyll synthesis after morphological growth in spring with the help of red edge bands. In this way, they refine SOS dates (Dong et al., 2015; Kleinsmann et al., 2023).

EBI and NDYI indices are better than greenness indices in monitoring reproductive phenology by using VIS bands. A plant being very green does not mean that it is flowering. These indices can capture the distinction between the two quite well. In forest phenology, especially in deciduous forests, they make it possible to separate flowering stages from leafing-related greenness signals through temporal analysis at the crown scale (Chen et al., 2019; d'Andrimont et al., 2020).

Anthocyanin and carotenoid sensitive indices such as ARI and CRI, and PSRI, can detect EOS with high accuracy by measuring the ratio of other pigments that become dominant after chlorophyll degradation with autumn senescence (Hill, 2013; Viña et al., 2012). Green-channel-focused indices such as GNDVI and CIG can overcome the saturation effect experienced by NDVI in dense forest canopies with high chlorophyll density, and can capture early leafing, stress-induced early yellowing, or physiological differences between species (Gao et al., 2024; Yan et al., 2025).

Table 2. Chlorophyll and pigment sensitive vegetation indices used in forest phenology studies, highlighting their primary physiological targets, spectral band dependencies, and mathematical formulations.

Index	**Index name**	**Reference(s)**	**Formula**
PRI	Photochemical Reflectance Index	(Gamon et al., 1992)	(R531 − R570) / (R531 + R570)
sPRI	Scaled Photochemical Reflectance Index	(Rahman et al., 2004)	((B11 − Bref) / (B11 + Bref) + 1) / 2
CCI	Chlorophyll/Carotenoid Index	(Gamon et al., 2016)	(B11 − B1) / (B11 + B1)
CIre	Chlorophyll Index Red-Edge	(Kleinsmann et al., 2023)	(NIR / RedEdge) − 1
NDRE	Normalized Difference Red-Edge Index	(Granero-Belinchón et al., 2020)	(NIR − RedEdge) / (NIR + RedEdge)
MTCI	MERIS Terrestrial Chlorophyll Index	(Dash & Ogutu, 2016)	(R753 − R708) / (R708 − R681)
GNDVI	Green Normalized Difference Vegetation Index	(Yan et al., 2025)	(NIR − Green) / (NIR + Green)
CIG	Chlorophyll Index Green	(Yan et al., 2025)	(NIR / Green) − 1
SIPI	Structure Insensitive Pigment Index	(Yan et al., 2025)	(NIR − Blue) / (NIR − Red)
ARI	Anthocyanin Reflectance Index	(Hill, 2013)	(1 / Green) − (1 / RedEdge)

CRI	Carotenoid Reflectance Index	(Hill, 2013)	(1 / Blue) − (1 / Green)
PSRI	Plant Senescence Reflectance Index	(Reyes-González et al., 2021)	(Red − Blue) / Green
NDYI	Normalized Difference Yellow Index	(d'Andrimont et al., 2020)	(Green − Blue) / (Green + Blue)
EBI	Enhanced Bloom Index	(Chen et al., 2019)	(Blue + Green + Red) / ((Blue / Green) × Red)
RGR	Red–Green Ratio	(Gamon et al., 1992)	Red / Green

3.3 Senescence and Stress-Related Indices

They are critical tools that monitor foliar degradation processes at the end of the vegetation growing season, changes in canopy water content, and physiological responses to environmental pressures (drought, frost, etc.) (Reyes-González et al., 2021; Dronova & Taddeo, 2022). The indices in this category are comprehensively presented in Table 3. Among these indices, PSRI is the most prominent index. This index sensitively determines changes in the ratio of carotenoids to chlorophyll in leaf content during senescence. In this way, it detects autumn transitions very well (Reyes-González et al., 2021; Yan et al., 2025).

RCC measures redness in the canopy. It is used as a basic indicator to quantify the leaf fall process during the EOS period (Toomey et al., 2015; Liu et al., 2020; Dronova & Taddeo, 2022). Water-content-sensitive indices such as NDWI, LSWI, and NDII can directly detect canopy water dynamics and drought-related phenological shifts through changes in tree water content (Delbart et al., 2005; Hill, 2013; Wu et al., 2014; Reyes-González et al., 2021).

The NFb index was developed to monitor changes in autumn leaf colors and especially browning. NDPI minimizes noise caused by snow cover or soil background. Thanks to the advantages they provide, these indices have enabled more accurate definition of seasonal cycles of forest ecosystems (Zhang et al., 2011; Wang et al., 2017; Reyes-González et al., 2021).

SIF (Solar-Induced Chlorophyll Fluorescence), one of the most modern and effective contributions in the literature, goes beyond being a reflectance index and measures the plant's "photosynthetic pulse," and can directly reveal that photosynthesis has stopped due to stress or dormancy (physiological phenology) even when the plant has not yet shed its green leaves (Magney et al., 2019; Dronova & Taddeo, 2022). Indicators such as NBR, which are used to monitor the condition of trees after forest fires and their responses under severe stress, provide important information in evaluating the resilience and recovery capacity of forest ecosystems (Yan et al., 2025).

Table 3. Senescence and stress-related spectral indices commonly used in forest phenology studies, with their formulations and key references.

Index	Index name	Reference(s)	Formula / Description
NDWI	Normalized Difference Water Index	Delbart et al., 2005	(NIR − SWIR_1) / (NIR + SWIR_1)
LSWI	Land Surface Water Index	Wu et al., 2014	(NIR − SWIR_2) / (NIR + SWIR_2)
NDII	Normalized Difference Infrared Index	Wang et al., 2017b	(NIR − SWIR) / (NIR + SWIR)
NDPI	Normalized Difference Phenology Index	Wang et al., 2017a	(NIR − (SWIR + Red)) / (NIR + (SWIR + Red))
NFb	Normalized Brownness Index	Zhang et al., 2011	1 − 1 / (1 + e^(a + b·t))
RCC	Red Chromatic Coordinate	Toomey et al., 2015	Red / (Red + Green + Blue)
NBR	Normalized Burn Ratio	Granero-Belinchon et al., 2020	(NIR − SWIR_2) / (NIR + SWIR_2)
PSRI	Plant Senescence Reflectance Index	Hill, 2013	(Red − Green) / NIR

4. Time-Series Analysis for Phenology Detection

Time series analysis is a fundamental methodology that enables the determination of critical phenometrics such as the start of the growing season (SOS), end of season (EOS), and peak of season (POS) by tracking seasonal changes in the spectral reflectance of vegetation over continuous data (Liu et al., 2022; Berra & Gaulton, 2021; Hu et al., 2024).

The most important feature of this analysis is that discrete data obtained from satellite or near-surface sensors are smoothed with mathematical methods such as the Savitzky–Golay filter, asymmetric Gaussian function, Fourier transform, or double logistic modeling, and transformed into continuous curves free from cloud, snow, and atmospheric noise (Zheng et al., 2022; Misra et al., 2016; Yan et al., 2025).

Among the most striking innovations in the literature are the use of deep learning architectures such as PhenoFormer by going beyond traditional threshold-based methods (Sainte Fare Garnot et al., 2024; Katal et al., 2022), multi-sensor data fusions such as Harmonized Landsat, Sentinel (HLS) (Bolton et al., 2020; Misra et al., 2020), and phenological monitoring at the individual tree crown scale using 3-meter resolution CubeSat data such as PlanetScope (Wu et al., 2021; Kleinsmann et al., 2023).

Thanks to these time series based approaches, forest phenology can be resolved in spatial and temporal dimensions not only as structural greening, but also as a complex biochemical cycle (Xu et al., 2021; Berra & Gaulton, 2021).

4.1 Preprocessing of vegetation index time series

Monitoring forest phenology using time series data of vegetation indices (VIs) requires a meticulous preprocessing process in order to remove atmospheric noise in raw data, ensure continuity, and extract meaningful biological stages (phenometrics). In the literature, this process is generally addressed in three main stages: data cleaning/masking, time series smoothing/reconstruction, and extraction of phenometrics (Zeng et al., 2020; Berra & Gaulton, 2021).

Data Cleaning, Masking, and Quality Control

Raw data acquired from remote sensing sensors may contain erroneous pixels. The first step to eliminate these is to use quality assurance layers such as MODIS (QA30) or Sentinel-2 (QA60/Sen2Cor) (Zheng et al., 2022; Misra et al., 2020). The obtained images are under the influence of noise such as clouds, shadows, aerosols, and haze. This situation distorts reflectance and causes results different from what they should be. Especially snow cover creates an artificial greenness signal on NDVI. This can cause deviation in the SOS date calculated with NDVI. In such cases, the snow effect needs to be filtered through masking, thresholding, alternative indices, and time series modeling (Sugiura et al., 2013; Jin et al., 2017). In addition, in order to normalize distortions caused by changes in the viewing angles of the sun and the sensor, Bidirectional Reflectance Distribution Function (BRDF) models are applied and reflectances are adjusted to a “nadir” viewing angle (Gray & Ewers, 2021; Wu et al., 2021). After these steps are completed, our data become ready for the next step as quality-controlled and cleaned.

Time-Series Smoothing and Reconstruction (Curve Fitting)

After cleaning the raw data, the stage of creating a continuous growth curve free from noise is entered. This stage is a critical preprocessing step used to obtain continuous daily data trajectories (Zheng et al., 2022). It is very critical in the accurate determination of phenometrics such as SOS and EOS. One of the methods used for this purpose is the Savitzky–Golay (S-G) filter. This filter reduces local noise without disrupting signal integrity (Chen et al., 2004; Zheng et al., 2022). In order to represent the growing season with a mathematical curve, Double Logistic and Asymmetric Gaussian functions are frequently used (Beck et al., 2006). Especially double logistic models are quite popular due to their ability to asymmetrically characterize the greening and senescence (aging) stages of vegetation (Zhang et al., 2003; Hu et al., 2024). To fill gaps in the time series, spline interpolation or Fourier filters that analyze periodic cycles are also among the alternative methods used (Thapa et al., 2021).

What stands out at this stage is innovative approaches. These approaches go beyond traditional mathematical models and come to the forefront in time series gap filling and trend detection processes with machine learning and deep learning based tools. DATimeS is a machine learning–based tool designed to solve the time series preprocessing, smoothing, and reconstruction problem. It fills gaps in time series with the help of machine learning–based regression models such as Gaussian Process Regression and statistical interpolations. As a result, it produces a biologically meaningful growth–senescence curve (Belda et al., 2020). The deep learning–based PhenoFormer is an innovative approach for reconstructing time series. This approach extracts the phenological structure of the time series from data rather than using manually defined mathematical forms. The model is robust to incomplete and irregular time series and produces not the smoothest curve, but the curve that best represents phenological transitions (Sainte Fare Garnot et al., 2024).

Extraction of Phenometrics

It is the conversion of seasonal transition dates into numerical phenological indicators based on the smoothed and reconstructed vegetation index curve. One of the commonly used approaches in the literature is threshold value methods. These are based on defining the days when the vegetation index reaches a certain percentage of its annual amplitude (for example 20% or 50%) as the start or end of the growing season (White et al., 2009; Zheng et al., 2022). However, fixed thresholds can produce inconsistent results under different latitude, climate, and species conditions. Determining the threshold value specifically according to these parameters increases the accuracy of phenological dates (Noumonvi et al., 2021). As an alternative to these, change point detection–based approaches are used. These approaches define the start and end of the season as the points where curvature reaches its maximum or the rate of change is highest (inflection points), by using the first, second, or third derivatives of the time series curve in order to capture phenological transitions in a more process-based manner (Zhang et al., 2003; Gonsamo et al., 2013; Thapa et al., 2021).

4.2 Interpretation and use of phenological metrics

The interpretation and use of phenological metrics are undergoing a major transformation from traditional greenness tracking toward the technical analysis of ecosystem functionality, biodiversity, and climate resilience (Dronova & Taddeo, 2022; Berra & Gaulton, 2021). These metrics go beyond merely calculating when a plant greens up and govern critical processes such as the carbon cycle and energy balance (Yan et al., 2025; Sainte Fare Garnot et al., 2024).

Biological and ecological interpretation of the metrics

Phenological metrics are fundamental indicators of the carbon cycle and energy balance in forest ecosystems. Especially temporal shifts in the dates when growth starts and ends directly affect the duration and intensity of photosynthetic activity. Detecting these shifts enables remote monitoring of changes in the annual carbon sequestration capacity of forests (Dronova & Taddeo, 2022). These changes stand out as a critical metric in the spatial- and species-level comparison of ecosystem responses to climate change (Hu et al., 2024). For example, the fact that some oak species leaf out early to avoid drought, while others leaf out up to six weeks later to protect themselves from frost and herbivorous insects, allows the ecosystem as a whole to gain buffering capacity against environmental risks (Gray & Ewers, 2021).

This interspecific phenological differentiation reflects not only the adaptive responses of individual species to environmental stresses, but also the holistic functioning and resilience of the ecosystem. For this reason, phenological metrics are today evaluated within the framework of Essential Biodiversity Variables (EBV), which allow monitoring ecosystem functionality and interspecific interactions (Dronova & Taddeo, 2022; Reyes-González et al., 2021). In this way, by monitoring phenological mismatches between the growth and flowering cycles of species and the activity timing of pollinating organisms, temporal shifts observed in phenological stages due to biodiversity loss can be interpreted as early warning signals of changes in energy and carbon fluxes in forest ecosystems (Dronova & Taddeo, 2022; Reyes-González et al., 2021).

Use of Metrics According to Species and Forest Structure

In forest phenology studies, the selection and interpretation of metrics (phenometrics) technically differ according to the species composition, structure of the forest, and the characteristics of the biome in which it is located. The most up-to-date approaches in the literature require the use of indices and models that are appropriate to the unique spectral and physiological dynamics of each forest structure (Dronova & Taddeo, 2022; Berra & Gaulton, 2021).

In Deciduous Broadleaf Forests (DBF), seasonal transitions are spectrally very pronounced, and phenometrics can generally be easily tracked through structural changes. Structural indices such as NDVI, EVI, and NIRv are quite successful in determining the start of season (SOS) and end of season (EOS) dates in DBF areas because they show high sensitivity to changes in leaf area index (LAI) and biomass (Liu et al., 2022; Yan et al., 2025). Since the processes of budburst and leaf expansion occur rapidly in these types, a sharp increase is observed in spectral curves (Kleinsmann et al., 2023). However, since NDVI can reach early saturation in broadleaf forests with dense canopy structure, the use of EVI or EVI2, which have higher resistance to saturation, provides more sensitive results in such areas (Yan et al., 2025; Huete et al., 2002).

In Evergreen Needleleaf Forests (ENF), since high color differences are not experienced in phenological processes, tracking through structural changes is limited. Traditional indices (NDVI, EVI) show weak correlation in determining SOS and EOS dates due to the low seasonal variation in greenness amount of evergreen trees. In this respect, it is one of the most technically challenging study areas (Bolton et al., 2020).

In Mixed Forests and Complex Structures (MF), the pixel-level signal reflects the phenological strategies of more than one species. For this reason, keeping threshold values fixed can lead to errors. In such forests, it is necessary to prefer dynamic thresholds optimized for species combinations (Noumonvi et al., 2021). Spatial resolution is important for monitoring phenology at the individual tree crown level. The use of high-resolution data such as PlanetScope (3 m) enables capturing 20–30 day phenological variations between species at the individual tree crown scale (Wu et al., 2021; Kleinsmann et al., 2023).

In Tropical and Aseasonal Forests, phenology proceeds asynchronously depending on precipitation regimes and sunlight duration. Since the crown diameter of most tropical trees is below 10 meters, it is difficult to monitor tropical phenology with traditional satellites (Wu et al., 2021). In these areas, CubeSat constellations with daily revisit frequency and UAV systems are of critical importance to capture short-term events such as budburst and fruiting (Gray & Ewers, 2021; Wang et al., 2020). Continuous cloud obstruction is encountered in these areas. Integrating with SAR data such as Sentinel-1, which are not affected by clouds, to fill gaps in optical data is a modern necessity for the continuity of phenological trajectories (Zhang et al., 2025; Yan et al., 2025).

Urban Forest Structures have different phenological calendars compared to natural forests due to the urban heat island effect. Due to concretized cities, temperatures are higher compared to surrounding rural settlements. This causes SOS dates in cities to occur earlier compared to rural areas, while causing delays in EOS dates (Hu et al., 2024). In these regions, OSAVI, which is resistant to soil effects, or EVI metrics, which normalize atmospheric effects, provide more reliable results than NDVI in monitoring urban vegetation dynamics in order to reduce parasitic effects such as sparse vegetation and building shadows (Kleinsmann et al., 2023; Hu et al., 2024; Yan et al., 2025).

Advanced Prediction and Monitoring Approaches

As a result of developments in the field of artificial intelligence and the models that have been produced, traditional methods continue to be replaced by machine/deep learning architectures. While phenometrics have traditionally been determined using mathematical curve fitting methods, recent approaches use deep learning architectures (Katal et al., 2022). Especially thanks to the self-attention mechanism they contain, transformer models can learn complex structures from time series and predict phenological stages (Sainte Fare Garnot et al., 2024). While doing this, not requiring a gap-filling process and being able to directly process irregular satellite data are among their greatest advantages (Tran et al., 2025). It has been determined that such innovative approaches show 11–13% higher accuracy compared to traditional machine learning models in out-of-distribution situations such as climate change (Sainte Fare Garnot et al., 2024). Long Short-Term Memory (LSTM) networks are used to model the memory effects of past meteorological conditions on forests (Liu et al., 2024). This method technically confirms that phenological awakening depends not only on instantaneous weather conditions but also on cumulative effects in previous months (Liu et al., 2024). New approaches that treat phenometric extraction as a dense regression problem increase prediction accuracy by estimating the temporal distance of each observation to the phenological event date. In this way, phenological transitions are defined using information distributed across the entire time series rather than being reduced to a single threshold or maximum point (Tran et al., 2025). The most important disadvantage of these deep learning strategies is that they require a large number of labeled data during training. Since it is not always possible to access a large amount of data, Self-Supervised Learning models have been developed to overcome this. For this purpose, Transformer models are pre-trained with millions of unlabeled satellite images, and then fine-tuned with a small number of ground observations to provide high-accuracy monitoring (Zhang et al., 2025).

It would be unfair to reduce advanced prediction and monitoring approaches only to deep learning and inference methods. Thanks to the integration of high-resolution satellite constellations and UAV data, forest phenology can be scaled to the tree crown level. High resolutions allow the detection of 20–30 day interspecific variations within forests (Wu et al., 2021; Kleinsmann et al., 2023). Harmonized Landsat and Sentinel-2 (HLS) data, combined with near-surface observations from PhenoCam networks (HP-LSP), eliminate spatial mismatches between satellite pixels and ground truth (Tran et al., 2025; Zhang et al., 2020). In forests, monitoring gene expression (qPCR and RNA-seq) enables the prediction of events such as flowering and budburst days before they become externally observable (Gray & Ewers, 2021).

5. Challenges and Limitations

Although the use of vegetation indices in monitoring forest phenology has the advantage of providing data over large areas, it faces significant technical limitations due to reasons such as the quality of the spectral signal, spatial scale, algorithm sensitivity, and the complexity of biological processes (Zeng et al., 2020; Berra & Gaulton, 2021). These limitations will be explained in two groups: classical problems and technical limitations, and innovative problems and limitations in deep learning architectures.

Classical Problems and Technical Limitations

Structural indices such as NDVI and EVI are insufficient in capturing seasonal variation in needleleaf forests where leaf amount remains constant throughout the year (Gamon et al., 2016). Low spectral amplitude leads to low correlation when extracting phenometrics with structural indices (Bolton et al., 2020; Liu et al., 2022). In deciduous forests, NDVI saturation occurs due to the presence of high biomass. This saturation causes difficulty in capturing critical developmental differences (Yan et al., 2025). In addition, changes in sun angle and sensor viewing angle (BRDF effect) cause fluctuations in index values even if there is no real change in vegetation (Thapa et al., 2021; Wang et al., 2020). In low spatial resolution data, a single pixel exists as a mixture of trees, understory, soil, and shadows, which causes the loss of species-level phenological signals. This situation results in the detection of earlier-than-actual SOS dates as scale increases (Noumonvi et al., 2021; Xu et al., 2021). Factors such as cloudiness, aerosols, and especially snow cover seriously distort index values (Shen et al., 2021). Sudden increases occurring in indices such as NDVI during snowmelt can create an artificial greening signal despite the absence of real biological growth, thereby distorting spring onset (SOS) dates (Jin et al., 2017; Cao et al., 2020).

Innovative Problems and Limitations in Deep Learning Architectures

Time series–based deep learning models such as CNN and LSTM cannot directly handle missing observations in the input data (Tran et al., 2025; Lobert et al., 2023). Before feeding these models, the gaps in the time series need to be filled with methods such as linear interpolation; this adds artificial noise to the model and reduces prediction accuracy and stability (B. Yang et al., 2022). CNN models scan the time series over a specific window (for example 3–5 neighboring daily points), therefore they learn only local dependencies (Tran et al., 2025). However, phenological processes include long-term temporal relationships based on "memory effects" originating months earlier; the failure of CNNs to capture these long-term dynamics increases uncertainty in phenometric predictions (Tran et al., 2025; Rußwurm & Körner, 2020). Although LSTM models are successful in predicting the general course and direction of forest canopy greenness, they generally struggle to accurately capture absolute index values and seasonal peak points in terms of magnitude (Liu et al., 2024).

Spatial mismatches between ground observations used to train deep learning models and satellite pixels lead to confusion and computational errors (Tran et al., 2022b). When a phenology label assigned to an individual tree is used to train a model with the average spectral signal of a 250–500 meter pixel, it can trigger systematic errors that cause the model to learn incorrect features (Ye et al., 2022).

6. Conclusions and Outlook

This book chapter focuses on presenting vegetation indices used in monitoring forest phenology within a holistic framework with their structural, physiological, and methodological dimensions. According to the reviewed studies, NDVI maintains its position as the most frequently used index in the literature due to its ease of calculation. However, it is limited because it reaches saturation in dense forest canopies and produces misleading greening signals by being affected by snow cover. EVI and its derivatives have largely reduced these limitations. Due to their higher sensitivity to canopy structure and resistance to atmospheric noise, they have produced successful results in tracking forest phenology.

One of the main outcomes is the necessity to consider forest phenology no longer only as a greening calendar, but as a multidimensional biological process directly related to the carbon cycle, energy balance, and ecosystem resilience. The evaluation of phenological metrics within the framework of Essential Biodiversity Variables (EBV) reveals that indicators such as interspecific asynchrony, length of season (LOS), and physiological awakening can be used as early warning signals of ecosystem responses to climate change. In this context, remote sensing–based phenology analysis becomes not only a descriptive but also a diagnostic and predictive tool.

Looking to the future, the most prominent trend is the integration of high spatial and temporal resolution with artificial intelligence–supported methods. Deep learning architectures such as Transformer and LSTM move phenometric extraction beyond approaches based on single thresholds by using information distributed across the entire time series, and they provide more stable results under conditions where data distributions shift, such as climate change. At the same time, thanks to the integration of PlanetScope, UAV, and PhenoCam data, phenological monitoring is shifted from the pixel scale to the individual tree crown scale, allowing intraspecific variations and microclimatic effects to be analyzed in detail at this level for the first time.

Finally, going beyond approaches based solely on optical data, the integration of active and physiologically sensitive sensors such as SIF, SAR, and LiDAR will play a key role in overcoming fundamental constraints such as cloudiness, saturation, and geometric effects. This multisensor and artificial intelligence–supported framework enables the operational-scale monitoring of forest phenology while providing a strong scientific infrastructure for decision support systems related to climate change, biodiversity loss, and forest health.

Acknowledgement

The authors acknowledge the EU COST (European Cooperation in Science and Technology) ant its Actions CA17134 “Optical Synergies For Spatiotemporal Sensing of Scalable Ecophysiological traits” (SENSECO) and Action CA22136 “Pan-European Network of Green Deal Agriculture and Forestry Earth Observation Science” (PANGEOS) for providing a platform for scientific networking and knowledge exchange related to this work.

References

Aktürk, E. (2024). Seasonal Vegetation Trends in Biomes of Türkiye: A Decade-Long (2014-2023) Analysis Using NDVI Time Series. *Bartın Orman Fakültesi Dergisi*, *26*(3), 1-1.

Badgley, G., Field, C. B., & Berry, J. A. (2017). Canopy near-infrared reflectance and terrestrial photosynthesis. *Science advances*, *3*(3), e1602244.

Beck, P. S., Atzberger, C., Høgda, K. A., Johansen, B., & Skidmore, A. K. (2006). Improved monitoring of vegetation dynamics at very high latitudes: A new method using MODIS NDVI. *Remote sensing of Environment*, *100*(3), 321-334.

Berra, E. F., & Gaulton, R. (2021). Remote sensing of temperate and boreal forest phenology: A review of progress, challenges and opportunities in the intercomparison of in-situ and satellite phenological metrics. *Forest Ecology and Management*, *480*, 118663.

Belda, S., Pipia, L., Morcillo-Pallarés, P., Rivera-Caicedo, J. P., Amin, E., De Grave, C., & Verrelst, J. (2020). DATimeS: A machine learning time series GUI toolbox for gap-filling and vegetation phenology trends detection. *Environmental Modelling & Software*, *127*, 104666.

Bolton, D. K., Gray, J. M., Melaas, E. K., Moon, M., Eklundh, L., & Friedl, M. A. (2020). Continental-scale land surface phenology from harmonized Landsat 8 and Sentinel-2 imagery. *Remote Sensing of Environment*, *240*, 111685.

Buddenbaum, H., & Hill, J. (2020). Imaging spectroscopy of forest ecosystems –

Exploiting the potential of hyperspectral data. HYPERedu, EnMAP education initiative, Trier University. Originally published August 2020, revised February 2023.

Camps-Valls, G., Campos-Taberner, M., Moreno-Martínez, Á., Walther, S., Duveiller, G., Cescatti, A., ... & Running, S. W. (2021). A unified vegetation index for quantifying the terrestrial biosphere. *Science Advances*, *7*(9), eabc7447.

Cao, M., Sun, Y., Jiang, X., Li, Z., & Xin, Q. (2021). Identifying leaf phenology of deciduous broadleaf forests from phenocam images using a convolutional neural network regression method. *Remote Sensing*, *13*(12), 2331.

Chen, J., Jönsson, P., Tamura, M., Gu, Z., Matsushita, B., & Eklundh, L. (2004). A simple method for reconstructing a high-quality NDVI time-series data set based on the Savitzky–Golay filter. *Remote sensing of Environment*, *91*(3-4), 332-344.

Chen, B., Jin, Y., & Brown, P. (2019). An enhanced bloom index for quantifying floral phenology using multi-scale remote sensing observations. *ISPRS Journal of Photogrammetry and Remote Sensing*, *156*, 108-120.

Crippen, R. E. (1990). Calculating the vegetation index faster. *Remote sensing of Environment*, *34*(1), 71-73.

Dash, J., & Ogutu, B. O. (2016). Recent advances in space-borne optical remote sensing systems for monitoring global terrestrial ecosystems. *Progress in Physical Geography*, *40*(2), 322-351.

d'Andrimont, R., Taymans, M., Lemoine, G., Ceglar, A., Yordanov, M., & van der Velde, M. (2020). Detecting flowering phenology in oil seed rape parcels with Sentinel-1 and-2 time series. *Remote sensing of environment*, *239*, 111660.

Delbart, N., Kergoat, L., Le Toan, T., Lhermitte, J., & Picard, G. (2005). Determination of phenological dates in boreal regions using normalized difference water index. *Remote Sensing of Environment*, *97*(1), 26-38.

Dronova, I., & Taddeo, S. (2022). Remote sensing of phenology: Towards the comprehensive indicators of plant community dynamics from species to regional scales. *Journal of Ecology*, *110*(7), 1460-1484.

Dong, T., Meng, J., Shang, J., Liu, J., & Wu, B. (2015). Evaluation of chlorophyll-related vegetation indices using simulated Sentinel-2 data for estimation of crop fraction of absorbed photosynthetically active radiation. *IEEE Journal of Selected Topics in Applied Earth Observations and Remote Sensing*, *8*(8), 4049-4059.

Gamon, J. A., Penuelas, J., & Field, C. B. (1992). A narrow-waveband spectral index that tracks diurnal changes in photosynthetic efficiency. *Remote Sensing of environment*, *41*(1), 35-44.

Gamon, J. A., Huemmrich, K. F., Wong, C. Y., Ensminger, I., Garrity, S., Hollinger, D. Y., ... & Peñuelas, J. (2016). A remotely sensed pigment index reveals photosynthetic phenology in evergreen conifers. *Proceedings of the National Academy of Sciences*, *113*(46), 13087-13092.

Gao, S., Yan, K., Liu, J., Pu, J., Zou, D., Qi, J., ... & Yan, G. (2024). Assessment of remote-sensed vegetation indices for estimating forest chlorophyll concentration. *Ecological Indicators*, *162*, 112001.

Gonsamo, A., Chen, J. M., & D'Odorico, P. (2013). Deriving land surface phenology indicators from CO2 eddy covariance measurements. *Ecological Indicators*, *29*, 203-207.

Guo, J., Liu, X., Ge, W., Zhao, L., Fan, W., Zhang, X., ... & Zhou, Z. (2024). Tracking photosynthetic phenology using spectral indices at the leaf and canopy scales in temperate evergreen and deciduous trees. *Agricultural and Forest Meteorology*, *344*, 109809.

Gray, R. E., & Ewers, R. M. (2021). Monitoring forest phenology in a changing world. *Forests*, *12*(3), 297.

Granero-Belinchon, C., Adeline, K., Lemonsu, A., & Briottet, X. (2020). Phenological dynamics characterization of alignment trees with Sentinel-2 imagery: A vegetation indices time series reconstruction methodology adapted to urban areas. *Remote Sensing*, *12*(4), 639.

Hill, M. J. (2013). Vegetation index suites as indicators of vegetation state in grassland and savanna: An analysis with simulated SENTINEL 2 data for a North American transect. *Remote Sensing of Environment*, *137*, 94-111.

Hu, M., Li, X., Xu, Y., Huang, Z., Chen, C., Chen, J., & Du, H. (2024). Remote sensing monitoring of the spatiotemporal dynamics of urban forest phenology and its response to climate and urbanization. *Urban Climate*, *53*, 101810

Huete, A. R. (1988). A soil-adjusted vegetation index (SAVI). *Remote Sensing of Environment*, *25*(3), 295–309..

Huete, A., Didan, K., Miura, T., Rodriguez, E. P., Gao, X., & Ferreira, L. G. (2002). Overview of the radiometric and biophysical performance of the MODIS vegetation indices. *Remote sensing of environment*, *83*(1-2), 195-213.

Hufkens, K., Friedl, M., Sonnentag, O., Braswell, B. H., Milliman, T., & Richardson, A. D. (2012). Linking near-surface and satellite remote sensing measurements of deciduous broadleaf forest phenology. *Remote Sensing of Environment*, *117*, 307-321.

Jiang, Z., Huete, A. R., Didan, K., & Miura, T. (2008). Development of a two-band enhanced vegetation index without a blue band. *Remote sensing of Environment*, *112*(10), 3833-3845.

Jin, H., & Eklundh, L. (2014). A physically based vegetation index for improved monitoring of plant phenology. *Remote Sensing of Environment*, *152*, 512-525.

Jordan, C. F. (1969). Derivation of leaf-area index from quality of light on the forest floor. *Ecology*, *50*(4), 663-666.

Katal, N., Rzanny, M., Mäder, P., & Wäldchen, J. (2022). Deep learning in plant phenological research: A systematic literature review. *Frontiers in Plant Science*, *13*, 805738.

Kleinsmann, J., Verbesselt, J., & Kooistra, L. (2023). Monitoring individual tree phenology in a multi-species forest using high resolution UAV images. *Remote Sensing*, *15*(14), 3599.

Klosterman, S., & Richardson, A. D. (2017). Observing spring and fall phenology in a deciduous forest with aerial drone imagery. *Sensors*, *17*(12), 2852.

Kumar, A., Khare, S., & Rossi, S. (2025). PhenoAI: A deep learning Python framework to process close-range time-lapse PhenoCam data. *Ecological Informatics*, *88*, 103134.

Li, R., Xia, H., Zhao, X., & Guo, Y. (2023). Mapping evergreen forests using new phenology index, time series Sentinel-1/2 and Google Earth Engine. *Ecological Indicators*, *149*, 110157.

Liu, Y., Wu, C., Sonnentag, O., Desai, A. R., & Wang, J. (2020). Using the red chromatic coordinate to characterize the phenology of forest canopy photosynthesis. *Agricultural and Forest Meteorology*, *285*, 107910.

Liu, Y., Wu, C., Tian, F., Wang, X., Gamon, J. A., Wong, C. Y., ... & Jassal, R. S. (2022). Modeling plant phenology by MODIS derived photochemical reflectance index (PRI). *Agricultural and Forest Meteorology*, *324*, 109095.

Liu, G., Migliavacca, M., Reimers, C., Kraft, B., Reichstein, M., Richardson, A. D., ... & Winkler, A. J. (2024). DeepPhenoMem V1. 0: deep learning modelling of canopy greenness dynamics accounting for multi-variate meteorological memory effects on vegetation phenology. *Geoscientific Model Development*, *17*(17), 6683-6701.

Lobert, F., Löw, J., Schwieder, M., Gocht, A., Schlund, M., Hostert, P., & Erasmi, S. (2023). A deep learning approach for deriving winter wheat phenology from optical and SAR time series at field level. *Remote Sensing of Environment*, *298*, 113800.

Magney, T. S., Bowling, D. R., Logan, B. A., Grossmann, K., Stutz, J., Blanken, P. D., ... & Frankenberg, C. (2019). Mechanistic evidence for tracking the seasonality of photosynthesis with solar-induced fluorescence. *Proceedings of the National Academy of Sciences*, *116*(24), 11640-11645.

Maxwell, A. E., Wilson, B. T., Holgerson, J. J., & Bester, M. S. (2023). Comparing harmonic regression and GLAD Phenology metrics for estimation of forest community types and aboveground live biomass within forest inventory and analysis plots. *International Journal of Applied Earth Observation and Geoinformation*, *122*, 103435.

Misra, G., Buras, A., & Menzel, A. (2016). Effects of different methods on the comparison between land surface and ground phenology—A methodological case study from south-western Germany. *Remote Sensing*, *8*(9), 753.

Misra, G., Cawkwell, F., & Wingler, A. (2020). Status of phenological research using Sentinel-2 data: A review. *Remote Sensing*, *12*(17), 2760.

Noumonvi, K. D., Oblišar, G., Žust, A., & Vilhar, U. (2021). Empirical approach for modelling tree phenology in mixed forests using remote sensing. *Remote Sensing*, *13*(15), 3015.

Orusa, T., Viani, A., Cammareri, D., & Borgogno Mondino, E. (2023). A google earth engine algorithm to map phenological metrics in mountain areas worldwide with landsat collection and sentinel-2. *Geomatics*, *3*(1), 221-238.

Rahman, A. F., Cordova, V. D., Gamon, J. A., Schmid, H. P., & Sims, D. A. (2004). Potential of MODIS ocean bands for estimating CO2 flux from terrestrial vegetation: A novel approach. *Geophysical Research Letters*, *31*(10).

Reyes-Gonzalez, E. R., Gomez-Mendoza, L., Barradas, V. L., & Teran-Cuevas, A. R. (2021). Cross-scale phenological monitoring in forest ecosystems: a content-analysis-based review. *International Journal of Biometeorology*, *65*(12), 2215-2227.

Richardson, A. J., & Weigand, C. L. (1977). Distinguishing vegetation from soil background information. *Photogrammetric engineering and remote sensing*, *43*(12).

Rußwurm, M., & Körner, M. (2020). Self-attention for raw optical satellite time series classification. *ISPRS journal of photogrammetry and remote sensing*, *169*, 421-435.

Rondeaux, G., Steven, M., & Baret, F. (1996). Optimization of soil-adjusted vegetation indices. *Remote sensing of environment*, *55*(2), 95-107.

Rouse, J. W., Haas, R. H., Schell, J. A., & Deering, D. W. (1974). Monitoring vegetation systems in the great plains with ERTS proceeding. In *Third earth reserves technology satellite symposium, greenbelt: NASA SP-351* (Vol. 30103017, p. 317).

Sainte Fare Garnot, V., Spafford, L., Lever, J., Sigg, C., Pietragalla, B., Vitasse, Y., ... & Wegner, J. D. (2024). Deep learning meets tree phenology modeling: PhenoFormer vs. process-based models. *arXiv e-prints*, arXiv-2410.

Sonnentag, O., Hufkens, K., Teshera-Sterne, C., Young, A. M., Friedl, M., Braswell, B. H., ... & Richardson, A. D. (2012). Digital repeat photography for phenological research in forest ecosystems. *Agricultural and Forest Meteorology*, *152*, 159-177.

Thapa, S., Garcia Millan, V. E., & Eklundh, L. (2021). Assessing forest phenology: a multi-scale comparison of near-surface (UAV, spectral reflectance sensor, phenocam) and satellite (MODIS, sentinel-2) remote sensing. *Remote Sensing*, *13*(8), 1597.

Toomey, M., Friedl, M. A., Frolking, S., Hufkens, K., Klosterman, S., Sonnentag, O., ... & Richardson, A. D. (2015). Greenness indices from digital cameras predict the timing and seasonal dynamics of canopy-scale photosynthesis. *Ecological Applications*, *25*(1), 99-115.

Tucker, C. J. (1979). Red and photographic infrared linear combinations for monitoring vegetation. *Remote sensing of Environment*, *8*(2), 127-150.

Tran, K. H., Zhang, X., Zhang, H. K., Shen, Y., Ye, Y., Liu, Y., ... & An, S. (2025). A transformer-based model for detecting land surface phenology from the irregular harmonized Landsat and Sentinel-2 time series across the United States. *Remote Sensing of Environment*, *320*, 114656.

Vaswani, A., Shazeer, N., Parmar, N., Uszkoreit, J., Jones, L., Gomez, A. N., ... & Polosukhin, I. (2017). Attention is all you need. *Advances in neural information processing systems*, *30*.

Viña, A., Tuanmu, M. N., Xu, W., Li, Y., Qi, J., Ouyang, Z., & Liu, J. (2012). Relationship between floristic similarity and vegetated land surface phenology: Implications for the synoptic monitoring of species diversity at broad geographic regions. *Remote Sensing of Environment*, *121*, 488-496.

Wang, C., Li, J., Liu, Q., Zhong, B., Wu, S., & Xia, C. (2017a). Analysis of differences in phenology extracted from the enhanced vegetation index and the leaf area index. *Sensors*, *17*(9), 1982.

Wang, X., Xiao, J., Li, X., Cheng, G., Ma, M., Che, T., ... & Wu, J. (2017b). No consistent evidence for advancing or delaying trends in spring phenology on the Tibetan Plateau. *Journal of Geophysical Research: Biogeosciences*, *122*(12), 3288-3305.

White, M. A., de Beurs, K. M., Didan, K., Inouye, D. W., Richardson, A. D., Jensen, O. P., ... & Lauenroth, W. K. (2009). Intercomparison, interpretation, and assessment of spring phenology in North America estimated from remote sensing for 1982–2006. *Global change biology*, *15*(10), 2335-2359.

Wu, C., Gonsamo, A., Gough, C. M., Chen, J. M., & Xu, S. (2014). Modeling growing season phenology in North American forests using seasonal mean vegetation indices from MODIS. *Remote Sensing of Environment*, *147*, 79-88.

Wu, S., Wang, J., Yan, Z., Song, G., Chen, Y., Ma, Q., ... & Wu, J. (2021). Monitoring tree-crown scale autumn leaf phenology in a temperate forest with an integration of PlanetScope and drone remote sensing observations. *ISPRS Journal of Photogrammetry and Remote Sensing*, *171*, 36-48.

Xu, K., Zhang, Z., Yu, W., Zhao, P., Yue, J., Deng, Y., & Geng, J. (2021). How spatial resolution affects forest phenology and tree-species classification based on satellite and up-scaled time-series images. *Remote Sensing*, *13*(14), 2716.

Xu, R., Zhao, S., & Ke, Y. (2020). A simple phenology-based vegetation index for mapping invasive spartina alterniflora using Google Earth engine. *IEEE Journal of Selected Topics in Applied Earth Observations and Remote Sensing*, *14*, 190-201.

Yan, K., Gao, S., Yan, G., Ma, X., Chen, X., Zhu, P., ... & Wang, Q. (2025). A global systematic review of the remote sensing vegetation indices. *International Journal of Applied Earth Observation and Geoinformation*, *139*, 104560.

Zeng, L., Wardlow, B. D., Xiang, D., Hu, S., & Li, D. (2020). A review of vegetation phenological metrics extraction using time-series, multispectral satellite data. *Remote Sensing of Environment*, *237*, 111511.

Zhang, X., Friedl, M. A., Schaaf, C. B., Strahler, A. H., Hodges, J. C., Gao, F., ... & Huete, A. (2003). Monitoring vegetation phenology using MODIS. *Remote sensing of environment*, *84*(3), 471-475.

Zhang, X., & Goldberg, M. D. (2011). Monitoring fall foliage coloration dynamics using time-series satellite data. *Remote Sensing of Environment*, *115*(2), 382-391.

Zhang, M., Li, G., Lu, D., Xu, C., Zhao, H., & Li, D. (2025). Self-supervised deep learning for detection of forest disturbance types in a subtropical ecosystem using transformer and Sentinel-1 and Sentinel-2 time series data. *International Journal of Digital Earth*, *18*(1), 2537325.

Zheng, W., Liu, Y., Yang, X., & Fan, W. (2022). Spatiotemporal variations of forest vegetation phenology and its response to climate change in northeast China. *Remote Sensing*, *14*(12), 2909.